Characterization and numerical simulation of liquid refrigerant flow emerging from a flooded evaporator tube bundle

by

William Evan Asher

B.S., Kansas State University, 2008
M.S., Kansas State University, 2014

AN ABSTRACT OF A DISSERTATION

submitted in partial fulfillment of the requirements for the degree

DOCTOR OF PHILOSOPHY

Department of Mechanical and Nuclear Engineering
College of Engineering

KANSAS STATE UNIVERSITY
Manhattan, Kansas

2019

Abstract

The distribution of liquid droplets emerging from an evaporator tube bundle is characterized for refrigerants R-123 and R-134a with a triangular and rotated triangular tube arrangement with a pitch of 1.167. The purpose of this research was to improve understanding of the droplet ejection process to aid in design of evaporators typically used in larger chiller systems. A laser and camera system captured images of the evaporator headspace at varying conditions. Conventional shadowgraphy techniques were applied to recognize and match droplets for velocity calculations. The evaporator conditions were varied with mass fluxes from 3.5 to 40.7 kg/s-m^2 (2250 to 30000 lb/hr-ft^2), top-rows heat fluxes from 5.3 to 31.5 kW/m^2 (1700 to 10000 Btu/hr-ft^2), and outlet saturation temperatures of 4.4 and 12.8 °C (40 and 55 °F). Conditions ranged from flooded to dryout on the top rows. Droplet number, size distribution, velocity, and liquid volume fraction are presented in the headspace above the bundle. A method to numerically duplicate the droplet loading in the headspace using CFD with a Lagrangian discrete-phase model is also presented and verified with R-134a and a triangular arrangement, providing a powerful design tool. Liquid distribution in the headspace is found to be a strong function of all varied properties, particularly mass flux, liquid level, and saturation temperature. Vapor shear is thought to lead to the majority of droplets generated, especially in the upper headspace. The high liquid-vapor density ratio of R-123 and corresponding high velocities make it particularly difficult to separate liquid droplets before they escape the tube bundle.

Characterization and numerical simulation of liquid refrigerant flow emerging from a flooded evaporator tube bundle

by

William Evan Asher

B.S., Kansas State University, 2008
M.S., Kansas State University, 2014

A DISSERTATION

submitted in partial fulfillment of the requirements for the degree

DOCTOR OF PHILOSOPHY

Department of Mechanical and Nuclear Engineering
College of Engineering

KANSAS STATE UNIVERSITY
Manhattan, Kansas

2019

Approved by:

Major Professor
Steven J. Eckels

Copyright

Abstract

The distribution of liquid droplets emerging from an evaporator tube bundle is characterized for refrigerants R-123 and R-134a with a triangular and rotated triangular tube arrangement with a pitch of 1.167. The purpose of this research was to improve understanding of the droplet ejection process to aid in design of evaporators typically used in larger chiller systems. A laser and camera system captured images of the evaporator headspace at varying conditions. Conventional shadowgraphy techniques were applied to recognize and match droplets for velocity calculations. The evaporator conditions were varied with mass fluxes from 3.5 to 40.7 kg/s-m^2 (2250 to 30000 lb/hr-ft^2), top-rows heat fluxes from 5.3 to 31.5 kW/m^2 (1700 to 10000 Btu/hr-ft^2), and outlet saturation temperatures of 4.4 and 12.8 °C (40 and 55 °F). Conditions ranged from flooded to dryout on the top rows. Droplet number, size distribution, velocity, and liquid volume fraction are presented in the headspace above the bundle. A method to numerically duplicate the droplet loading in the headspace using CFD with a Lagrangian discrete-phase model is also presented and verified with R-134a and a triangular arrangement, providing a powerful design tool. Liquid distribution in the headspace is found to be a strong function of all varied properties, particularly mass flux, liquid level, and saturation temperature. Vapor shear is thought to lead to the majority of droplets generated, especially in the upper headspace. The high liquid-vapor density ratio of R-123 and corresponding high velocities make it particularly difficult to separate liquid droplets before they escape the tube bundle.

Table of Contents

List of Figures

List of Tables

Acknowledgements

The author would like to thank ASHRAE Technical Committees 1.3, Heat Transfer and Fluid Flow and 8.5, Liquid to Refrigerant Heat Exchangers for their expertise and guidance with this work as a part of the research and report for RP-1556 [1], especially the members of the PMS. Gratitude is also given to Wolverine for their donation of the enhanced tubes used in this project.

Funding for this research was also partially obtained from the Institute for Environmental Research (IER). IER is a multidisciplinary research group focused on heat transfer and interactions of humans with the environment. Research on human interactions with environment focus on clothing and personal cooling systems [2-8]. Heat transfer research ranges from work on environmentally friendly refrigerants [9-17] to enhanced heat transfer surfaces [18-21].

Nomenclature

a	Acceleration (m/s^2 or ft/s^2)
A	Surface area (m^2 or ft^2)
A_c	Between-tube cross-sectional area (m^2 or ft^2)
C	Heat transfer correction coefficient for Wilson plot
C_{drag}	Drag coefficient
C_{ij}	Convection of Reynolds stresses
c_p	Specific heat (J/kg-K or Btu/lb-°R)
d	Droplet diameter (µm)
$\bar{d}$	Mean droplet diameter of Rosin-Rammler curve (m)
d_{max}	Maximum droplet diameter of Rosin-Rammler curve (m)
d_{min}	Minimum droplet diameter of Rosin-Rammler curve (m)
D	Diameter (m or µm)
$\bar{D}$	Average droplet diameter (mm)
$D_{L,ij}$	Molecular diffusion of Reynolds stresses
$D_{T,ij}$	Turbulent diffusion of Reynolds stresses
e	Euler's number
F	Force (N)
$\vec{F}$	Force vector or discrete phase additional acceleration term
F_{ij}	Production of Reynolds stresses by system rotation
G	Mass flux (kg/m^2-s b/hr-ft^2)
G_{ij}	Buoyancy production of Reynolds stresses
$\vec{g}$	Gravitational acceleration (m/s^2 or ft/s^2)
H	Bin height (mm)
h	Specific enthalpy (J/kg or Btu/lb)
h_i	Inner tube heat transfer coefficient (W/m^2-K or Btu/hr-ft^2-°R)
h_o	Outer tube heat transfer coefficient (W/m^2-K or Btu/hr-ft^2-°R)
k	Shape parameter of Rosin-Rammler curve
I	Unit tensor
m	Mass (kg)
$\dot{m}$	Mass flow rate (kg/s or lb/hr)
$\dot{m}_v$	Mass liquid flow rate per binned velocity, all diameters (kg/s)
$\dot{m}_{v,d}$	Mass liquid flow rate per binned velocity and per binned diameter (kg/s)

$\dot{m}_T$	Total mass liquid- flow rate (kg/s)
n	Number of droplets or shape parameter of Rosin-Rammler curve
P	Pressure (Pa or PSI)
P_{ij}	Production of Reynolds stresses
p	Static pressure (Pa)
q	Heat transfer (kW or Btu/hr)
q''	Heat flux (kW/m^2 or Btu/hr-ft^2)
Re	Reynolds number
R_w	Wall resistance (K/kW or °R-hr/Btu)
S_m	Continuity equation source term
S_{user}	Source term of Reynolds stresses defined by user
T	Temperature (°C or °F)
t	Time (s)
U_ϕ	Uncertainty, liquid volume fraction
v	Vertical velocity (m/s)
V	Volume (mm^3)
W	Bin width (mm)
x	Quality
Y	Height coordinate (mm)
Y_d	Cumulative mass fraction based on droplet diameter
Y_v	Cumulative mass fraction based on droplet velocity

Abbreviations

CFD	Computational fluid dynamics
DOF	Depth of focus (mm)
DPM	Discrete phase model
$LMTD$	Log mean temperature difference (K or °R)
PIV	Particle image velocimetry
RANS	Reynolds-averaged Navier-Stokes
RSM	Reynolds stress model
VFD	Variable frequency drive
VI	Virtual instrument

Greek Symbols

Δt	Time between images (ns)
ε_{ij}	Dissipation of Reynolds stresses
ϕ	Liquid volume fraction
φ_{ij}	Pressure strain from Reynolds stresses
π	Pi
ρ	Density (kg/m^3 or lb/ft^3)
ρ_d	Particle density
μ	Viscosity (m^2/s)

$\bar{\bar{\tau}}$	Stress tensor (N/m^2)
τ_r	Droplet relaxation time

Subscripts

$2nd\ row$	second from top row
A	image A
B	image B
bin	per bin
$bundle$	total bundle
$buoyancy$	buoyancy
$droplet$	droplet
$gravity$	gravity
$high$	denotes high bound of bin
low	denotes low bound of bin
i	inner or Einstein notation index
i	Einstein notation index
in	tube inlet
l	liquid
o	outer
out	tube outlet
pb	pre-boiler
r	refrigerant
ts	test section
$top\ row$	top row
v	vapor
$tube$	per tube
w	water
x	x-component

Operators

∇	Del
δ_{ij}	Kronecker delta

Chapter 1 - Introduction and Literature Review

Control of liquid carryover in most larger refrigeration systems of shell-and-tube construction is a significant design issue. Achieving control requires an understanding of the mechanisms that create liquid droplets and methods of preventing migration of liquid droplets out of the evaporator. Two primary mechanisms assumed to play a role in the formation of droplets are shear and wave action. High vapor velocity causes shear in the bundle that entrains droplets into the flow. Depending on liquid distribution within the bundle, a liquid layer may exist above the bundle. The wave action of this layer may form droplets that entrain into the vapor flow. Aerodynamic forces, gravity, and droplet morphology are thought to control the migration of the liquid droplets once in the evaporator headspace. The refrigerant used, capacity of the chiller, and bundle geometry determine gas velocities within the bundle and headspace. These velocities are crucial in droplet carryover. With low-pressure refrigerant R-123, a vapor velocity of 15 m s^{-1} in the gaps between tubes can be expected, capable of lifting droplets of millimeter scale. For the same conditions, a refrigerant such as R-134a will only have a velocity of 2 m s^{-1}, reducing expected droplets to sub-millimeter size. Vapor in the headspace slows as the cross-sectional area increases and larger droplets fall back onto the bundle. Evaporation of liquid in the headspace, dictated by the thermodynamic conditions of the flow, can also affect droplet morphology. Slightly superheated vapor with saturated liquid droplets in the flow field can occur, wherein droplets may evaporate as they flow through the headspace. Droplets may impact upon the walls of the headspace and objects such as distribution plates placed in the path of the flow. Finally, droplets can coalesce into larger droplets, exceeding the carrying capacity of the vapor and falling back to the bundle. Experimental data would allow the means to understand the relative impact of aerodynamic forces, thermodynamics (heat transfer), and wave breakup, enabling better headspace design.

The goal of the research project was to experimentally record the liquid droplets that emerge from the top of a tube bundle under typical operating conditions. Data generated includes droplet position, velocity, and size within the headspace of the bundle for varied operating conditions. The experimental data should provide insight into the physics that control movement and liquid formation within the headspace, providing critical validation data for those doing numerical simulation.

1.1 Bundle Heat Transfer and Pressure Drop

The large experimental facilities required for research lead to shell-side evaporator performance receiving significantly less experimentation in the past than other evaporation arrangements. The study of local heat transfer and pressure drop as refrigerant flows through enhanced-tube bundles primarily using 19.05 mm (0.75 inch) tubes with a standard pitch of 1.167 is one important class of experiments with refrigerant shell-side evaporators. Van Rooyen and Thome [22] [23] studied R-134a and R-236fa in enhanced-tube bundles, documenting local heat transfer coefficients and pressure drop in the bundle. Gorgy and Eckels [13] documented similar data for R-123 and R-134a on enhanced-tube bundles of standard pitch while with the same facility results for variable-pitch bundles were given for R-134a by Gorgy and Eckels [14], and for R-123 [15]. Robinson and Thome [24] studied R-134a, R-410A, and R-507A in a similar bundle of standard pitch. All four heat-transfer studies had saturation temperatures of 4 and 15 °C, mass fluxes from 4 to 55 kg $s^{-1}m^{-2}$, and heat fluxes from 15 to 70 kW m^{-1}. Ribatski, Saiz Jabardo and da Silva [25] investigated R-123 nucleate boiling on arrays of horizontal tubes with various pitches and heat fluxes from 0.5 to 40 kW m^{-2}, obtaining a correlation for heat-transfer coefficients. In Kondo [26], pressure drop across various horizontal tube bundles for mixtures of air and water were measured. In none of these experiments was the headspace observed.

1.2 Bundle Flow Patterns

Flow-pattern studies within the bundle represent another class of experiments done on this standard rectangular bundle. van Rooyen, Agostini, Borhani and Thome [27] used a clear dummy tube with a digital high-speed video camera and a laser light/photodiode, as well as pressure-drop measurements, to predict internal flow patterns. Schlup and Eckels [28] also report flow patterns in an enhanced-tube bundle by using a borescope and complementing experimental data with numerical analysis. Kanizawa and Ribatski [29] studied vertical air-water flow across a tube bundle, using both pressure drop and capacitive sensors to quantify void fractions and flow patterns within the bundle. Development of flow-pattern maps from flow-visualization data has been attempted in a number of studies [30-33].

1.3 Liquid Visualization

The current study used a shadowgraphy technique to characterize droplets. With this method, a camera captures images of objects backlit by a light source, with the objects being delineated from their transparent medium by differences in refraction and opacity. Specifically, the objects are illuminated by the light source, and the area that the camera sees consists of a bright background with dark areas corresponding to the objects' boundaries. For this work, a dual-pulse Nd-Yag laser was the light source and a 4-megapixel camera was used. Of note, the equipment used in this work can also be used for particle image velocimetry (PIV) applications such as in Li, Eckels, Mann and Zhang [18]. In Dai, Chou and Faeth [34], both a single- and double-pulsed laser system were coupled with a film camera to capture droplet formation from turbulent liquid wall jets. Hay, Liu and Hanratty [35] incorporated use of a CCD sensor instead of film to speed processing in order to verify characteristics of two-phase annular flow in a vertical pipe. For Patruno, Marchioro Ystad, Marchetti, Dorao, Svendsen and Jakobsen [36] shadowgraphy was incorporated by use of a continuous white light source coupled with a high-speed digital camera to capture data on liquid entrainment from a wetted wire in high-gas-flow-rate cross flow. Castrejón-García, Castrejón-Pita, Martin and Hutchings [37] applied a shadowgraphy technique using an SLR camera to characterize both jets and inkjet spray. To apply shadowgraphy to characterize diesel injector spray, Blaisot and Yon [38] used nanosecond flash lamps with a CCD camera with microscope optics, as well as described a method to account for out-of-focus droplets. Both Kashdan, Shrimpton and Whybrew [39] and Kashdan, Shrimpton and Whybrew [40] described development and use of an analysis technique to improve accounting of out-of-focus droplets and use of an infra-red diode laser, coupled with a CCD camera, to compare results with those of phase-Doppler anemometry for small fuel droplets produced by a pressure-swirl atomizer. Legrand, Nogueira, Lecuona and Hernando [41] demonstrated a method to develop 3-D droplet data using only a single camera by observing defocus of droplets and their overlap. The methods chosen for this work most closely follow the methods of Hay, Liu and Hanratty [35].

1.4 Intra-bundle Numerical Simulation

A final class of tube bundle research involves numerical simulation of two-phase pool boiling. Ahmadpour, Noori Rahim Abadi and Meyer [42] used a Eulerian-Eulerian approach with a two-dimensional model to predict volume fraction within a bundle for a variety of refrigerants at a variety of conditions, achieving good agreement with the experimental results of Gupta [43], Jung, Kim, Ko and Song [44], and Kang [45]. Ahmadpour was inspired by the work of Minocha, Joshi, Nayak and Vijayan [46], which again used an Eulerian-Eulerian approach, albeit with a three-dimensional volume-of-fluid model. However, all these numerical simulations have been within the bundle, with no attention paid to the headspace. To date, no numerical simulations have been found modeling the headspace of evaporator bundles beyond the work of Asher and Eckels [47].

1.5 Numerical Studies

While there exists a lack of literature regarding numerical simulation of the headspace itself, many works have explored single and multi-phase numerical simulations in other applications. To find the single-phase vapor flow field, this work uses the finite-volume method ANSYS Fluent employing the Reynolds averaged Navier-Stokes (RANS) model combined with the Reynolds stress model (RSM) in order to close the equations [48, 49]. Many other programs, methods, and models can be employed, however. Among the other possible methods are large eddy simulation (LES) and direct numerical simulation (DNS). DNS does not require modeling, but is unsuitable for high Reynolds number flow due to the memory and CPU constraints it would impose. LES lies in a middle ground between RANS and DNS in terms of both computing cost and the ability to model the whole of turbulent scales that may exist. With LES, small eddies are modeled while large eddies are solved directly [48].

In order to simulate droplets in this work, the discrete phase model of Fluent (a Eulerian-Lagrangian approach) was employed [48]. With this method, the dispersed phase (in this work, droplets) is solved by tracking large numbers of discrete droplet by integrating a force balance on each droplet, with the forces partially being from the continuous vapor flow field already solved from the Navier-Stokes equations. This is commonly referred to as the discrete phase model (DPM). This approach is far from the only method with which dispersed items (droplets, particles, bubbles) can be simulated.

The two methods for dealing with multiphase flow are the Eulerian-Lagrangian approach and the Eulerian-Eulerian. The Eulerian-Lagrangian method was previously described. The Eulerian-Eulerian approach, wherein the focus is on the fluid motion in a specific location, is used to model separate yet interacting phases. Three different models are used with the Eulerian-Eulerian approach: volume of fluid (VOF), the Eulerian model, and the mixture model. The VOF model is largely used where the position of the interface between separate fluids is desired, but requires a mesh size smaller than the dispersed region of interest. The mixture model is largely used when the phases move at similar velocities in a homogeneous flow. The Eulerian model is used to model separate but interacting phases. For modeling of droplets, bubbles, or particles in a flow, the mixture model and Eulerian model are suggested [48]. Table 1.1 lists a multitude of works that modeled items such as bubbles, droplets, and particles interacting with a flow, including some that combined methods.

Table 1.1 Examples of multiphase numerical simulation publications

Source	Method	Phases of interest	Description
Bagul, Pilkhwal, Vijayan and Joshi [50]	DPM	Liquid in vapor	Simulation using OpenFOAM to model water droplets in air in Advanced Heavy Water Reactor separation drum. Compared with experimental results.
Beetham and Capecelatro [51]	DPM	Solid in vapor	Solid biomass and sand particles simulated in nitrogen for a vertical riser. Includes heat transfer and chemical reactions. Compared with experimental results
Behjat, Shahhosseini and Marvast [52]	DPM & Eulerian	Liquid in solid-vapor	Simulation of oil spray in a fluid catalytic cracking riser reactor including heat transfer, evaporation, and coalescence
Ghaffarkhah, Dijvejin, Shahrabi, Moraveji and Mostofi [53]	VOF-DPM	Liquid and liquid in vapor	Simulation of water and natural gas condensate drops in continuous vapor phase of a three-phase separator compared with experimental results
Hua [54]	VOF-DPM	Vapor in liquid-vapor	Effects of small dispersed bubbles modeled by DPM on a large bubble modeled with VOF in liquid compared with experimental results
Jiang, Siamas, Jagus and Karayiannis [55]	DPM & many others	Liquid in vapor	Review and summary of the physical models and methods used in vapor-liquid two-phase jet flows. RANS, Direct numerical simulation (DNS), LES, subgrid-scale (SGS) models are all presented and discussed

Laleh, Svrcek and Monnery [56]	DPM, VOF, Mixture, & Eulerian	Many variants of liquid, solid, and vapor pairings	A review of CFD methods, their historic use and future applicability to multiphase oil and gas separators
Laleh, Svrcek and Monnery [57]	DPM	Liquid in liquid; liquid in vapor	CFD study of oilfield separator compared with classic design methods and experimental data
Mancini, Alberti, Dammann, Santo, Eckel, Kolb and Weber [58]	DPM	Liquid in vapor	Simulation of gasification of glycol in an oxygen-nitrogen mixture. Includes chemical modelling and radiative heat transfer
Rafee, Rahimzadeh and Ahmadi [59]	DPM	Liquid in vapor	Simulation of airflow and droplet flow inside a wave-plate mist eliminator. Comparison with experimental results
Sardina, Jareteg, Ström and Sasic [60]	Mixture & DPM	Vapor in liquid	Investigation of mesoscale dynamics in bubbly flows; comparison between Euler-Euler and Euler-Lagrangian
Ström, Lundström and Andersson [61]	DPM	Solid in vapor	Comparison of DPM schemes for simulation of urea spray
Torfeh and Kouhikamali [62]	DPM	Liquid in vapor	Simulation of mist flow regime to investigate simulated heat transfer and non-equilibrium

Xu, Liu and Tang [63]	VOF-DPM	Solid in liquid-vapor	Numerical simulation of gas bubbles rising through column of liquid and dispersed solid particles compared with experimental results
Zhao, Yang, Yang and Liu [64]	DPM, Mixture, & Drift Flux (Mixture variant)	Solid in vapor	Simulation and comparison of particle dispersion using three models in a ventilated room compared with experimental data collected by phase Doppler anemometry

1.6 Summary

This report presents the unique experimental facility developed to measure the droplet size, velocity and count in the headspace of an enhanced tube bundle used with R-123 and R-134a and two different bundle configurations. This includes both the bundle system and the optical system. The methods of operating the system and capturing data are also detailed. The techniques used to determine droplet size and velocities are then presented. The bundle flow parameters such as mass flux and average bundle heat flux are also discussed. Each bundle orientation and refrigerant receives a chapter to discuss results. A discussion and summary of the experimental results follows. Finally, a method for numerically simulating the liquid distribution in the headspace is described and a comparison is made with experimental results.

Chapter 2 - Facility Description

2.1 Test Facility

The flooded evaporator test section with clear optical sight glasses is the central component of the system as shown in Figure 2.1. Each main loop of the test facility is detailed in the following sections. The refrigerant circulation is maintained by a pump and thus operates at a single pressure and is described in the next section. Two water loops are used to transfer energy for boiling the refrigerant with heat supplied by steam, while condensation is accomplished with chilled glycol. The final section also describes the optical equipment used in the shadowgraphy technique.

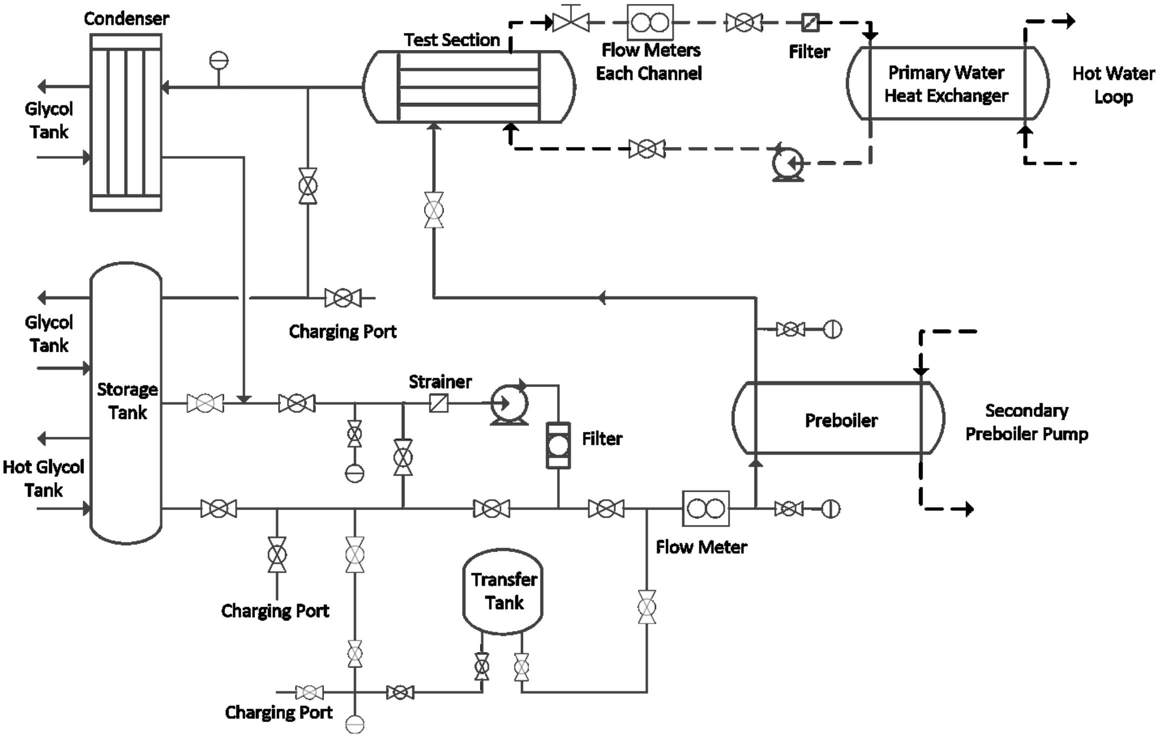

Figure 2.1 Facility schematic

2.2 Refrigerant Loop

Figure 2.1 shows the refrigerant leaving the test section to be condensed in a large brazed plate heat exchanger. Minimizing the pressure drop between test section and condenser is critical for the use of low-pressure refrigerant R-123. The condenser is an Alfa-Laval model ACH-500EQ with a maximum load placed upon it of 81 kW (23 ton) and having a refrigerant inlet of 7.6 cm (3 inch). For the first triangular bundle with R-134a, a FlatPlate model C60 with 5.1 cm (2 inch) inlet and similar capacity was used, though it was replaced with the Alfa-Laval for all subsequent testing. At the highest mass flux with R-123, vapor velocities in the 5.1 cm (2 inch) line leading up to the condenser approached 100 m/s and lead to large pressure drops. Any liquid entrained in the vapor evaporated and depressed the vapor temperature to near the glycol temperature, causing a “pinch” and preventing full condensation before returning to the refrigerant pump. Replacement with a condenser with a larger inlet allowed for testing with R-123 to continue.

The refrigerant pump is a Liquiflo model 39F magnetically driven gear pump with a capacity of 1.3 L/s (21 GPM) and delivers up to 1551.3 kPa (225 PSI) maximum pressure. The refrigerant pump in located 3 m (10 ft) below the bundle entrance in a pit and the NPSH is maintained by a static liquid head. A storage tank is installed parallel to the condenser allowing adjustment of the refrigerant charge for each test point. A filter dryer is used upstream of the pump and is for moisture and particulate control. Following the pump, a Micro Motion Coriolis model CMF050 flow meter measures liquid refrigerant mass flow rate (±0.1% of rate). After passing through the flowmeter, refrigerant moves through the pre-boiler and then rises 2 m [6 ft] to the test section. Throughout the refrigerant loop, pressure is measured with standard strain gauge pressure transducers (±0.15% FS) and temperature is measured with calibrated thermistors (±0.1 °C). Pressure transducers are Viatran model 245, with an absolute pressure range of 0-620.5 kPa (0-90 PSI) for R-134a and 0-103.4 kPa (0-15 PSI) for R-123. As necessary, degassing of the refrigerant loop is accomplished with the storage unit and test section set in a natural circulation mode by rearrangement of valves and bypassing of certain sections. Flowing of chilled water through the test section sets up a temperature difference to drive condensation and promote accumulation of air at the highest point in the system.

2.3 Pre-boiler water circuit

The pre-boiler is a shell and tube heat exchanger with the refrigerant circulating in the tubes (two passes), and the heating water circulating in the shell. The pre-boiler water circuit contains a pump, flow meter, filter, and secondary heat exchanger. The water pump is a centrifugal type 2.2 kW (3 HP) pump controlled through a variable frequency drive. The flow meter is a Micro Motion model CMF100 (±0.1% of rate). A secondary heat exchanger in the loop provides heat to the circuit from the hot water circuit.

2.4 Hot Water Circuit

The hot water circuit supplies the load to the facility. The hot water circuit consists of three pumps, a storage tank, a steam heat exchanger, and two additional heat exchangers that exchange heat with the pre-boiler water circuit and primary water circuit. All the pumps are 2.2 kW (3 HP) centrifugal pumps. One pump at a fixed speed circulates water from the storage tank to the other pumps and back through the steam heat exchanger. A PID controller regulates the temperature of the circuit by regulating the amount of steam through a pneumatically actuated valve. The other two pumps are controlled by variable frequency drives to regulate the amount of heat exchanged with the primary and pre-boiler water loops.

2.5 Primary water circuit

The primary water circuit consists of a pump, flow meters, a filter, test section, and a heat exchanger with the hot water circuit. The pump is a variable frequency drive powered 14.9 kW

(20 HP) centrifugal pump. Water flows from the pump into a manifold that splits the flow into five channels for the triangular bundle arrangement and six channels for the rotated triangular arrangement. The individual channels then flow into and out of the test section. From the test section, each channel flows through its own Micro Motion Coriolis CMF025 flow meter (±0.1% of rate). Gate valves are used on each channel to balance the flow between channels. The channels then recombine in a manifold and flow through a 25 micron filter. The flow then passes through the tube and shell heat exchanger with the hot water circuit and back to the water pump.

2.6 Test Section

The central part of the test facility is the bundle test section shown in Figure 2.3. The two-phase refrigerant mixture from the pre-boiler is distributed at the bottom of the bundle by four inlet tubes that come in through the bottom of the bundle and are capped with 8 downward facing tubes (downward facing u-tubes at top of each inlet). Refrigerant then passes upward over Wolverine Turbo-ESP 3-D enhanced tubes with both internal and external enhancements shown in Figure 2.2.

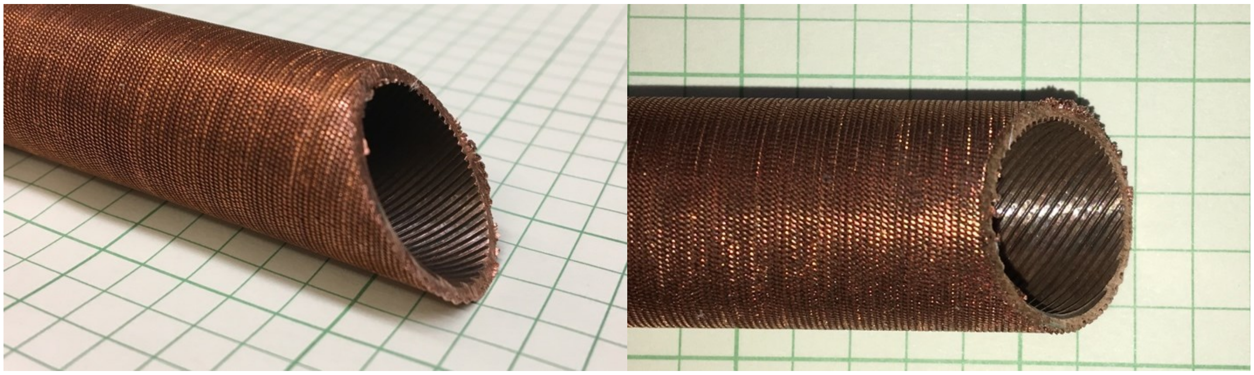

Figure 2.2 Enhanced tube close-ups

The tubes have a nominal outer diameter of 19.05 mm (0.75 inch) and inner diameter of 15.88 mm (0.63 inch). The length of the tubes within the bundle is 1.0 m (39.4 inch) to minimize end effects. The refrigerant is evaporated by heat transferred from the heated water flowing through the tubes. The water flow rate in each circuit is measured with the coriolis meters described in Section 2.5. Inlet and outlet water temperature of each tube are measured with Measurement Specialties model 4150-1/8-6.00-72-TH55036 thermistors (±0.1 °C).

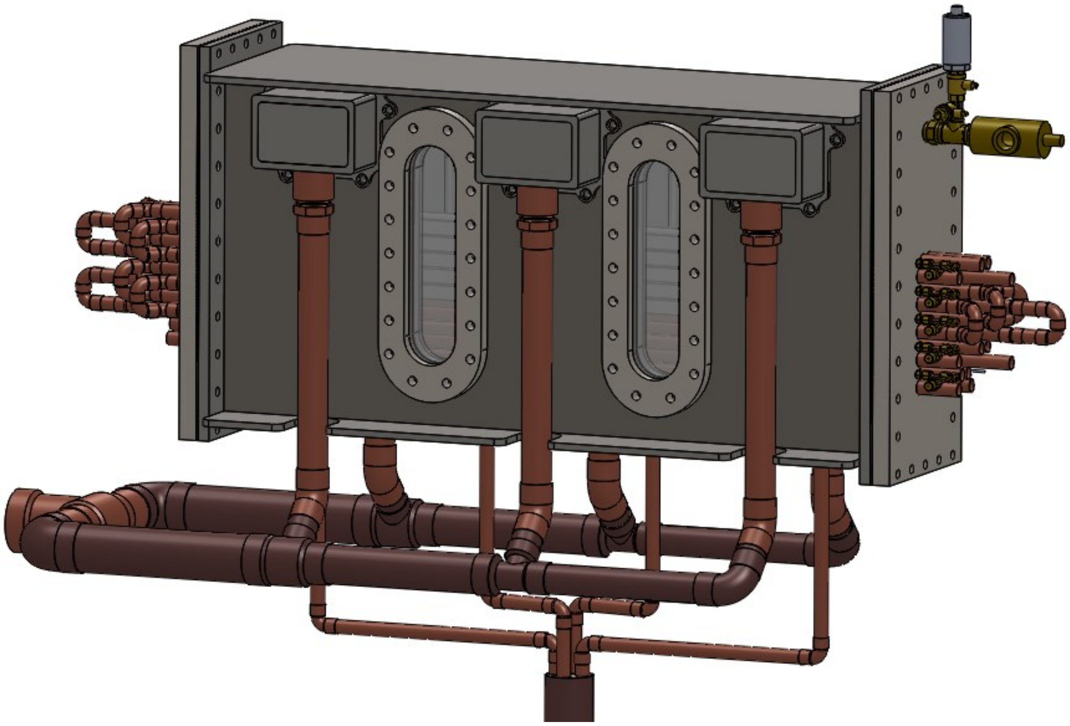

Figure 2.3 Test section model

After passing around the tubes, the resultant refrigerant vapor and liquid droplets (if the droplets exist) passes through a distribution plate. The and out of the test section through 6 ports spaced equally on both sides of the bundle. The distribution plate induces a measured pressure drop that helps to balance vertical flow. The ports collect into a manifold and the refrigerant vapor passes on to the condenser, as visible in Figure 2.3

The test section is a rectangular pressure vessel that is essentially a shell and tube heat exchanger; the refrigerant flows upwards across the tube bundle while water circulates in the tubes. The test section accommodates both high and low pressure refrigerants up to a gage pressure of 827 kPa (120 PSI) and a pressure relief valve is employed to protect the system. Its inner dimensions are 0.4254 m (16.75 inch) high, 98.4 mm (3.875 inch) wide, and 1 m (39.37 inch) deep. Inserts reduce the width of the test section to 66.7 mm [2.63 inch]. For flow visualization, the test section also includes four large sight glasses to provide clear view ports into the bundle centered on 1/3 spacing of the bundle length. The inner borosilicate sight glass is 34.8 mm (1.37 inch) thick with an index of refraction of 1.474 at the laser's wavelength of 532 nm. The inner sight glass serves to create a flat inner wall in the test section and prevent refrigerant from escaping between the inner and outer walls of the test section. The outer soda-lime sight glass is 15.7 mm (0.62 inch) thick and has a refractive index of 1.526 and serves as the outer pressure surface of the test section.

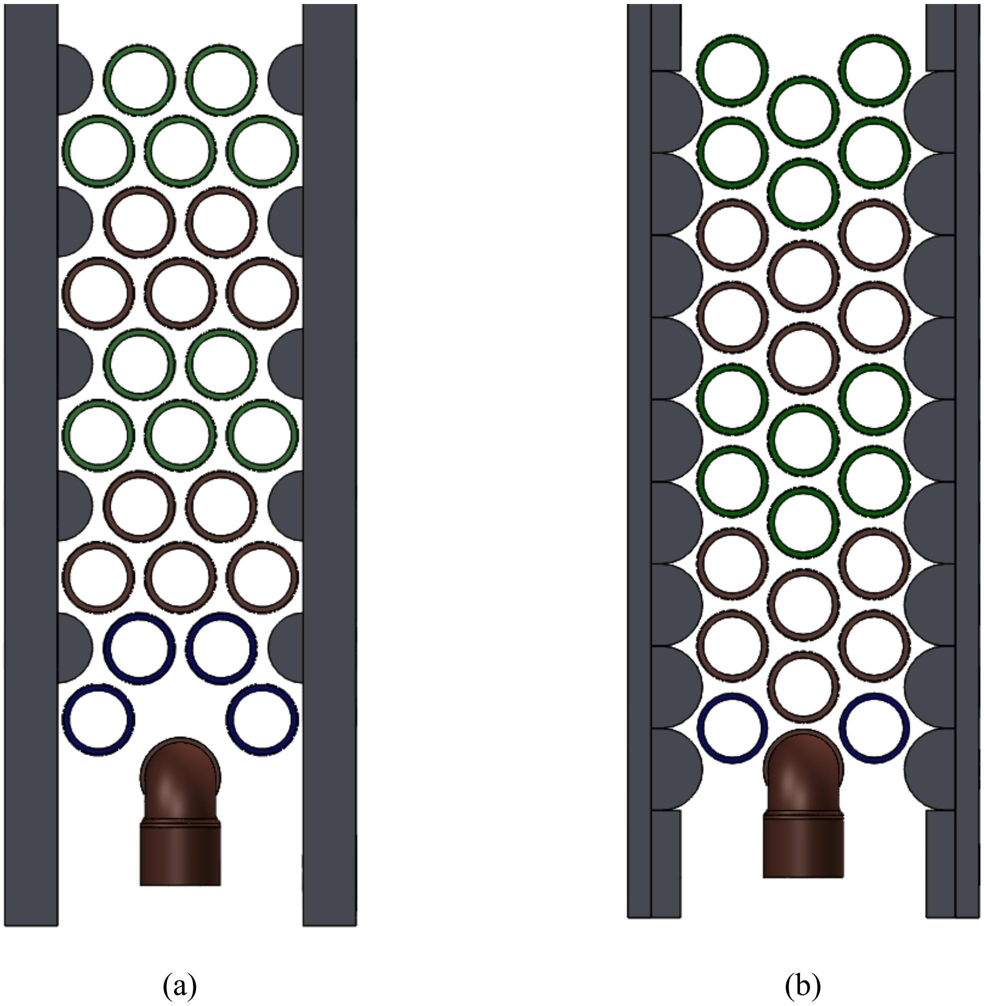

(a) (b)

Figure 2.4 Bundle arrangement: (a) triangular, (b) rotated triangular

There were two different bundle arrangements tested: triangular and rotated triangular. For both cases the pitch to diameter ratio was 1.167. For the triangular case, shown in Figure 2.4(a), rows are horizontal with each of the five water columns making four passes through the test section after entering at the bottom and exiting at the top. Viewed end-on from the right side of the model in Figure 2.3, those tubes colored brown show flow into the page while those tubes colored green show flow out of the page. The bottom 4 tubes, colored blue, are inactive dummy tubes to help distribute the refrigerant flow before reaching the 20 active tubes.

For the rotated triangular arrangement shown in Figure 2.4(b), the rows are staggered, with each of the six water columns making four passes through the test section. To maintain the same headspace as the triangular arrangement, the inactive tubes were reduced to 1 partial row of two tubes. To maintain the same mass flux as with the triangular bundle, the gap between the half-tubes is half that used with the triangular bundle. For both arrangements, the headspace ranges from 139 mm (5.48 inch) to 154 mm (6.14 inch) above the top tubes, with a width of 66.7 mm (2.63 inch) as shown in Figure 2.5. Both arrangements have the same distance between the uppermost tube and top of the headspace. The distribution plate at the top of the headspace is 1.52 mm thick, extends the full length of the bundle, and contains 50 holes with a diameter of 8.13 mm. The holes alternate between 11.5 mm and 25 mm away from the peak and are uniformly spaced axially a distance of 38.46 mm. Note that axial denotes along the long dimension of the bundle, or rather, in and out of the page in Figure 2.5.

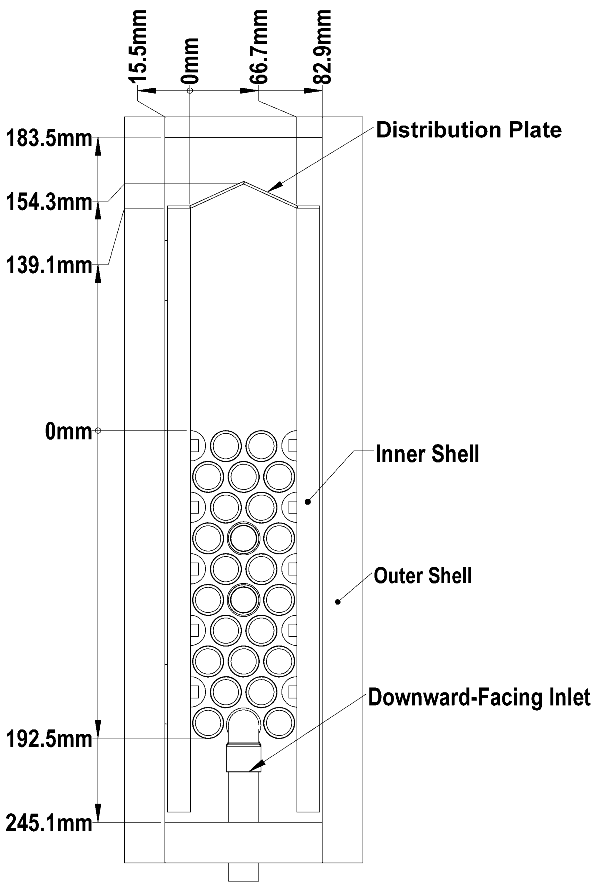

Figure 2.5 Test section dimensions

2.7 Optical System

A schematic of the shadowgraphy system is shown in Figure 2.6. This system is composed of components common to PIV and particle sizing systems, namely a light source and camera. A Quantel model EverGreen 200 Nd:YAG laser generates the dual pulse used to determine velocity at a wavelength of 532 nm. The spacing of the pulses is based on the expected maximum velocity and ranges from 240 to 1100 μs, with an uncertainty of 10 ns. The analysis and ultimately the accuracy of the backlight system depends on the uniformity of the light as seen by the camera.

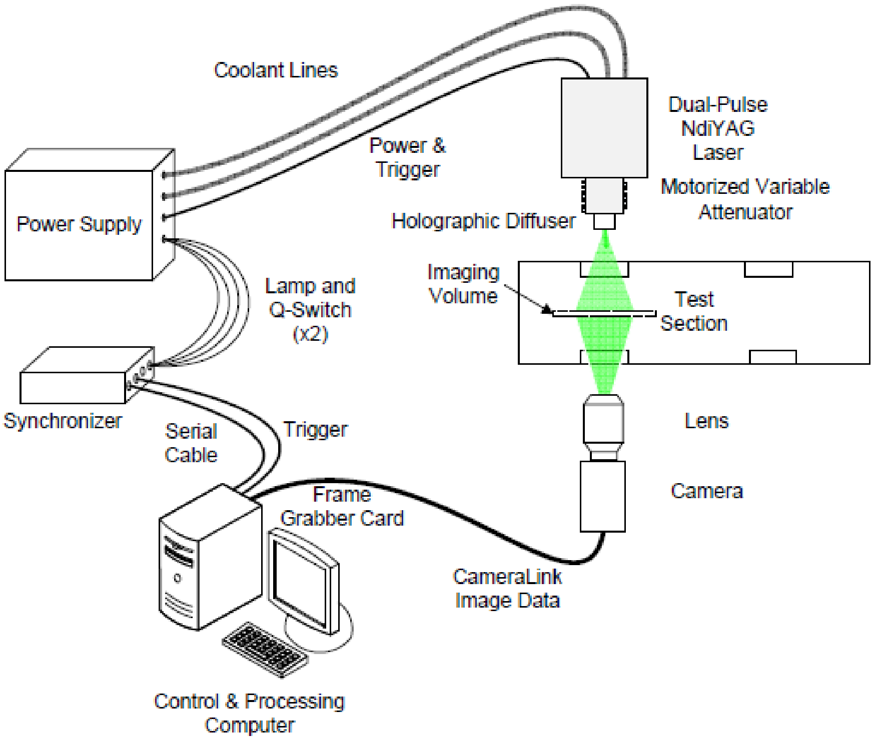

Figure 2.6 Optical system diagram

The current system use a Quantel attenuator and Thorlabs model ED1-C50-MD top-hat holograph diffuser to backlight the 76 mm (3 inch) by 125 mm (4 inch) viewing window. An opaque plastic sheet is placed on the laser-side window to prevent damage to the camera and distribute the backlight more uniformly. The laser, attenuator, and light shield are visible in Figure 2.7.

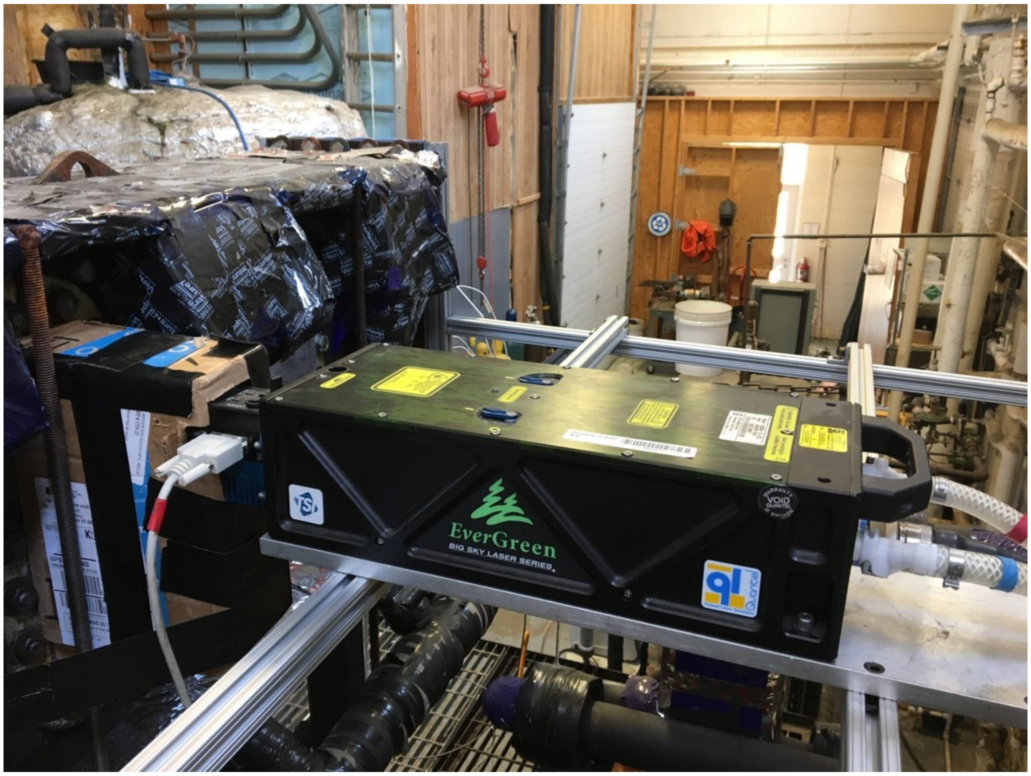

Figure 2.7 Laser side of optical system

The camera side of the optical system is shown in Figure 2.8. Two sets of optics are used on the camera (100 mm and 50 mm focal length lenses) allowing fields of view of approximately 50 mm and 100 mm respectively. The 50 mm lens is a Nikon Nikkor f/1.8 D AF while the 100 mm lens is a Tokina f/2.8 AT-X M100 AF Pro D. Both lenses are fitted with Tiffen neutral-density 0.9 filters to allow for higher laser intensities. The lower magnification lens has the advantage of visualizing the entire cross-section of the bundle head space window while the higher magnification lens allows for the capture of smaller droplets. The TSI Powerview Plus 4MP camera is mounted on a horizontal Vernier stage with 0.1 mm markings for precise location of the focal plane across the bundle width. A copper tube with vents cut into it is mounted on the outer edge of the window nearest the camera. Compressed air is directed through the tube onto the window to prevent fogging when operating at lower temperatures.

Figure 2.8 Camera side of optical system

The camera and associated imaging optics (lenses) connect with the droplet size and velocity vector analysis software. The capture software used is TSI's Insight 4G. The image pairs generated by the system require multiple analysis steps before droplet size, distribution, and matched particle velocity are determined. The following chapter outlines how those images and associated thermodynamic data are captured.

Chapter 3 - System Operation and Data Collection

Two sets of data were collected for each run: thermodynamic characteristics of the system and images of the droplet behavior. To collect this data, it was necessary to create steady-state conditions within the system at the desired conditions. This section details both how those conditions were achieved and the process for collecting the data.

3.1 System Operation

To operate the system, it was necessary to know the conditions in the system at a given instant. As such, an Agilent 34980A mainframe and associated DAQ modules were used along with a custom National Instruments virtual instrument (VI) to read and convert signals from the system's instrumentation captured by the DAQ. The VI, shown in Figure 3.1, also was used to calculate the various system parameters as described in Chapter 5 and control the VFDs driving the pumps described in Chapter 2. Thermodynamic data for each tube and each portion of the system were displayed and recorded.

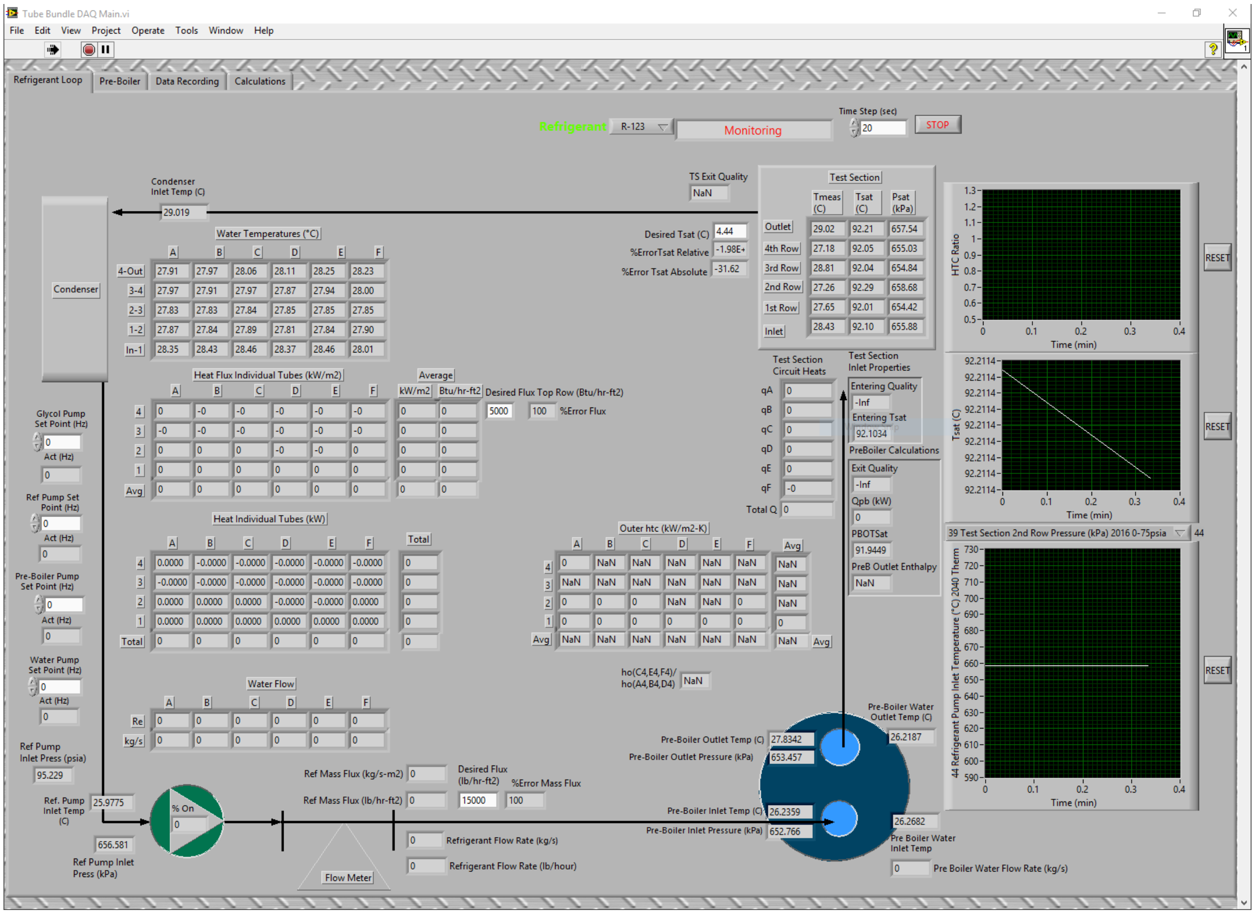

Refrigerant: R-123

Monitoring

Time Step (sec): 20

TS Exit Quality: NaN

Condenser Inlet Temp (C): 29.019

Desired Tsat (C): 4.44

%ErrorTsat Relative: -1.98E+

%Error Tsat Absolute: -31.62

Test Section

	Tmeas (C)	Tsat (C)	Psat (kPa)
Outlet	29.02	92.21	657.54
4th Row	27.18	92.05	655.03
3rd Row	28.81	92.04	654.84
2nd Row	27.26	92.29	658.68
1st Row	27.65	92.01	654.42
Inlet	28.43	92.10	655.88

Water Temperatures (°C)

	A	B	C	D	E	F
4-Out	27.91	27.97	28.06	28.11	28.25	28.23
3-4	27.97	27.91	27.97	27.87	27.94	28.00
2-3	27.83	27.83	27.84	27.85	27.85	27.85
1-2	27.87	27.84	27.89	27.81	27.84	27.90
In-1	28.35	28.43	28.46	28.37	28.46	28.01

Heat Flux Individual Tubes (kW/m2)

	A	B	C	D	E	F	Average kW/m2	Average Btu/hr-ft2
4	0	-0	-0	-0	-0	-0	0	0
3	-0	-0	-0	-0	-0	-0	0	0
2	0	0	0	-0	-0	0	0	0
1	0	0	0	0	0	0	0	0
Avg	0	0	0	0	0	0	0	0

Desired Flux Top Row (Btu/hr-ft2): 5000

%Error Flux: 100

Test Section Circuit Heats

qA: 0
qB: 0
qC: 0
qD: 0
qE: 0
qF: -0
Total Q: 0

Test Section Inlet Properties

Entering Quality: -Inf
Entering Tsat: 92.1034

PreBoiler Calculations

Exit Quality: -Inf
Qpb (kW): 0
PBOTSat: 91.9449
PreB Outlet Enthalpy: NaN

Glycol Pump Set Point (Hz): 0
Act (Hz): 0

Ref Pump Set Point (Hz): 0
Act (Hz): 0

Pre-Boiler Pump Set Point (Hz): 0
Act (Hz): 0

Water Pump Set Point (Hz): 0
Act (Hz): 0

Ref Pump Inlet Press (psia): 95.229

Ref. Pump Inlet Temp (C): 25.9775

Ref Pump Inlet Press (kPa): 656.581

% On: 0

Heat Individual Tubes (kW)

	A	B	C	D	E	F	Total
4	0.0000	-0.0000	-0.0000	-0.0000	-0.0000	-0.0000	0
3	-0.0000	-0.0000	-0.0000	-0.0000	-0.0000	-0.0000	0
2	0.0000	0.0000	0.0000	-0.0000	-0.0000	0.0000	0
1	0.0000	0.0000	0.0000	0.0000	0.0000	0.0000	0
Total	0	0	0	0	0	0	0

Outer htc (kW/m2-K)

	A	B	C	D	E	F	Avg
4	0	NaN	NaN	NaN	NaN	NaN	NaN
3	NaN	NaN	NaN	NaN	NaN	NaN	NaN
2	0	0	0	NaN	NaN	0	NaN
1	0	0	0	0	0	0	0
Avg	NaN	NaN	NaN	NaN	NaN	NaN	NaN

ho(C4,E4,F4)/ho(A4,B4,D4): NaN

Water Flow

	A	B	C	D	E	F
Re	0	0	0	0	0	0
kg/s	0	0	0	0	0	0

Ref Mass Flux (kg/s-m2): 0

Ref Mass Flux (lb/hr-ft2): 0

Desired Flux (lb/hr-ft2): 15000

%Error Mass Flux: 100

Refrigerant Flow Rate (kg/s): 0

Refrigerant Flow Rate (lb/hour): 0

Pre-Boiler Outlet Temp (C): 27.8342

Pre-Boiler Outlet Pressure (kPa): 653.457

Pre-Boiler Water Outlet Temp (C): 26.2187

Pre-Boiler Inlet Temp (C): 26.2359

Pre-Boiler Inlet Pressure (kPa): 652.766

Pre Boiler Water Inlet Temp: 26.2682

Pre Boiler Water Flow Rate (kg/s): 0

39 Test Section 2nd Row Pressure (kPa) 2016 0-75psia: 44

Figure 3.1 Control and acquisition VI

The desired operating conditions were reached by adjusting the chiller temperature, hot water tank temperature, various pumps and valves, and amount of refrigerant in the system. For certain operating conditions it was necessary to drain the preboiler of water to prevent freezing of the water when it was desired to have refrigerant enter the test section sub-cooled.

Startup was achieved by turning on in rapid succession the hot water tank controller, glycol valve, and then all pumps needed for operation. Depending on the state of the system before start, it was occasionally necessary to delay the start of certain pumps to prevent either overheating (and thus over-pressurizing) or freezing the system. The refrigerant pump VFD was then set to a condition that would roughly achieve the desired mass flux. Changes to pump speeds, valves, and the hot water tank controller were then iterated to reach the desired operating conditions.

To control the liquid level in the test section, refrigerant was transferred into and out of the system by controlling the temperature in the storage tank shown in Figure 2.1 via the transfer tank. A scale attached to the transfer tank allowed for monitoring the direction of flow. The first point tested was always the flooded condition such that the next liquid level could be achieved by simply removing refrigerant from the system.

3.2 Data Capture

Once the system had reached steady-state at the desired conditions, the DAQ was set to record, capturing data for the duration of the image capture in intervals of 20 seconds. Steady-state was set to be when outlet saturation temperatures stayed within less than 0.2 ºC (0.4 ºF) of the desired value over five minutes. Imaging then proceeded using the optical system. Imaging began at position J and then moved inward through K, L, and for early testing, M, and N as shown in Figure 3.2 below, where each position denotes a different imaging depth above the bundle.

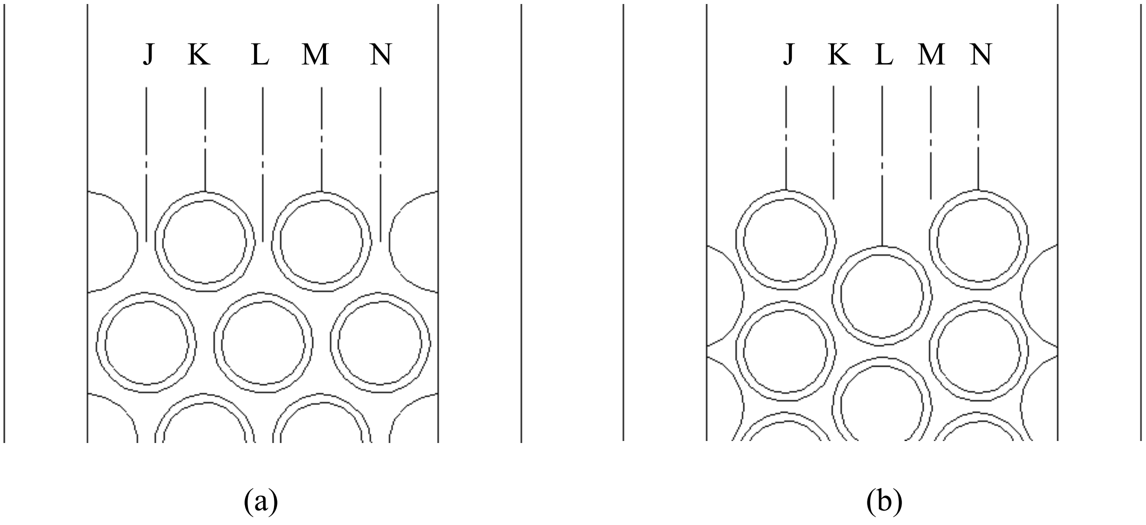

(a) (b)

Figure 3.2 Imaging locations: (a) Triangular bundle, (b) Rotated triangular bundle

The triangular bundle's imaging locations are shown in Figure 3.2 (a) while the rotated triangular bundle's imaging locations are shown in Figure 3.2 (b). The relative position of these imaging locations relative to the center of bundle are shown in Table 3.1 below, where negative values are approaching the camera and positive values moving away from the camera.

Table 3.1: Imaging locations per bundle

	Relative Position (mm)		**Description**	
Image Location	**Triangular**	**Rotated Triangular**	**Triangular**	**Rotated Triangular**
J	-22.2	-19.2	Between tube and half tube	Above tube
K	-11.1	-9.6	Above tube	Between tubes
L	0	0	Between center tubes	Above center tube
M	11.1	9.6	Above tube	Between tubes
N	22.2	19.2	Between tube and half tube	Above tube

Imaging data for all locations (J though N) were taken for the triangular bundle with R-134a. Due to an increase in droplet density with R-123, imaging locations M and N were often dropped for the triangular bundle and left out completely for both R-123 and R-134a with the rotated triangular bundle. Past the center of the bundle, liquid on the windows and droplets between the camera and imaging location made it impossible to accurately capture droplets for most tests.

At each imaging location, 100 pairs of images were taken. Once all imaging locations had been captured with the 50 mm lens, the 100 mm lens was rapidly installed and calibrated in the method described in section 4.3. Capturing then proceeded through the imaging locations again. Once all images had been captured for a liquid level, recording of thermodynamic data was stopped. Using the transfer tank, liquid was removed from the system to lower the liquid level. Adjustments to the system were made to reach the desired conditions and stabilize the system and then images were captured again. The final liquid set of images for a given set of conditions were taken in the dryout condition.

Once all data for a bundle was taken, images were analyzed to quantify droplet behavior. The following section describes how images were analyzed and describes the calibration steps necessary to extract data about the droplets.

Chapter 4 - Image Analysis

For any droplet imaged, three main quantities are desired: droplet diameter, position, and velocity. All properties of a droplet are quantified by the capture software. Droplet diameter is defined by the projected area diameter and is based on the pixels recognized inside the droplet shadow. In other words, $D_{droplet} = \sqrt{4 \cdot A_{pixels}/\pi}$. Position is height of a droplet centroid referenced to top of the uppermost tubes in the bundle in millimeters. Velocities reported are the vertical components of velocities. Horizontal velocities, though recorded, are not used for analysis but are included in the appendices. Velocities are calculated as the droplet shift centroid-centroid between image pairs divided by the time step between each image of the pair. As such, vertical velocity is given by

$$v = \frac{Y_B - Y_A}{\Delta t} \tag{4.1}$$

4.1 Image Processing

To make it possible to recognize droplets through the TSI capture software, each image was manipulated to highlight the captured droplets from the background. A Python script was written to complete all image manipulation outside of the TSI software to allow for greater control and remove complexity from the process in the capture software. There are five main steps to this script: scaling, intensity inversion, background subtraction, filtering, and masking. An example of an image prior to the script is shown below in Figure 4.1.

Figure 4.1 Unprocessed image

Scaling is necessary to present a uniform background illumination to the rest of the processing, as subtle variations in output intensity were observed with the laser over each run's set of 100 image pairs. The intensity of the brightest pixel in each image is found and then divided from 4095, the maximum intensity possible for a 12-bit image. The resulting multiplier is then applied to each pixel in the image.

A greyscale inversion was then applied to each image. Formerly dark droplets now appear bright while empty space appears dark. As the capture software uses thresholding to recognize droplets, it is necessary to have droplets have higher intensity than the background.

To remove stationary objects and artifacts from the image and make empty space more uniform in intensity, a background subtraction was performed on each run of 100 image pairs.

An image was created by finding the average intensity of each of the individual pixels from all images in a run. This image was then subtracted from all images in the run, leaving mostly droplets in each image.

Following the background subtraction, a local median filter of 3 pixels was used to more sharply define droplets and remove noise. A multiplier of 5 was then applied to each pixel and then an image mask was used to set pixels with an intensity less than 1000 to 0. The end result of the script is shown in Figure 4.2, which is Figure 4.1 after processing. Droplets, or rather pixels possibly to be recognize as droplets are shown in white or grey. Images at this point were ready to have droplets recognized.

Figure 4.2 Processed image

4.2 Droplet Recognition

All droplet recognition was carried out using version 11 of TSI Insight 4G. Droplet recognition occurs in two main steps: particle sizing and particle matching. Particle matching takes the pre-processed images and determines all possible droplets by use of thresholding. For our processing, the threshold was set to 999. As the images were previously manipulated to mask all areas with an intensity below 1000, this means any visible pixels on our pre-processed images were available to the sizing kernel.

The particle sizing kernel was set to recognize droplets from as small as 2 pixels up to as large as 70 and 156 pixels for the 50 mm and 100 mm lenses, respectively. The upper limit corresponds to a maximum droplet diameter of approximately 4000 µm. Furthermore, to filter out possible non-droplets like liquid structures on the inner glass wall, droplets were limited to a circularity from 0.4 to 2 to favor recognizing the more circular droplets. A droplet's circularity is defined by $Circularity = 4 \cdot Area/Perimeter^2$.

Particle matching allows for the setting of the maximum allowable particle shift. As stated previously, timing settings were set based on an expected maximum droplet velocity and a shift of ±30 pixels both vertically and horizontally. Droplets were allowed a maximum size difference between images in a pair of 35%. As droplet motion for a bundle includes both rising and falling droplets, no local motion match or neighborhood particle matching algorithms were used.

The droplet recognition process creates a .PAR file (a comma-separated value file) corresponding to each image. The files contain data on each droplet's location, velocity (if matched), circularity, and other relevant information, including whether the droplet was matched between each image in a pair.

4.3 Calibration

Three main types of calibration images were taken with this data. A Thorlabs model R3L3S4P2 distortion target was used as a check of the droplet recognition & matching ability of the software. This target, shown in Figure 4.3 has opaque circular dots with diameters from 62.5 to 1000 μm and spacings from 125 to 2000 μm. Results of this check show an uncertainty in droplet diameter of ±21 μm for droplets larger than 100 μm using the 50 mm lens and ±11 μm for droplets larger than 50 μm using the 100mm lens.

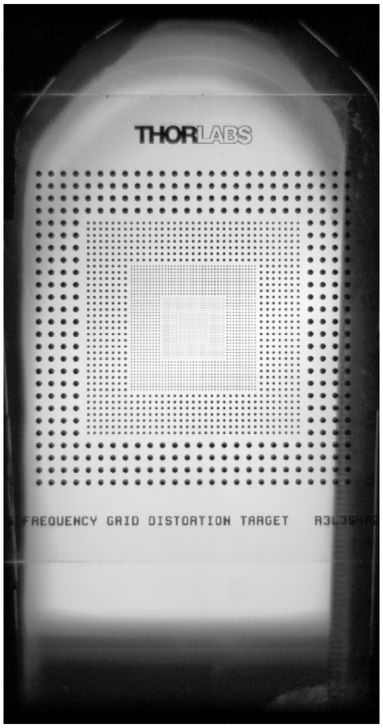

Figure 4.3 Calibration target for sizing

A calibration image was also taken for each liquid level and lens in an experiment. A representative image for the 50 mm lens is shown in Figure 4.4. The horizontal Vernier stage is set to a position of 0 mm and then the lens is focused on a clear plastic ruler with opaque spacing lines & text. The text & lines are located against the exterior wall of our outer test section sight glass, so focusing on the ruler means the camera is focused on the outer wall.

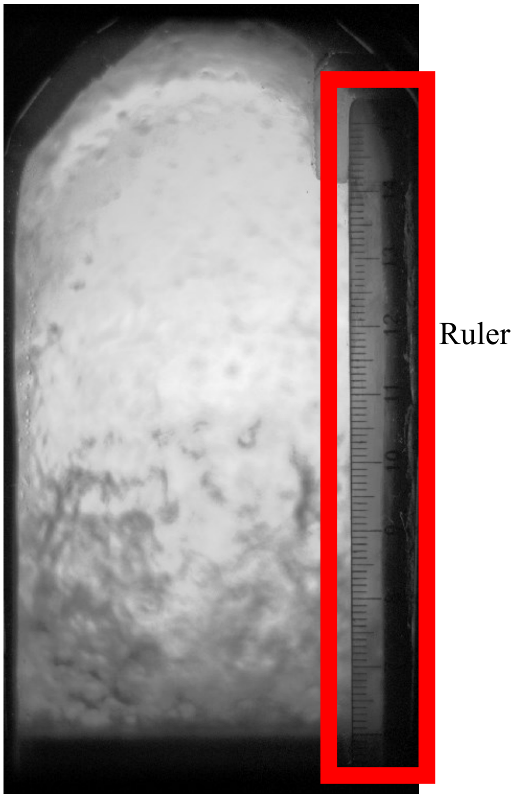

Figure 4.4 Calibration image for focusing on outer wall

A final set of calibration images is taken at the inner wall to determine the height of the top of the bundle relative to the camera image. The Vernier stage is set to 36.5 mm and the bundle is front-lit to expose the nearest half tube as seen in Figure 4.5. The flat side of the aluminum half-tubes are in focus and the top corresponds to the top of the bundle.

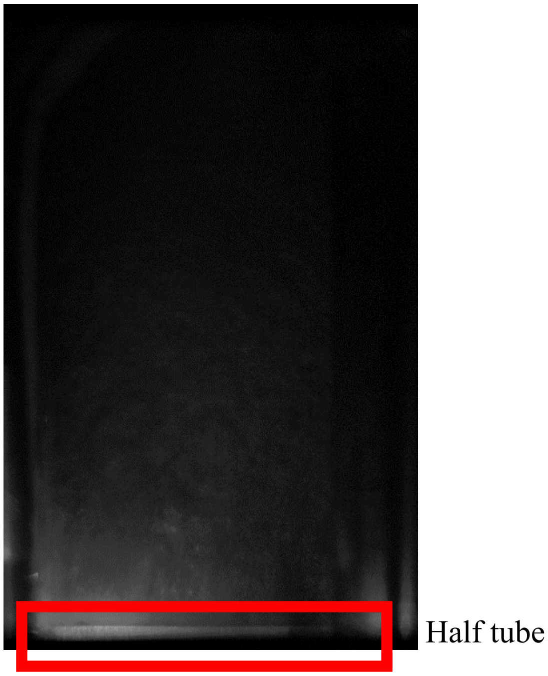

Figure 4.5 Calibration image for bundle height

The focusing and bundle height calibration images of Figure 4.4 and Figure 4.5 are both used to set up the droplet recognition processor of the capture software. The ruler of the focusing images is used to determine the pixel to μm ratio necessary to convert images into measurements. The bundle height images are used to set the origin for processed data to the top of the bundle.

4.4 Depth of Focus

Any use of cameras and lenses will involve a depth of focus (DOF). For this application, the depth of focus refers to the axial distance for which images in the focal plane remain in focus. For both lenses, DOFs were calculated based on the distances between the camera sensor, outer lens, and focal plane as well as the pixel size and resolution of the camera. For the 50 mm lens, this resulted in a calculated DOF of 3.52 mm, while for the 100 mm lens the calculated DOF was 1.37 mm. These DOFs were then verified by focusing on a target and moving the Vernier stage in and out until the target moved out of focus.

Chapter 5 - Bundle Calculations

The focus of this study is the headspace droplet distribution and morphology, but it is important to tie those properties to typical operating conditions within a bundle evaporator. Parameters such as mass flux, heat flux, and exit quality describe or are an effect of the operating conditions. In this section, the equations used to calculate those parameters are presented, as well as the uncertainties associated with measurements, calculated parameters, and imaging.

5.1 Mass Flux

Mass flux is determined from the measured refrigerant mass flow rate and the physical parameters of the bundle. It is important to note that mass flux for a bundle is generally defined based on the minimum area encountered in the bundle. From our nominal outer tube diameter of 19.05 mm (0.75 inch) and pitch-diameter ratio of 1.167, this gives a minimum gap of 3.175 mm (0.125 inch) between adjacent tubes. For our bundle, each row has three gaps or the equivalent and our rows are 1 m (39.37 inch), yielding a fluid cross-sectional area of 9525 mm^2 (14.76 inch^2). This can be expressed by

$$G = \frac{\dot{m}_r}{A_c} \tag{5.1}$$

with mass fluxes ranging from 3.5 kg/m^2-s (2250 lb/hr-ft^2) to 40.7 kg/m^2-s (30000 lb/hr-ft^2). Testing with R-134a occurred at two mass fluxes: 20.3 kg/m^2-s (15000 lb/hr-ft^2) and 40.7 kg/m^2-s (30000 lb/hr-ft^2). The same mass fluxes were tested with R-123, but additionally, tests were run at mass fluxes of 3.5 kg/m^2-s (2250 lb/hr-ft^2), 7.1 kg/m^2-s (5200 lb/hr-ft^2), and 10.2 kg/m^2-s (7500 lb/hr-ft^2) to achieve vapor headspace velocities matching or similar to those of R-134a.

5.2 Heat Flux

Heat flux is determined from the measured water temperature and pressure drop across a tube, the water flow rate through the tube, and the nominal tube outer area. The heat and heat flux, respectively, for a given tube is

$$q_{tube} = \dot{m}_w \left[c_{p,w}(T_{in} - T_{out}) + \frac{(P_{in} - P_{out})}{\rho_w} \right] \quad \textbf{(5.2)}$$

$$q"_{tube} = \frac{q_{tube}}{A_o} \quad \textbf{(5.3)}$$

where the specific heat and density are evaluated at the average of the inlet and outlet conditions. For our testing, the heat fluxes reported are the average of the top two rows. In other words, there is a top-rows heat flux $q"_{top-rows}$, which is the mean of the fluxes of the top rows of the bundle. With the triangular bundle, the top rows are considered to be the five uppermost rows as shown in Figure 5.1(a), shown in green. With the rotated triangular bundle, the top-rows heat flux is evaluated from the mean of the top six uppermost rows as shown in Figure 5.1(b), shown in green.

(a) Triangular arrangement

(b) Rotated triangular arrangement

Figure 5.1 Top rows heat flux

Nominal top-row heat fluxes for R-134a were 15.8 kW/m^2 (5000 Btu/hr-ft^2) and 31.5 kW/m^2 (10000 Btu/hr-ft^2), though the maximum achievable heat fluxes for the 20.3 kg/m^2-s (15000 lb/hr-ft^2) mass flux condition ranged from 20.5 kW/m^2 (6500 Btu/hr-ft^2) to 23.3 kW/m^2

(7400 Btu/hr-ft^2). The maximum varied depending on both the bundle configuration and refrigerant saturation temperature. For R-123, top-row heat fluxes ranged from 3.5 kW/m^2 (1100 Btu/hr-ft^2) to 31.5 kW/m^2 (10000 Btu/hr-ft^2), dependent on mass flux, bundle configuration, and refrigerant saturation temperature.

5.3 Inlet Quality

An inlet quality to the bundle was determined from the refrigerant's preboiler inlet enthalpy, the amount of heat transferred into the refrigerant in the preboiler, and refrigerant's pressure at the test section inlet. The preboiler heat transfer is found from

$$q_{pb} = \dot{m}_w c_{p,w}\left(T_{pb,in} - T_{pb,out}\right) \tag{5.4}$$

where heat transfer due to pressure drop across the preboiler is neglected. The preboiler inlet enthalpy is calculated from REFPROP[65-68] using the measured refrigerant pressure and temperature. The exit enthalpy of the preboiler is then calculated from

$$h_{pb,out} = \frac{q_{pb}}{\dot{m}_r} + h_{pb,in} \tag{5.5}$$

which is assumed to be the same as the test section inlet enthalpy, $h_{pb,out} = h_{ts,in}$. The inlet quality to the test section is then calculated by

$$x_{ts,in} = \frac{h_{ts,in} - h(liquid, P_{ts,in})}{h(vapor, P_{ts,in}) - h(liquid, P_{ts,in})} \tag{5.6}$$

where the saturated liquid and vapor enthalpies have been evaluated in REFPROP at the test section inlet pressure.

To achieve most heat fluxes described in Section 5.2, it was not necessary to add any energy to the refrigerant in the preboiler. In those cases the refrigerant entered the test section subcooled. However, for high mass flux, low heat flux conditions, the preboiler was used, resulting in measurable test section inlet qualities.

5.4 Exit Quality

An exit quality from the bundle was determined from the refrigerant test section inlet enthalpy, the amount of heat transferred into the refrigerant in the bundle, and the test section outlet refrigerant pressure. The bundle heat transfer is found from

$$q_{bundle} = \sum_{all\ tubes} q_{tube} \tag{5.7}$$

where q_{tube} is found from Equation (5.2). The test section inlet enthalpy is that described in section 5.3. The test section outlet enthalpy is then calculated from

$$h_{ts,out} = \frac{q_{bundle}}{\dot{m}_r} + h_{ts,in} \tag{5.8}$$

Using the test section's outlet pressure, the exit quality is calculated from

$$x_{ts,outlet} = \frac{h_{ts,out} - h(liquid, P_{ts,out})}{h(vapor, P_{ts,out}) - h(liquid, P_{ts,out})} \tag{5.9}$$

where the saturated liquid and vapor enthalpies have been evaluated in REFPROP.

Exit qualities generally ranged from 90% to 100%. However, qualities as low as 70% were measured with R-123 at the higher mass flux, indicating significant liquid carryover.

5.5 Heat Transfer Coefficient Ratio

The outer heat transfer coefficient of each tube was calculated. Using the Modified Wilson Plot method of Gorgy and Eckels (2010) and the Gnielinski correlation, the inner heat transfer coefficient was found. The C factor found was 3.28, closely matching Wolverine's provided value of 3.34. The outer heat transfer coefficient was then found from

$$h_o = \left[\frac{LMTD}{q''_{tube}} - R_w A_o - \frac{A_o}{h_i A_i}\right]^{-1} \tag{5.10}$$

The heat transfer coefficient ratio (htc ratio) is defined as the ratio of the average outer heat transfer coefficients of the top and second-from-top rows.

$$htc\ ratio = \frac{h_{o,top\ row}}{h_{o,2nd\ row}} \tag{5.11}$$

The htc ratio was used to gauge non-flooded liquid levels. Regardless of the amount of liquid above the tubes, the htc ratio was nearly constant. As refrigerant was removed from the system and the liquid level dropped, the onset of a drop in the htc ratio was deemed the ideal liquid level. For dryout conditions, the htc ratio was held to approximately half the flooded value. Typical values of the htc ratio were 0.5-0.6 for dryout, 0.95 to 1.05 for ideal, and 1.05 to 1.2 for a flooded bundle.

5.6 Liquid Volume Fraction

It is possible, from the data collected, to calculate liquid volume fraction as a function of height above the tubes. Liquid fraction is found by calculating the total liquid droplet volume per binned height of 5 mm. Droplets are assumed to be spheres with a diameter being the software-calculated projected diameter described in the image analysis chapter. For cases in which droplets span more than one bin, corrections are made using the volume formula for a spherical cap. The total liquid volume is then averaged over the 100 images that make up a set. The total bin volume is also calculated by multiplying our region of interest by the bin height and the depth of focus. So, the bin volume is given by (35 mm)·(5mm)·(DOF), where the DOF is dependent on the lens used and is described in section 4.4.

The liquid volume fraction is then the ratio of liquid volume to bin volume and is placed at the center of the bin's bounds (e.g. if a bin spans from 50 to 55 mm, the liquid fraction is placed at 52.5 mm). The procedure above is used to handle droplets that span more than one bin.

An approximation of the discrete method described above is shown in (5.12). In (5.13), the total liquid volume per bin (with per-bin denoted by *i*) is divided by the number of droplets (*n*) per bin, giving the average droplet volume. The average droplet diameter per bin ($\overline{D}_i$) is then found from the average droplet volume. Both the number of droplets and average droplet diameter per bin are then used in (5.12) to find the liquid fraction per bin. The form of (5.12) is useful for finding the uncertainty in liquid fraction as described in the next section.

$$\phi_{bin} = n_{bin} \frac{\pi \overline{D}_{bin}^{3}}{6H \cdot W \cdot DOF} \tag{5.12}$$

$$\overline{D}_{bin} = \sqrt[3]{\frac{6V_{l,total,bin}}{n_{bin}}} \tag{5.13}$$

5.7 Uncertainty

Uncertainties exist both in thermodynamic bundle parameters and in droplet data. A quantification of uncertainties is important even when difficult to carry out. Table 5.1 below details known or estimated uncertainties for various measurements.

Table 5.1 Measurement Uncertainties

Variable	**Uncertainty**	**Notes**
Temperature, T	±0.01 °C (0.02 °F)	Thermistors
Pressure, P	±0.15% full scale	Strain gauge transducers
Flow, $\dot{m}$	±0.1% reading	Coriolis type
Laser pulse, Δt	±10 ns	Image time uncertainty
Depth of Focus, DOF	±0.5 mm ±0.2 mm	50 mm lens, 100 mm lens
Droplet diameter, D	±21 µm ±9 µm	50 mm lens, 100 mm lens
Droplet Count	±10% value	

The uncertainties for temperature, pressure, flow, and timing uncertainty are based on manufacturer's specifications. For both temperature and pressure, sensors were calibrated and showed uncertainties lower than what is shown in Table 5.1. The uncertainty for depth of focus is based on observation of our images and the understanding that out of focus droplets outside our measurement volume might be included in our results. The uncertainty for droplet diameter is statistical and based on the calibration testing of Section 4.3 involving the target shown in Figure 4.3. The droplet count uncertainty is found from a manual inspection of a sampling of images, identifying cases wherein both droplets were not counted and non-droplets were counted.

Propagation of uncertainty analysis is performed in the manner described in Figliola and Beasley [69] on our calculated parameters to find their resultant uncertainty. For liquid volume fraction, the estimated uncertainty is given by

$$U_{\phi} = \sqrt{\left(\frac{\partial \phi}{\partial n} U_n\right)^2 + \left(\frac{\partial \phi}{\partial \overline{D}} U_{\overline{D}}\right)^2 + \left(\frac{\partial \phi}{\partial DOF} U_{DOF}\right)^2} \qquad \textbf{(5.14)}$$

and is derived from the parameters of Equation (5.12). Uncertainty values for the liquid fraction are shown on their charts later in the report. Carrying out propagation of uncertainty on our calculated parameters yields the resulting uncertainties shown in Table 5.2.

Table 5.2 Parameter Uncertainties

Variable	Equation	Uncertainty	Notes
Mass Flux, G	(5.1)	± 0.96% value	Limited by tube diameter uncertainty
Top Rows Heat Flux, $q_{toprows}$	(5.3)	± 4.1% value	Limited by temperature uncertainty
Inlet Quality, $x_{ts,i}$	(5.6)	± 0.04% value	
Exit Quality, $x_{ts,o}$	(5.9)	± 3.7% value	Limited by temperature uncertainty

For both the top rows heat flux, uncertainties are typically with ±1.6% of the indicated value, but increase up to ±4.1% for the low mass flux tests with R-123 that match headspace velocities of R-134a due to low temperature differentials across tubes. Mass flux uncertainty is primarily due to uncertainty in the diameter of the enhanced tubes.

Chapter 6 - Introduction to Results

Results for each bundle and refrigerant combination are presented in the following chapters. The triangular orientation with R-134a is presented first, the triangular bundle with R-123 second, the rotated triangular bundle with R-134a third, and presented last is the rotated triangular orientation with R-123. Each results chapter begins by laying out the matrix of eight thermodynamic conditions that was tested, specifying the variations of mass flux, heat flux, and outlet saturation temperature. The number and description of which liquid levels were tested is also presented. Each chapter then contains a presentation of the baseline set of data that was collected with the 50 mm lens and an outlet saturation temperature of 12.8 °C (55 °F), mass flux of 20.3 kg/m^{2}s (15000 lb/hr-ft^2), and top rows heat flux of 15.7 kW/m^2 (5000 Btu/hr-ft^2) at the ideal liquid level. A comparison is then briefly made of data captured with the 100 mm lens at the same conditions. Following the baseline data, each variation (liquid level, mass flux, heat flux, etc) is explored, comparing within the set of orientation-refrigerant results. Finally, a summary is given of each bundle.

Chapter 7 - Triangular Bundle with R-134a

Results for the triangular bundle arrangement with R-134a are of the greatest interest to industry. This set of results was also the first set of data taken, and thus has the largest amount of data due to not knowing how results would present themselves. This is the base set of data by which all variations of refrigerant and bundle arrangement are compared. First presented in the chapter is the overall test matrix for the bundle, describing the thermodynamic conditions of testing as well as the variation in liquid levels. Then, the baseline set of data is presented. Finally, the effect of the each variation is explored. The complete set of data may be found in Appendix A.

7.1 Test Matrix

This set of data contained the largest number of distinct test points, with the most liquid levels and camera positions. Overall, eight thermodynamic conditions were tested as shown in Table 7.1 below.

Table 7.1 Test matrix, triangular bundle with R-134a

Thermodynamic Condition	Outlet Saturation Temperature, °C (°F)	Mass Flux, kg/m^2-s (lb/hr-ft^2)	Top Rows Heat Flux, kW/m^2 (Btu/hr-ft^2)
1	4.4 (40)	20.3 (15000)	15.7 (5000)
2	4.4 (40)	20.3 (15000)	23.3 (7400)
3	4.4 (40)	40.7 (30000)	15.7 (5000)
4	4.4 (40)	40.7 (30000)	31.5 (10000)
5	12.8 (55)	20.3 (15000)	15.7 (5000)
6	12.8 (55)	20.3 (15000)	22.7 (7200)
7	12.8 (55)	40.7 (30000)	15.7 (5000)
8	12.8 (55)	40.7 (30000)	31.5 (10000)

Note that the top rows heat flux listed at 23.3 kW/m^2 (7400 Btu/hr-ft^2) and 22.7 kW/m^2 (7200 Btu/hr-ft^2) represent the maximum heat flux possible with the bundle for a refrigerant mass flux of 20.3 kg/m^2-s (15000 lb/hr-ft^2) at their respective outlet saturation temperatures.

This set of results also contained the most liquid levels tested. For the first thermodynamic condition listed in Table 7.1, five liquid levels were tested as listed in Table 7.2. The column heading of "Designation" corresponds to the similar liquid level used in the rest of the bundle & refrigerant combinations.

Table 7.2 Liquid level descriptions, thermodynamic condition 1, triangular bundle with R-134a

Liquid Level	Description	Designation
1	25 mm (1 inch) liquid above tubes	Flooded
2	19 mm (0.75 inch) liquid above tubes	NA
3	13 mm (0.5 inch) liquid above tubes	NA
4	Liquid just above tubes	Ideal
5	Liquid below tubes	Near-Dryout

After processing, it was seen that liquid levels 1-3 were very similar with the exception of simply shifting results downward by the difference in liquid level. Liquid level 5, noted as near-dryout, occurred where significant heat transfer was still detected in the top two tubes, but a pool of liquid through which vapor was passing was not visible. This resulted in a heat transfer coefficient ratio of approximately 0.9 to 0.95

For the thermodynamic conditions 2 through 8, liquid levels were as shown in Table 7.3. The only difference from the first thermodynamic condition is the discontinuation of the 19 mm (0.75 inch) liquid level. For all other bundle and refrigerant testing, the 13 mm (0.5 inch) liquid level was also discontinued.

Table 7.3 Liquid level descriptions, thermodynamic conditions 2-8, triangular bundle with R-134a

Liquid Level	Description	Designation
1	25 mm (1 inch) liquid above tubes	Flooded
2	13 mm (0.5 inch) liquid above tubes	NA
3	Liquid just above tubes	Ideal
4	Liquid below tubes	Near-Dryout

This set of data also contained the largest number of imaging locations. Images were captured in all the locations shown in Figure 3.2(a), from J to N across the span of the bundle. Images locations past L became difficult to accurately recognize droplets due to the distortion of liquid between the camera and imaging location, but are still included. Overall, 320 sets of 100 image pairs were captured, meaning a data set of 64000 images for the bundle. After the image analysis described in Chapter 4, the results in the following section were found.

7.2 Baseline data

An example of processed images for the baseline data is shown in Figure 7.1. Droplets are shown in shades of grey and pink, while background and vapor are shown as black. The baseline results for R-134a with the triangular bundle are shown in Figure 7.2 through Figure 7.8 for the 50 mm lens. These figures show thermodynamic condition 5 of Table 7.1, with an outlet saturation temperature of 12.8 °C (55 °F), mass flux of 20.3 kg/m^{2}s (15000 lb/hr-ft^2), and top rows heat flux of 15.7 kW/m^2 (5000 Btu/hr-ft^2) and was taken at the ideal liquid level in the J location of Figure 3.2(a). The data shown in histogram form is the mean of 100 images (first image per image pair of a run). The velocity distribution histogram only show droplets which were matched between image pairs and again is a plot of averages. Height vs velocity vs diameter and height vs diameter vs velocity plots only include droplets that were matched, but they do include droplets from all 100 images.

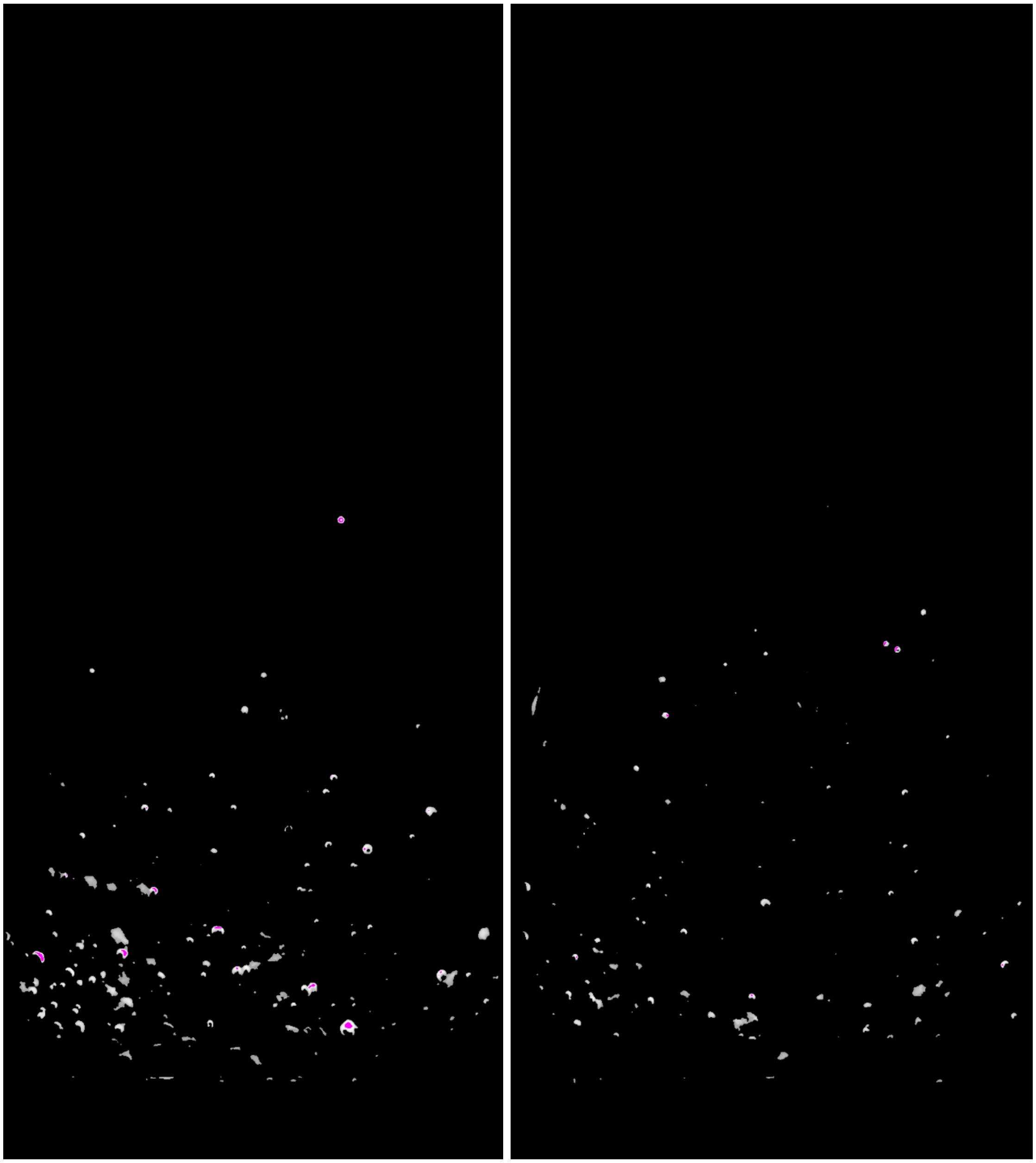

Figure 7.1 Processed images, triangular bundle, R-134a, 12.8 °C (55 °F), 20.3 kg/m^{2}s (15000 lb/hr-ft^2), 15.7 kW/m^2 (5000 Btu/hr-ft^2), ideal liquid level, 50 mm lens, image location J

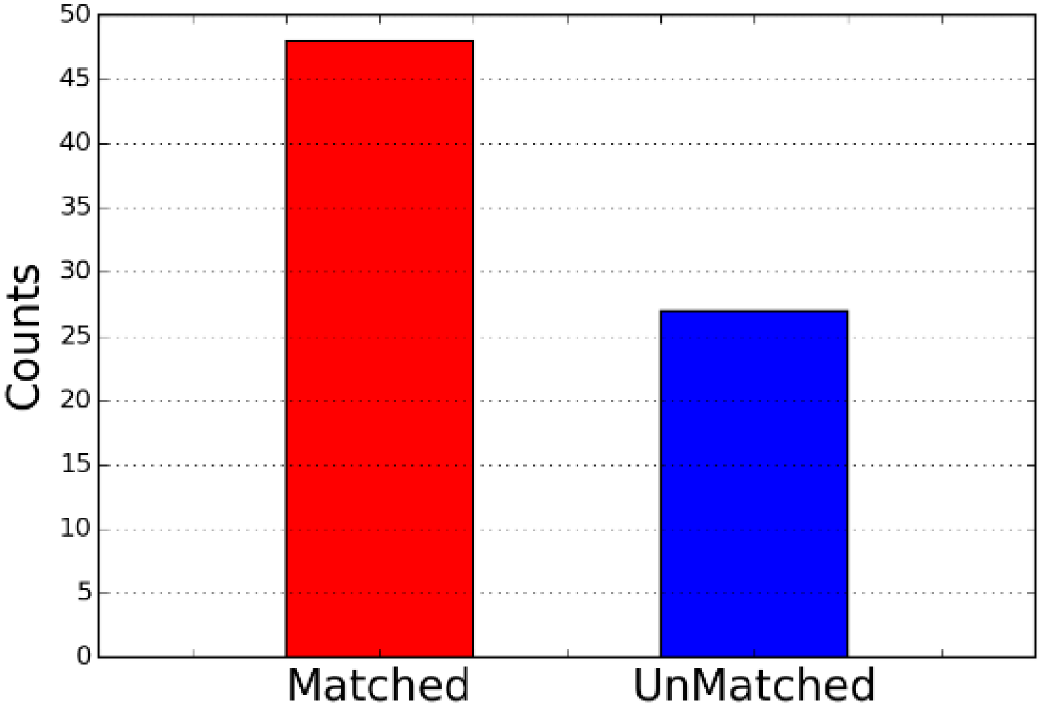

Figure 7.2 Matched counts, triangular bundle, R-134a, 12.8 °C (55 °F), 20.3 kg/m^{2}s (15000 lb/hr-ft^2), 15.7 kW/m^2 (5000 Btu/hr-ft^2), ideal liquid level, 50 mm lens, image location J

Figure 7.2, showing matched vs unmatched counts, gives a representation of how many droplets were matched between images in an image pair. It also provides for a quick count of the average number of droplets per image. Figure 7.2 shows that average of 75 droplets were counted per image and that 64% of these droplets were deemed a match by the droplet recognition software.

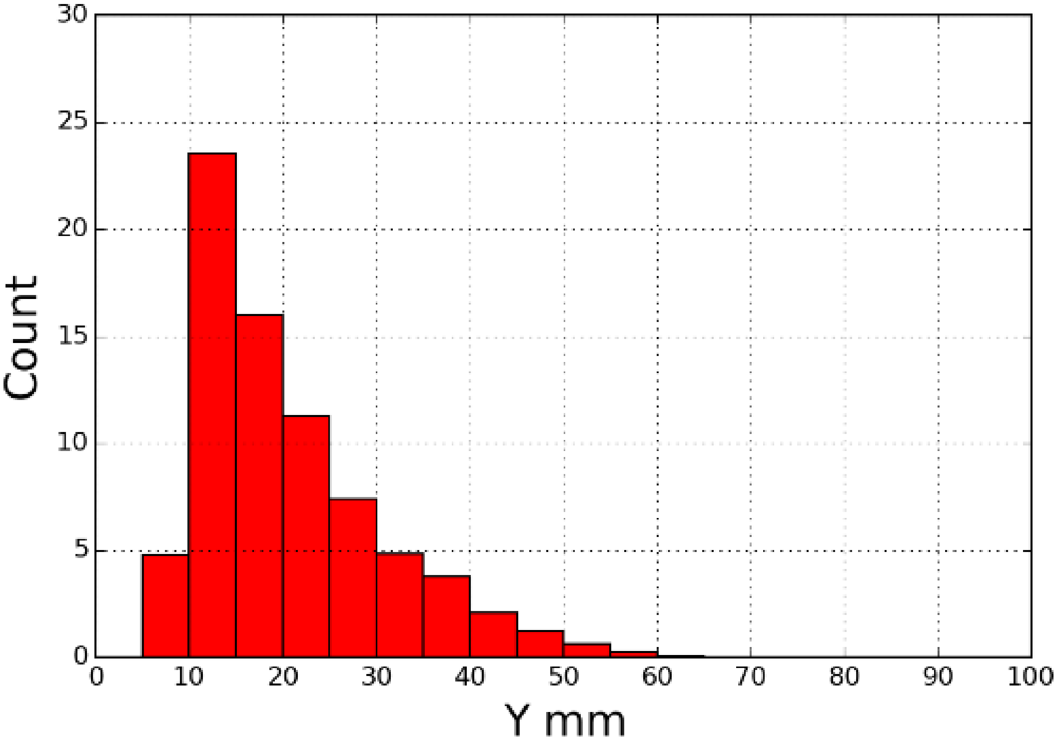

Figure 7.3 Height distribution, triangular bundle, R-134a, 12.8 °C (55 °F), 20.3 kg/m^{2}s (15000 lb/hr-ft^2), 15.7 kW/m^2 (5000 Btu/hr-ft^2), ideal liquid level, 50 mm lens, image location J

Figure 7.3 shows the distribution of droplets vs height. Counts are shown in bins 5 mm high. The distribution of droplets skews towards the bottom of the headspace, with the majority of droplets found in the first 20 mm above the tubes. The highest droplets recognized are between 60 and 65 mm above the tubes. Note that the first bin from 0 - 5 mm is completely masked and the bin from 5 to 10 mm is partially masked, explaining the zero and low counts, respectively. It is not possible to recognize droplets too close to the tubes.

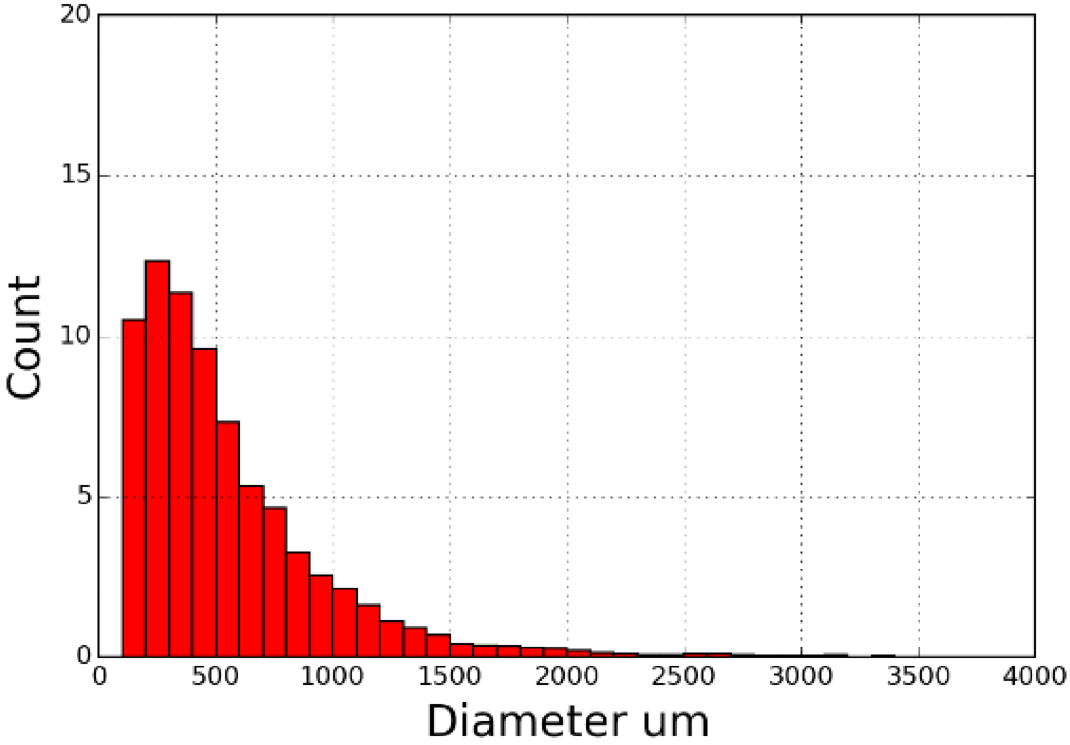

Figure 7.4 Size distribution, triangular bundle, R-134a, 12.8 °C (55 °F), 20.3 kg/m^{2}s (15000 lb/hr-ft^2), 15.7 kW/m^2 (5000 Btu/hr-ft^2), ideal liquid level, 50 mm lens, image location J

Figure 7.4 shows the size distribution of droplets. Droplets are binned for every 100 µm, with the majority of droplets recognized being beneath 600 µm. Droplets above 2000 µm have been recognized, but their number are small compared to droplets with smaller diameters. No droplets are counted below 100 µm as the 50 mm lens is limited to droplets of 2 pixels or greater diameter, or rather, 114 µm. Droplet recognition in the 100 to 200 µm bin size is also restricted, again due to the cutoff at 114 µm, thus the slight decrease in the bin count. Note that for any figure in this chapter or Appendix A with an axis labelled “Diameter um”, um denotes µm.

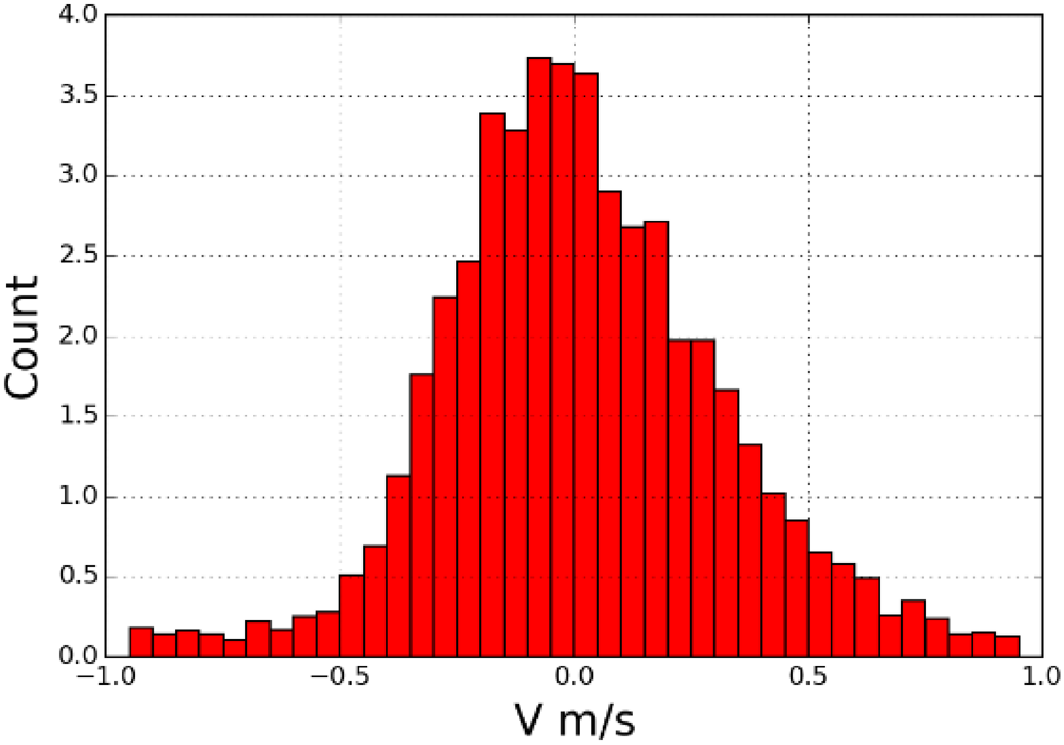

Figure 7.5 Velocity distribution, triangular bundle, R-134a, 12.8 °C (55 °F), 20.3 kg/m²s (15000 lb/hr-ft²), 15.7 kW/m² (5000 Btu/hr-ft²), ideal liquid level, 50 mm lens, image location J

Figure 7.5 shows the velocity distribution of droplets within the headspace. Droplets are binned for every 0.05 m/s. Droplet counts are approximately symmetrical about zero-velocity. This symmetry indicates that droplets that are seen rising, at least those captured with the 50 mm lens, are likely also falling back down, meaning that droplets are remaining within the headspace and not exiting.

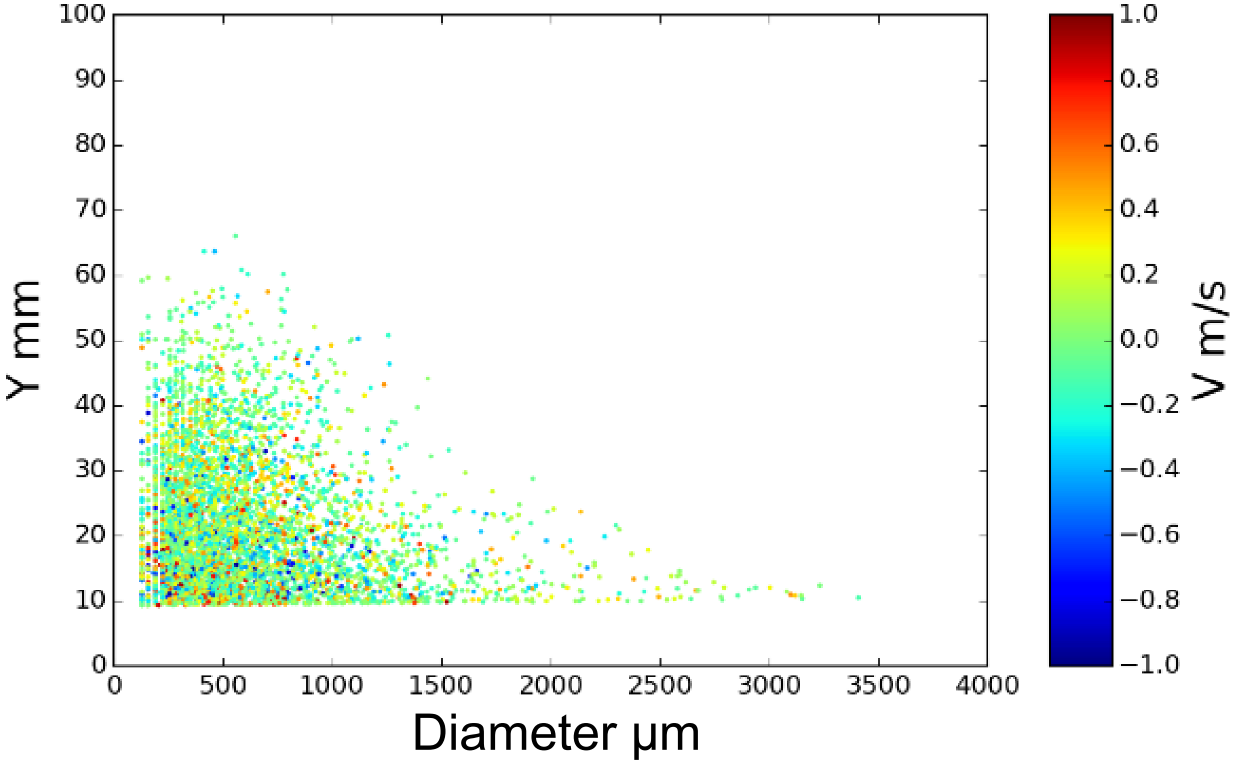

Figure 7.6 Height vs diameter vs velocity, triangular bundle, R-134a, 12.8 °C (55 °F), 20.3 kg/m²s (15000 lb/hr-ft²), 15.7 kW/m² (5000 Btu/hr-ft²), ideal liquid level, 50 mm lens, image location J

Figure 7.6 shows all droplets captured over all 100 images, plotting height vs diameter. Color shows velocity, with red colors indicating positive velocities and blue colors indicating negative velocities. Most droplets are shown to lie under 60 mm in height and below 2000 µm in diameter. The figure also shows a lack of large droplets high within the headspace. A similar figure is shown next.

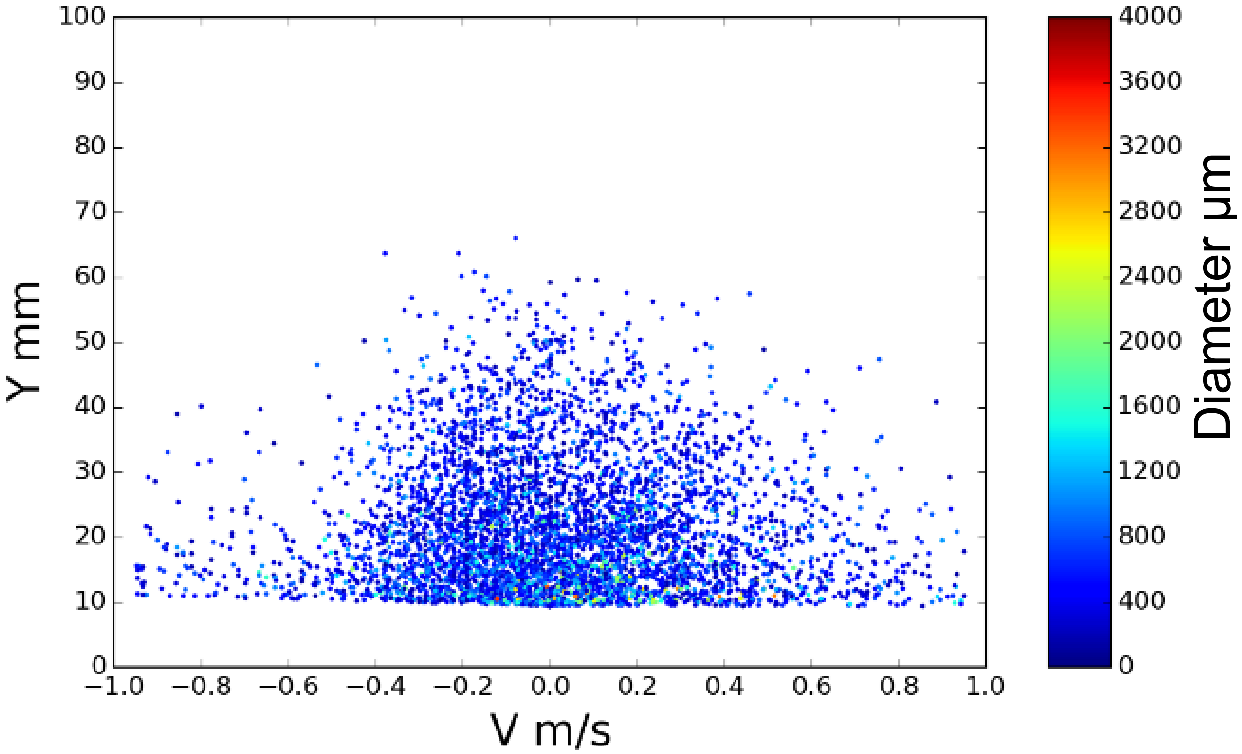

Figure 7.7 Height vs velocity vs diameter, triangular bundle, R-134a, 12.8 °C (55 °F), 20.3 kg/m^{2}s (15000 lb/hr-ft^2), 15.7 kW/m^2 (5000 Btu/hr-ft^2), ideal liquid level, 50 mm lens, image location J

Figure 7.7 shows all droplets captured over all 100 images, plotting height vs velocity. Color indicates diameter, ranging from a diameter of 0 μm for dark blue to 4000 μm for dark red. Again, a fairly symmetrical distribution in velocities is shown, centering close to zero for droplets higher in the headspace. Droplets between 0 and 10 mm are masked as it is not possible to recognize droplets that close to the tubes.

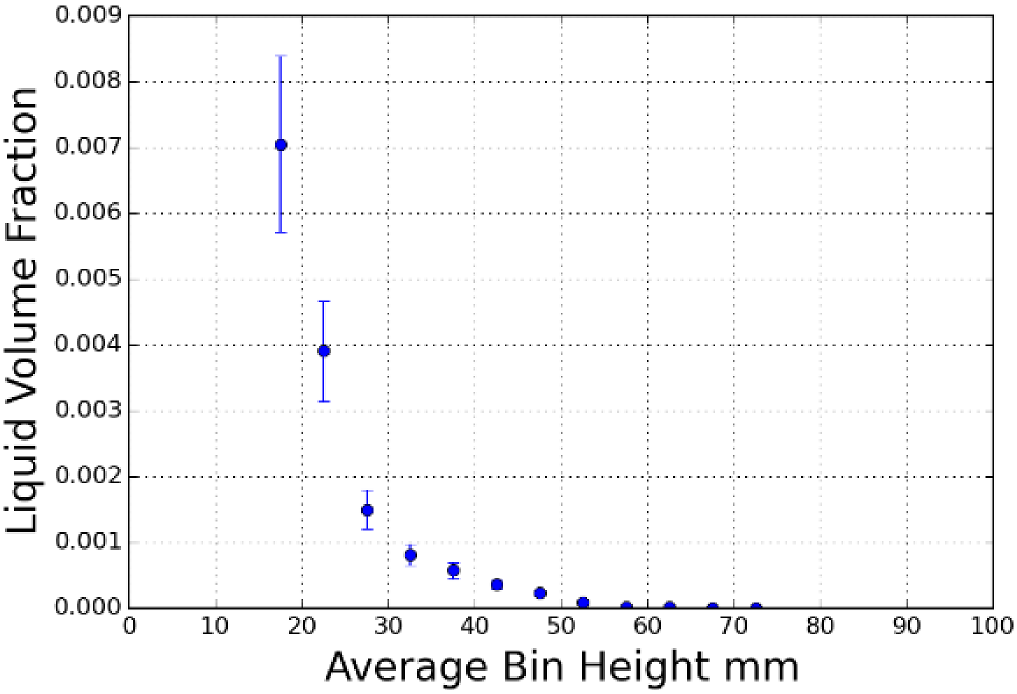

Figure 7.8 Liquid volume fraction, triangular bundle, R-134a, 12.8 °C (55 °F), 20.3 kg/m^{2}s (15000 lb/hr-ft^2), 15.7 kW/m^2 (5000 Btu/hr-ft^2), ideal liquid level, 50 mm lens, image location J

Figure 7.8 shows the liquid volume fraction vs height, with each point located at the center of a 5 mm bin height. These values were calculated in the manner described in Section 5.6, with uncertainties as described in Section 5.7 and are the average of all 100 images. The total liquid volume has greatly decreased by 30 mm above the tubes and is practically zero by 60mm while Figure 7.3 shows significant counts between 30 to 60 mm. This indicates that small droplets make up the bulk of recognized droplets above 30 mm. This difference illustrates the value of calculating the liquid volume fraction, as it combines the effect of both droplet counts and droplet size into one number.

The results with the 50 mm lens are briefly compared with those taken with the 100 mm lens in Figure 7.9. Several differences are noted. Figure 7.9(a) shows a higher percentage of matched droplets (67% vs 64%) than with the 50 mm lens in Figure 7.2. However, it also shows fewer droplets counted.

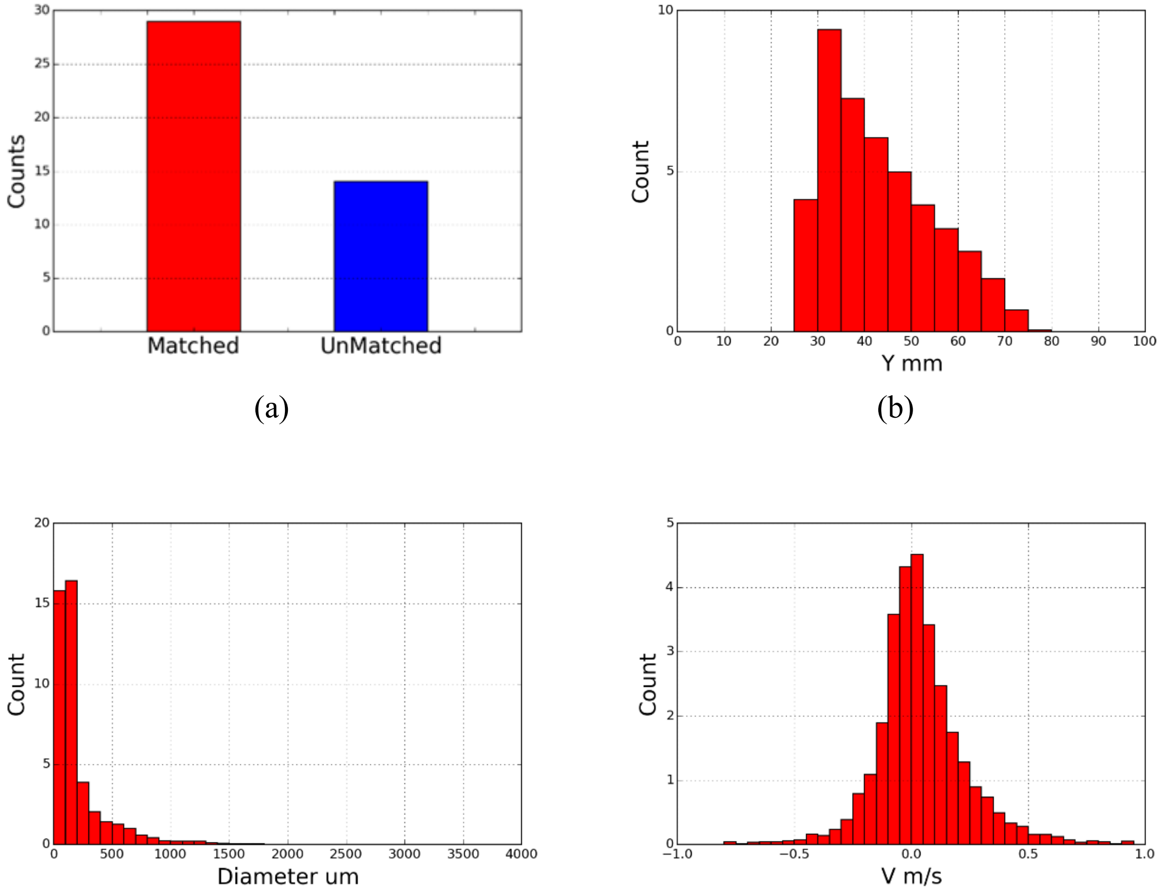

(a) (b)

(c) (d)

Figure 7.9 Data summary, 100 mm lens, triangular bundle, R-134a, 12.8 °C (55 °F), 20.3 kg/m^{2}s (15000 lb/hr-ft^2), 15.7 kW/m^2 (5000 Btu/hr-ft^2), ideal liquid level, image location J: (a) total counts, (b) counts versus height, (c) counts versus size, and (d) velocity distribution

The reason for fewer total droplets counted is two-fold. First, as described in section 4.4, the depth of focus for the 100 mm lens is less than half that of the 50 mm lens, meaning that the imaging volume is smaller. Second, in observing the height distributions of Figure 7.9(b) and Figure 7.3, no droplets are recognized below 25 mm. The 100 mm lens has a smaller field of view than the 50 mm lens. However, the 100 mm lens is able to see smaller droplets than the 50 mm lens. This is seen by droplets being recognized in Figure 7.9(b) up to 80 mm as opposed to 60 mm and having the peak count occurring at 35-40 mm as opposed to 10-15 mm. with the 50 mm lens. The recognition of smaller droplets is also seen by observing the droplet size distributions of Figure 7.9(c) and Figure 7.4. Most of the droplets recognized with the 100 mm lens are beneath 100 μm in diameter. Finally, comparing the velocity distributions of Figure 7.5 and Figure 7.9(d), again a mostly symmetrical distribution is seen. However, fewer droplets are seen with extremes at the end of the velocity scale. This again is explained by the smaller field of view with the 100 mm lens, as it does not see droplets near the tubes where higher velocities would be expected.

7.3 Variations

7.3.1 Liquid Level

The effect of liquid level for the triangular bundle with R-134a is shown in Figure 7.10. Figure 7.10(a) and (c) are at liquid level 1, the flooded condition of Table 7.3 while (b) and (d) are at liquid level 4, near dryout. Fewer droplets are seen overall with the near-dryout condition when compared with the baseline case of section 7.2 and the flooded case of Figure 7.10(a) and (b). The shape of the size distributions is similar in all cases, with a tendency towards smaller droplets. The baseline height distribution and near-dryout height distribution have a similar shape, though the distribution in the near-dryout case is both lower in height by about 10 mm and in number. The flooded height distribution can be seen to shift upward in the headspace compared to the ideal case by about 30 mm, explained by the peak liquid level count in the flooded case being approximately 1 inch (25 mm) above that of the ideal case.

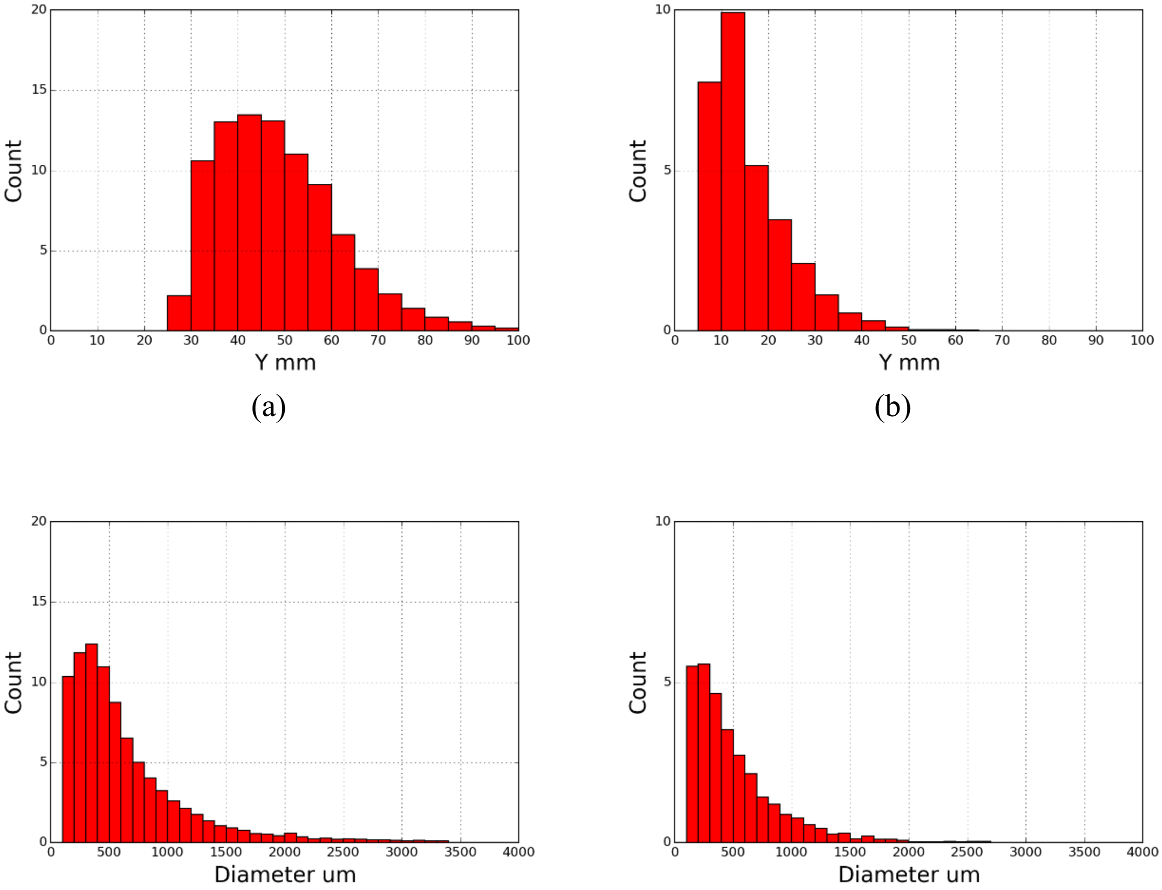

(a) (b)

(c) (d)

Figure 7.10 Liquid level comparison, triangular bundle, R-134a, 12.8 °C (55 °F), 20.3 kg/m^{2}s (15000 lb/hr-ft^2), 15.7 kW/m^2 (5,000 Btu/hr-ft^2), 50 mm lens, image location J: (a) flooded height distribution; (b) near-dryout height distribution, (c) flooded size distribution, (d) near-dryout size distribution

7.3.2 Mass Flux

Figure 7.11 shows the effect of varying mass flux, with (a) and (c) displaying the baseline case, and (b) and (d) displaying the higher mass flux of 40.7 kg/m^{2}s (30000 lb/hr-ft^2). Not only are the droplet counts of Figure 7.11(b) much higher than those of the baseline in (a), droplets are shown to reach up to 100 mm, 40 mm higher than with the baseline. Similarly, the velocity distribution of Figure 7.11(b) shows much higher counts as well as higher velocities than (c). The higher mass flux results also show a slight skew towards a positive velocity, indicating droplets may be leaving the test section. Note that (c) has a bin size of 0.05 m/s and (d) has a bin size of 0.1 m/s.

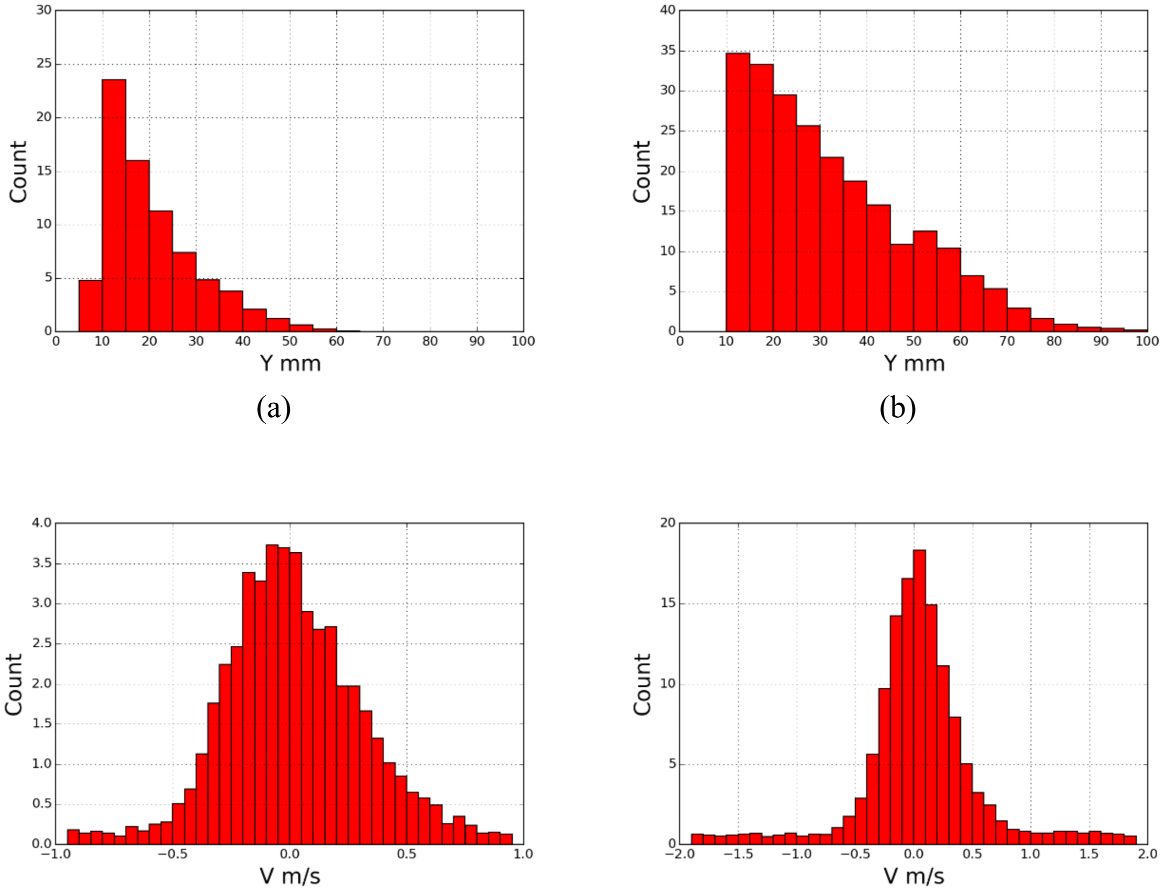

(a) (b)

(c) (d)

Figure 7.11 Mass flux comparison, triangular bundle, R-134a, 12.8 °C (55 °F), 15.7 kW/m^2 (5000 Btu/hr-ft^2), ideal liquid level, 50 mm lens, image location J: (a) 20.3 kg/m^{2}s (15000 lb/hr-ft^2) height distribution; (b) 40.7 kg/m^{2}s (30000 lb/hr-ft^2) height distribution, (c) 20.3 kg/m^{2}s (15000 lb/hr-ft^2) velocity distribution, (d) 40.7 kg/m^{2}s (30000 lb/hr-ft^2) velocity distribution

7.3.3 Saturation Temperature

Figure 7.12 shows the effect of varying outlet saturation temperature, with (a) and (c) displaying the baseline while (b) and (d) show the saturation temperature at 4.4 °C (40 °F). Both height and velocity distributions show increased counts with a lower saturation temperature. For the height distributions, the lower saturation temperature data show droplets extending up to 100 mm above the tubes, compared with 60 mm for the baseline. Velocities likewise show a positive skew for the lower saturation temperature contrasted with the symmetrical distribution for the baseline.

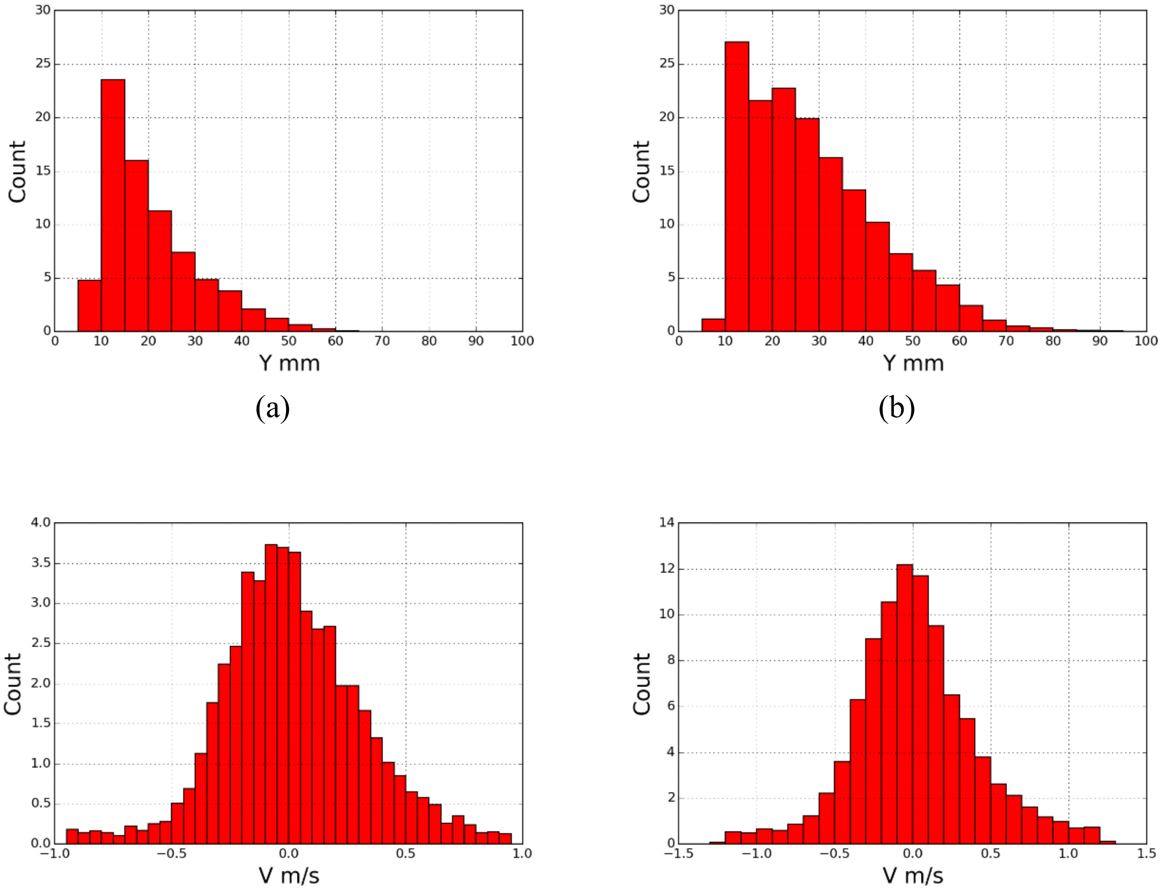

(a) (b)

(c) (d)

Figure 7.12 Saturation temperature comparison, triangular bundle, R-134a, 20.3 kg/m^{2}s (15000 lb/hr-ft^2), 15.7 kW/m^2 (5000 Btu/hr-ft^2), 50 mm lens, image location J: (a) 12.8 °C (55 °F) height distribution; (b) 4.4 °C (40 °F) height distribution, (c) 12.8 °C (55 °F) velocity distribution, (d) 4.4 °C (40 °F) velocity distribution

The variation between saturation temperatures can be explained by the difference in vapor densities between the two temperatures. The vapor density at the baseline case is approximately 30% higher than for R-134a at 4.4 °C (40 °F). Assuming the same mass flux, this would yield both between-tube and headspace velocities approximately 30% higher for the lower saturation temperature condition. The effect would be similar to increasing the mass flux by 30% while maintaining the baseline saturation temperature.

7.3.4 Heat Flux

As the difference between the baseline heat flux and the variant is only 7.0 kW/m^2 (2200 Btu/hr-ft^2), the higher mass flux condition is used to show the effect of varying heat flux. Figure 7.13(a) shows the higher mass flux condition with an upper rows heat flux of 15.7 kW/m^2 (5000 Btu/hr-ft^2) while (b) has a heat flux of 31.5 kW/m^2 (10000 Btu/hr-ft^2).

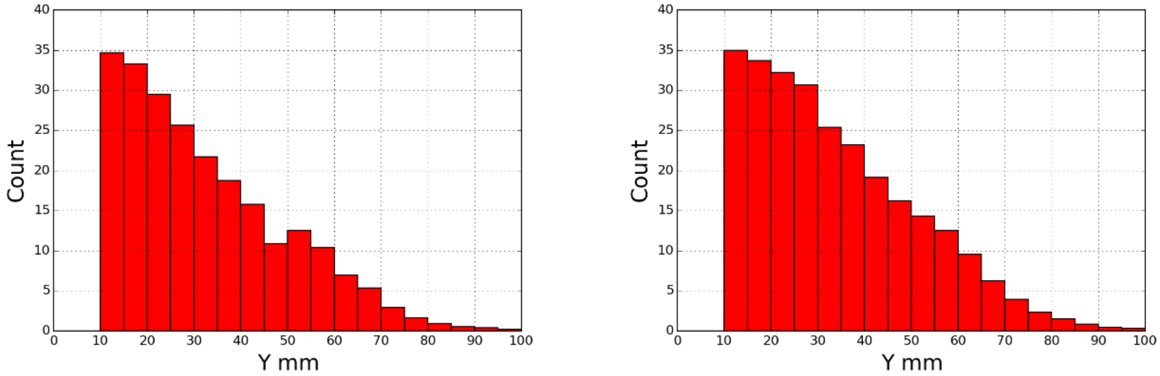

(a) (b)

Figure 7.13 Heat flux comparison, triangular bundle, R-134a, 12.8 °C (55 °F), 40.7 kg/m^{2}s (30000 lb/hr-ft^2), 50 mm lens, image location J: (a) 15.7 kW/m^2 (5000 Btu/hr-ft^2) height distribution; (b) 31.5 kW/m^2 (10000 Btu/hr-ft^2) height distribution

No significant difference is seen between the two cases. Both have a similar distribution, overall count, and reach up to the same height in the headspace. Heat flux has little effect with this bundle with R-134a.

7.3.5 Summary

For the triangular bundle with R-134a, eight thermodynamic conditions were tested. Liquid level, mass flux, and saturation temperature were found to have significant effects on droplet distribution and velocity within the headspace. Heat flux was not found to have a significant effect.

Chapter 8 - Triangular Bundle with R-123

The triangular bundle arrangement with R-123 was the second bundle and refrigerant combination tested. This set of results was also the first where liquid levels and imaging locations were standardized. It was also one of the most difficult sets of data to obtain as it required the installation of a new, larger condenser in the system to account for the high volume of vapor exiting from the test section necessary to reach the desired test conditions. It also posed difficulties with the higher number of droplets reaching the top of the headspace and flowing back down the walls to the bundle, making imaging difficult due to liquid on the glass walls. The complete set of data may be found in Appendix B.

8.1 Test Matrix

Again, eight thermodynamic conditions were tested. However, some additional points were added to allow matching velocities in the bundle and headspace with those used with R-134a. The standard plus added conditions are shown in Table 8.1below.

Table 8.1 Test matrix, triangular bundle with R-123

Thermodynamic Condition	Outlet Saturation Temperature, °C (°F)	Mass Flux, kg/m^2-s ($lb/hr\text{-}ft^2$)	Top Rows Heat Flux, kW/m^2 ($Btu/hr\text{-}ft^2$)
1	4.4 (40)	20.3 (15000)	15.7 (5000)
2	4.4 (40)	40.7 (30000)	15.7 (5000)
3	4.4 (40)	40.7 (30000)	31.5 (10000)
4	12.8 (55)	3.46 (2550)	5.4 (1700)
5	12.8 (55)	10.2 (7500)	11.0 (3500)
6	12.8 (55)	20.3 (15000)	15.7 (5000)
7	12.8 (55)	40.7 (30000)	15.7 (5000)
8	12.8 (55)	40.7 (30000)	31.5 (10000)

Conditions 4 and 5 are variations in which an attempt was made to match the interstitial velocities (and thus headspace velocities) of the low and high mass fluxes with R-134a. The mass flux of 3.06 kg/m^2-s (2250 lb/hr-ft^2) matches the interstitial and headspace velocities found with R-134a at a mass flux of 20.3 kg/m^2-s (15000 lb/hr-ft^2). The top rows heat flux of 5.4 kW/m^2 (1700 Btu/hr-ft^2) was the maximum possible for R-123 in this bundle configuration. Unfortunately, the mass flux of 10.2 kg/m^2-s (7500 lb/hr-ft^2), intended to match the interstitial and headspace velocities found with R-134a for a mass flux of 40.7 kg/m^2-s (30000 lb/hr-ft^2), is 40% higher than it should be. Also, mass fluxes at these low levels were difficult to control due to how slow the refrigerant pump needed to run, so mass fluxes were able to range up to 10.9 kg/m^2-s (8000 lb/hr-ft^2).

For this set of data, the number of liquid levels was reduced to three. These levels are described in Table 8.2. As little difference was seen between liquid levels when the bundle was flooded, a single flooded level was taken. For R-123, this still proved difficult to obtain as R-123 generated much more liquid in the headspace than R-134a. A pool of liquid through which vapor bubbled up was never apparent, so a decision was made to instead choose a point at which up to 25 mm (1 inch) of the sight glass above the tubes was obscured by droplets on the wall. Even this proved difficult at times for acquiring good images. For the ideal liquid level, the point at which the htc ratio began to decrease was chosen. The dryout liquid level was chosen to be ½ of the ideal liquid level htc ratio. Essentially, this was the point at which the two top tubes were dried out while the next three rows were still wetted.

Table 8.2 Liquid level descriptions, triangular bundle with R-123

Liquid Level	Description	Designation
1	19-25 mm (0.75-1 inch) apparent liquid on sight glass above tubes	Flooded
2	Liquid just above tubes	Ideal
3	Liquid below tubes	Dryout

Three image locations were taken, as much for brevity as necessity. Little difference was found with the first bundle test past the center of the bundle. Especially for the high mass flux conditions, it was impossible to image past the center of the bundle due to out-of-focus droplets between the imaging plane and the camera distorting the image. As such, imaging locations M and N were largely discontinued except for lower mass flux and/or low liquid level conditions when good images could be produced. Overall, 161 sets of 100 image pairs were captured, meaning a data set of 32200 images.

8.2 Baseline data

An example of processed images for the baseline data is shown in Figure 8.1. Droplets are shown in shades of grey and pink, while background and vapor are shown as black. Towards the edge of the images are visible wave shaped structures. These structures are liquid drops on the wall, but in processing are largely masked. The baseline results for R-123 with the triangular bundle are shown in Figure 8.2 through Figure 8.8 for the 50 mm lens. These figures show thermodynamic condition 6 of Table 8.1, with an outlet saturation temperature of 12.8 °C (55 °F), mass flux of 20.3 kg/m^{2}s (15000 lb/hr-ft^2), and top rows heat flux of 15.7 kW/m^2 (5000 Btu/hr-ft^2) and was taken at the ideal liquid level in the J location of Figure 3.2(a). The data shown in histogram form is the mean of 100 images (first image per image pair of a run). The velocity distribution histogram only show droplets which were matched between image pairs. Height vs velocity vs diameter and height vs diameter vs velocity plots only include droplets that were matched, but they do include droplets from all 100 images.

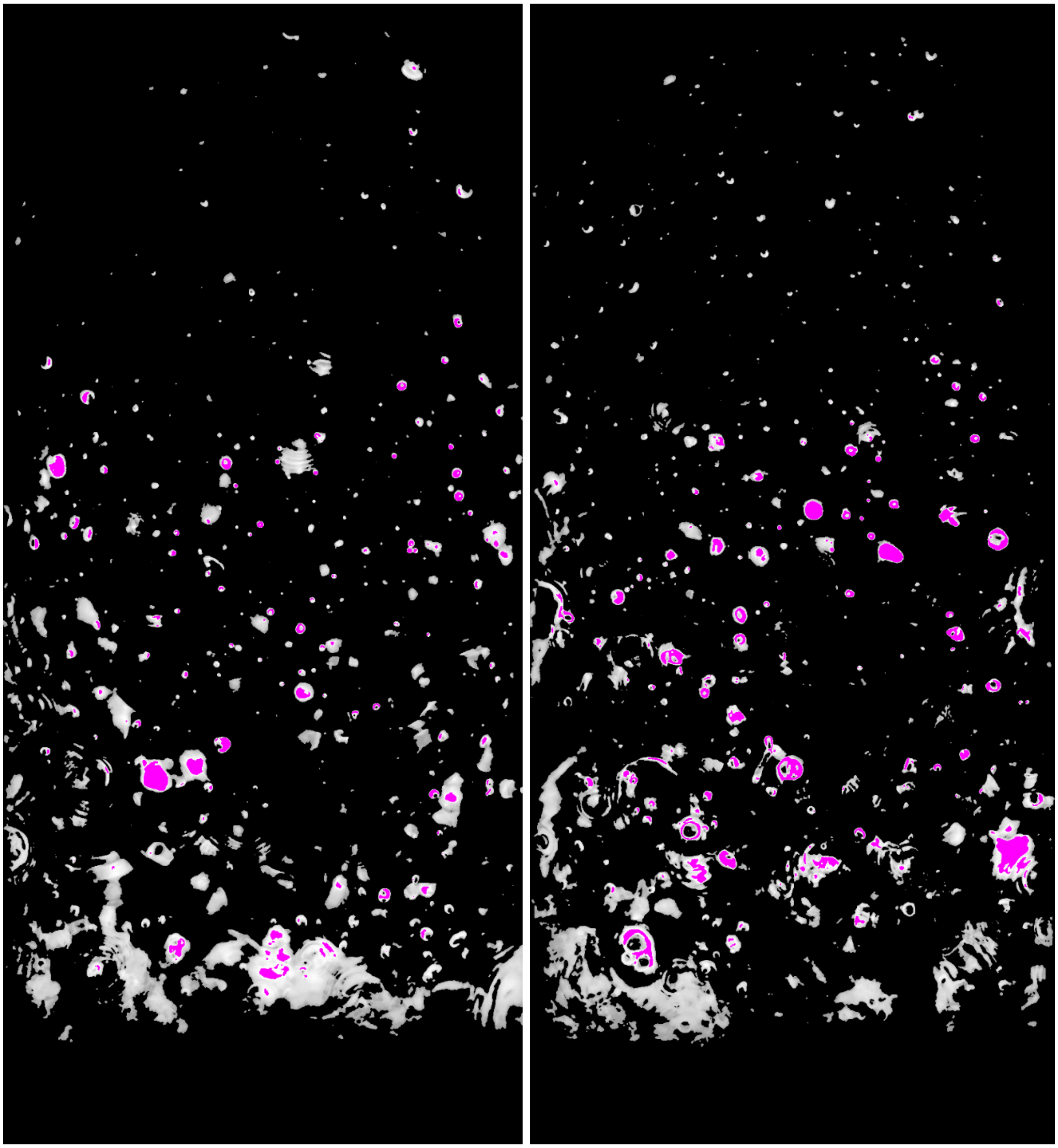

Figure 8.1 Processed images, triangular bundle, R-123, 12.8 °C (55 °F), 20.3 kg/m^{2}s (15000 lb/hr-ft^2), 15.7 kW/m^2 (5000 Btu/hr-ft^2), ideal liquid level, 50 mm lens, image location J

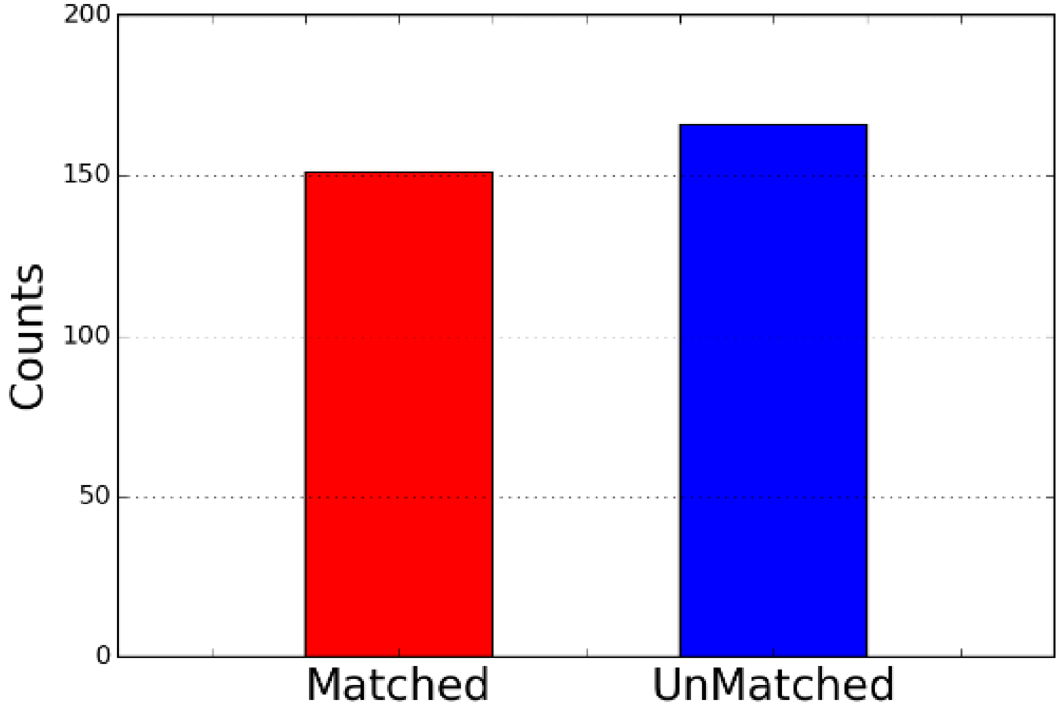

Figure 8.2 Matched counts, triangular bundle, R-123, 12.8 °C (55 °F), 20.3 kg/m^{2}s (15000 lb/hr-ft^2), 15.7 kW/m^2 (5000 Btu/hr-ft^2), ideal liquid level, 50 mm lens, image location J

Figure 8.2, showing matched and unmatched counts, gives a representation of how many droplets were matched between images in an image pair. Figure 8.2 shows that an average of 315 droplets were counted per image and that 48% of these droplets were deemed a match by the droplet recognition software. This low match rate is not unusual for this and the higher mass flux conditions. The large number of droplets with R-123 makes both recognition and matching difficult.

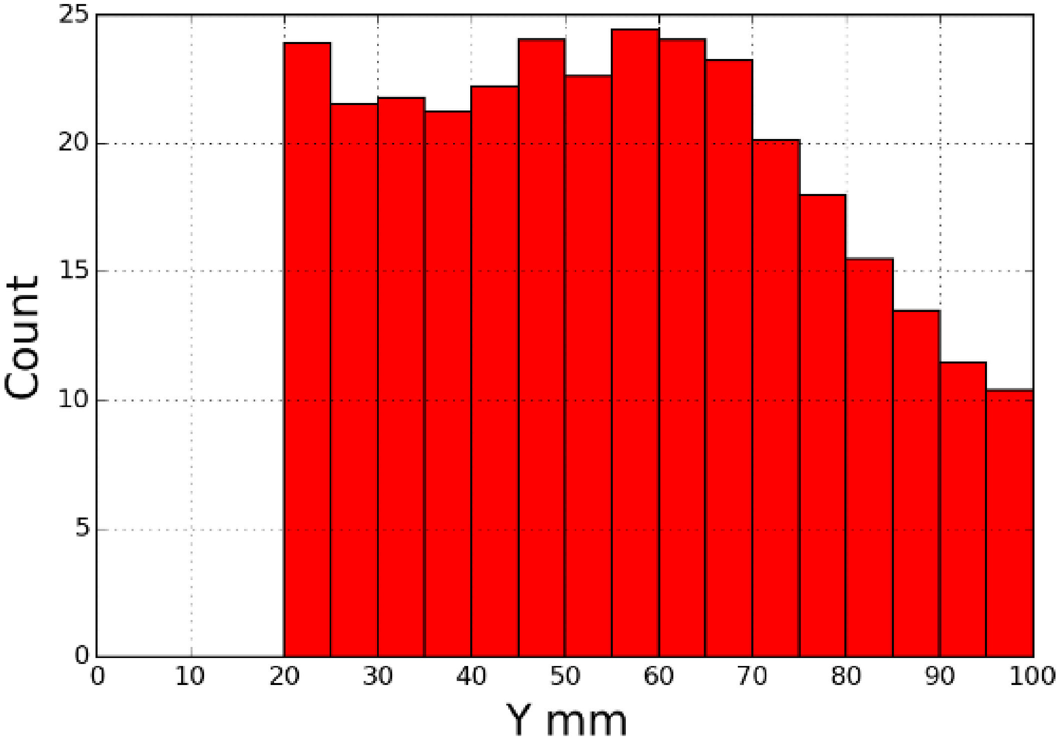

Figure 8.3 Height distribution, triangular bundle, R-123, 12.8 °C (55 °F), 20.3 kg/m^{2}s (15000 lb/hr-ft^2), 15.7 kW/m^2 (5000 Btu/hr-ft^2), ideal liquid level, 50 mm lens, image location J

Figure 8.3 shows the distribution of droplets vs height above the tubes. Droplets are binned every 5 mm of height. A peak of about 28 droplets/image count is seen between 55 and 60 mm above the tubes, decreasing from that point to 10 droplets/image by 100 mm above the tubes. Droplet counts between 20 and 60 mm above the tube are approximately constant, but a peak does exist at the first bin from 20 to 25 mm.

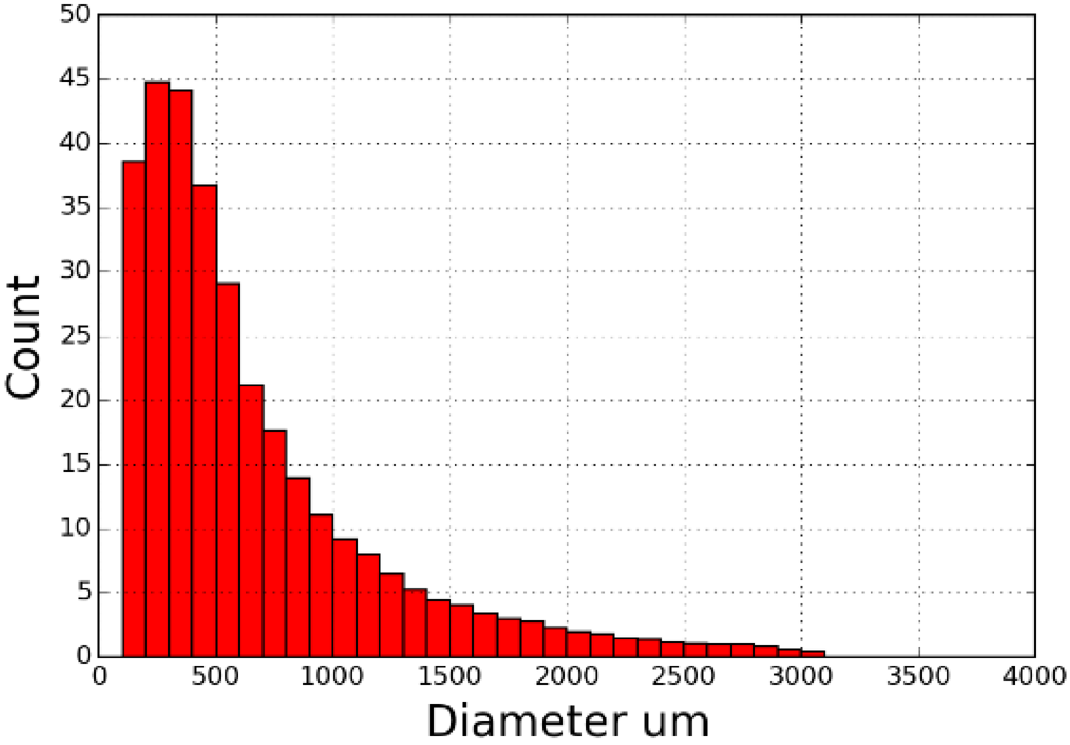

Figure 8.4 Size distribution, triangular bundle, R-123, 12.8 °C (55 °F), 20.3 kg/m^{2}s (15000 lb/hr-ft^2), 15.7 kW/m^2 (5000 Btu/hr-ft^2), ideal liquid level, 50 mm lens, image location J

Figure 8.4 shows the size distribution of droplets. Droplets are binned for every 100 μm of diameter, with the majority of droplets recognized sized beneath 600 μm and a peak of 45 droplets/image for droplets of 200 to 300 μm. Droplets up to 3100 μm have been recognized, but their numbers are miniscule compared to droplets with smaller diameters. Note that for any figure in this chapter or Appendix B with an axis labelled “Diameter um”, um denotes μm.

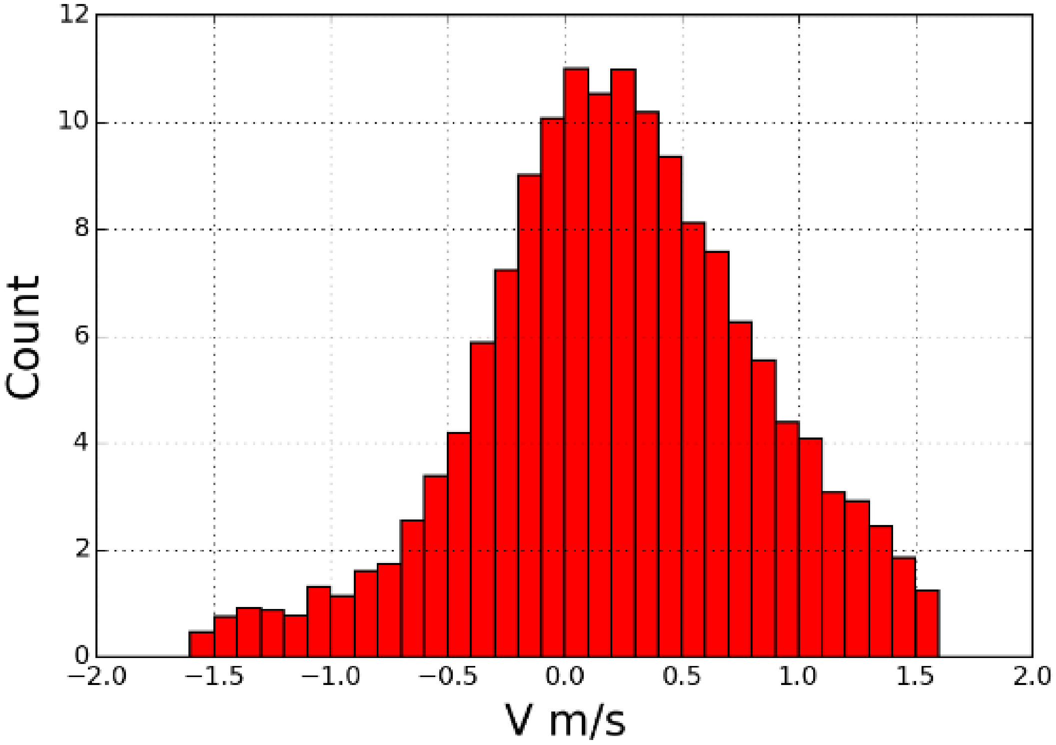

Figure 8.5 Velocity distribution, triangular bundle, R-123, 12.8 °C (55 °F), 20.3 kg/m^{2}s (15000 lb/hr-ft^2), 15.7 kW/m^2 (5000 Btu/hr-ft^2), ideal liquid level, 50 mm lens, image location J

Figure 8.5 shows the velocity distribution of droplets within the headspace. Droplets are binned for every 0.1 m/s. Droplet velocities of ±1.6 m/s have been recognized. Droplet counts are not symmetrical about zero, reaching a peak count between 0 and 0.3 m/s. This positive skew indicates a net outflow of droplets out of the test section, or at least out of the field of view of the camera. This positive skew indicates that more droplets are rising than falling and that refrigerant is leaving with a quality less than 1. Indeed, a thermodynamic balance of the test section shows an exit quality approaching 90%.

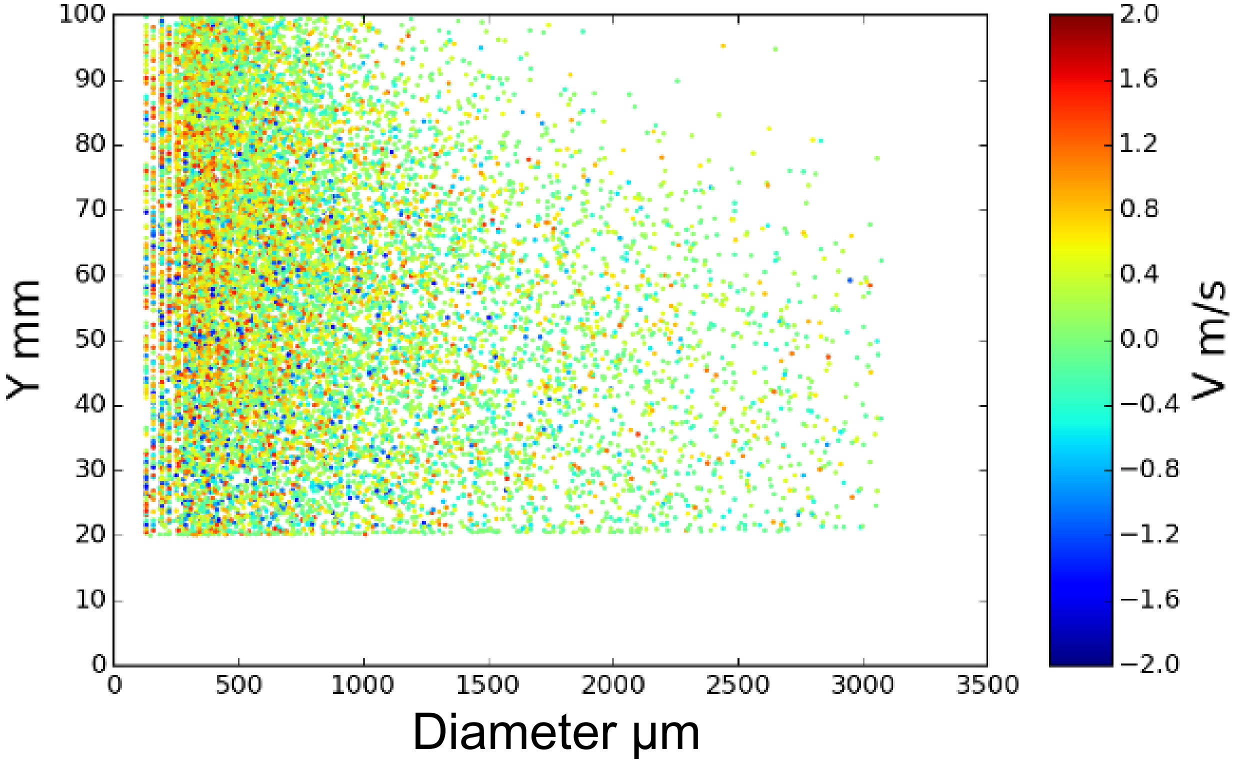

Figure 8.6 Height vs diameter vs velocity, triangular bundle, R-123, 12.8 °C (55 °F), 20.3 kg/m^{2}s (15000 lb/hr-ft^2), 15.7 kW/m^2 (5000 Btu/hr-ft^2), ideal liquid level, 50 mm lens, image location J

Figure 8.6 shows matched droplets captured over all 100 images, plotting height vs diameter. Color shows velocity, with red colors indicating positive velocities and blue colors indicating negative velocities. Droplets extend between 20 to 100 mm above the tube bundle, with diameters up to 3100 µm. Large diameter droplets are recognized up to the top of the headspace, but primarily lie in the region below 70 mm.

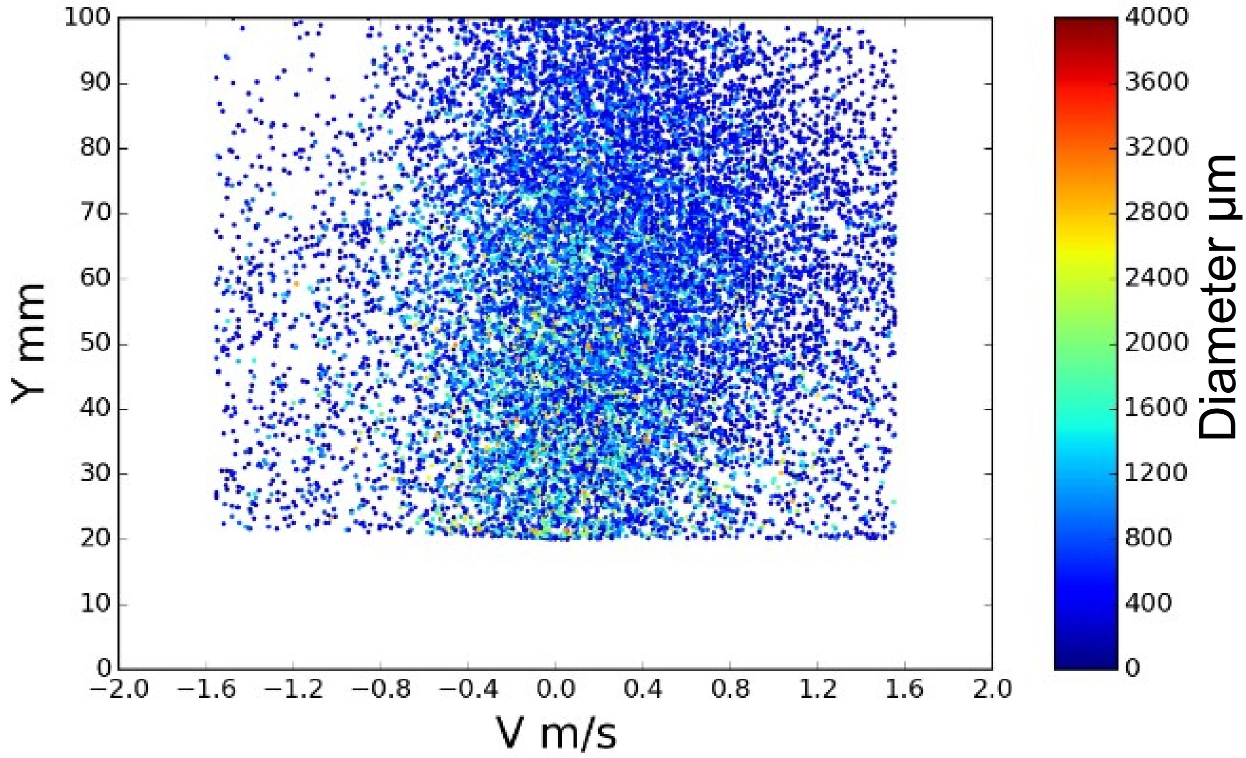

Figure 8.7 Height vs velocity vs diameter, triangular bundle, R-123, 12.8 °C (55 °F), 20.3 kg/m²s (15000 lb/hr-ft²), 15.7 kW/m² (5000 Btu/hr-ft²), ideal liquid level, 50 mm lens, image location J

Figure 8.7 shows matched droplets captured over all 100 images, plotting height vs velocity. Color indicates diameter, ranging from a diameter of 0 μm for dark blue to 4000 μm for dark red. A higher density of droplets is seen to the positive side of zero velocity. Larger droplets are generally seen closer to the tube bundle.

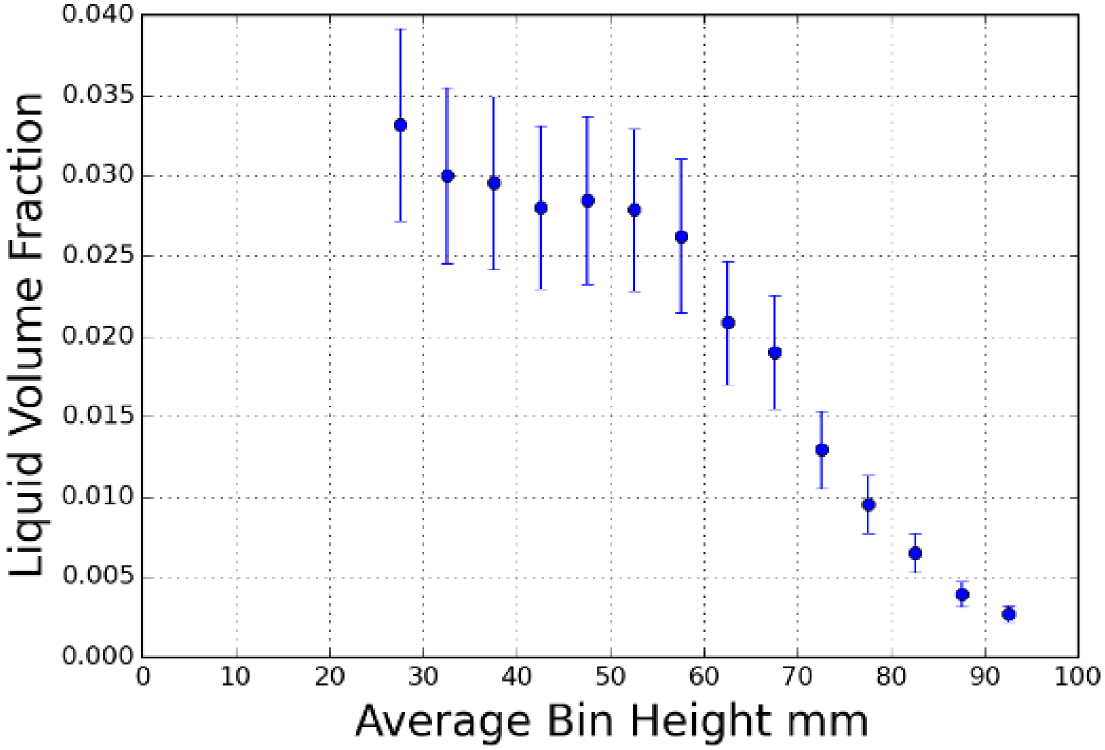

Figure 8.8 Liquid volume fraction, triangular bundle, R-123, 12.8 °C (55 °F), 20.3 kg/m^{2}s (15000 lb/hr-ft^2), 15.7 kW/m^2 (5000 Btu/hr-ft^2), ideal liquid level, 50 mm lens, image location J

Figure 8.8 shows the liquid volume fraction vs height, with each point located at the center of a 5 mm bin height. These values were calculated in the manner described in Section 5.6 with uncertainties as described in Section 5.7 and are the average of all 100 images. A rapid decrease is seen in liquid volume fraction from 60 mm to the top of the headspace, similar to the decrease in droplet counts seen in Figure 8.3. From 25 to 60 mm, liquid volume fraction shows a slight decrease whereas droplet counts show a slight increase. Both combined show larger droplets decreasing in number while smaller droplets increase from 25 to 60 mm above the tubes. Past 60 mm, all droplets decrease in number. The difference between the figures shows the value of calculating the liquid volume fraction, as it combines the effect of both droplet counts and droplet size.

The results for the 100 mm lens are presented for comparison purposes with the 50 mm lens in Figure 8.9. Several differences are noted. Figure 8.9(a) shows a lower percentage of matched droplets (41% vs 48%) than with the 50 mm lens in Figure 8.2. It also shows a slightly higher droplet count.

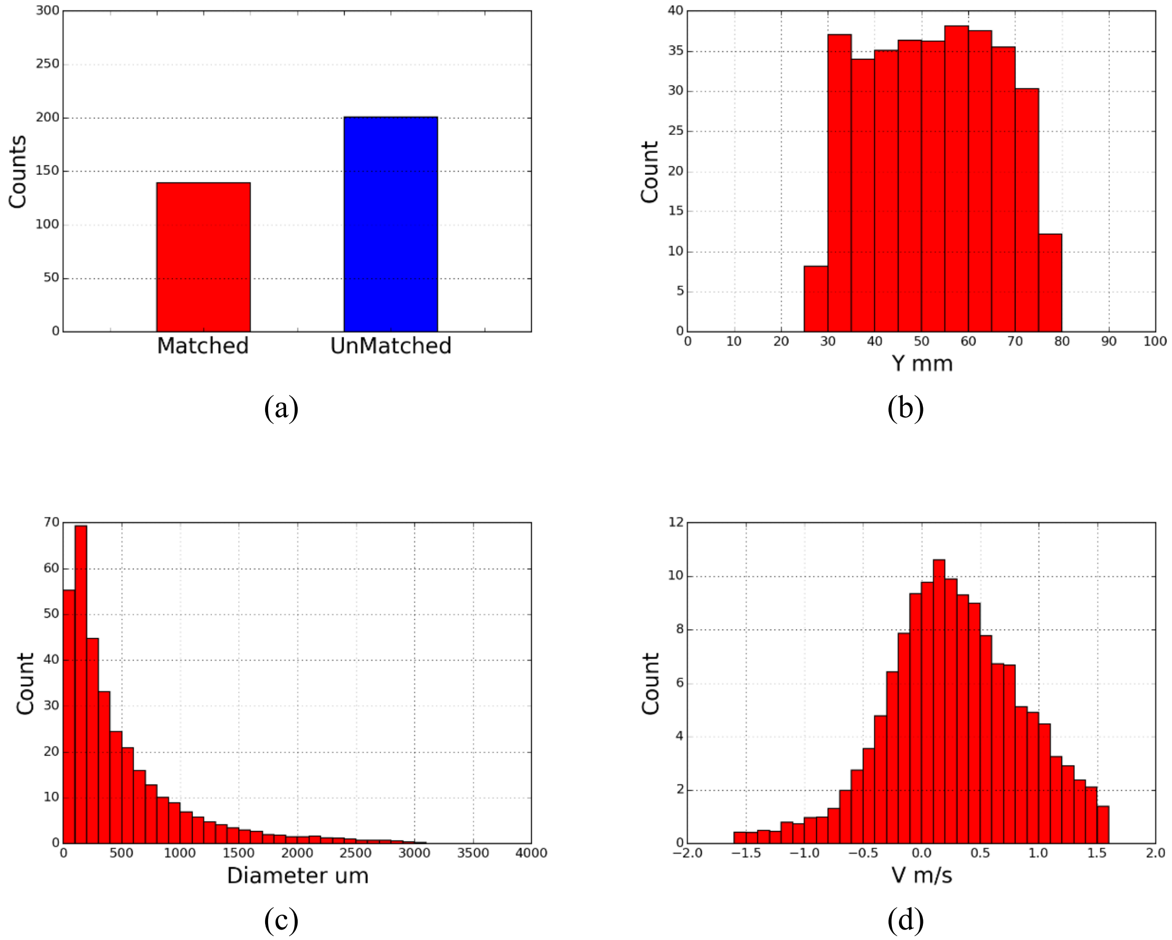

(a) (b)

(c) (d)

Figure 8.9 Data summary, 100 mm lens, triangular bundle, R-123, 12.8 °C (55 °F), 20.3 kg/m^{2}s (15000 lb/hr-ft^2), 15.7 kW/m^2 (5000 Btu/hr-ft^2), ideal liquid level, image location J: (a) total counts, (b) counts versus height, (c) counts versus size, and (d) velocity distribution

The higher counts are explained both by the reduced depth of focus of the 100 mm lens and by comparing Figure 8.9(c) and Figure 8.4. The 50 mm lens shows similar size distribution for droplets 300 μm and larger, but the 100 mm lens shows much greater counts for droplets under 300 μm. Note also that the height distribution of Figure 8.9(b) shows near constant counts up to 75 mm while the 50 mm lens in Figure 8.3 shows a decrease in counts from 60 mm on. This indicates that droplets smaller than 300 μm are persisting through the top of the 100 mm lens field of view. The reduction in recognized droplets between 75 and 80 mm can be explained by the smaller field of view with the 100 mm lens. Indeed, the highest droplet recognized with the 100 mm lens in this run occurs 77 mm, meaning three-fifths of the 5 mm bin is not covered by the camera. Examining Figure 8.9(d), a positive velocity skew is seen, similar to that of Figure 8.5.

8.3 Variations

8.3.1 Liquid Level

The effect of liquid level for the triangular bundle with R-123 is shown in Figure 8.10. Figure 8.10(a) and (c) are at liquid level 1, the flooded condition of Table 7.3 while (b) and (d) are at liquid level 3, dryout. Many fewer droplets are seen overall with the dryout condition when compared with the baseline case of section 7.2 and the flooded case of Figure 8.10 (a) and (b). However, droplets are seen through to the top of the headspace for all liquid levels. The shape of the size distributions is similar in all cases, with a tendency towards smaller droplets.

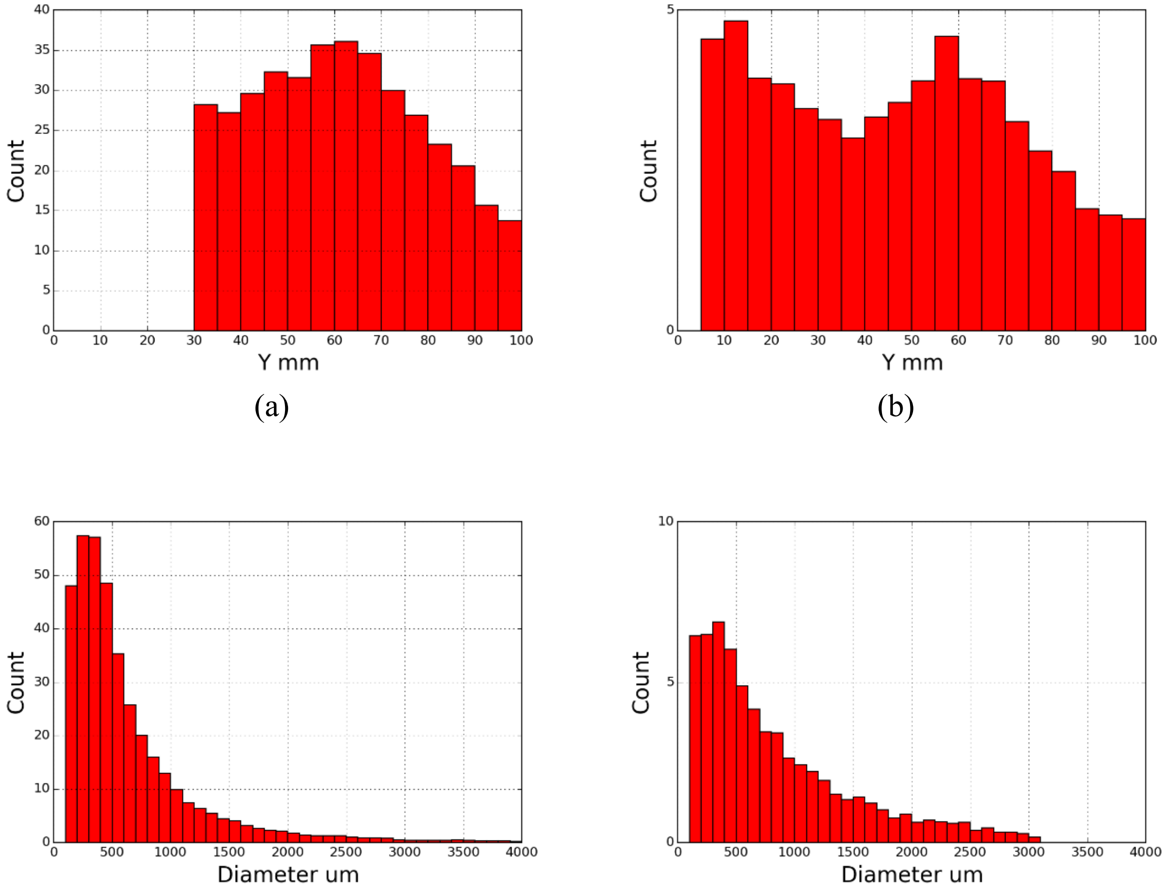

(a) (b)

(c) (d)

Figure 8.10 Liquid level comparison, triangular bundle, R-123, 12.8 °C (55 °F), 20.3 kg/m^{2}s (15000 lb/hr-ft^2), 15.7 kW/m^2 (5,000 Btu/hr-ft^2), 50 mm lens, image location J: (a) flooded height distribution; (b) near-dryout height distribution, (c) flooded size distribution, (d) dryout size distribution

8.3.2 Mass Flux

Figure 8.11 shows the effect of varying mass flux, with (c) being the baseline. Mass flux ranges from 3.46 kg/m^{2}s (2550 lb/hr-ft^2) in (a) to 40.7 kg/m^2-s (30000 lb/hr-ft^2) in (d). Both (c) and (d) have a top rows heat flux of 5.4 kW/m^2 (5000 Btu/hr-ft^2) while the lower mass fluxes of (a) and (b) are at lower heat fluxes, limited by the carrying capacity of the refrigerant and bundle. Droplet counts are seen to not only increase but also tend to flatten out with increasing height as mass flux is increased. By the high mass flux condition of (d) droplet counts are near flat across the headspace, with only a gradual decrease from a peak at 40 to 45 mm.

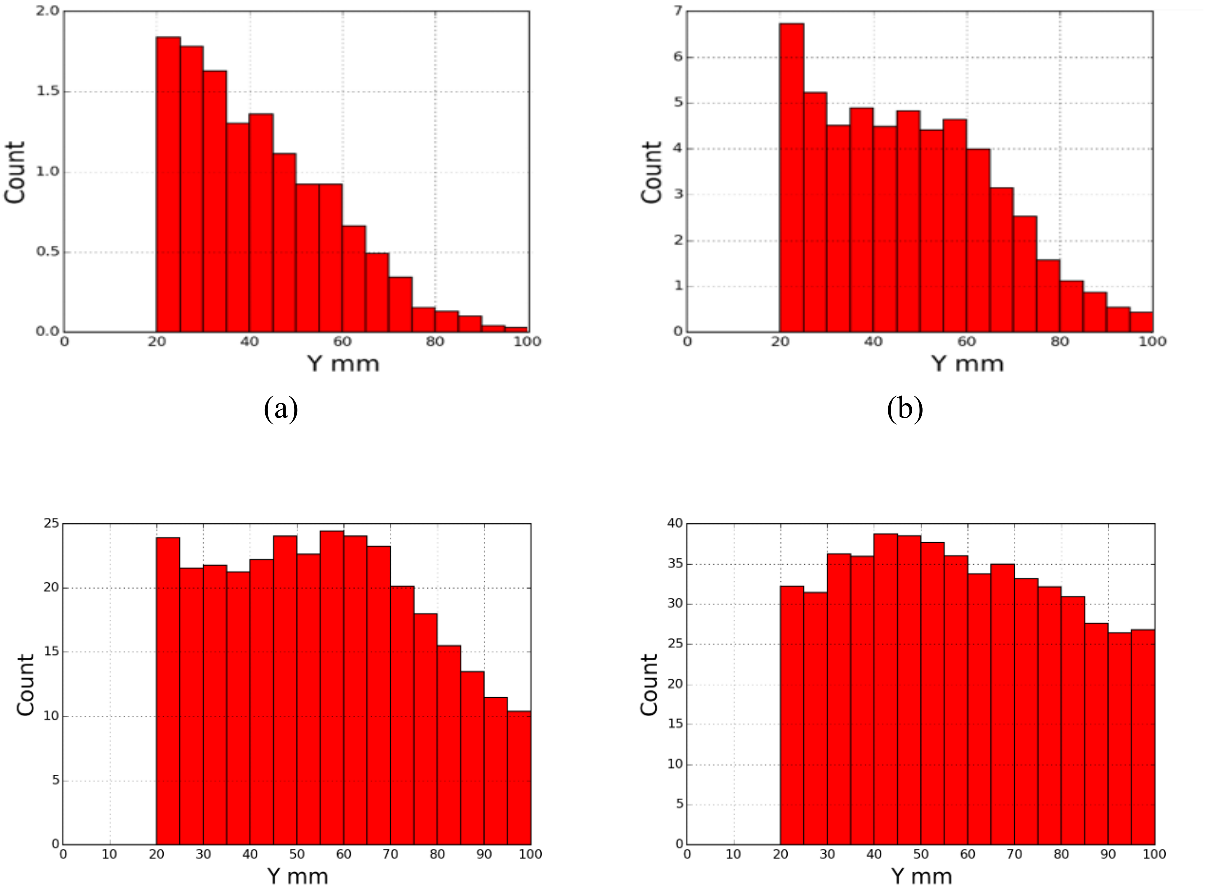

(a) (b)

(c) (d)

Figure 8.11 Mass flux comparison, height distribution, triangular bundle, R-123, 12.8 °C (55 °F), ideal liquid level, 50 mm lens, image location J: (a) 3.46 kg/m^{2}s (2550 lb/hr-ft^2), (b) 10.2 kg/m^{2}s (7500 lb/hr-ft^2), (c) 20.3 kg/m^{2}s (15000 lb/hr-ft^2), (d) 40.7 kg/m^{2}s (30000 lb/hr-ft^2)

Figure 8.12 shows velocity distributions for the same thermodynamic conditions as Figure 8.11. The lowest mass flux shows very low counts roughly centered about zero-velocity, indicating that refrigerant is remaining within the headspace. Figure 8.12(b) shows higher counts and a slight positive skew, indicating liquid may be leaving. The highest mass flux velocity distribution in (d) shows a definite positive skew, with well over half of the droplets recognized rising in the headspace. Note that (a) has a bin size of 0.05 m/s, (b) and (c) have a bin size of 0.1 m/s, and (d) has a bin size of 0.25 m/s.

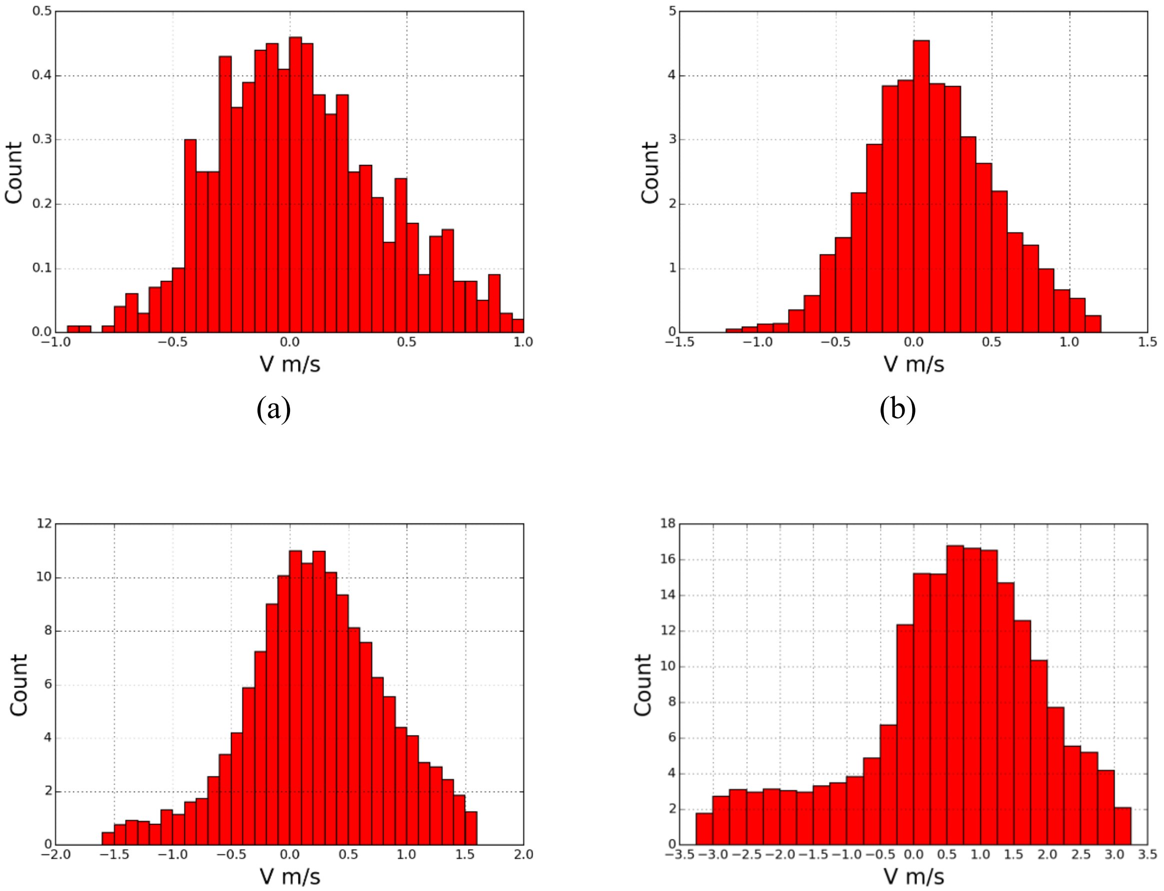

(a) (b)

(c) (d)

Figure 8.12 Mass flux comparison, velocity distribution, triangular bundle, R-123, 12.8 °C (55 °F), ideal liquid level, 50 mm lens, image location J: (a) 3.46 kg/m^{2}s (2550 lb/hr-ft^2), (b) 5.4 kg/m^{2}s (7500 lb/hr-ft^2), (c) 20.3 kg/m^{2}s (15000 lb/hr-ft^2), (d) 40.7 kg/m^{2}s (30000 lb/hr-ft^2)

8.3.3 Saturation Temperature

Figure 8.13 shows the effect of varying outlet saturation temperature, with (a) and (c) displaying the baseline while (b) and (d) show setting the saturation temperature at 4.4 °C (40 °F). The lower saturation temperature results of (b) show both greater counts in the height distribution than the baseline of (a) and a different distribution. Droplets counts have a slow rise from 20 mm to reach a peak and then begin to drop off after 70 mm with the lower saturation temperature, whereas the baseline results show approximately constant results until 60 mm and then a halving of counts for height increasing to 100 mm. The slow rise in droplet counts from 20 to 70 mm for (c) may be explained by larger droplets in that section blocking the recognition of smaller droplets.

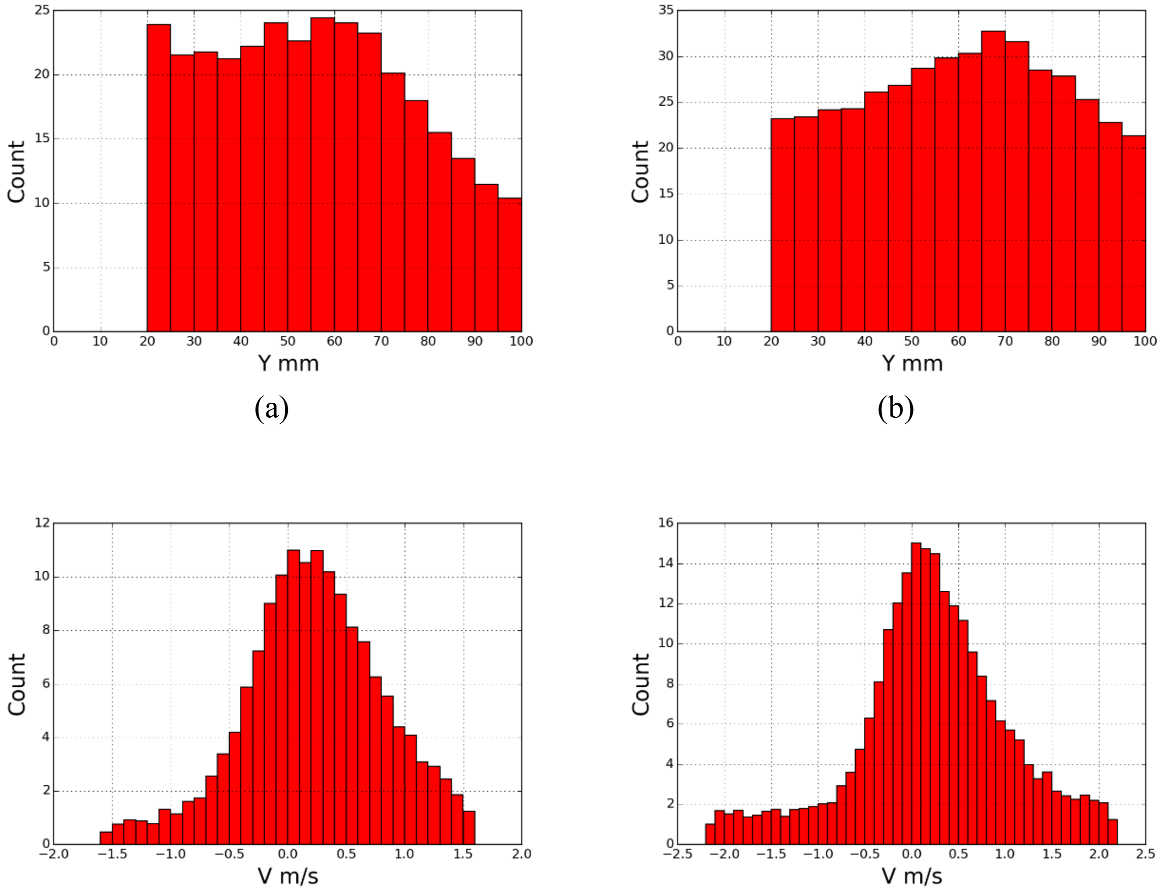

(a) (b)

(c) (d)

Figure 8.13 Saturation temperature comparison, triangular bundle, R-123, 20.3 kg/m^{2}s (15000 lb/hr-ft^2), 15.7 kW/m^2 (5000 Btu/hr-ft^2), 50 mm lens, image location J: (a) 12.8 °C (55 °F) height distribution; (b) 4.4 °C (40 °F) height distribution, (c) 12.8 °C (55 °F) velocity distribution, (d) 4.4 °C (40 °F) velocity distribution

Both velocity distributions show a positive skew, indicating recognized droplets are primarily rising rather than falling. Note that both (c) and (d) have a bin size of 0.1 m/s. Higher counts are seen with the lower saturation temperature than the baseline. The lower saturation temperature results also show velocities to ±2.2 m/s, while the higher saturation temperature results show velocities to ±1.6 m/s. The difference between the two conditions can be explained by the vapor densities at their saturation temperatures. The vapor density of R-123 at the lower saturation temperature is 40% lower than at the higher saturation temperature. This leads to 40% higher vapor velocities in both between the tubes and in the headspace, similar to increasing the mass flux at the higher saturation temperature by 40%.

8.3.4 Heat Flux

In lieu of the baseline case with a higher heat flux, the thermodynamic conditions to match velocities with R-134a were taken instead. As such, the results with a mass flux of 40.7 kg/m^{2}s (30000 lb/hr-ft^2) are used instead to examine the effect of varying heat flux. Figure 8.14 compares thermodynamic conditions 7 and 8 of Table 8.1, with (a) and (c) covering the 15.7 kW/m^2 (5000 Btu/hr-ft^2) condition and (b) and (d) covering the 31.5 kW/m^2 (10000 Btu/hr-ft^2) condition. Higher counts and a different distribution are seen with the lower heat flux results. Whereas the lower heat flux results show a peak of 38 droplets/image at 40 to 45 mm, decreasing to 27 droplets/image at the top of the headspace, the higher heat flux results show a constant droplet count of about 23 droplets/image up to 60 mm, then a rise to 34 droplets/image at the top of the headspace. When the velocity distributions are examined, a stronger positive skew is seen with the lower heat flux results.

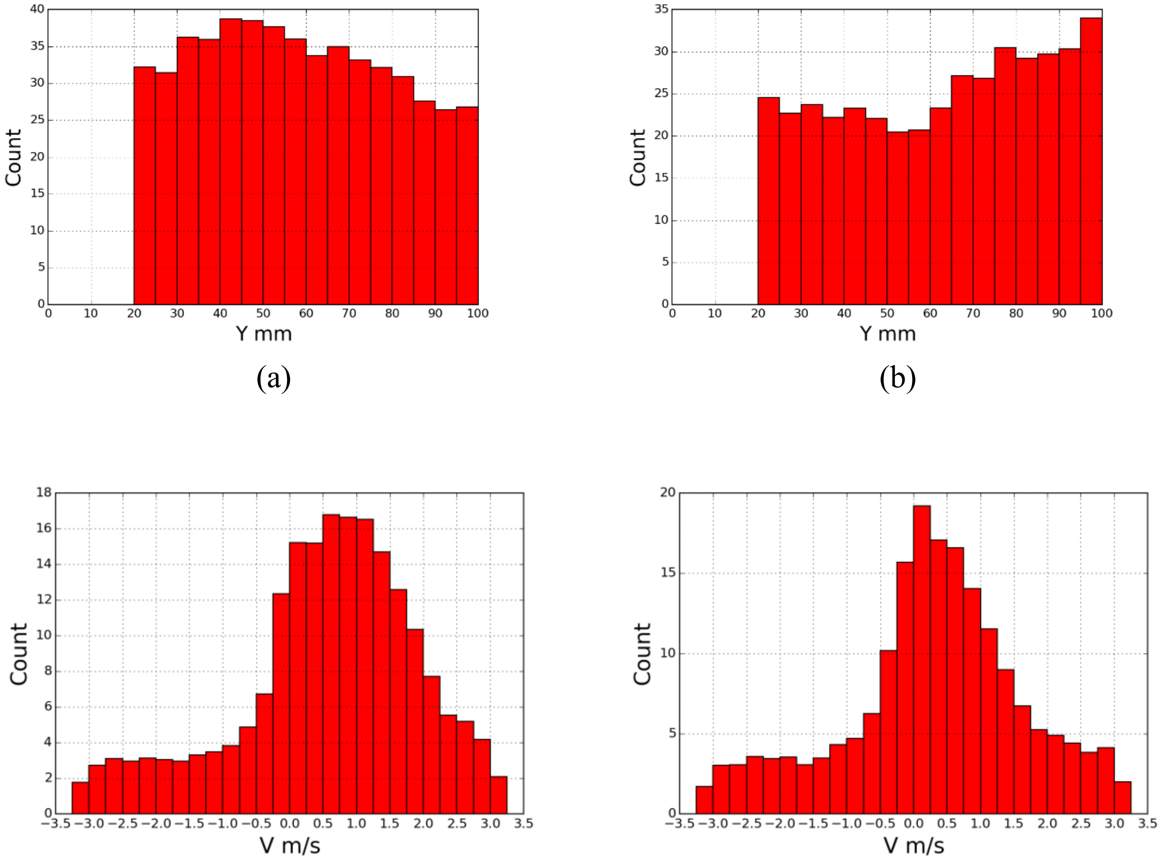

(a) (b)

(c) (d)

Figure 8.14 Heat flux comparison, triangular bundle, R-123, 12.8 °C (55 °F), 40.7 kg/m²s (30000 lb/hr-ft²), 50 mm lens, image location J: (a) 15.7 kW/m² (5000 Btu/hr-ft²) height distribution; (b) 31.5 kW/m² (10000 Btu/hr-ft²) height distribution

8.3.5 Summary

For the triangular bundle with R-123, eight thermodynamic conditions were tested. Overall, higher droplet counts were seen than with R-134a. In addition, all the variables tested (mass flux, saturation temperature, etc.) showed an influence on droplet counts and distribution, including heat flux, which showed little to no effect with R-134a in the triangular bundle.

Chapter 9 - Rotated Triangular Bundle with R-134a

The rotated triangular bundle proved to have its own challenges. Not only did it require a full teardown and replacement of the test section, the geometry of the rotated triangular arrangement, shown in Figure 2.4(b) posed additional challenges in imaging. Chief among these challenges was a fountain effect in the center of the bundle, ejecting liquid onto the sight glass. This was the fourth and final refrigerant and bundle combination tested, occurring after the rotated triangular bundle with R-123. The complete set of data may be found in Appendix C

9.1 Test Matrix

Thermodynamic conditions tested were nominally the same as those with the rotated triangular bundle with R-134a. Table 9.1 lists those eight conditions.

Table 9.1 Test matrix, rotated triangular bundle with R-134a

Thermodynamic Condition	Outlet Saturation Temperature, °C (°F)	Mass Flux, kg/m^2-s (lb/hr-ft^2)	Top Rows Heat Flux, kW/m^2 (Btu/hr-ft^2)
1	4.4 (40)	20.3 (15000)	15.7 (5000)
2	4.4 (40)	20.3 (15000)	21.7 (6900)
3	4.4 (40)	40.7 (30000)	15.7 (5000)
4	4.4 (40)	40.7 (30000)	31.5 (10000)
5	12.8 (55)	20.3 (15000)	15.7 (5000)
6	12.8 (55)	20.3 (15000)	21.4 (6800)
7	12.8 (55)	40.7 (30000)	15.7 (5000)
8	12.8 (55)	40.7 (30000)	31.5 (10000)

Note that the top rows heat flux listed at 21.7 kW/m^2 (6900 Btu/hr-ft^2) and 21.4 kW/m^2 (6800 Btu/hr-ft^2) represent the maximum heat flux possible with the bundle for a refrigerant mass flux of 20.3 kg/m^2-s (15000 lb/hr-ft^2) at their respective outlet saturation temperatures. As with the triangular bundle with R-123, three liquid levels were taken. Those liquid levels are listed in Table 9.2.

Table 9.2 Liquid level descriptions, rotated triangular bundle with R-134a

Liquid Level	Description	Designation
1	19-25 mm (0.75-1.0 inch) liquid above tubes	Flooded
2	Liquid just above tubes	Ideal
3	Liquid below tubes	Dryout

Images were captured in three of the locations shown in Figure 3.2(b), from J to L. Overall, 138 sets of 100 image pairs were captured, meaning a data set of 27600 images for the bundle. After the image analysis described in Chapter 4, the results in the following section were found.

9.2 Baseline data

An example of processed images for the baseline data is shown in Figure 9.1. Droplets are shown in shades of grey and pink, while background and vapor are shown as black. Note the larger structures circled towards the bottom of the right image. This is liquid that has been thrown against the wall. The baseline results for R-134a with the rotated triangular bundle are shown in Figure 9.2 through Figure 9.8 for the 50 mm lens. These figures show thermodynamic condition 5 of Table 9.1, with an outlet saturation temperature of 12.8 °C (55 °F), mass flux of 20.3 kg/m^{2}s (15000 lb/hr-ft^2), and top rows heat flux of 15.7 kW/m^2 (5000 Btu/hr-ft^2) and was taken at the ideal liquid level in the L location of Figure 3.2(b), the center of the bundle. The rotated triangular arrangement produces a fountain effect, with droplets exiting the center of the bundle and falling towards the walls. The data shown in histogram form is the mean of 100 images (first image per image pair of a run). The velocity distribution histogram only shows droplets which were matched between image pairs. Height vs velocity vs diameter and height vs diameter vs velocity plots only include droplets that were matched, but they do include droplets from all 100 images.

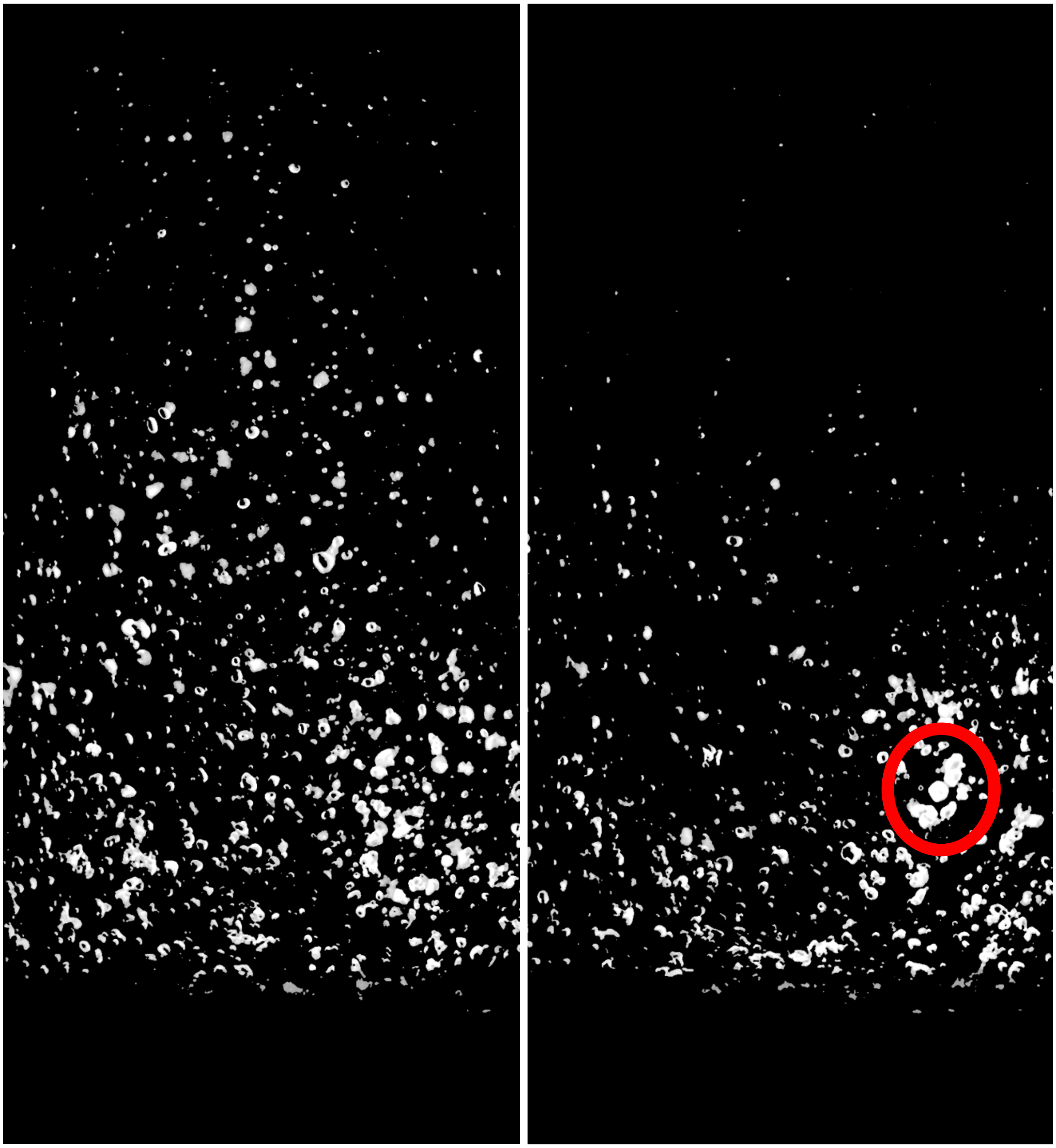

Figure 9.1 Processed images, rotated triangular bundle, R-134a, 12.8 °C (55 °F), 20.3 kg/m^{2}s (15000 lb/hr-ft^2), 15.7 kW/m^2 (5000 Btu/hr-ft^2), ideal liquid level, 50 mm lens, image location L

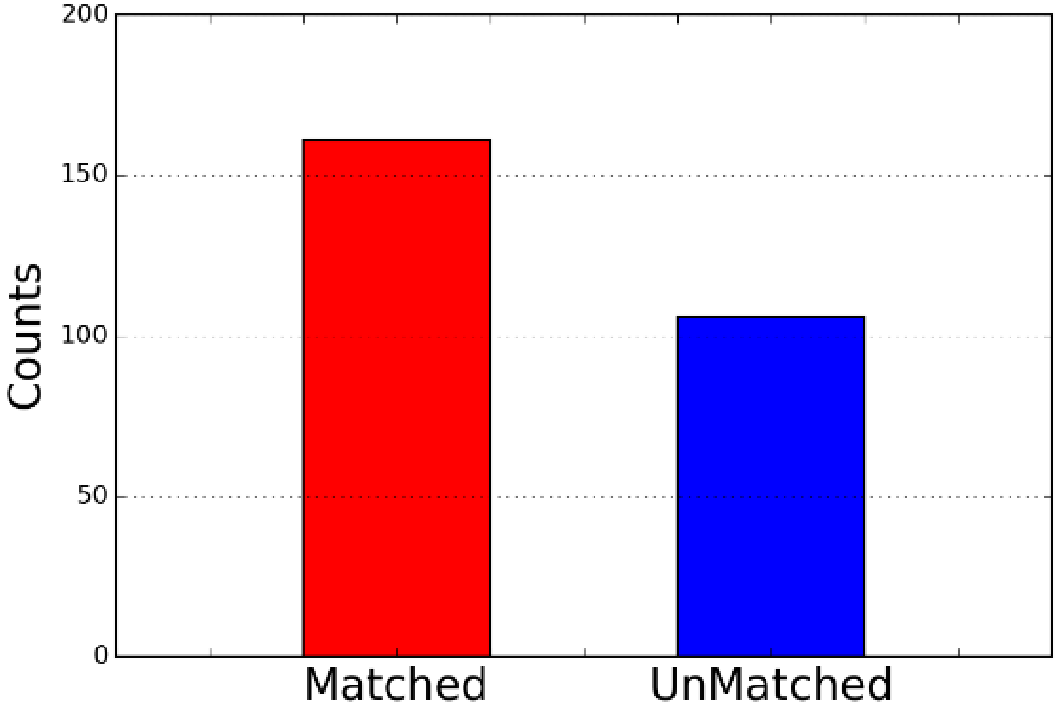

Figure 9.2 Matched counts, rotated triangular bundle, R-134a, 12.8 °C (55 °F), 20.3 kg/m^{2}s (15000 lb/hr-ft^2), 15.7 kW/m^2 (5000 Btu/hr-ft^2), ideal liquid level, 50 mm lens, image location L

Figure 9.2, showing matched vs unmatched counts, gives a representation of how many droplets were matched between images in an image pair. It also provides for a quick count of the average number of droplets per image. Figure 9.2 shows that an average of approximately 270 droplets were counted per image and that 61% of these droplets were deemed a match by the droplet recognition software.

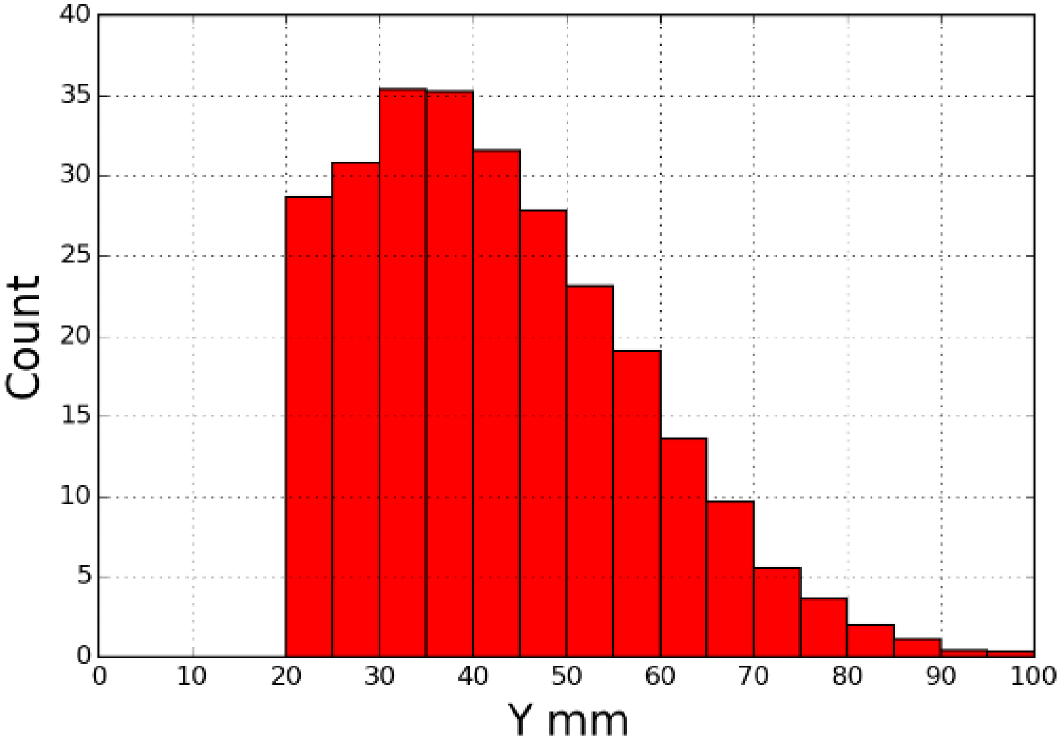

Figure 9.3 Height distribution, rotated triangular bundle, R-134a, 12.8 °C (55 °F), 20.3 kg/m^{2}s (15000 lb/hr-ft^2), 15.7 kW/m^2 (5000 Btu/hr-ft^2), ideal liquid level, 50 mm lens, image location L

Figure 9.3 shows the distribution of droplets vs height. Counts are shown in bins 5 mm high. The peak droplet count of about 35 droplets/image occurs between 30-40 mm above the tubes, with a rapid decrease in counts following. A small number of droplets are seen up to the top of the headspace. This is consistent with the results obtained from the triangular bundle with R-134a.

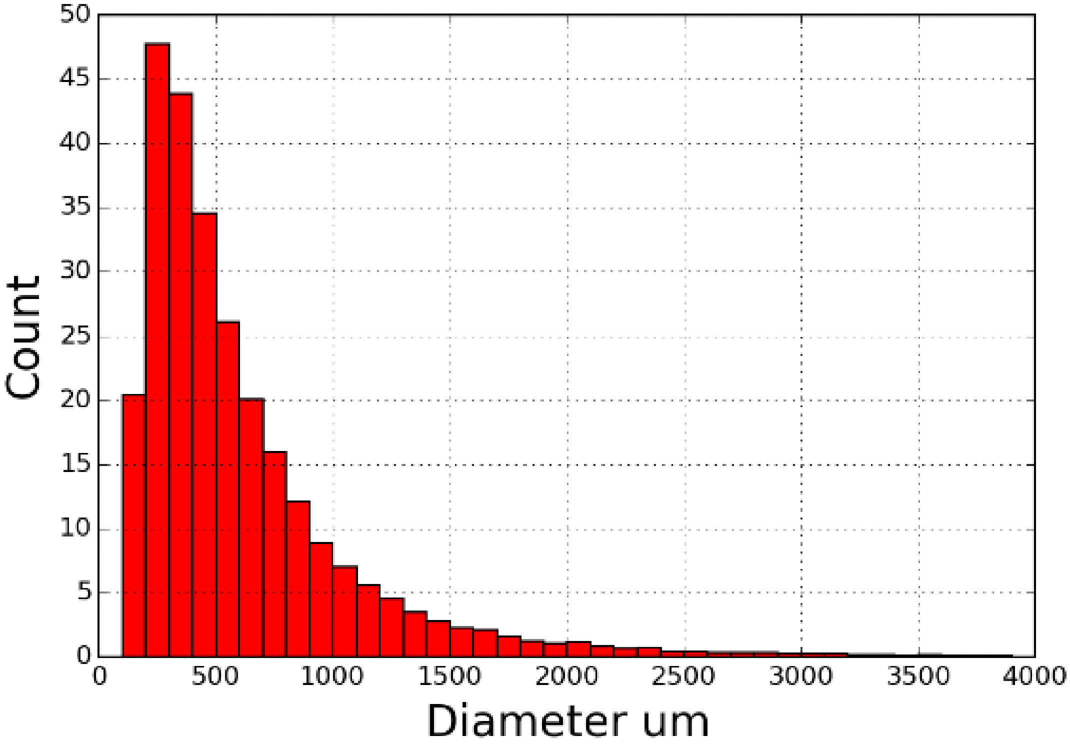

Figure 9.4 Size distribution, rotated triangular bundle, R-134a, 12.8 °C (55 °F), 20.3 kg/m^{2}s (15000 lb/hr-ft^2), 15.7 kW/m^2 (5000 Btu/hr-ft^2), ideal liquid level, 50 mm lens, image location L

Figure 9.4 shows the size distribution of droplets. Droplets are binned for every 100 µm, with most droplets recognized being beneath 600 to 700 µm. The peak droplet count is for droplets with a diameter of 200 to 300 µm. Droplets above 2000 µm have been recognized, but their number are small compared to droplets with smaller diameters. Note that for any figure in this chapter or Appendix C with an axis labelled “Diameter um”, um denotes µm.

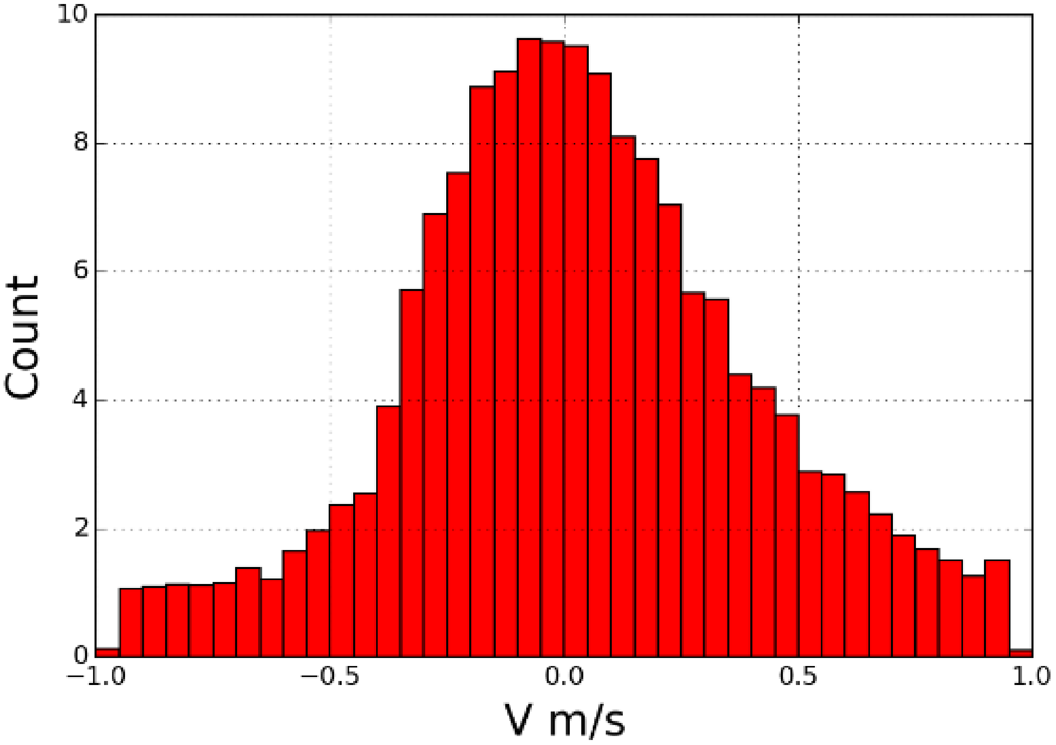

Figure 9.5 Velocity distribution, rotated triangular bundle, R-134a, 12.8 °C (55 °F), 20.3 kg/m^{2}s (15000 lb/hr-ft^2), 15.7 kW/m^2 (5000 Btu/hr-ft^2), ideal liquid level, 50 mm lens, image location L

Figure 9.6 shows the velocity distribution of droplets within the headspace. Droplets are binned for every 0.05 m/s. The velocity distribution has a slight net-positive skew, however, with a negative peak at about -0.05 to -0.1 m/s. Note from Figure 9.3 that droplets have been masked below 20 mm. This was due to droplets impacting the sight glass and distorting the image. The lack of imaging in this area of the image may explain the negative peak to the velocity count.

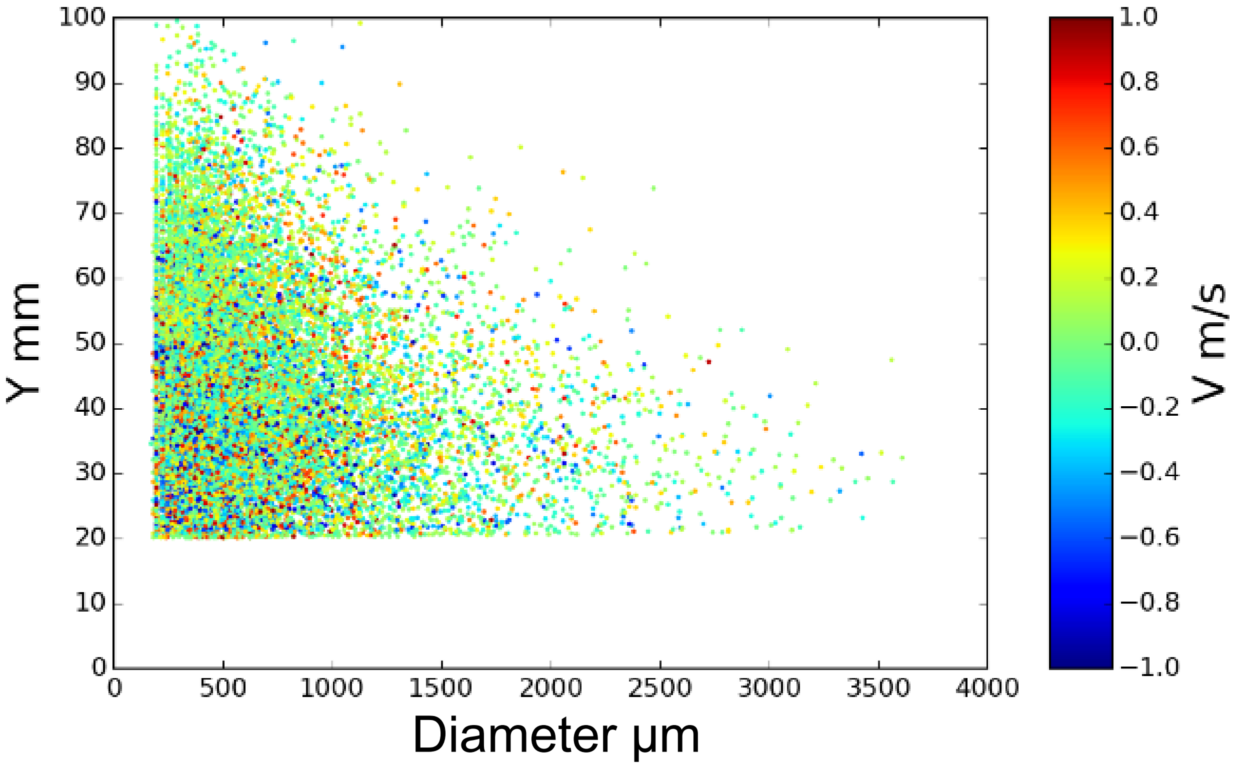

Figure 9.6 Height vs diameter vs velocity, rotated triangular bundle, R-134a, 12.8 °C (55 °F), 20.3 kg/m^{2}s (15000 lb/hr-ft^2), 15.7 kW/m^2 (5000 Btu/hr-ft^2), ideal liquid level, 50 mm lens, image location L

Figure 9.6 shows matched droplets captured over all 100 images, plotting height vs diameter. Color shows velocity, with red colors indicating positive velocities and blue colors indicating negative velocities. Droplets have been recognized throughout the height of the headspace, as well as throughout the range of diameters. The masking mentioned in the previous section is evident.

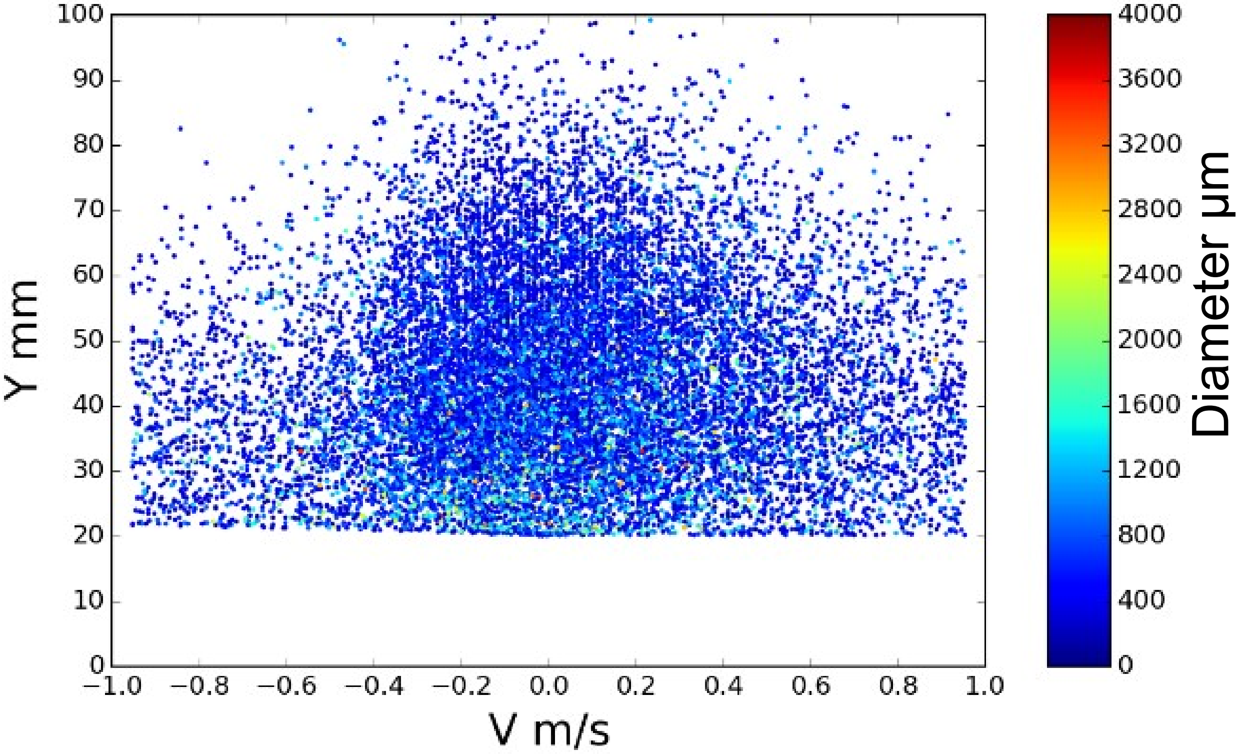

Figure 9.7 Height vs velocity vs diameter, rotated triangular bundle, R-134a, 12.8 °C (55 °F), 20.3 kg/m^{2}s (15000 lb/hr-ft^2), 15.7 kW/m^2 (5000 Btu/hr-ft^2), ideal liquid level, 50 mm lens, image location L

Figure 9.7 shows matched droplets captured over all 100 images, plotting height vs velocity. Color indicates diameter, ranging from a diameter of 0 µm for dark blue to 4000 µm for dark red. Droplet density seems roughly symmetrical about zero-velocity, with the greatest concentration existing beneath 70 mm. Larger droplets are primarily seen below 50 mm above the tubes.

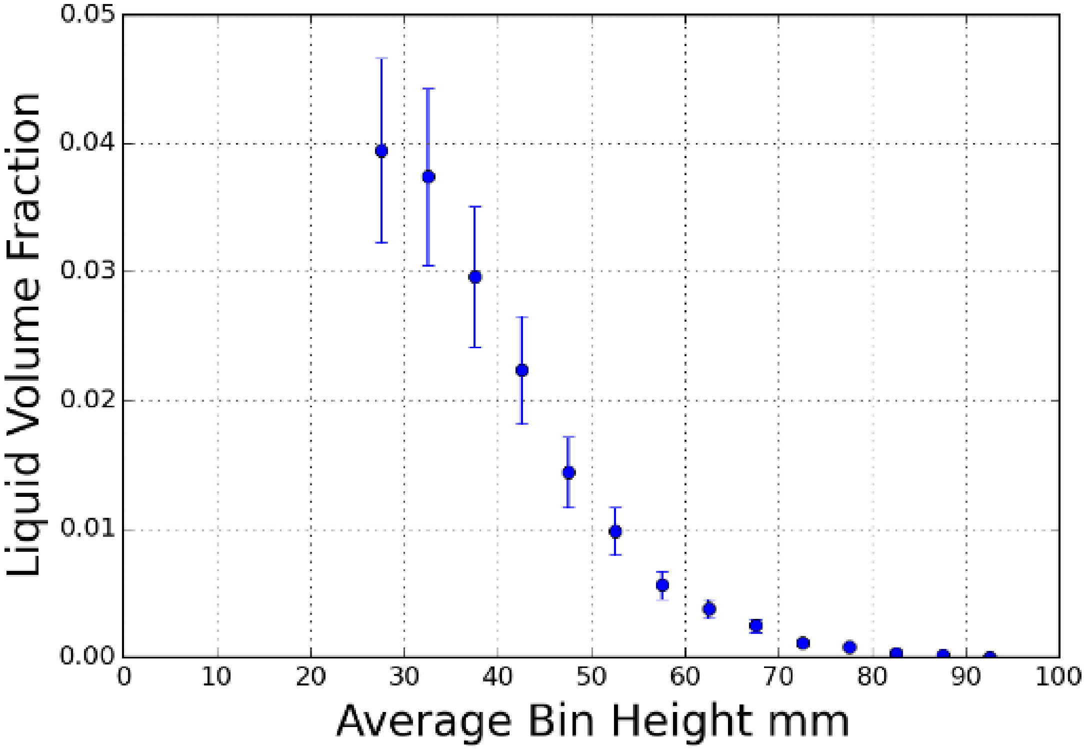

Figure 9.8 Liquid volume fraction, rotated triangular bundle, R-134a, 12.8 °C (55 °F), 20.3 kg/m^{2}s (15000 lb/hr-ft^2), 15.7 kW/m^2 (5000 Btu/hr-ft^2), ideal liquid level, 50 mm lens, image location L

Figure 9.8 shows the liquid volume fraction vs height, with each point located at the center of a 5 mm bin height. These values were calculated in the manner described in Section 5.6 with uncertainties as described in Section 5.7 and are the average of all 100 images. Whereas the height distribution of Figure 9.3 shows a peak in counts at 30-40 mm above the tubes, the liquid volume fraction shows a peak instead between 25-30 mm. This may indicate a transition from predominately large diameter droplets to smaller droplets. Otherwise, results largely follow those of distribution of Figure 9.3, with a decrease from the peak to nearly zero by the top of the headspace.

The results with the 50 mm lens are briefly compared with those taken with the 100 mm lens in Figure 9.9. Several differences are noted. Figure 9.9(a) shows a higher percentage of matched droplets (73% vs 61%) than with the 50 mm lens in Figure 9.2.

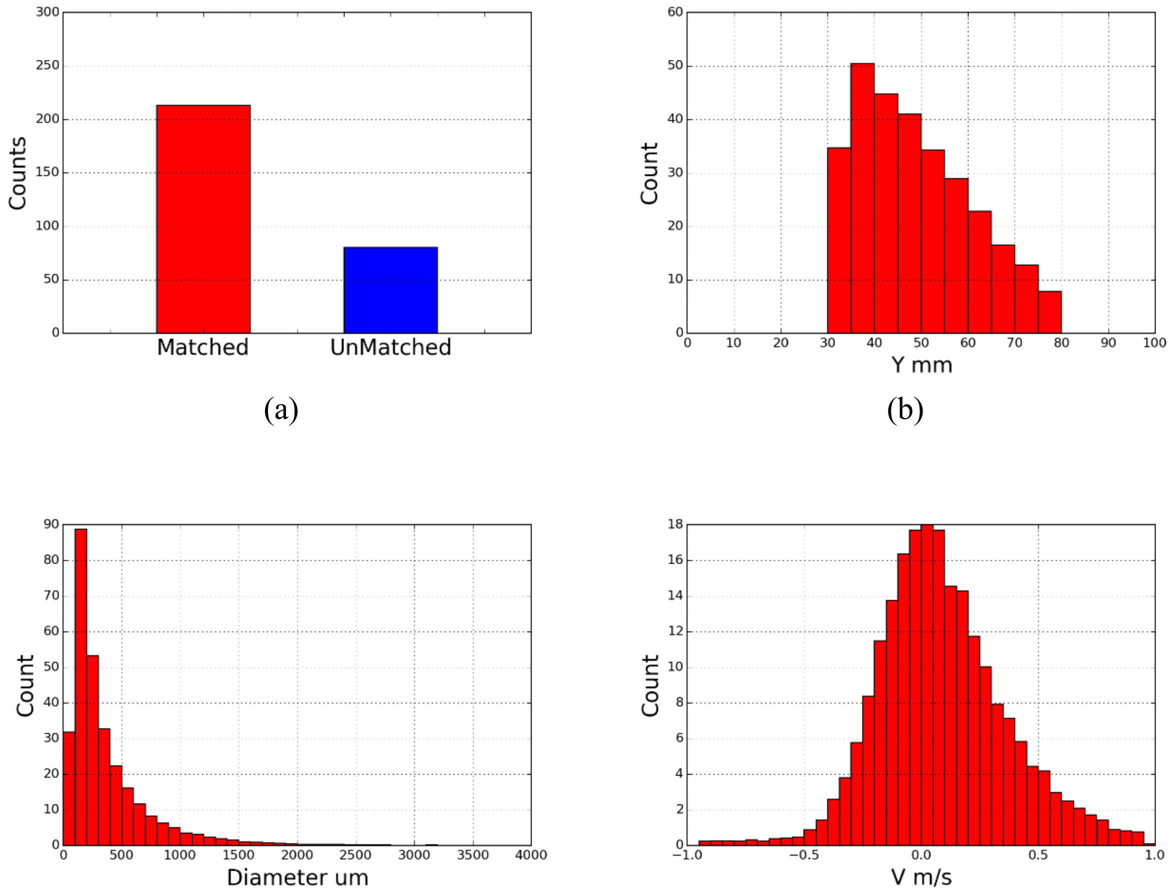

(a) (b)

(c) (d)

Figure 9.9 Data summary, 100 mm lens, rotated triangular bundle, R-134a, 12.8 °C (55 °F), 20.3 kg/m^{2}s (15000 lb/hr-ft^2), 15.7 kW/m^2 (5000 Btu/hr-ft^2), ideal liquid level, image location L: (a) total counts, (b) counts versus height, (c) counts versus size, and (d) velocity distribution

Comparing the 50 mm lens height distribution of Figure 9.3 with the 100 mm lens of Figure 9.9(b), the peak count is shown at nearly the same height. The 100 mm lens is however limited in its field of view, so it is unknown what occurs lower than 30 mm or above 80 mm. In addition, the lowest droplet recognized with the 100 mm lens occurred at 32 mm, indicating that two-fifths of the bin was not visible with the 100 mm lens. The rate at which counts drop off as height increases is similar, however. Examining the size distribution, the 100 mm lens in Figure 9.9(c) shows its highest counts between 100 and 200 μm in diameter and shows small counts up to 3600 μm. Figure 9.3 shows a similar distribution, but is unable to resolve droplets below 200 μm. Comparing the velocity distribution, both the 50 mm lens in Figure 9.5 and 100 mm Figure 9.9(d) show a net positive skew in velocities, indicating more droplets recognized are rising than falling. However, the 100 mm lens has a positive peak as opposed to the negative peak with the 50 mm lens. As the height distributions show few if any droplets are leaving the headspace, a net-zero velocity distribution would be expected, indicating that falling droplets in the first 20-30 mm are likely not being counted.

9.3 Variations

9.3.1 Image Location

Unlike with any other bundle and refrigerant combination, the L image location was chosen to compare among results. This is due to a fountaining effect that occurs in the center of the bundle where two flow paths combine. Examining Figure 9.11, we can see the effects of this fountain. In (a) and (b), we see the height and velocity distributions for the J location, respectively. The peak velocity count appears between -0.05 to -0.1 m/s and a peak count of 29 droplets/image occurs between 30-40 mm above the tubes. Progressing towards the center of the bundle, at location K in Figure 9.10(c) and (d) a peak velocity count is still seen in the -0.05 to -0.1 m/s bin and a peak count of nearly 35 droplets/image occurs between 30-40 mm above the tubes.

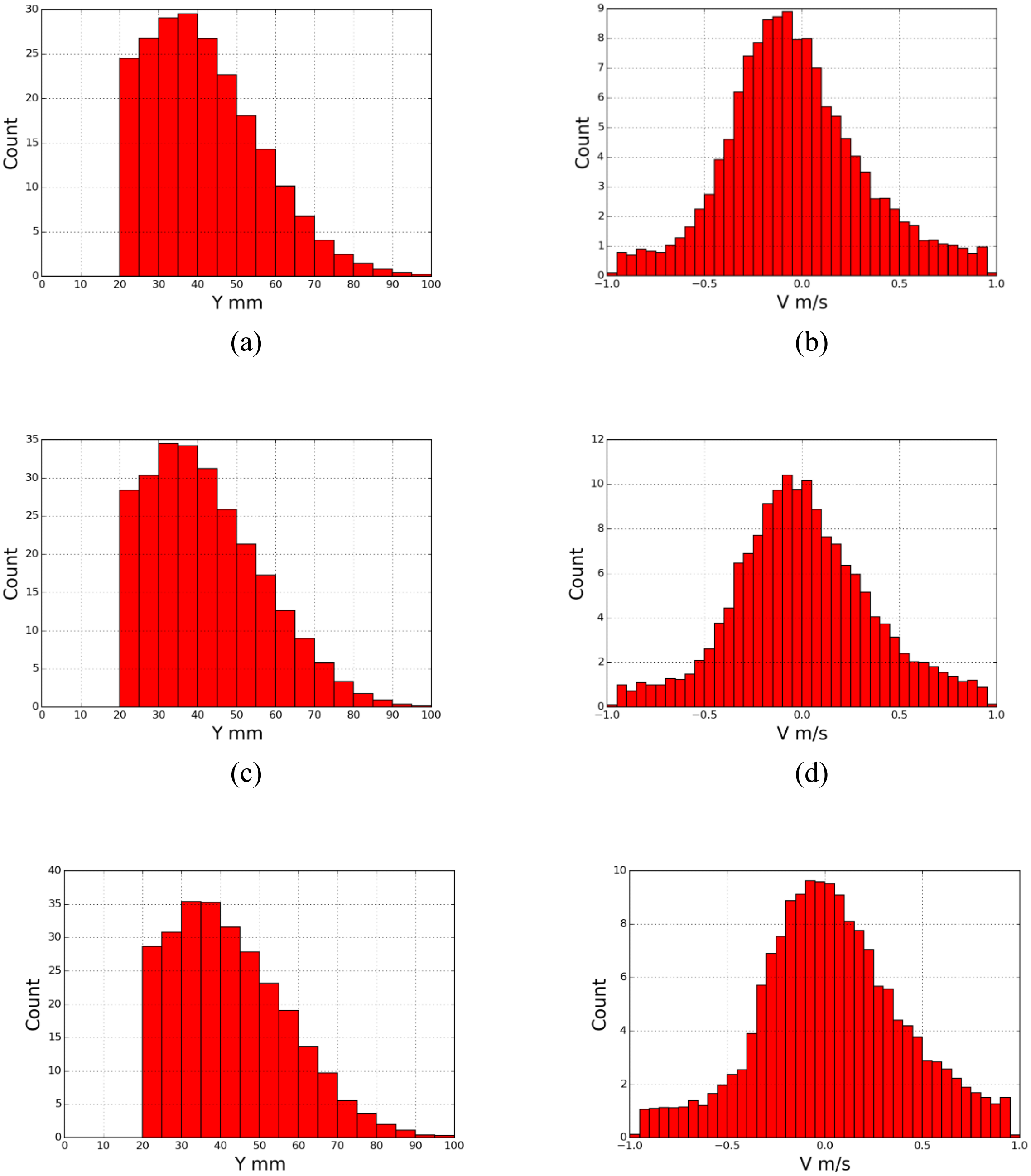

(a) (b)

(c) (d)

(e) (f)

Figure 9.10 Image location comparison, rotated triangular bundle, R-134a, 12.8 °C (55 °F), 20.3 kg/m²s (15000 lb/hr-ft²), 15.7 kW/m² (5,000 Btu/hr-ft²), 50 mm lens, image, ideal liquid level: (a) image location J height distribution; (b) image location J velocity distribution, (c) image location K height distribution, (d) image location K velocity distribution, (e) image location L height distribution, (f) image location L velocity distribution

Finally, at the center of the bundle at image location L in (e) and (d), the peak velocity count is still in the -0.05 to -0.1 m/s bin, but the velocity distribution is skewed slightly positive while the highest peak county on the height distribution of just over 35 droplets/image is seen in the 30-40 mm bins. As droplets in the L location have the greatest likelihood of reaching the top of the headspace, it is the location used for comparisons within the bundle results.

9.3.2 Liquid Level

The effect of liquid level for the rotated triangular bundle with R-134a is shown in Figure 9.11. Figure 9.11(a) and (c) are at liquid level 1, the flooded condition of Table 9.2 while (b) and (d) are at liquid level 3, dryout. Very few droplets are seen with the dryout condition when compared with the baseline case of section 9.2 and the flooded case of (a). Surprisingly, fewer droplets are seen in the flooded case than with the baseline. The peak for the flooded case occurs at 50-55 mm above tubes while for the baseline the peak count occurs between 35 and 40 mm. A possible reason for this may be the pool of liquid in the flooded case dampening droplets ejecting from the tubes. Both the flooded case and baseline show droplets reaching the top of the headspace while the dryout case only recognizes droplets up to 75 mm above the tubes. Trends for the size distributions are similar for all liquid levels.

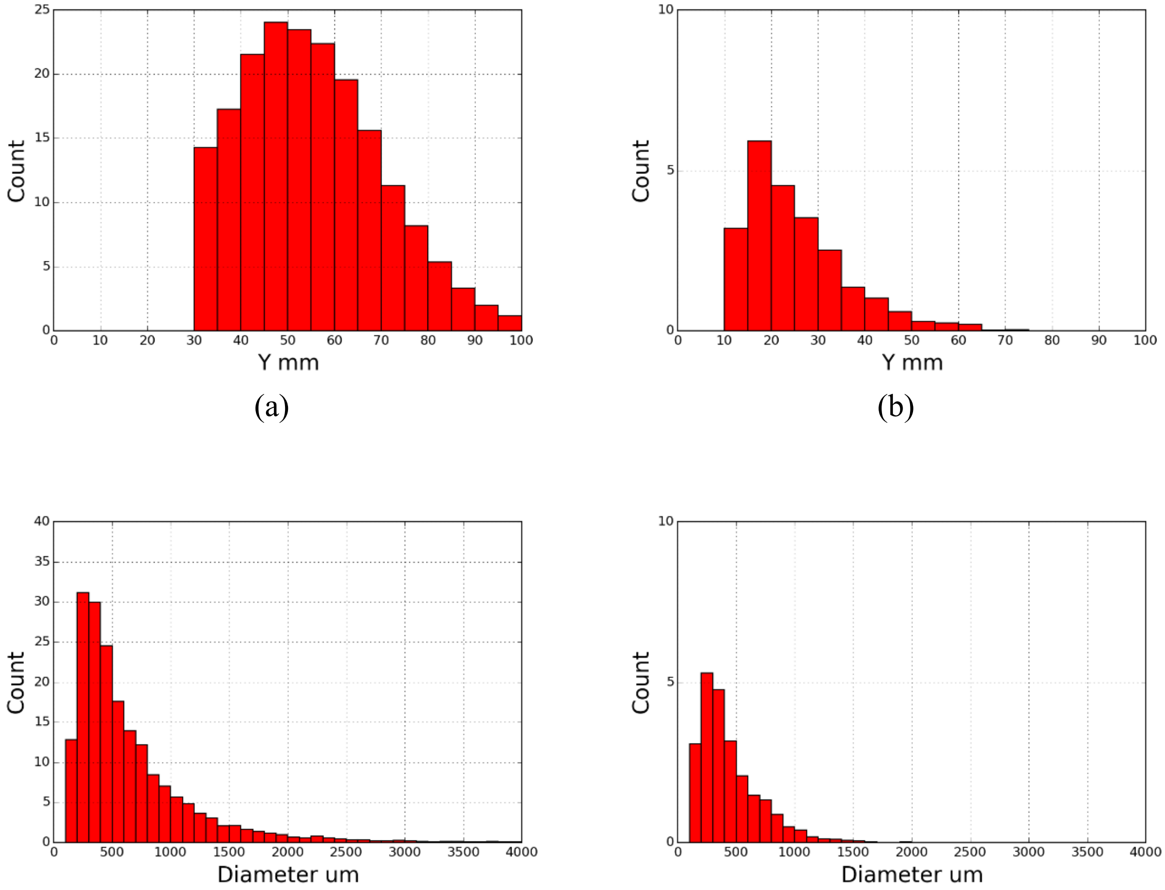

(a) (b)

(c) (d)

Figure 9.11 Liquid level comparison, rotated triangular bundle, R-134a, 12.8 °C (55 °F), 20.3 kg/m^{2}s (15000 lb/hr-ft^2), 15.7 kW/m^2 (5,000 Btu/hr-ft^2), 50 mm lens, image location L: (a) flooded height distribution; (b) dryout height distribution, (c) flooded size distribution, (d) dryout size distribution

9.3.3 Mass Flux

Figure 9.12 shows the effect of varying mass flux, with (a) and (c) displaying the baseline case, and (b) and (d) displaying the higher mass flux of 40.7 kg/m^2-s (30000 lb/hr-ft^2). Examining the height distributions, the higher mass flux of (b) shows much greater counts that extend up to the top of the viewing area. Indeed, the number of droplets per bin is roughly only halved between the peak count and the 95 to 100 mm bin. For the velocity distribution, the higher mass flux in (d) shows a positive peak velocity between 0 to 0.1 m/s and a positive skew.

The baseline in (c) shows a positive skew, but a negative peak from -0.1 to -0.05 m/s. Note that the bin size for (c) is 0.05 m/s with a range of ±1.0 m/s while for (d) the bin size is 0.1 m/s and has a range from ±2.0 m/s.

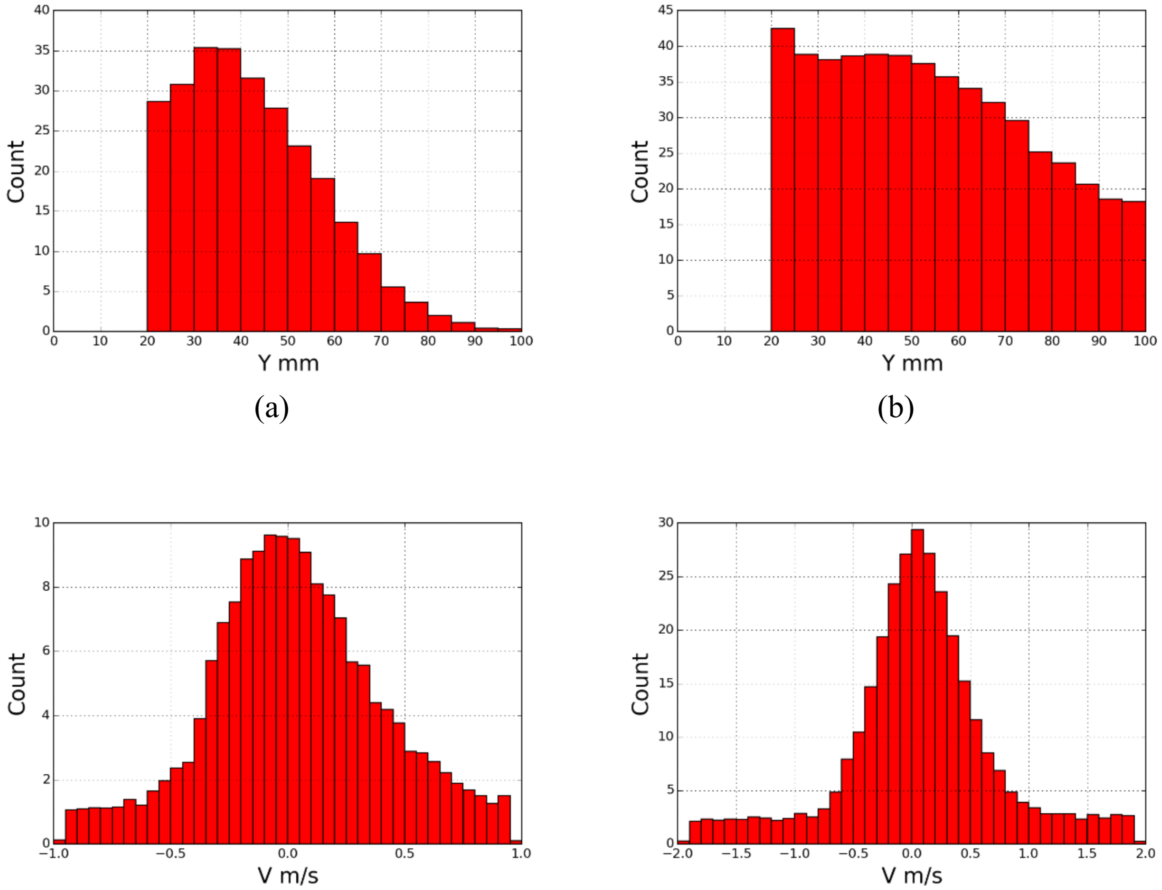

(a) (b)

(c) (d)

Figure 9.12 Mass flux comparison, rotated triangular bundle, R-134a, 12.8 °C (55 °F), 15.7 kW/m^2 (5000 Btu/hr-ft^2), ideal liquid level, 50 mm lens, image location L: (a) 20.3 kg/m^{2}s (15000 lb/hr-ft^2) height distribution; (b) 40.7 kg/m^{2}s (30000 lb/hr-ft^2) height distribution, (c) 20.3 kg/m^{2}s (15000 lb/hr-ft^2) velocity distribution, (d) 40.7 kg/m^{2}s (30000 lb/hr-ft^2) velocity distribution

9.3.4 Saturation Temperature

Figure 9.13 shows the effect of varying outlet saturation temperature, with (a) and (c) displaying the baseline while (b) and (d) show setting the saturation temperature at 4.4 °C (40 °F). Both height and velocity distributions show increased counts with a lower saturation temperature. For the height distributions, the lower saturation temperature data in (b) show a similar curve to the baseline in (a) as height increases, but higher droplet counts overall. Both height distributions show a peak between 30 to 35 mm above the tubes. Velocities likewise show a positive skew for the lower saturation temperature contrasted with the symmetrical distribution for the baseline.

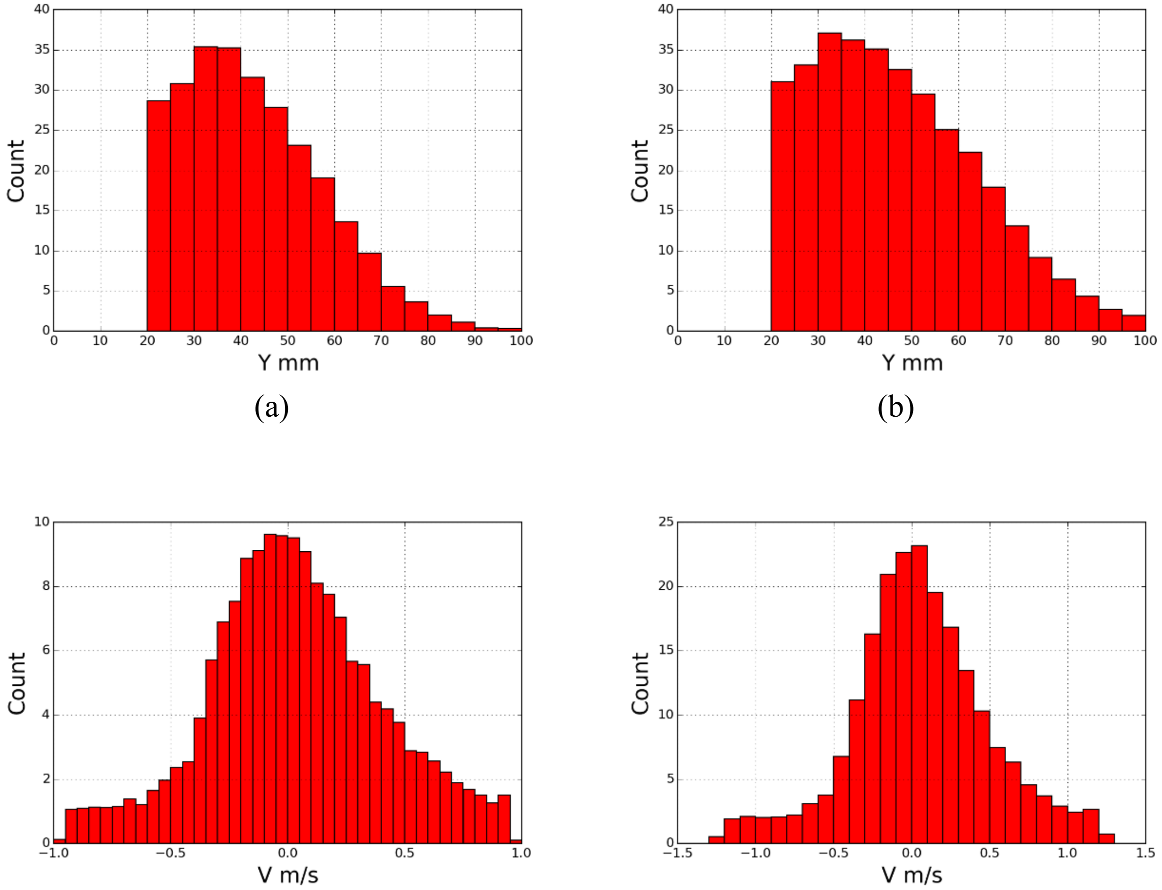

(a) (b)

(c) (d)

Figure 9.13 Saturation temperature comparison, triangular bundle, R-134a, 20.3 kg/m^{2}s (15000 lb/hr-ft^2), 15.7 kW/m^2 (5000 Btu/hr-ft^2), 50 mm lens, image location L: (a) 12.8 °C (55 °F) height distribution; (b) 4.4 °C (40 °F) height distribution, (c) 12.8 °C (55 °F) velocity distribution, (d) 4.4 °C (40 °F) velocity distribution

For the velocity distribution, though both show a positive skew, the lower saturation temperature data in (d) also show a positive peak between 0 to 0.1 m/s whereas the baseline in (c) shows a negative peak. Note that the bin size for (c) is 0.05 m/s with a range of ±1.0 m/s while for (d) the bin size is 0.1 m/s and has a range from ±1.5 m/s.

As with the triangular bundle with R-134a, the variation between counts at different saturation temperatures can be explained by the difference in vapor densities between the two temperatures. The vapor density at the baseline case is approximately 30% higher than for R-134a at 4.4 °C (40 °F). Assuming the same mass flux, this would yield both between-tube and headspace velocities approximately 30% higher for the lower saturation temperature condition. The effect would be similar to increasing the mass flux by 30% while maintaining the baseline saturation temperature.

9.3.5 Heat Flux

As the difference between the baseline heat flux and the variant is only 5.7 kW/m^2 (1800 Btu/hr-ft^2), the higher mass flux condition is used to show the effect of varying heat flux. Figure 9.14(a) and (c) show the higher mass flux condition with an upper rows heat flux of 15.7 kW/m^2 (5000 Btu/hr-ft^2), while (b) and (d) have a heat flux of 31.5 kW/m^2 (10000 Btu/hr-ft^2). Comparing the height distributions, the higher heat flux of (b) shows both higher counts and a flatter profile, only dropping from approximately 45 droplets/image at the peak to 33 droplets/image at the top of the imaging space. The lower heat flux of (a) instead shows a peak of approximately 43 droplets/image that drops at the top of the headspace to 18 droplets/image. Velocity distributions are different as well, with the higher heat flux of (d) having a flatter distribution in velocity counts than the lower heat flux of (c); in other words, a larger standard deviation in velocity counts for the higher heat flux. A higher heat flux would require more liquid contacting tubes to achieve. As such, the fountaining effect previously described may be entraining droplets into the flow greater with a higher heat flux than with a lower heat flux.

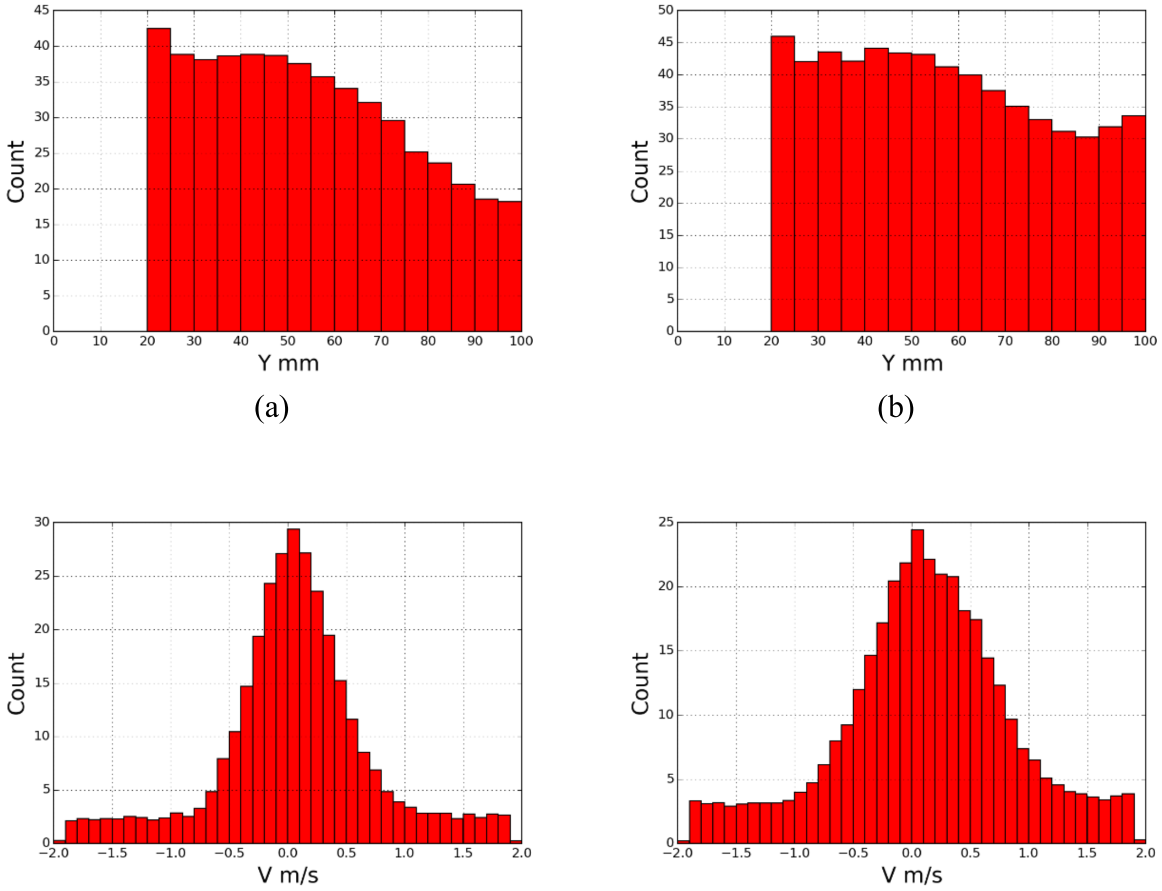

(a) (b)

(c) (d)

Figure 9.14 Heat flux comparison, triangular bundle, R-134a, 12.8 °C (55 °F), 40.7 kg/m^{2}s (30000 lb/hr-ft^2), 50 mm lens, image location L: (a) 15.7 kW/m^2 (5000 Btu/hr-ft^2) height distribution; (b) 31.5 kW/m^2 (10000 Btu/hr-ft^2) height distribution; (c) 15.7 kW/m^2 (5000 Btu/hr-ft^2) velocity distribution; (d) 31.5 kW/m^2 (10000 Btu/hr-ft^2) velocity distribution

9.3.6 Summary

For the rotated triangular bundle with R-134a, eight thermodynamic conditions were tested. All the variables tested (mass flux, saturation temperature, etc.) showed an influence on droplet counts and distribution. Unlike the triangular bundle with the same refrigerant, this bundle did show varying behavior with varying heat flux.

Chapter 10 - Rotated Triangular Bundle with R-123

The rotated triangular bundle arrangement with R-123 was the third bundle and refrigerant combination to be tested. This testing directly followed the triangular bundle with R-123 to avoid the need to change out both refrigerant and instrumentation. As with the triangular bundle with R-123, it also posed difficulties by generating more droplets, making imaging difficult due to liquid on the glass walls. This was compounded by the fountain effect of the rotated triangular arrangement discussed in Chapter 9. The complete set of data may be found in Appendix D.

10.1 Test Matrix

Again, eight thermodynamic conditions were tested. As with the triangular bundle with R-123, variations were made to allow matching velocities with R-134a data as well as the standard conditions identified in the work statement. As such, there are differences from the testing conditions with R-134a, shown in Table 10.1 below.

Table 10.1 Test matrix, rotated triangular bundle with R-123

Thermodynamic Condition	Outlet Saturation Temperature, °C (°F)	Mass Flux, kg/m^2-s (lb/hr-ft^2)	Top Rows Heat Flux, kW/m^2 (Btu/hr-ft^2)
1	4.4 (40)	20.3 (15000)	15.7 (5000)
2	4.4 (40)	40.7 (30000)	15.7 (5000)
3	4.4 (40)	40.7 (30000)	31.5 (10000)
4	12.8 (55)	3.46 (2550)	3.47 (1100)
5	12.8 (55)	7.05 (5200)	6.0 (1900)
6	12.8 (55)	20.3 (15000)	15.7 (5000)
7	12.8 (55)	40.7 (30000)	15.7 (5000)
8	12.8 (55)	40.7 (30000)	31.5 (10000)

Conditions 4 and 5 are variations in which an attempt was made to match the interstitial velocities of the low and high mass fluxes with R-134a at otherwise identical conditions. The mass flux of 3.06 kg/m^2-s (2250 lb/hr-ft^2) matches the interstitial and headspace velocities found with R-134a for a mass flux of 20.3 kg/m^2-s (15000 lb/hr-ft^2). The top rows heat flux of 3.47 kW/m^2 (1100 Btu/hr-ft^2) was the maximum possible for R-123 with the rotated triangular configuration. Unlike the test matrix of the triangular bundle with R-123, test condition 5 at 7.05 kg/m^2-s (5200 lb/hr-ft^2) does match the headspace and interstitial velocities of the higher mass flux condition with R-134a at 40.7 kg/m^2-s (30000 lb/hr-ft^2). Again, the heat flux of 6.0 kW/m^2 (1900 Btu/hr-ft^2) was the maximum obtainable at the given mass flux.

For this set of data, the number of liquid levels was set to two. These levels are described in Table 10.2. Due to the fountain effect of the rotated triangular bundle and compounded by the use of R-123, the flooded liquid level was discontinued. However, the ideal liquid level was maintained as liquid level 2. For the ideal liquid level, the point at which the htc ratio began to rapidly decrease was chosen again. The dryout liquid level was chosen to be ½ of the ideal liquid level htc ratio. Essentially, this was the point at which the top three tubes were in dryout out while the next three rows were still wetted.

Table 10.2 Liquid level descriptions, rotated triangular bundle with R-123

Liquid Level	Description	Designation
2	Liquid just above tubes	Ideal
3	Liquid below tubes	Dryout

As with the triangular bundle with R-123, three image locations were taken, largely due to the impossibility of gleaning information past the center of the bundle.

10.2 Baseline data

An example of processed images for the baseline data is shown in Figure 10.1. Droplets are shown in shades of grey and pink, while background and vapor are shown as black. Circled towards the edge of the images are visible wave shaped structures. These structures are from liquid on the wall, but in processing are largely masked. The baseline results for R-123 with the rotated triangular bundle are shown in Figure 10.2 through Figure 10.8 for the 50 mm lens. These figures show thermodynamic condition 6 of Table 8.1, with an outlet saturation temperature of 12.8 °C (55 °F), mass flux of 20.3 kg/m^2-s (15000 lb/hr-ft^2), and top rows heat flux of 15.7 kW/m^2 (5000 Btu/hr-ft^2) and was taken at the ideal liquid level in the J location of Figure 3.2(a). Data from the K and L locations was taken, but for comparison the J location is used due to the difficulty in resolving droplets due to the high density typically seen. The data shown in histogram form is the mean of 100 images (first image per image pair of a run). The velocity distribution histogram only show droplets which were matched between image pairs. Height vs velocity vs diameter and height vs diameter vs velocity plots only include droplets that were matched over all 100 images.

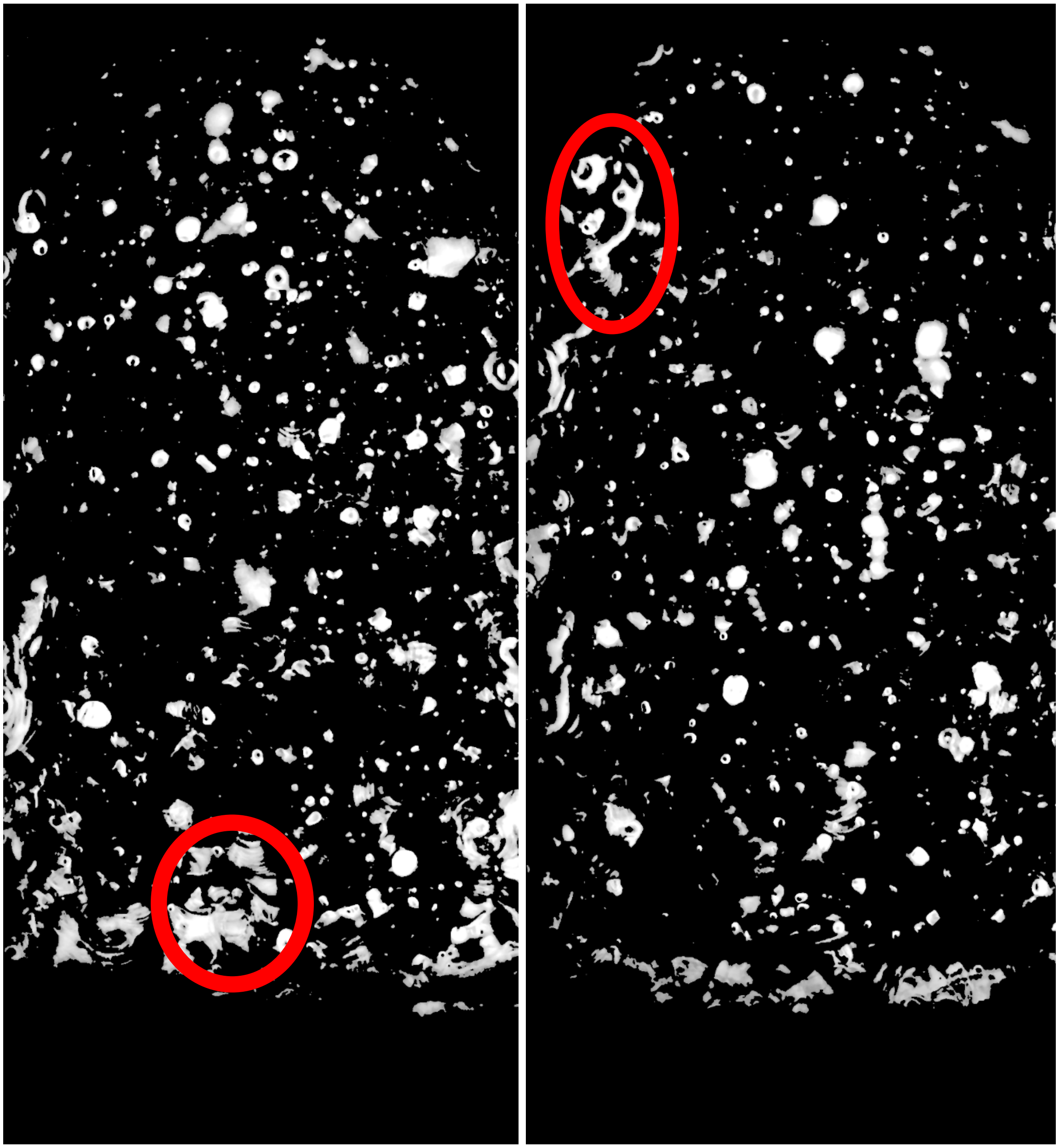

Figure 10.1 Processed images, rotated triangular bundle, R-123, 12.8 °C (55 °F), 20.3 kg/m²s (15000 lb/hr-ft²), 15.7 kW/m² (5000 Btu/hr-ft²), ideal liquid level, 50 mm lens, image location J

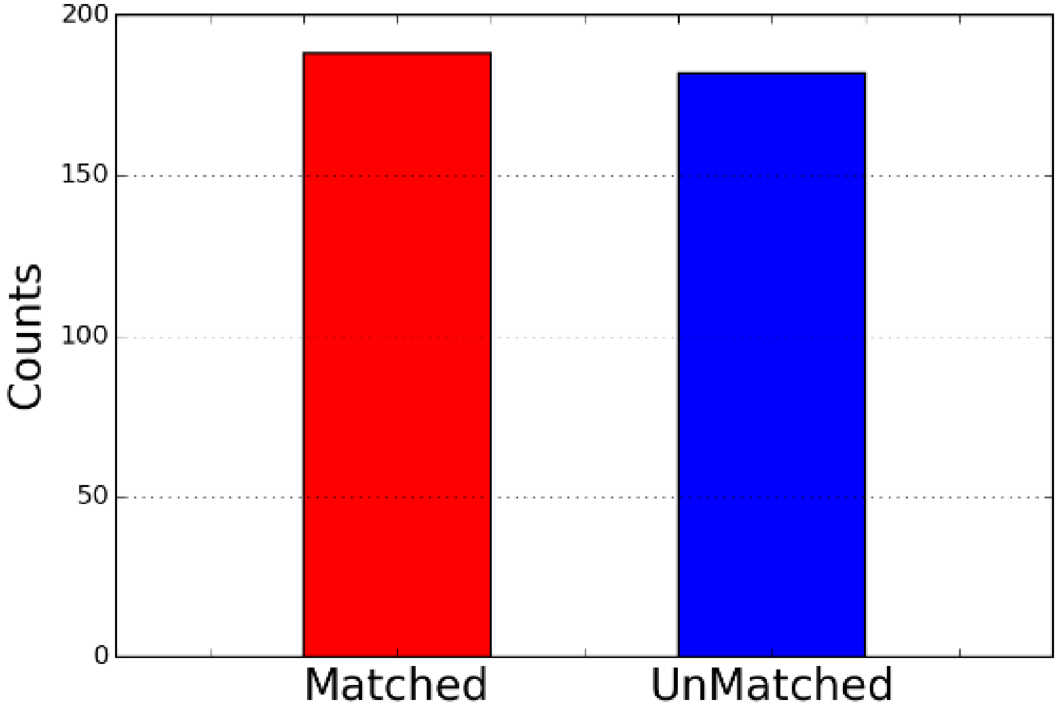

Figure 10.2 Matched counts, rotated triangular bundle, R-123, 12.8 °C (55 °F), 20.3 kg/m^{2}s (15000 lb/hr-ft^2), 15.7 kW/m^2 (5000 Btu/hr-ft^2), ideal liquid level, 50 mm lens, image location J

Figure 10.2, showing matched and unmatched counts, gives a representation of how many droplets were matched between images in an image pair. An average of 370 droplets were counted per image and 51% of these droplets were deemed a match by the droplet recognition software. This low match rate is not unusual for this and the higher mass flux conditions. The large number of droplets with R-123 makes both recognition and matching difficult.

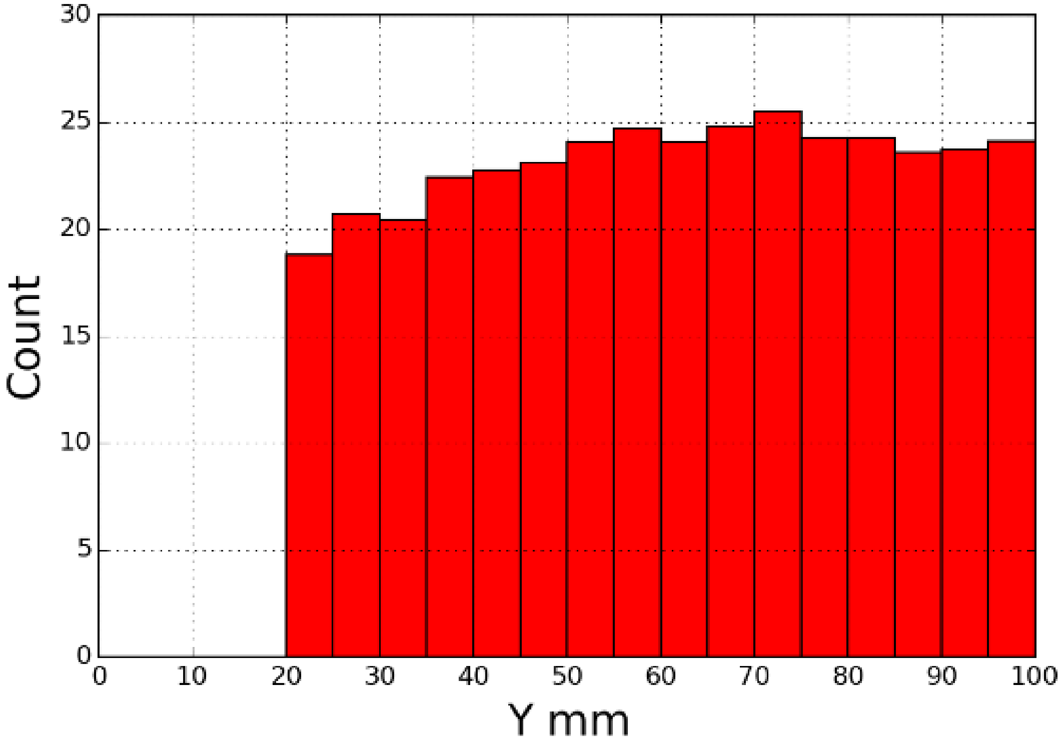

Figure 10.3 Height distribution, rotated triangular bundle, R-123, 12.8 °C (55 °F), 20.3 kg/m^{2}s (15000 lb/hr-ft^2), 15.7 kW/m^2 (5000 Btu/hr-ft^2), ideal liquid level, 50 mm lens, image location J

Figure 8.3 shows the distribution of droplets vs height above the tubes. Droplets are binned every 5 mm of height. Droplet counts are near constant about 24 droplets/image from 50 mm through the top of the image. The slow rise in droplet counts from 20 to 50 mm may be due to larger droplets obscuring smaller droplets lower in the headspace. The existence of a large number of droplets in the highest bin indicates that droplets are leaving the test section or impacting the distribution plate at the top of the bundle.

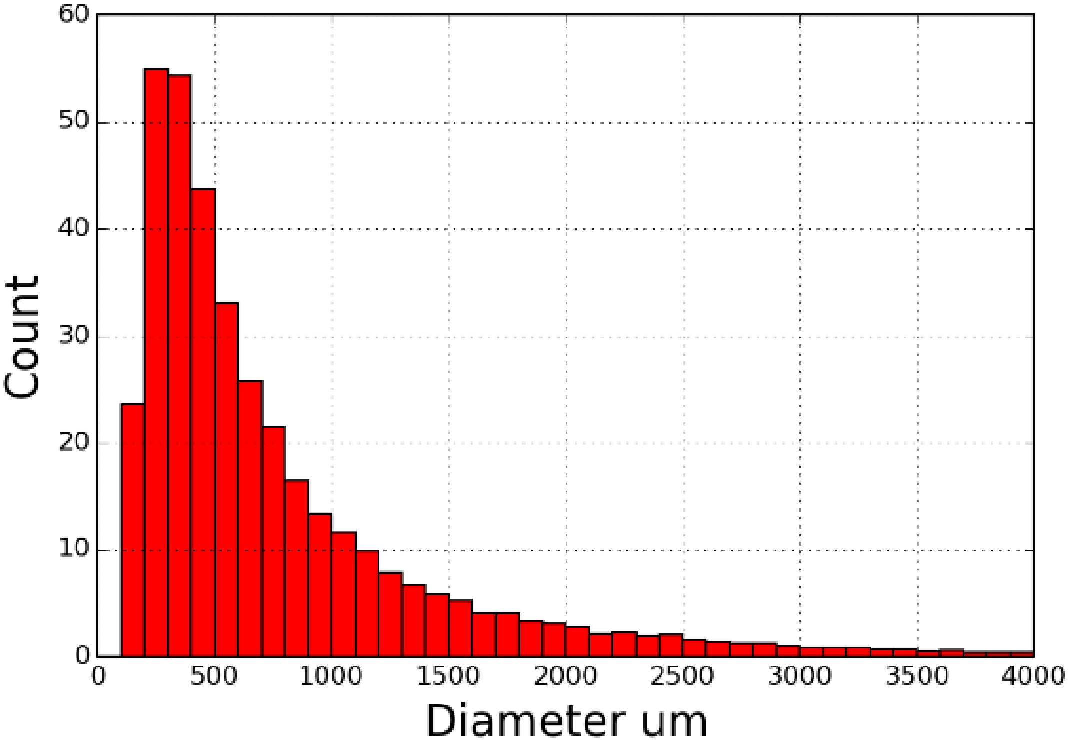

Figure 10.4 Size distribution, rotated triangular bundle, R-123, 12.8 °C (55 °F), 20.3 kg/m^{2}s (15000 lb/hr-ft^2), 15.7 kW/m^2 (5000 Btu/hr-ft^2), ideal liquid level, 50 mm lens, image location J

Figure 8.4 shows the size distribution of droplets. Droplets are binned for every 100 µm of diameter, with the majority of droplets recognized sized beneath 600 µm and a peak of 55 droplets/image for droplets of 200 to 400 µm. Droplets throughout the range of sizes allowed have been recognized, up to 4000 µm, though droplets are generally much smaller. Note that for any figure in this chapter or Appendix D with an axis labelled “Diameter um”, um denotes µm.

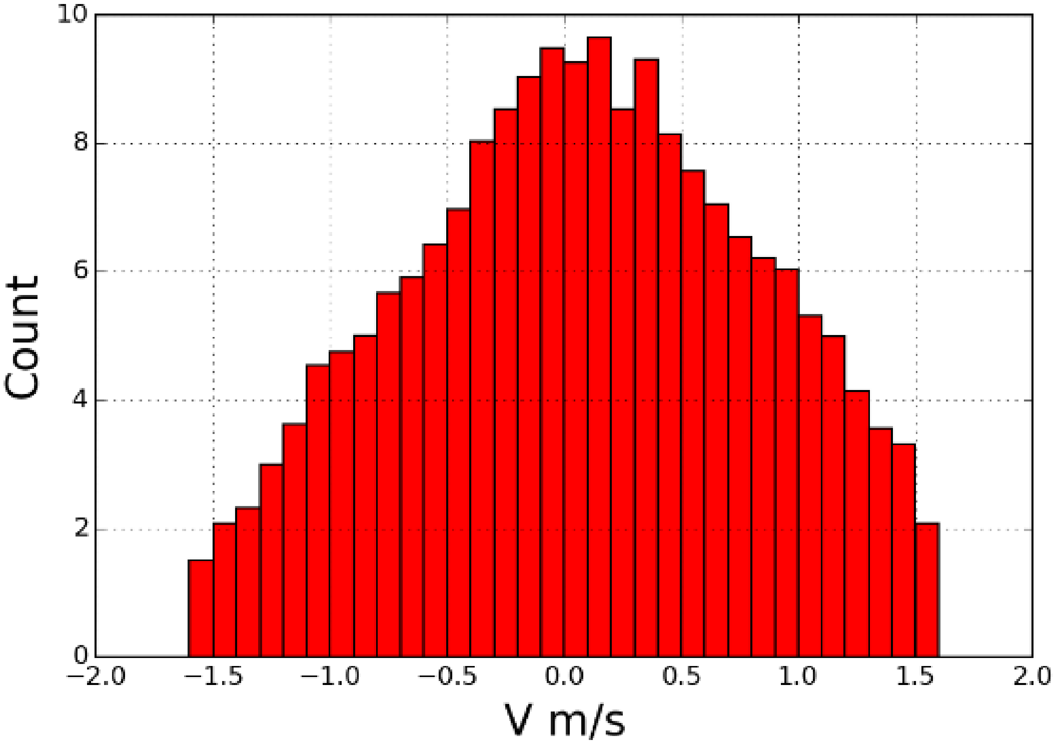

Figure 10.5 Velocity distribution, rotated triangular bundle, R-123, 12.8 °C (55 °F), 20.3 kg/m^{2}s (15000 lb/hr-ft^2), 15.7 kW/m^2 (5000 Btu/hr-ft^2), ideal liquid level, 50 mm lens, image location J

Figure 10.5 shows the velocity distribution of droplets within the headspace. Droplets are binned for every 0.1 m/s. Droplet velocities of ±1.6 m/s have been recognized. Droplet counts are not symmetrical about zero, reaching a peak count between 0.1 and 0.2 m/s. Not only is the peak positive and standard deviation larger than previously seen, but the distribution strongly skews positive as well. This positive skew indicates a net outflow of droplets out of the test section, or at least out of the field of view of the camera. This positive skew indicates that more droplets are rising than falling and that refrigerant is leaving with a quality less than 1. Indeed, a thermodynamic balance of the test section shows an exit quality of 0.95. That number is high enough, though, to indicate that smaller droplets are primarily what is leaving.

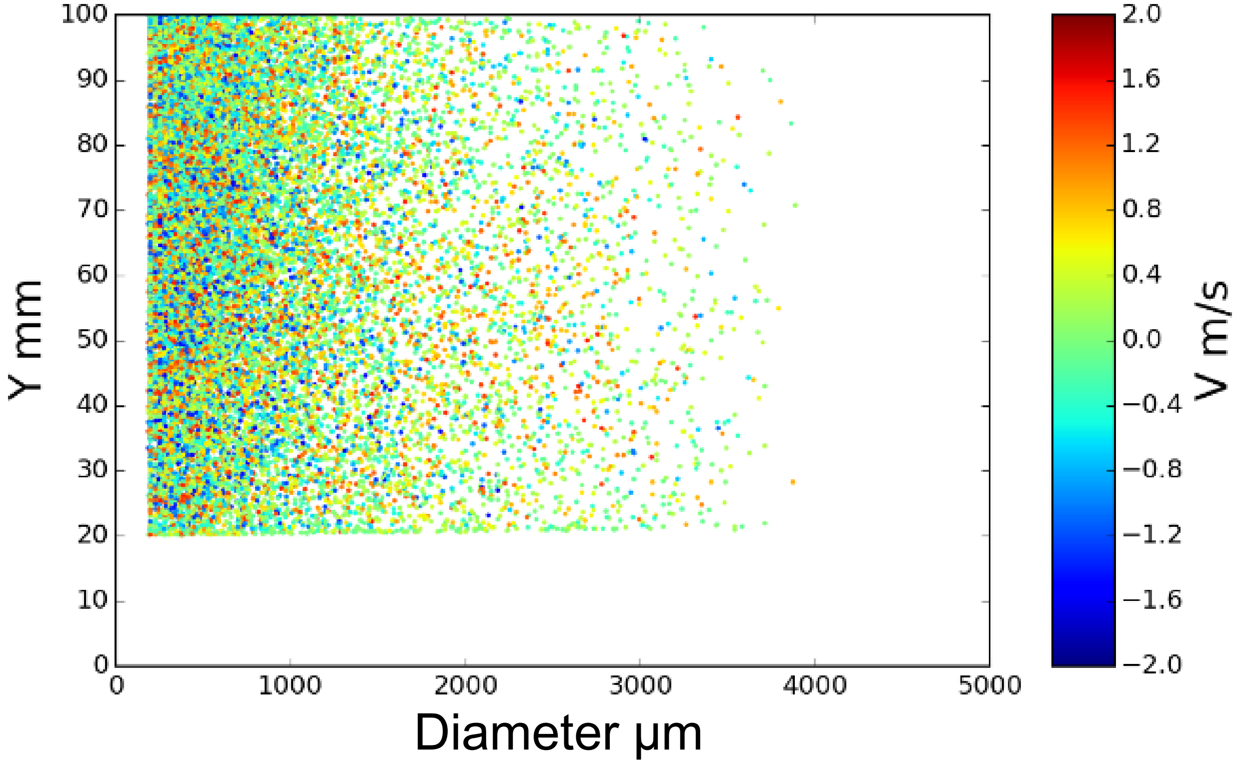

Figure 10.6 Height vs diameter vs velocity, rotated triangular bundle, R-123, 12.8 °C (55 °F), 20.3 kg/m^{2}s (15000 lb/hr-ft^2), 15.7 kW/m^2 (5000 Btu/hr-ft^2), ideal liquid level, 50 mm lens, image location J

Figure 10.6 shows all matched droplets captured over all 100 images, plotting height vs diameter. Color represents velocity, with red colors indicating positive velocities and blue colors indicating negative velocities. Droplets extend between 20 to 100 mm above the tube bundle, with diameters nearly up to 4000 µm. Large diameter droplets are recognized up to the top of the headspace.

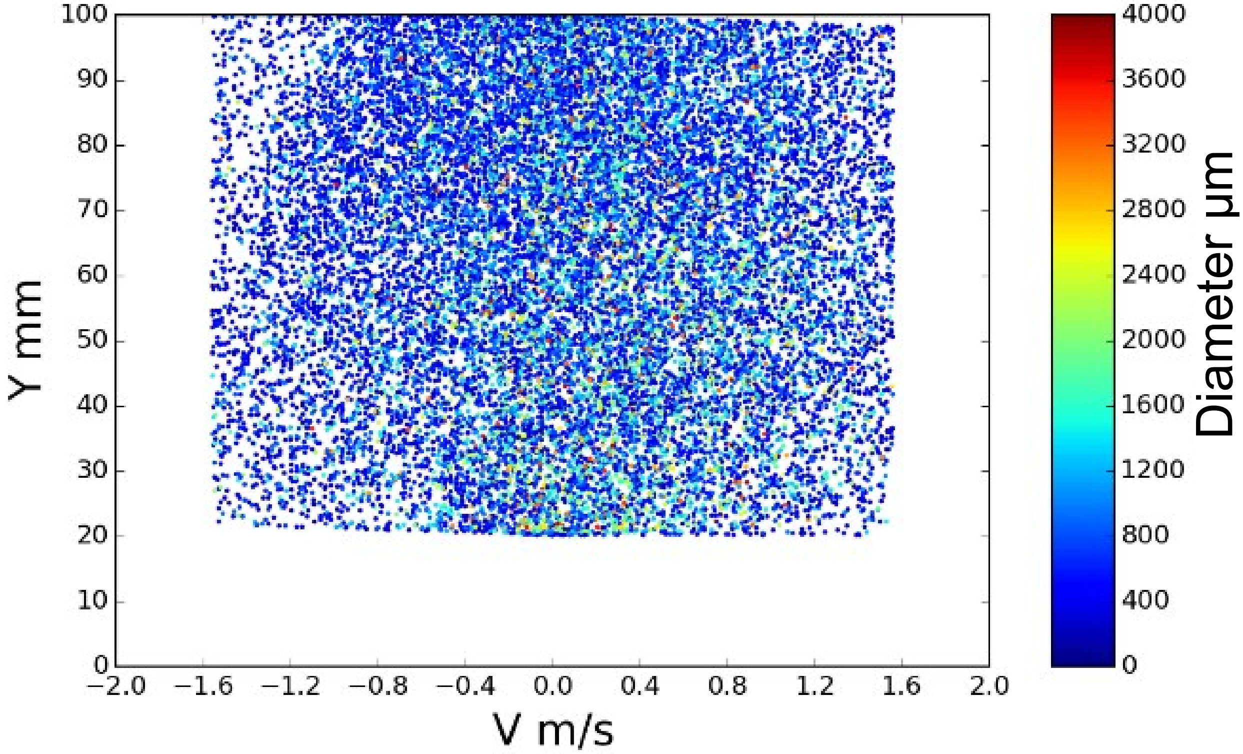

Figure 10.7 Height vs velocity vs diameter, rotated triangular bundle, R-123, 12.8 °C (55 °F), 20.3 kg/m^{2}s (15000 lb/hr-ft^2), 15.7 kW/m^2 (5000 Btu/hr-ft^2), ideal liquid level, 50 mm lens, image location J

Figure 10.7 shows all matched droplets captured over all 100 images, plotting height vs velocity. Color indicates diameter, ranging from a diameter of 0 µm for dark blue to 4000 µm for dark red. Droplets of all sizes are seen throughout the headspace, though smaller droplets dominate the chart.

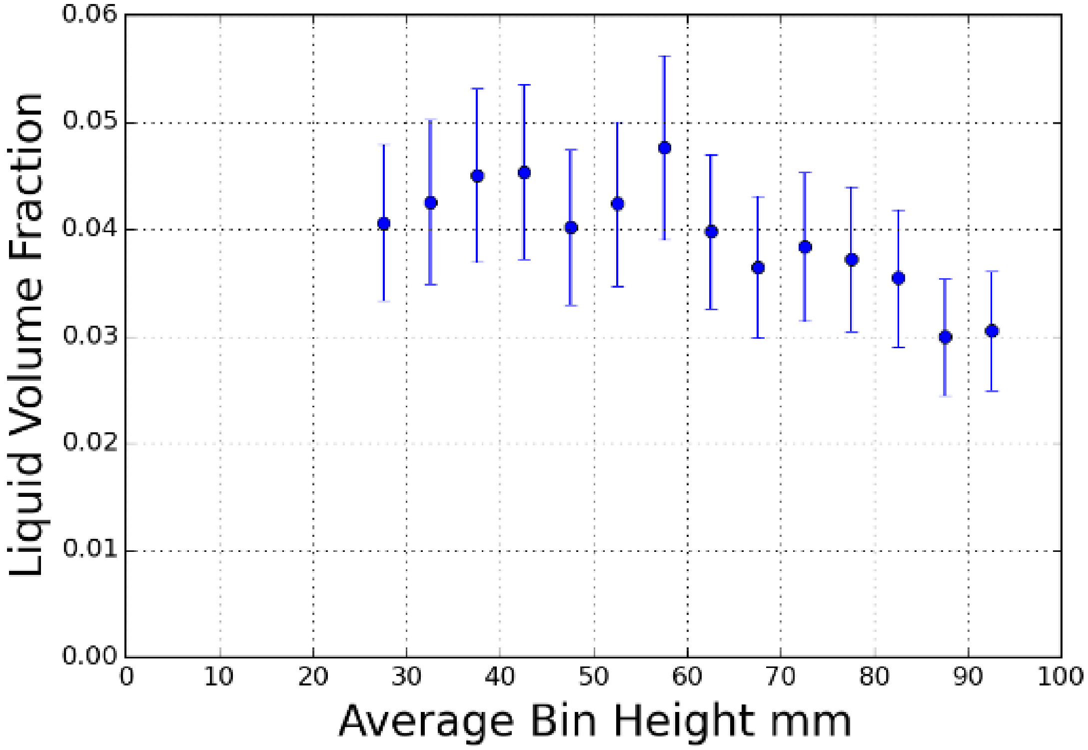

Figure 10.8 Liquid volume fraction, rotated triangular bundle, R-123, 12.8 °C (55 °F), 20.3 kg/m^{2}s (15000 lb/hr-ft^2), 15.7 kW/m^2 (5000 Btu/hr-ft^2), ideal liquid level, 50 mm lens, image location J

Figure 10.8 shows the liquid volume fraction vs height, with each point located at the center of a 5 mm bin height. These values were calculated in the manner described in section 0 with uncertainties as described in section 5.7 and are a representation of all 100 images. A peak is seen between 55 and 60 mm, with a slight decrease as height increases. As with the height distribution of Figure 10.3, a significant liquid fraction at the top of the headspace indicates that droplets are leaving the viewing area of the camera and exiting the test section or impacting the distribution plate at the top of the bundle. Combined with both the height distribution and the size distribution of Figure 10.4, we see a transition from larger droplets being recognized to smaller droplets at about 60 mm.

The results with the 50 mm lens are compared with those taken with the 100 mm lens in Figure 10.9. Several differences are noted. Figure 10.9(a) shows a lower percentage of matched droplets (47% vs 51%) than with the 50 mm lens in Figure 10.2. While the velocity distribution of (c) has a positive skew, the peak is negative or nearly zero. The peak droplet count of (b) occurs between 75 and 80 mm, as opposed to near constant distribution of Figure 10.3 for the 50 mm lens. This indicates further the dominance of smaller droplets higher in the headspace.

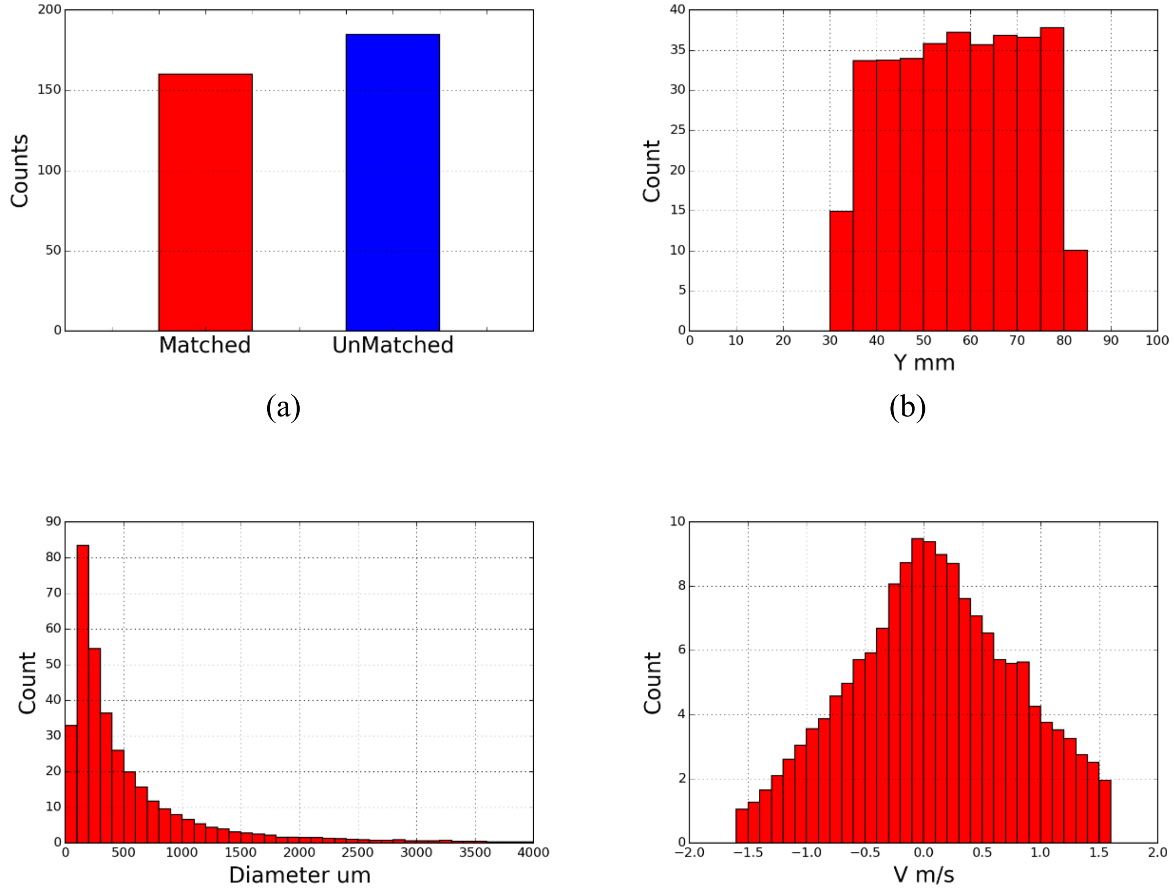

(a) (b)

(c) (d)

Figure 10.9 Data summary, 100 mm lens, rotated triangular bundle, R-123, 12.8 °C (55 °F), 20.3 kg/m^{2}s (15000 lb/hr-ft^2), 15.7 kW/m^2 (5000 Btu/hr-ft^2), ideal liquid level, image location J: (a) total counts, (b) counts versus height, (c) counts versus size, and (d) velocity distribution.

10.3 Variations

10.3.1 Liquid Level

The effect of liquid level for the rotated triangular bundle with R-123 is shown Figure 10.10. Figure 10.10(a) and (c) are at liquid level 2, the ideal condition of Table 10.2 while (b) and (d) are at liquid level 3, dryout. Fewer droplets are seen overall with the dryout condition. Interestingly, the velocity distribution for the dryout case of (d) is strongly skewed positive. Examining the size distributions of (e) and (f) helps explain this. The dryout condition is much more strongly skewed towards smaller droplets than the ideal condition, with very few droplets over 2000 µm. As the dryout condition has little liquid contacting the top row, there is less chance for liquid to be passing those tubes, hence smaller droplets are likely what is entrained in the vapor. A peak is seen in the height distribution between 15 to 20 mm above the tubes for the dryout liquid level in (b), as opposed to the near constant counts of (a) for the ideal liquid level. However, once counts fall off at about 35 mm, the height distribution is near constant throughout the rest of the headspace.

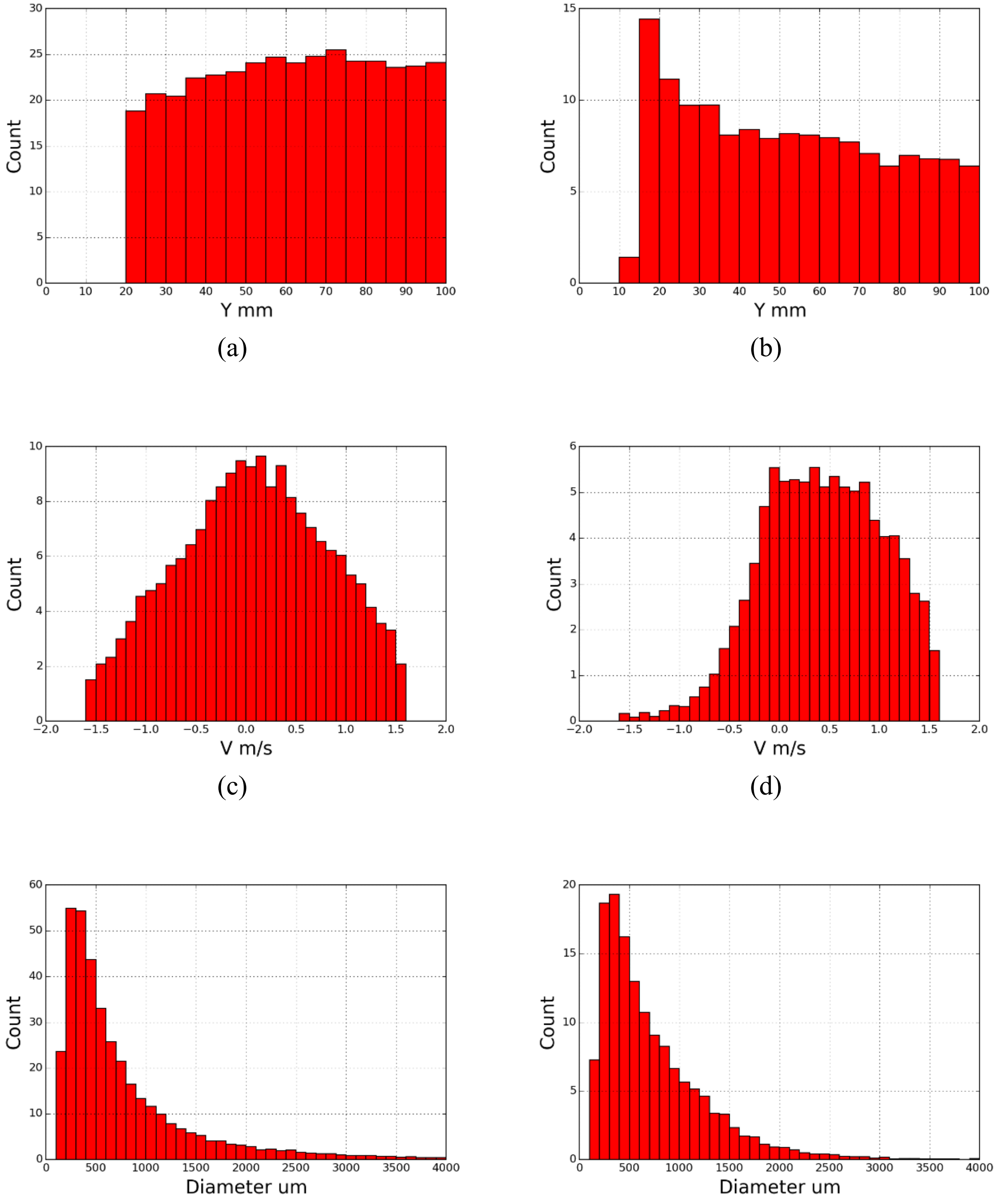

(a) (b)

(c) (d)

(e) (f)

Figure 10.10 Liquid level comparison, rotated triangular bundle, R-123, 12.8 °C (55 °F), 20.3 kg/m²s (15000 lb/hr-ft²), 15.7 kW/m² (5,000 Btu/hr-ft²), 50 mm lens, image location J: (a) ideal height distribution, (b) dryout height distribution, ideal velocity distribution, dryout velocity distribution, (e) ideal size distribution, (f) dryout size distribution

10.3.2 Mass Flux

Figure 10.11 and Figure 10.12 shows the effect of varying mass flux, comparing height distribution and velocity distribution, respectively. A progression is seen in the height distribution, with both more droplets recognized and an increase in droplets higher in the headspace, with both the baseline in (c) and higher mass flux condition in (d) showing a near constant distribution with height. Even with the low and moderate mass flux conditions of (a) and (b), droplets are seen at the top of the headspace.

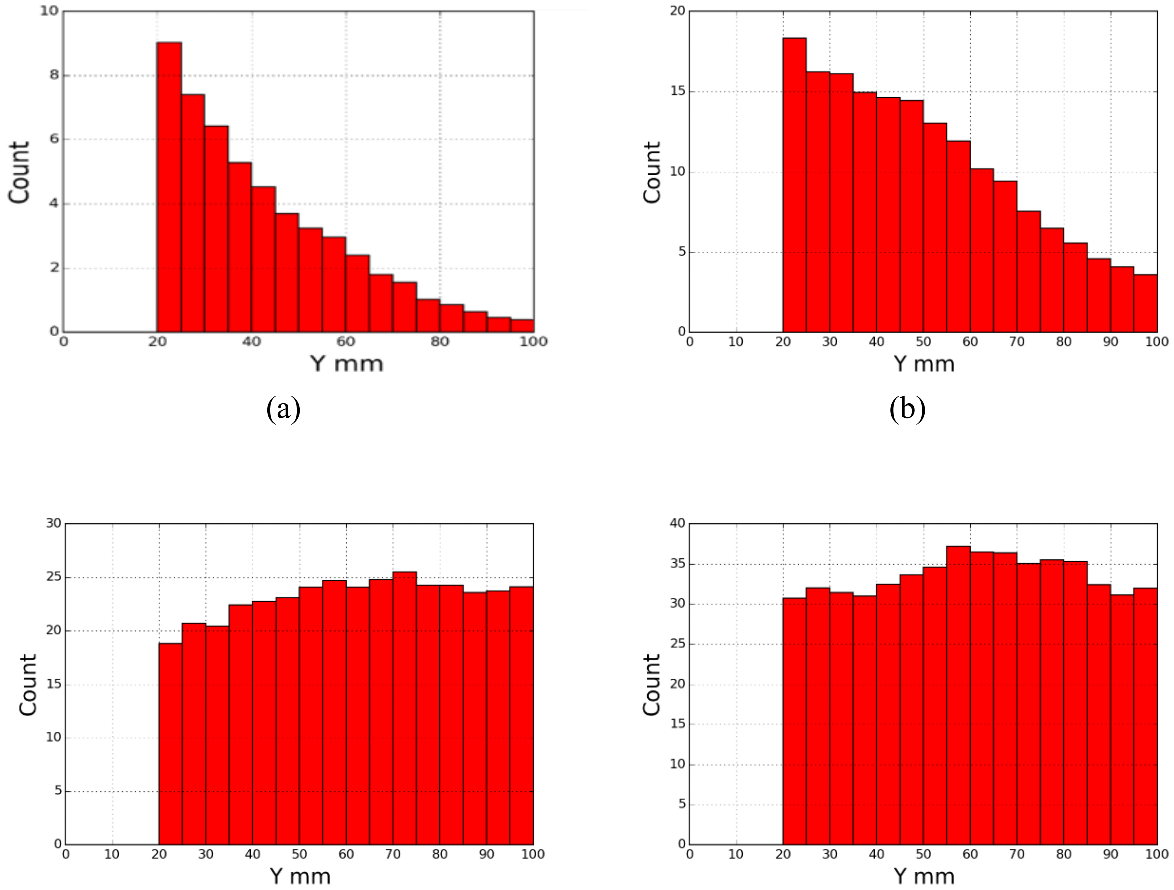

(a) (b)

(c) (d)

Figure 10.11 Mass flux comparison, height distribution, rotated triangular bundle, R-123, 12.8 °C (55 °F), ideal liquid level, 50 mm lens, image location J: (a) 3.46 kg/m^{2}s (2550 lb/hr-ft^2), (b) 7.05 kg/m^{2}s (5200 lb/hr-ft^2), (c) 20.3 kg/m^{2}s (15000 lb/hr-ft^2), (d) 40.7 kg/m^{2}s (30000 lb/hr-ft^2)

Examining the velocity distributions in Figure 10.12, we see a corresponding trend. The lowest mass flux of (a) shows very low counts and a near-symmetrical distribution about zero velocity, with possibly a slight skew towards positive velocities. Increasing the mass flux in (b), a slightly larger skew towards positive velocities is seen. This trend continues as mass flux increases in (c) and (d), with a very prominent skew with the highest mass flux. Note that (a) has a bin size of 0.05 m/s, (b) and (c) have a bin size of 0.1 m/s, and (d) has a bin size of 0.25 m/s.

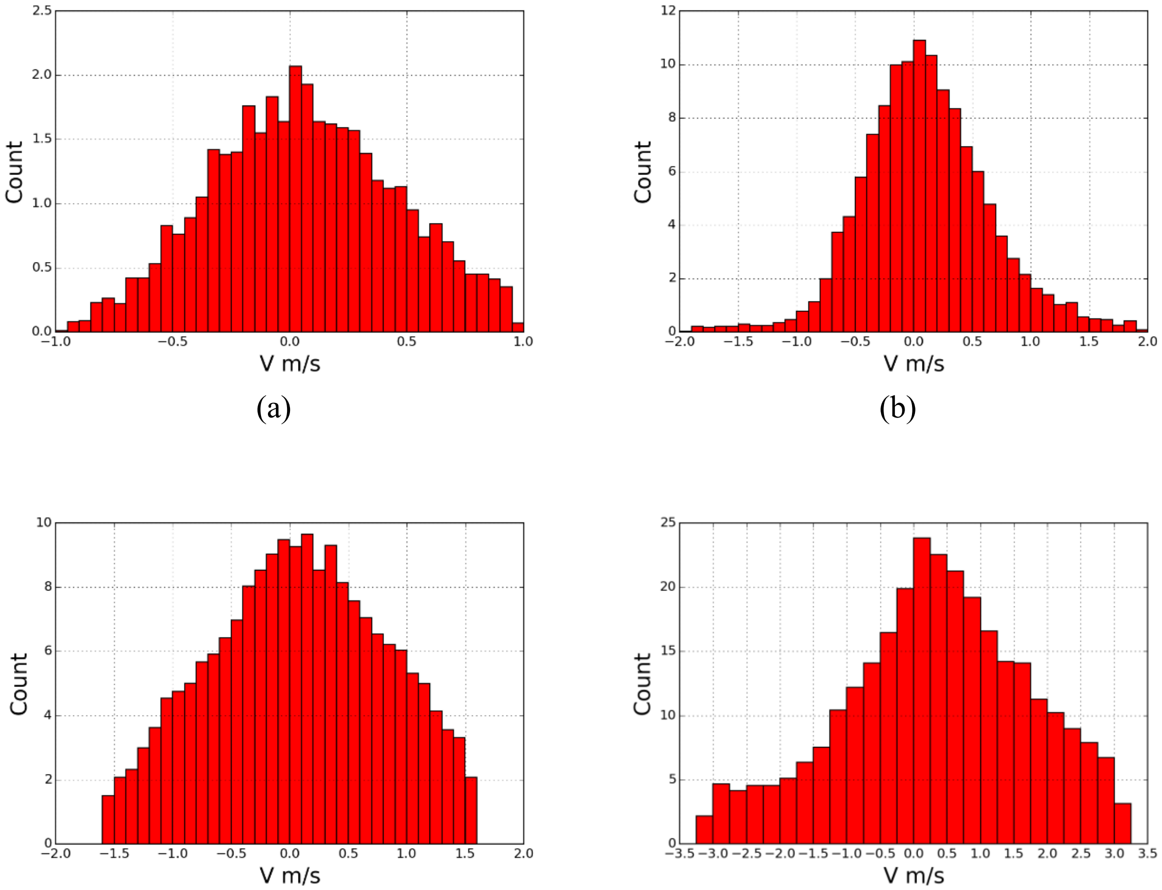

(a) (b)

(c) (d)

Figure 10.12 Mass flux comparison, velocity distribution, rotated triangular bundle, R-123, 12.8 °C (55 °F), ideal liquid level, 50 mm lens, image location J: (a) 3.46 kg/m^{2}s (2550 lb/hr-ft^2), (b) 7.05 kg/m^{2}s (5200 lb/hr-ft^2), (c) 20.3 kg/m^{2}s (15000 lb/hr-ft^2), (d) 40.7 kg/m^{2}s (30000 lb/hr-ft^2)

10.3.3 Saturation Temperature

Figure 10.13 shows the effect of varying outlet saturation temperature, with (a) and (c) displaying the baseline while (b) and (d) show setting the saturation temperature at 4.4 °C (40 °F). Counts are similar, but opposite of all previous results, higher counts are seen with the higher saturation temperature.

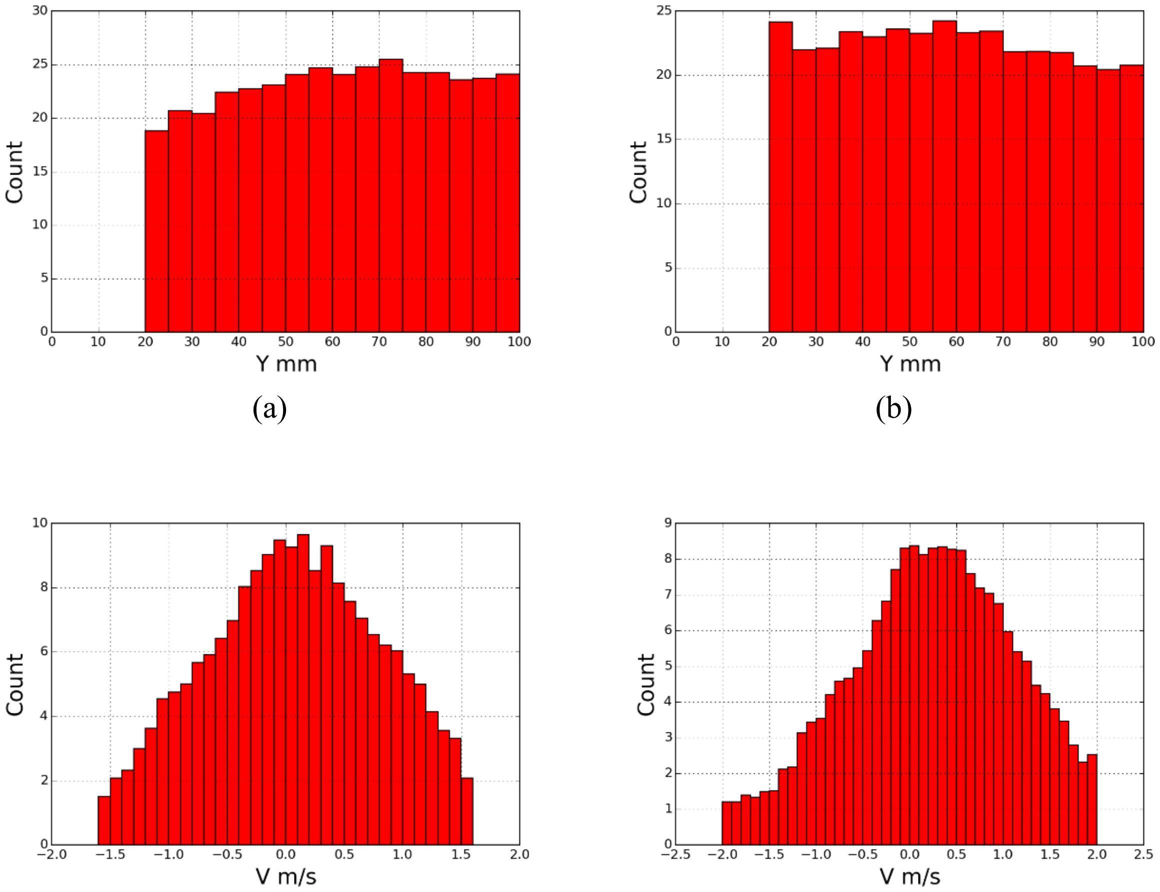

(a) (b)

(c) (d)

Figure 10.13 Saturation temperature comparison, rotated triangular bundle, R-123, 20.3 kg/m²s (15000 lb/hr-ft²), 15.7 kW/m² (5000 Btu/hr-ft²), 50 mm lens, image location J: (a) 12.8 °C (55 °F) height distribution; (b) 4.4 °C (40 °F) height distribution, (c) 12.8 °C (55 °F) velocity distribution, (d) 4.4 °C (40 °F) velocity distribution

Even though vapor velocities for the lower saturation temperature should be 40% higher than the higher saturation temperature condition, higher counts are seen for the 12.8 °C (55 °F) condition. The difference between this result and the previous bundle and refrigerant combinations is unknown, but may be due to the fountain effect and the need to image at the location nearest to the camera.

10.3.4 Heat Flux

In lieu of the baseline case with a higher heat flux, the thermodynamic conditions to match velocities with R-134a were taken instead. As such, the results with a mass flux of 40.7 kg/m^{2}s (30000 lb/hr-ft^2) are used instead to examine the effect of varying heat flux. Figure 10.14 compares thermodynamic conditions 7 and 8 of Table 10.1, with (a) and (c) covering the 15.7 kW/m^2 (5000 Btu/hr-ft^2) condition and (b) and (d) covering the 31.5 kW/m^2 (10000 Btu/hr-ft^2) condition. Results are similar, but higher counts are seen with the higher heat flux. For the height distribution, both show a decrease, a rise to a peak, and then a decrease as height increases. For both the peak occurs near 60 mm. For the velocity distributions, similar results are again seen between the two heat fluxes. For both, a peak occurs between 0 and 0.25 m/s. A very similar curve is seen as well, with a prominent skew towards positive velocities. Overall, compared to other variations tested, heat flux is not a strong actor with this bundle and refrigerant combination.

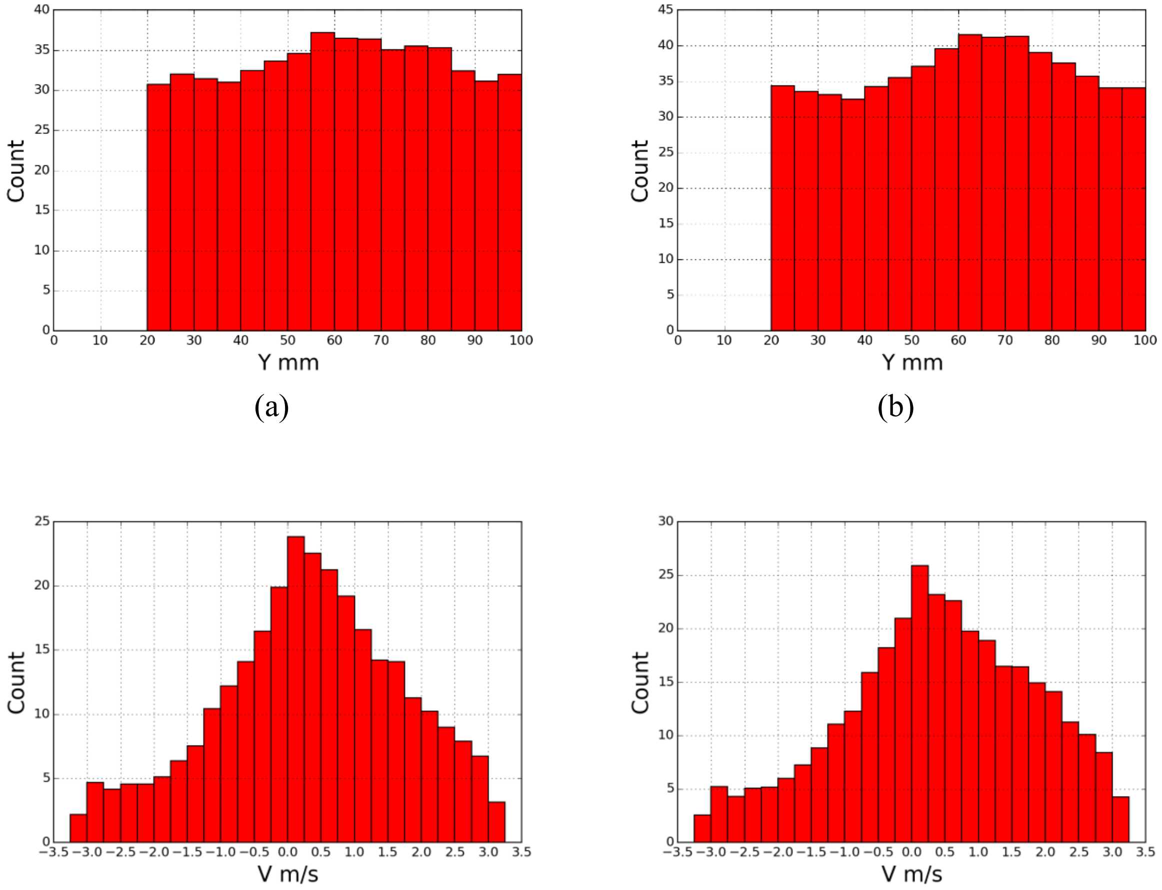

(a) (b)

(c) (d)

Figure 10.14 Heat flux comparison, rotated triangular bundle, R-123, 12.8 °C (55 °F), 40.7 kg/m^{2}s (30000 lb/hr-ft^2), 50 mm lens, image location J: (a) 15.7 kW/m^2 (5000 Btu/hr-ft^2) height distribution; (b) 31.5 kW/m^2 (10000 Btu/hr-ft^2) height distribution

10.3.5 Summary

For the triangular bundle with R-123, eight thermodynamic conditions were tested. All variables tested showed an effect on droplet counts and distributions, however results were not the same as with the triangular bundle with R-123. Unlike with the triangular bundle with R-123, heat flux was not a strong actor on droplet distribution and velocity. Likewise, varying saturation temperature did not show a strong effect and indeed was reverse of the effect noted with the triangular bundle.

Chapter 11 - Experimental Summary & Discussion

Two dominant mechanisms are thought to generate droplets: vapor shear and surface tension dominated wave action. The relative effect of each is controlled by all the mechanisms examined: mass flux, liquid level, refrigerant, etc. Two major flow regions within the headspace can be identified based on the expected vapor velocities. First, the maximum velocity can be expected to occur in the gaps between tubes at the highest point in the tube bundle. For R-123 at the highest mass flux tested with a saturation temperature of 4.4 °C (40 °F), this velocity could be as high as 15 m/s. The second flow region is at a higher point in the headspace where the velocity jets have dissipated and the flow is more or less uniform and seven times slower. These expected velocities can be used to determine corresponding terminal droplet sizes, which gives a static picture of the expected size distribution. This chapter will first cover how those velocities should affect droplet behavior. It will then compare the effects of the test conditions varied across bundles and refrigerants, with the effect of those velocities in mind.

11.1 Droplet dynamics

The terminal velocity of a droplet can be calculated from a force balance. Terminal velocity for this paper is defined as the vapor velocity for which a stationary droplet's acceleration is zero, i.e., the droplet is neither rising nor falling. We also define a corresponding terminal droplet diameter, meaning that for a given vapor velocity, droplets larger than the terminal diameter would be expected to fall and droplets smaller would be expected to rise. Gravitational forces work to pull droplets down while drag force, and to a much lesser extent, buoyancy, work to draw droplets up. The equations for each force and the overall balance are given in the equations below.

$$F_{gravity} = \frac{\pi \rho_l g D^3}{6} \tag{11.1}$$

$$F_{drag} = \frac{\pi \rho_v C_{drag} v_v^2 D^2}{8} \tag{11.2}$$

$$F_{buoyancy} = \frac{\pi \rho_v g D^3}{6} \tag{11.3}$$

$$\Sigma F = m_{droplet} a = F_{drag} + F_{buoyancy} - F_{gravity} \tag{11.4}$$

The drag coefficient of (11.2) is correlated to the Reynolds number as suggested by White [70] shown in (11.5), applicable for Reynolds numbers in the range $0.1 < \mathrm{Re} < 2 \cdot 10^5$.

$$\mathrm{C}_{drag} = \frac{24}{Re} + \frac{6}{1 + \sqrt{Re}} + 0.4 \tag{11.5}$$

$$Re = \frac{\rho_v v_v D}{\mu_v} \tag{11.6}$$

To find the terminal diameter, acceleration in (11.4) is set to zero and diameter is iterated for a given mass flux to balance the equation. This results in Figure 11.1 and Figure 11.2, which show terminal diameter vs mass flux for the between-tube and headspace regions, respectively. Note that for both figures the mass flux shown is the between-tube mass flux as defined in Section 5.1.

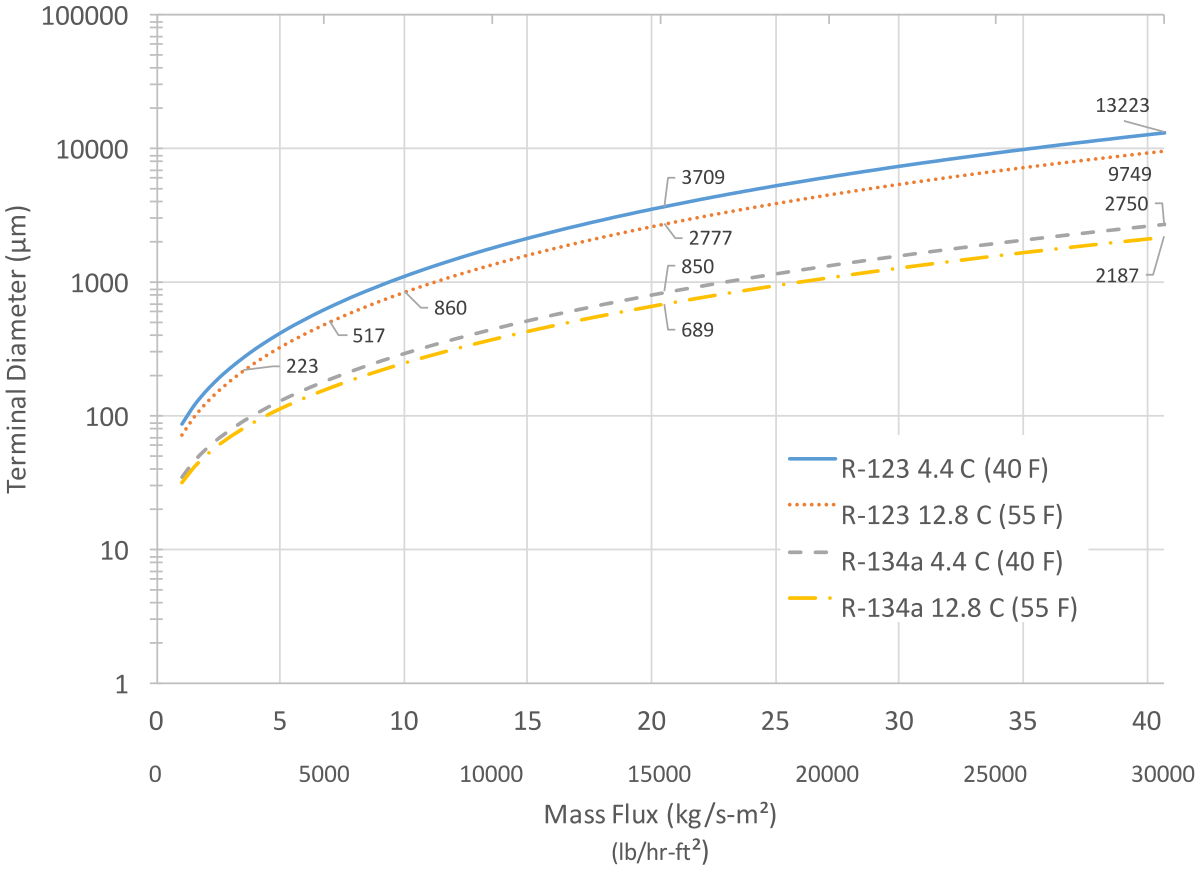

Figure 11.1 Expected between-tube terminal droplet diameter vs mass flux per refrigerant and saturation temperature

In Figure 11.1 a clear difference is seen between the diameters of droplets expected to be entrained between the tubes for the two refrigerants. For instance, for a temperature of 4.4 °C (40 °F) at the highest mass flux tested, droplets smaller than 13223 μm would be expected to rise with R-123 as opposed to 2750 μm for the same conditions with R-134a. Correspondingly, droplets larger than those diameters would be expected to sink and not make it out from within the bundle into the headspace. As such, this figure largely shows the maximum droplet size to expect in the headspace and does not consider whether it will be carried out. This analysis does not consider vena contracta between the tubes causing localized higher velocities. A smaller difference is seen by varying temperature for a given refrigerant, with a terminal diameter of

9749 µm expected for R-123 at 12.8 °C (55 °F) at the highest mass flux vs the 13223 µm at 4.4 °C (40 °F). Each data callout is at a mass flux tested for a given refrigerant and saturation temperature.

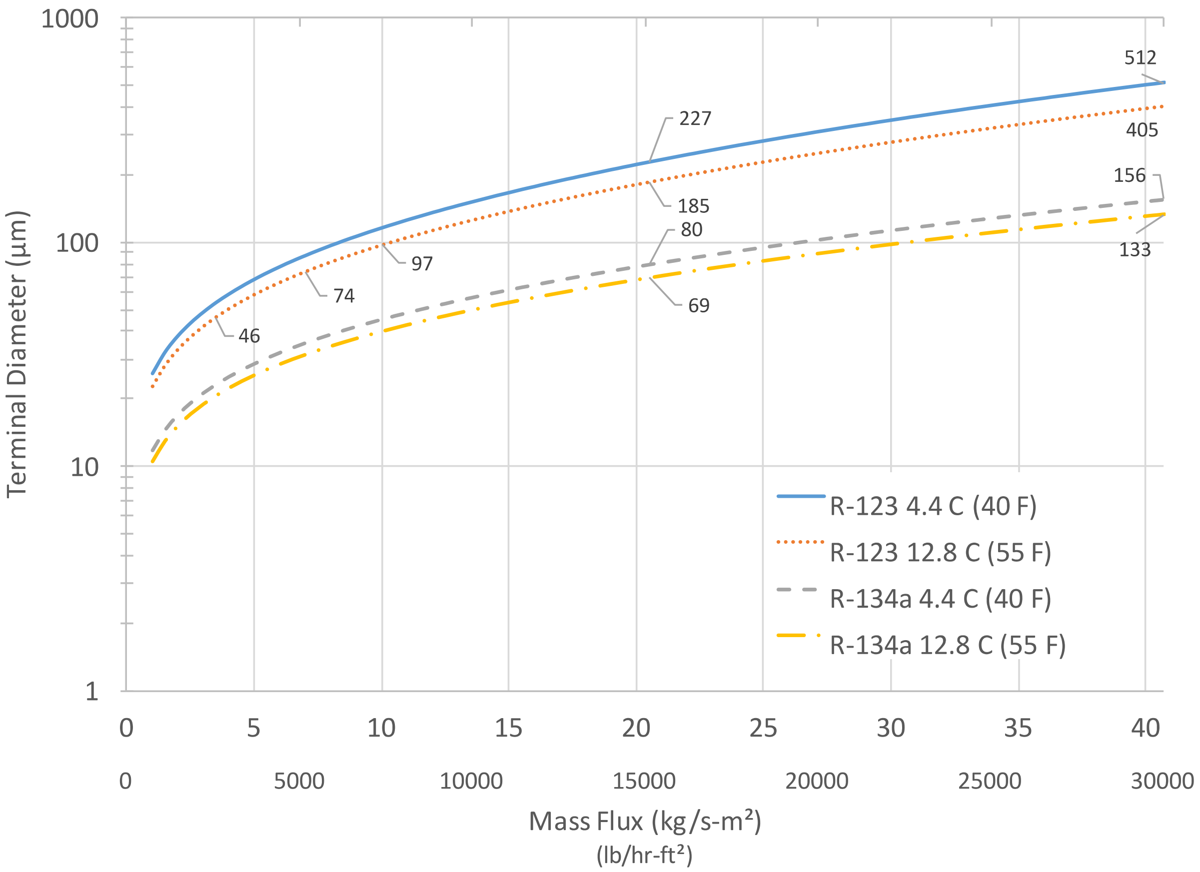

Figure 11.2 Expected headspace terminal droplet diameter vs mass flux per refrigerant and saturation temperature

In Figure 11.2, similar differences are seen in the headspace terminal droplet diameter as with Figure 11.1. Again, the largest differences are seen between refrigerants rather than between saturation temperatures. While Figure 11.1 may show that large droplets can be ejected into the headspace from the tubes, without sufficient initial velocity, they may be too large to be carried out of the test section by the vapor flowing in the headspace. For example, the lofting ability of the vapor drops from 2750 µm to 156 µm from the bundle to the headspace, 17 times less. However, with sufficient momentum, large droplets can possibly escape.

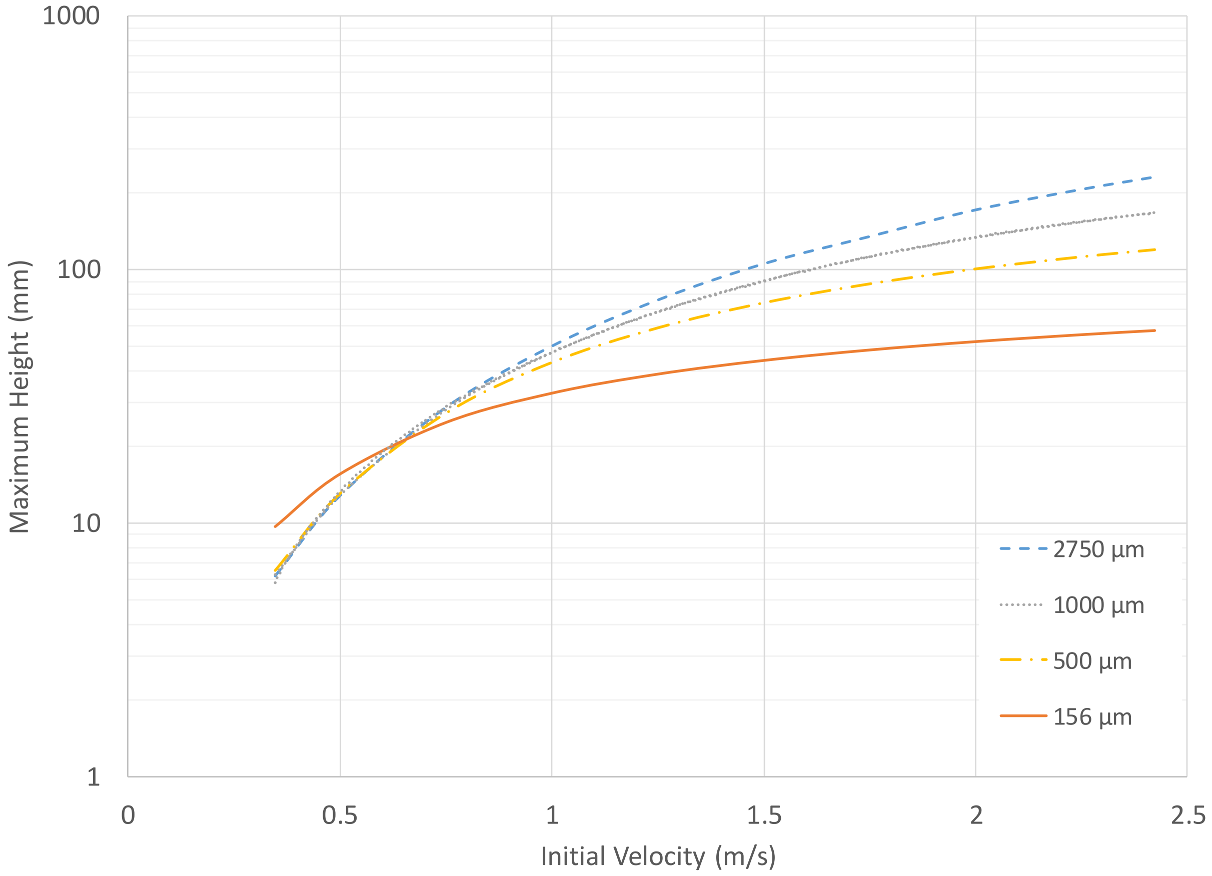

Figure 11.3 Maximum droplet height vs initial velocity per diameter, R-134a, 4.4 Cº (40 ºF), 40.7 kg/m^{2}s (30000 lb/hr-ft^2)

Figure 11.3 is based on a simulation of droplets using equations (11.1) through (11.6). For a given initial velocity and droplet diameter, the maximum height the droplet would achieve is calculated. The data shown is for R-134a at 4.4 ºC (40 ºF) and at the highest mass flux of 40.7 kg/m^{2}s (30000 lb/hr-ft^2). A 156 µm droplet would only achieve 57 mm above the tubes at the maximum initial velocity that would be expected, 2.4 m/s. Recall from Figure 11.2 that this is the terminal droplet size for these conditions, meaning at its apex, the droplet would be expected to neither rise nor fall. Droplets smaller than 156 μm would be carried out by drag and buoyancy from the flowing vapor.

Compare with the 2750 μm droplet, which would achieve a maximum height of 232 mm if launched with the full between-tube velocity. This is the terminal droplet size for between the tubes so this velocity would be unlikely if not impossible. A velocity of 1.5 m/s would give sufficient momentum to launch a 2750 μm droplet to 106 mm, beyond the limits of our imaging. Droplets between 156 and 2750 μm show the role momentum plays. For a 1000 μm droplet, 1.6 m/s is sufficient to exceed 100 mm while for a 500 μm droplet, 2 m/s is required. From these figures, it is shown that both large droplets with sufficient velocity, as well as small droplets able to be carried by vapor, are capable of escaping the test section. Interestingly, it also shows there is a range of droplet sizes for which there is an insufficient or unreasonable velocity to escape the test section. Regardless, this analysis does not consider collision, either with droplets, the test section's walls, or the flow distribution plate at the top of the test section. It also does not consider droplet fragmentation due to aerodynamic forces. The underlying analysis, however, does provide a basis for understanding the behaviors seen in the sections to follow.

A summary of Figure 11.1 through Figure 11.3 for six of the refrigerant, mass flux, and temperature combinations is shown in Figure 11.4 This figure shows the initial velocity required at a given condition for a given droplet diameter to rise to 100 mm above the tubes. For each curve, the leftmost line denotes the headspace terminal droplet diameter. Droplets smaller than this value would be carried out by vapor alone, regardless of initial velocity. The rightmost line for a given curve denotes the between-tube terminal droplet diameter, or rather, the largest droplet that would be expected to be carried into the headspace from between the tubes. The curved or nearly horizontal part of each curve shows the minimum initial velocity required for a droplet of a given diameter to achieve 100 mm above the tubes. All curves approach a value of approximately 1.4, which can be understood from the ballistic equations

$$\frac{1}{2}v^2 = gh \tag{11.7}$$

$$v = \sqrt{2gh} \tag{11.8}$$

where v is the initial velocity, h is the maximum height, and g is gravitational acceleration. For a value of gravity of 9.8 m/s^2 and a desired height of 100 mm, a required initial velocity of 1.4 m/s is found. So, for this simulation with droplets approaching and exceeding 2000 μm, aerodynamic forces play a diminishing role.

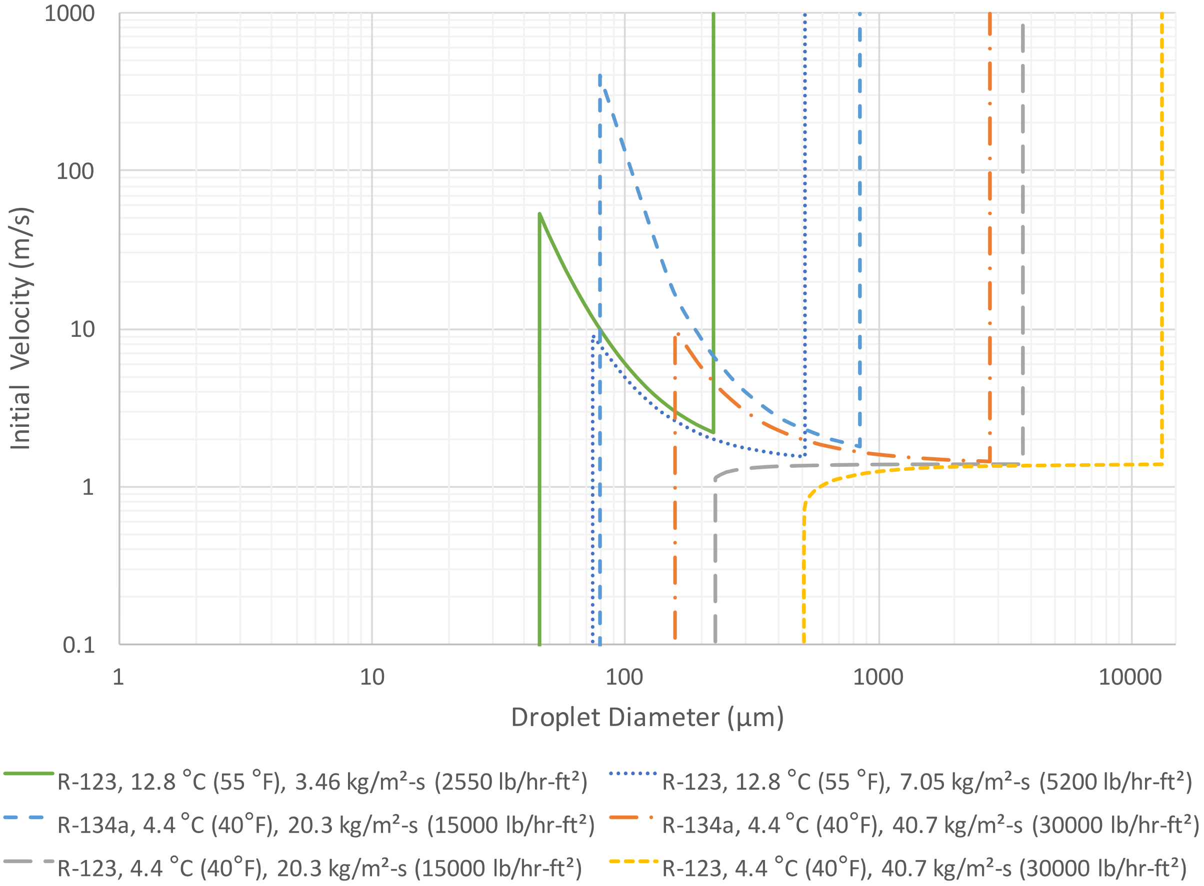

Figure 11.4 Required initial velocity vs diameter to reach 100 mm above the tubes

As an example, take R-123 at 40.7 kg/m^2-s (30000 lb/hr-ft^2). Droplets smaller than 513 µm would be carried out by the drag and buoyancy forces of the vapor alone, regardless of initial velocity. As the vapor headspace velocity would be 2.15 m/s, a minimum initial velocity of 1.128 m/s is sufficient for a 700 µm droplet to reach 100 mm. Consider instead R-134a at the same mass flux. Droplets smaller than 156 µm would be carried out regardless of initial velocity. However, an initial velocity of 10 m/s is required for a droplet just over 156 µm to reach 100 mm. As the maximum between-tube velocity for this condition would be 2.42 m/s, corresponding to a droplet diameter on the curve of 371 µm, droplets between 156 and 371 µm would never either have sufficient drag nor initial momentum to reach 100 mm. A droplet of 498 µm with an initial velocity of 2.0 m/s, a 1700 µm droplet with 1.5 m/s, or a 2750 µm droplet with an initial velocity of 1.393 m/s could all reach 100 mm, but droplets in the range of 156 to 371 µm would not be expected to do so. For R-134a at 20.3 kg/m^2-s (15000 lb/hr-ft^2), the between-tube velocity of 1.21 m/s rules out all droplets larger than 80 µm from reaching 100 mm or escaping the test section. For R-123 at 12.8 C° (55 °F) and 7.05 kg/m^2-s (5200 lb/hr-ft^2) (matching the same velocities as R-134a at the same saturation temperature), droplets from 74 to 258 µm would not be expected to reach 100 mm and for 3.46 kg/m^2-s (2550 lb/hr-ft^2), like with the lower mass flux with R-134a, no droplets larger than 46 µm, the headspace terminal droplet diameter, should be able to reach 100 mm.

From these figures, it is shown that both large droplets with sufficient velocity, as well as small droplets able to be carried by vapor, are capable of escaping the test section. Interestingly, it also shows that for certain conditions, there is a range of droplet sizes for which there is an insufficient or unreasonable velocity to escape the test section. Regardless, this analysis does not consider collision, either with droplets, the test section's walls, or the flow distribution plate at the top of the test section. It also does not consider droplet fragmentation due to aerodynamic forces. The underlying analysis, however, does provide a basis for understanding the behaviors seen in the sections to follow.

11.2 Mass Flux

For comparison of test conditions, liquid volume fraction is used, as it incorporates both count, diameter, and height into a convenient form. Results were collected with both the standard 20.3 kg/m^{2}s (15000 lb/hr-ft^2) and 40.7 kg/m^{2}s (30000 lb/hr-ft^2) for both R-123 and R-134a. Figure 11.5 shows the triangular bundle arrangement at the standard mass fluxes with both refrigerants, holding all other variables constant.

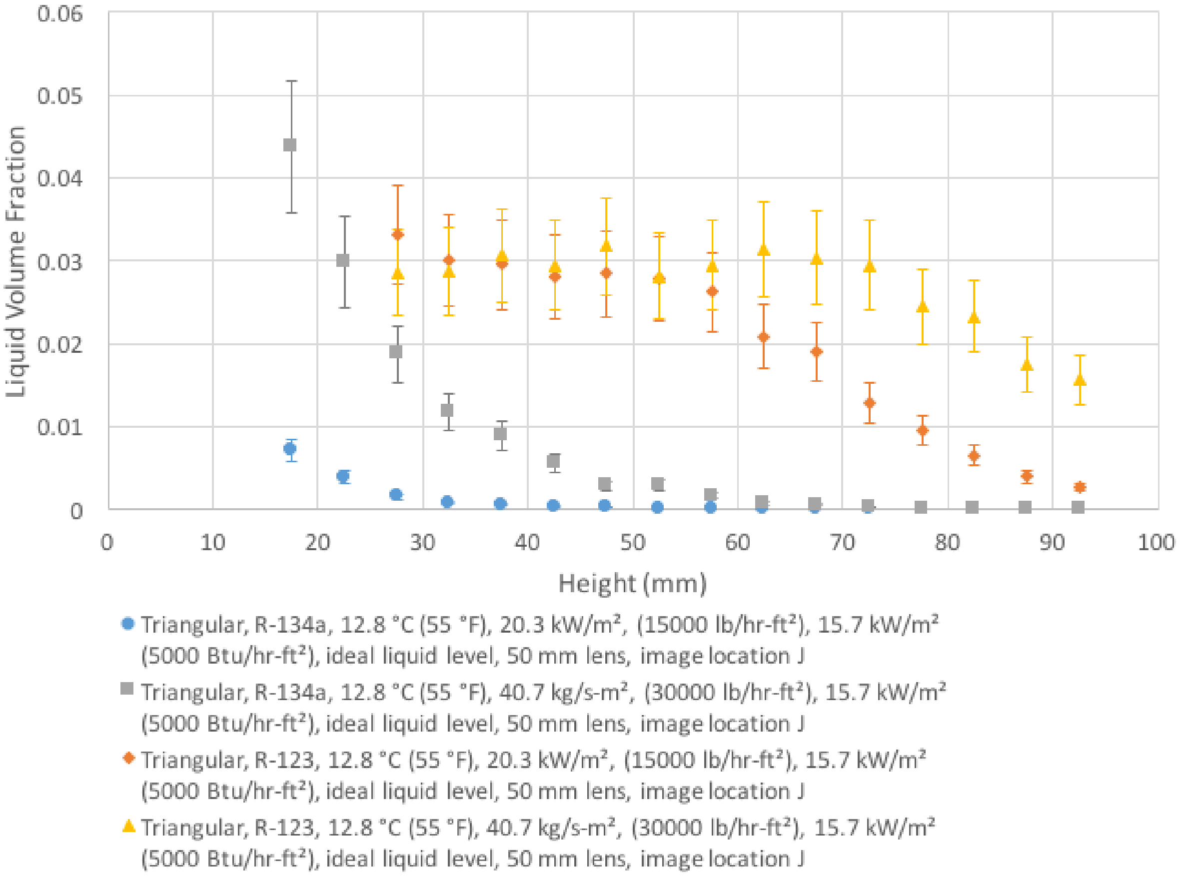

Figure 11.5 Mass flux variation, liquid volume fraction vs height, triangular bundle

For both refrigerants, a marked difference is seen between mass fluxes. For R-134a at the higher mass flux, the liquid fraction where measured is up to six times higher lower in the headspace and is shown to persist out to nearly 60 mm above the tubes whereas the lower mass flux liquid fraction is nearly zero by 30 mm. For R-123, both mass fluxes show a similar liquid fraction up to a height of 60 mm. At that height, the lower mass flux begins to drop off while the higher mass flux persists for an additional 15 mm. Both show an appreciable liquid fraction at the top of the headspace.

For the rotated triangular arrangement with R-134a shown in Figure 11.6, again a difference is seen between mass fluxes. For a given liquid fraction, the higher mass flux shows a shift upwards in the headspace of approximately 25 mm. The higher mass flux also shows both a higher peak liquid fraction and an appreciable liquid fraction at the top of the headspace.

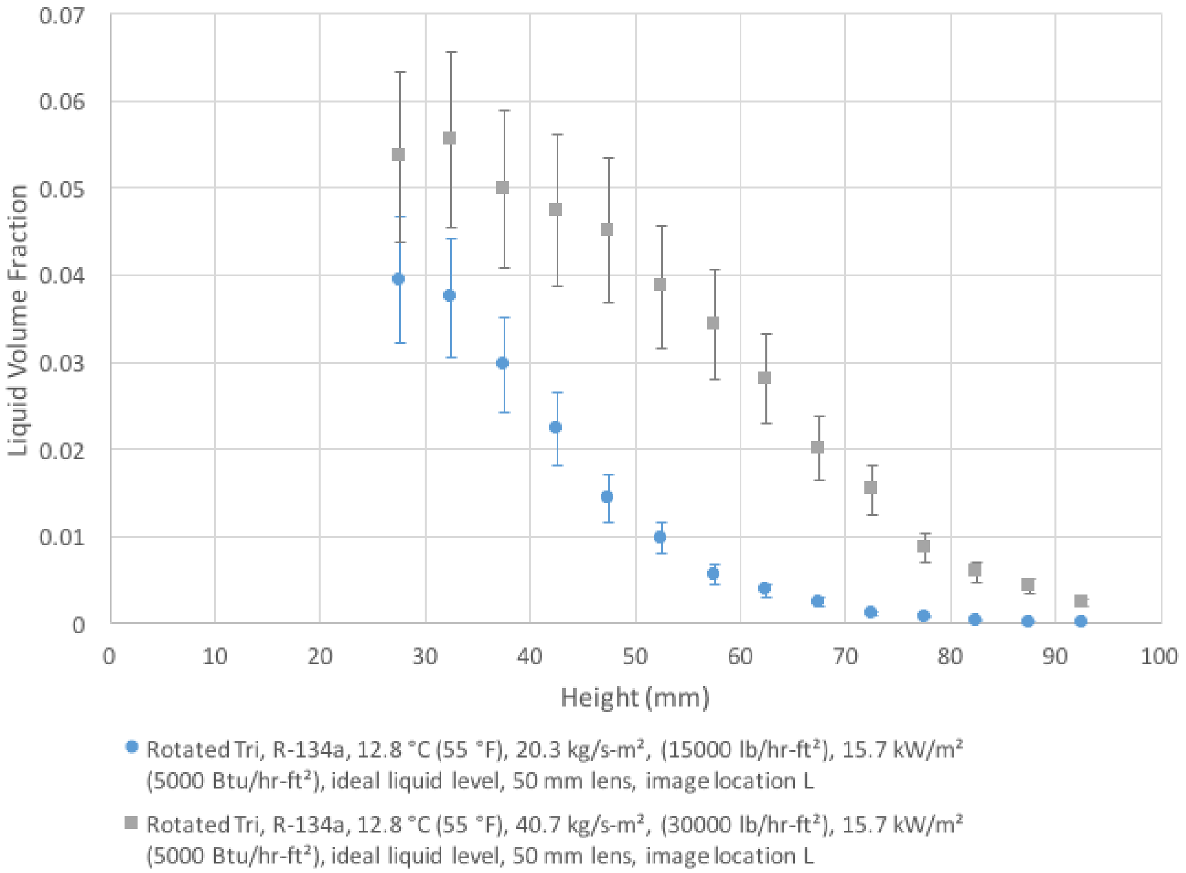

Figure 11.6 Mass flux variation, liquid volume fraction vs height, rotated triangular bundle, R-134a

An unexplained result is seen with R-123 and the rotated triangular arrangement in Figure 11.7. The lower mass flux actually shows a higher liquid fraction throughout the entirety of the headspace. This phenomenon persists even when accounting for all other variations, including liquid level, saturation temperature, or the use of the higher magnification lens. One possible reason for the discrepancy with both the triangular results with both refrigerants and the rotated triangular results with R-134a may be that the fountain effect throws liquid towards the glass more effectively at the higher mass flux, obscuring droplets that otherwise would be counted. Another may be that the higher velocities expected with the higher mass flux lead to a shift towards smaller droplets not visible with either lens. Regardless, with all variations, mass flux is shown to play a role in droplet distribution

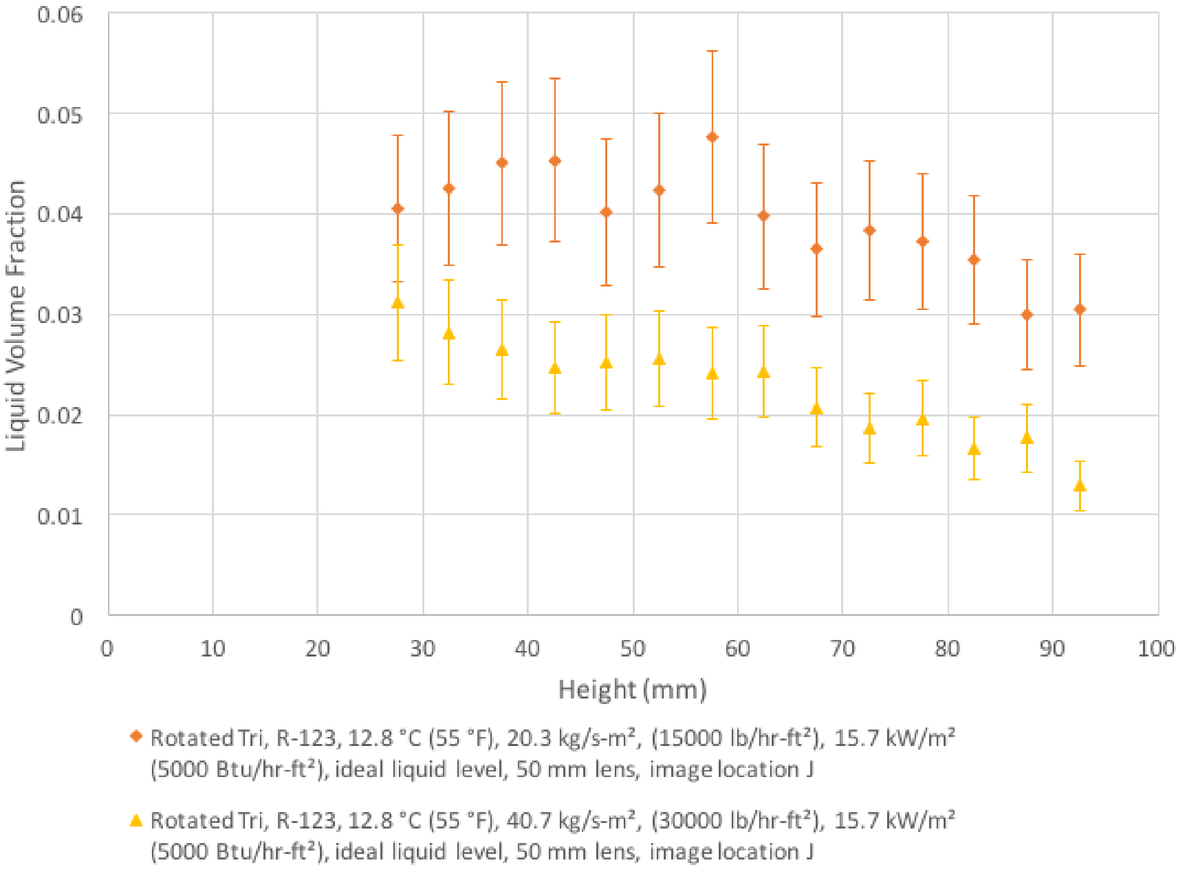

Figure 11.7 Mass flux variation, liquid volume fraction vs height, rotated triangular bundle, R-123

11.3 Outlet Saturation Temperature

Figure 11.8 compares the result of varying outlet saturation temperature for both refrigerants with the triangular bundle. For both refrigerants, the lower saturation temperature results in a higher liquid volume fraction. Indeed, this figure appears very similar to the variation in mass flux seen in Figure 11.5. As discussed in previously, the decrease in temperature results in vapor velocity increases of 30% to 40% for R-134a and R-123, respectively. Curiously, the liquid volume fraction of approximately 0.05 for R-123 at the lower saturation temperature is even higher than the high mass flux condition of 0.03 in Figure 11.5, though the higher mass flux results in a higher exiting liquid fraction.

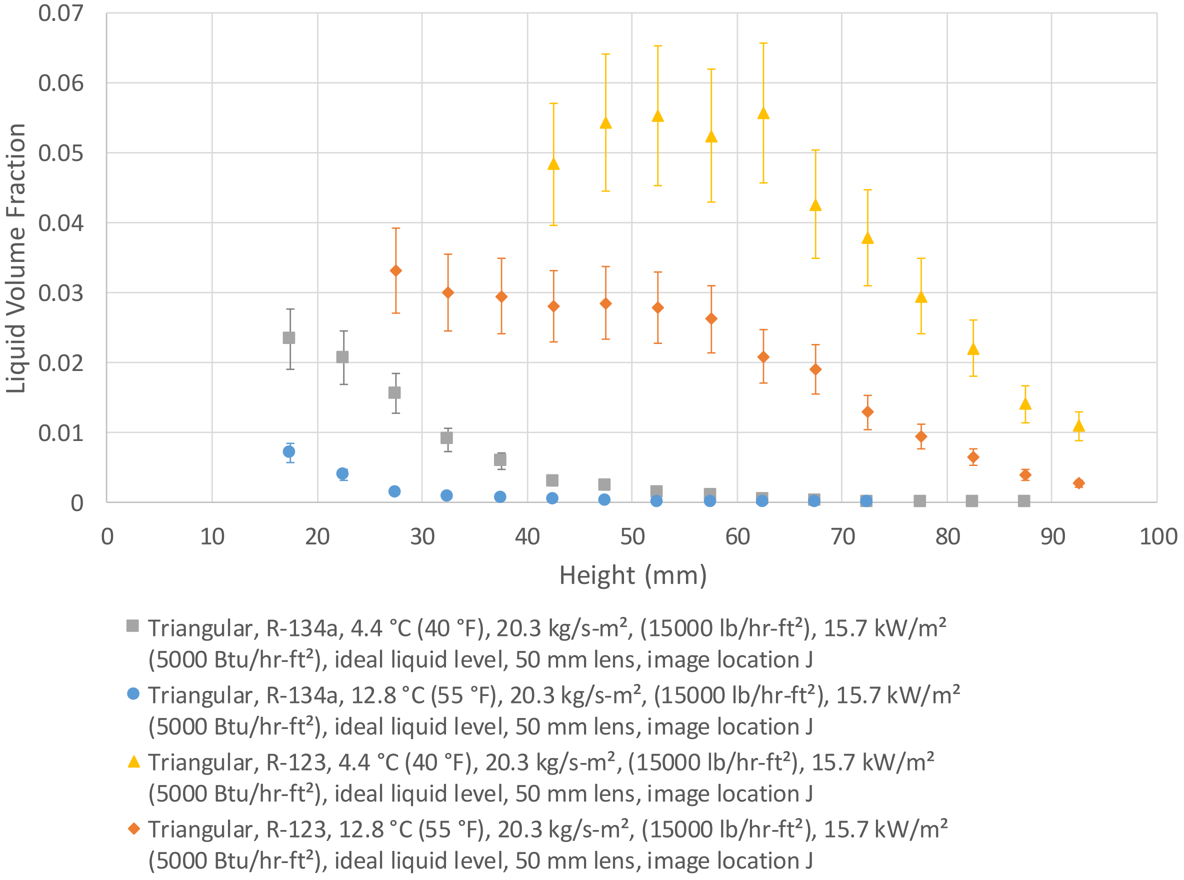

Figure 11.8 Saturation temperature variation, liquid volume fraction vs height, triangular bundle

Figure 11.9 shows the variation of liquid volume fraction with saturation temperature for the rotated triangular bundle. Little appreciable difference is seen with the results for R-134a, though the lower saturation temperature does show a slightly higher liquid volume fraction lower in the headspace. R-123, however, shows an increase in liquid fraction at all heights. Both saturation temperatures with R-123 show liquid leaving the headspace.

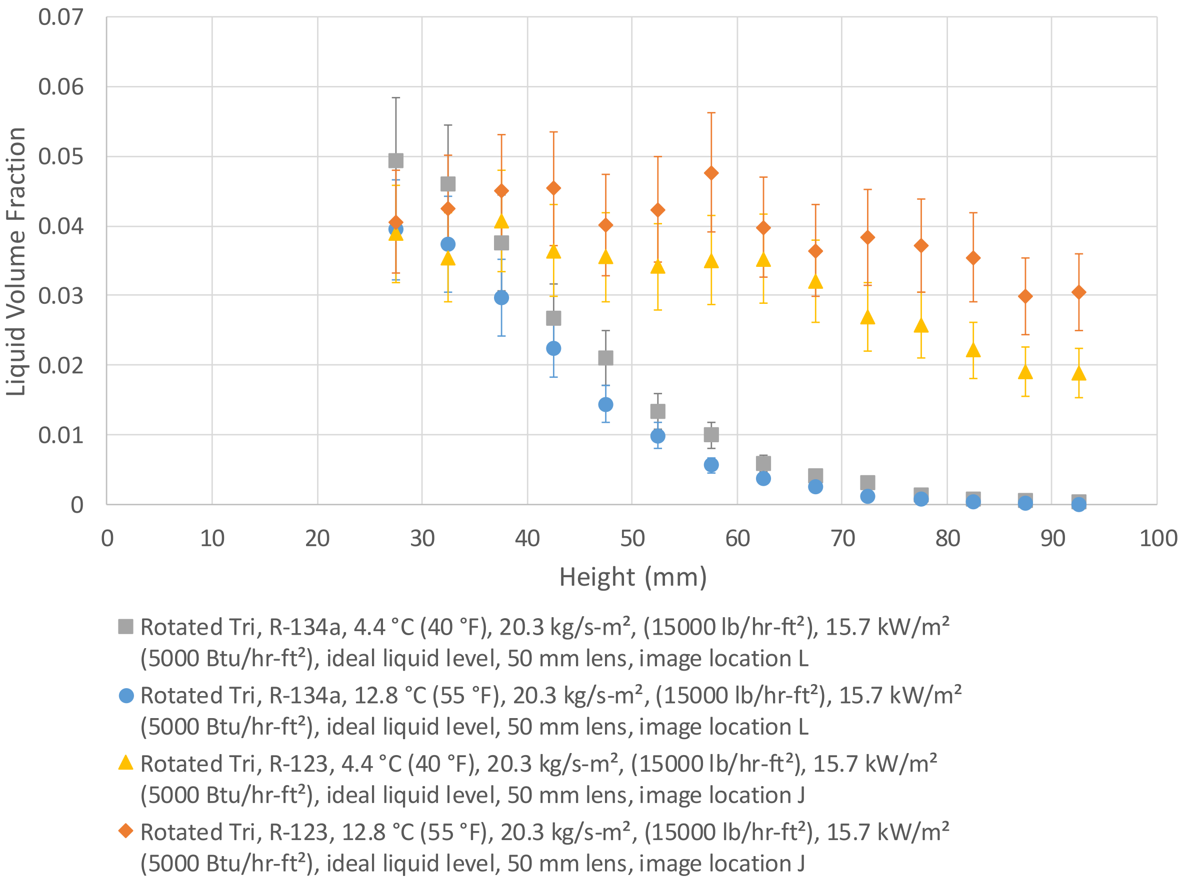

Figure 11.9 Saturation temperature variation, liquid volume fraction vs height, rotated triangular bundle

11.4 Heat Flux

Figure 11.10 compares the effect of heat flux on droplet distribution for the triangular bundle. Shown are R-134a at two mass fluxes as well as R-123 at the higher mass flux. In all cases, an increase in heat flux results in a higher liquid volume fraction. The effect of varying heat flux is least significant with R-134a at the higher mass flux of 40.7 kg/m^{2}s (30000 lb/hr-ft^2), resulting in a very slightly higher liquid fraction for a given height. Indeed, results between the heat flux at 15.7 kW/m^2 (5000 Btu/hr-ft^2) and 31.5 kW/m^2 (10000 Btu/hr-ft^2) are within the uncertainty of each other up until 40 mm above the tubes. Liquid fraction also comes back together by the top of the headspace. For R-123, results for different heat fluxes significantly diverge after 60 mm, with a three-fold increase in liquid fraction at the top of the headspace for the higher heat flux. This is likely due to the higher tube wetting needed to achieve the higher heat flux, increasing the possibly of droplets being entrained and ejected.

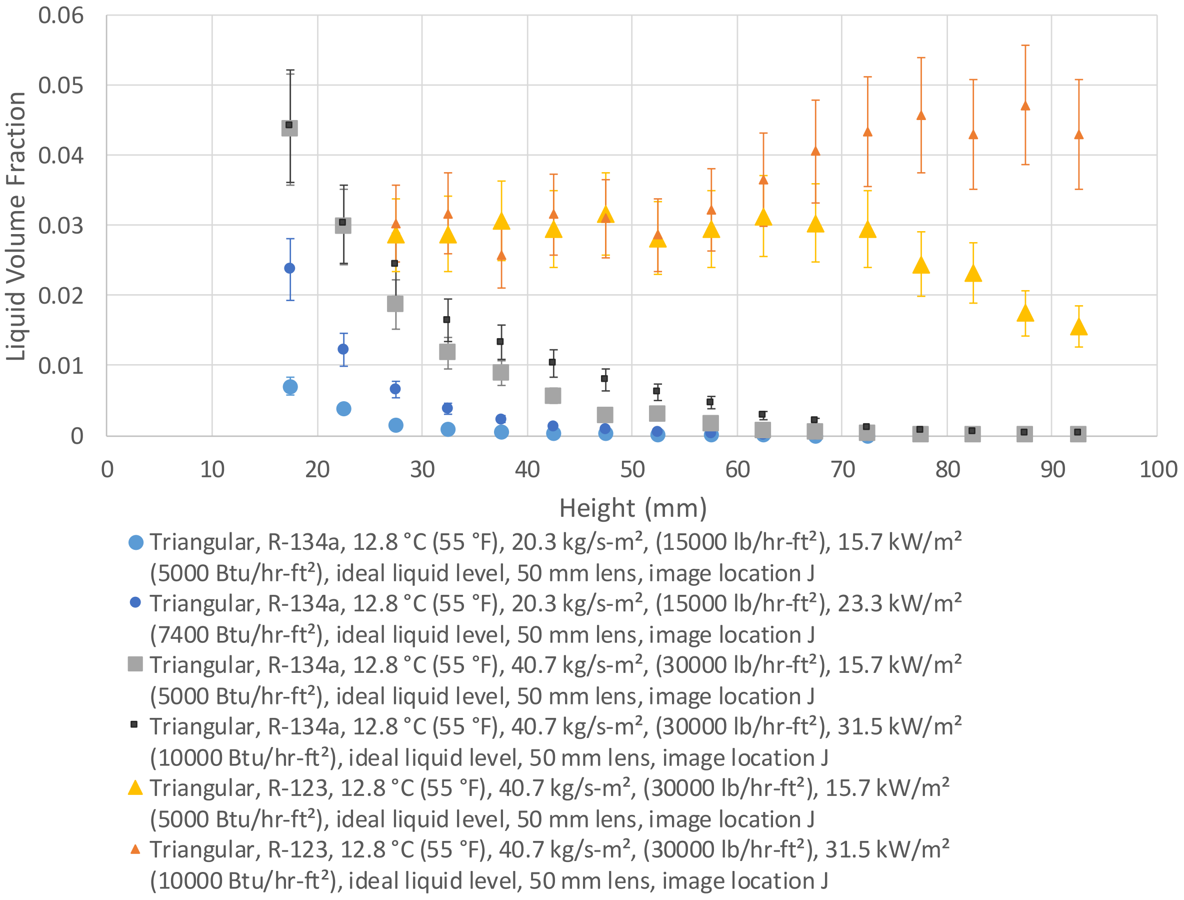

Figure 11.10 Top-rows heat flux variation, liquid volume fraction vs height, triangular bundle

For the rotated triangular bundle in Figure 11.11, heat flux is again shown to have an effect. Shown are the result of varying heat flux for R-134a at 20.3 kg/m^{2}s (15000 lb/hr-ft^2) and R-123 at 40.7 kg/m^{2}s (30000 lb/hr-ft^2). Results for R-123 show a slightly higher liquid fraction at all heights with the higher heat flux of 31.5 kW/m^2 (10000 Btu/hr-ft^2), but the difference is within the uncertainty. Results for R-134a differ significantly until near the top of the headspace.

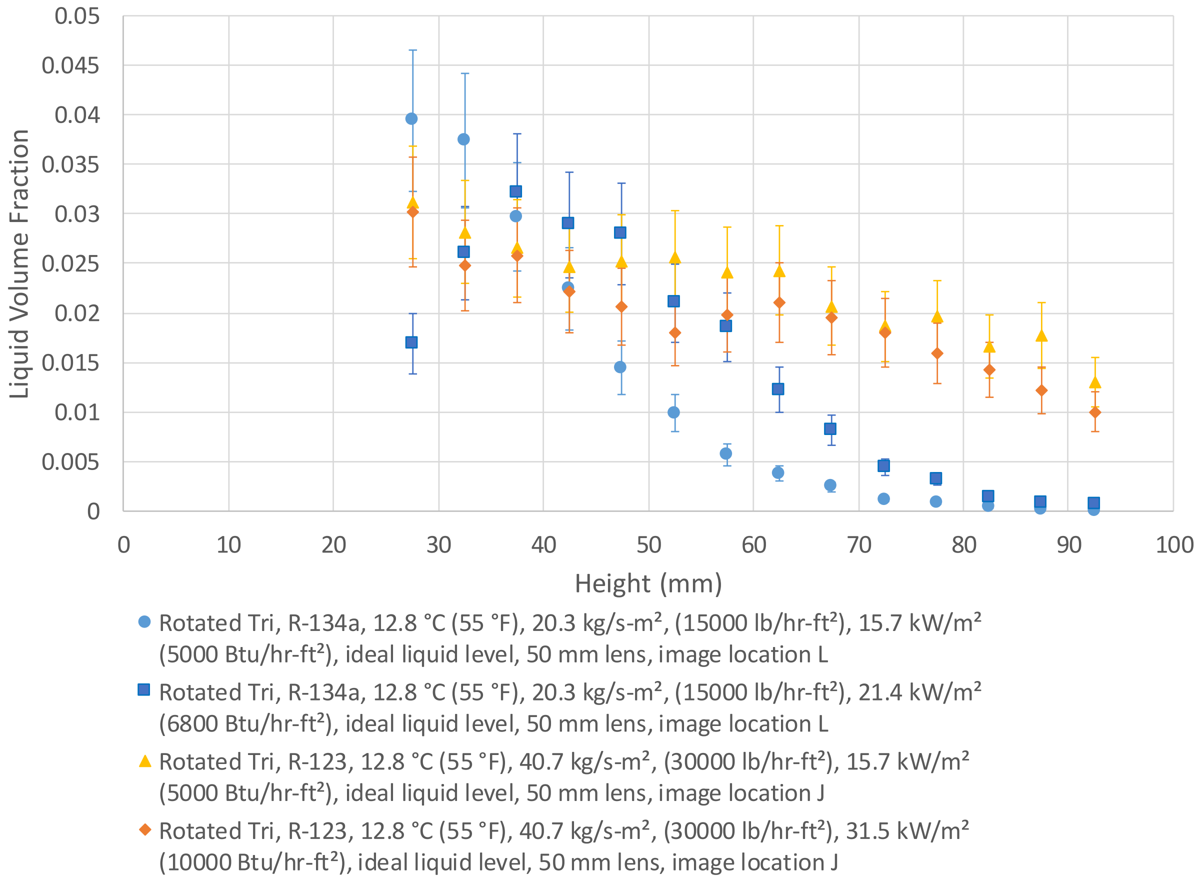

Figure 11.11 Top-rows heat flux variation, liquid volume fraction vs height, rotated triangular bundle

11.5 Bundle Orientation

Figure 11.12 compares bundle orientation for R-134a at two mass fluxes. For both mass fluxes the rotated triangular bundle results in a higher liquid volume fraction, both overall and higher in the headspace. At the higher mass flux of 40.7 kg/m^2-s (30000 lb/hr-ft^2), the rotated triangular bundle actually shows an appreciable liquid fraction at the top of the headspace. The rotated triangular result at the lower mass flux of 20.3 kg/m^2-s (15000 lb/hr-ft^2) is actually higher than for the triangular bundle at the higher mass flux.

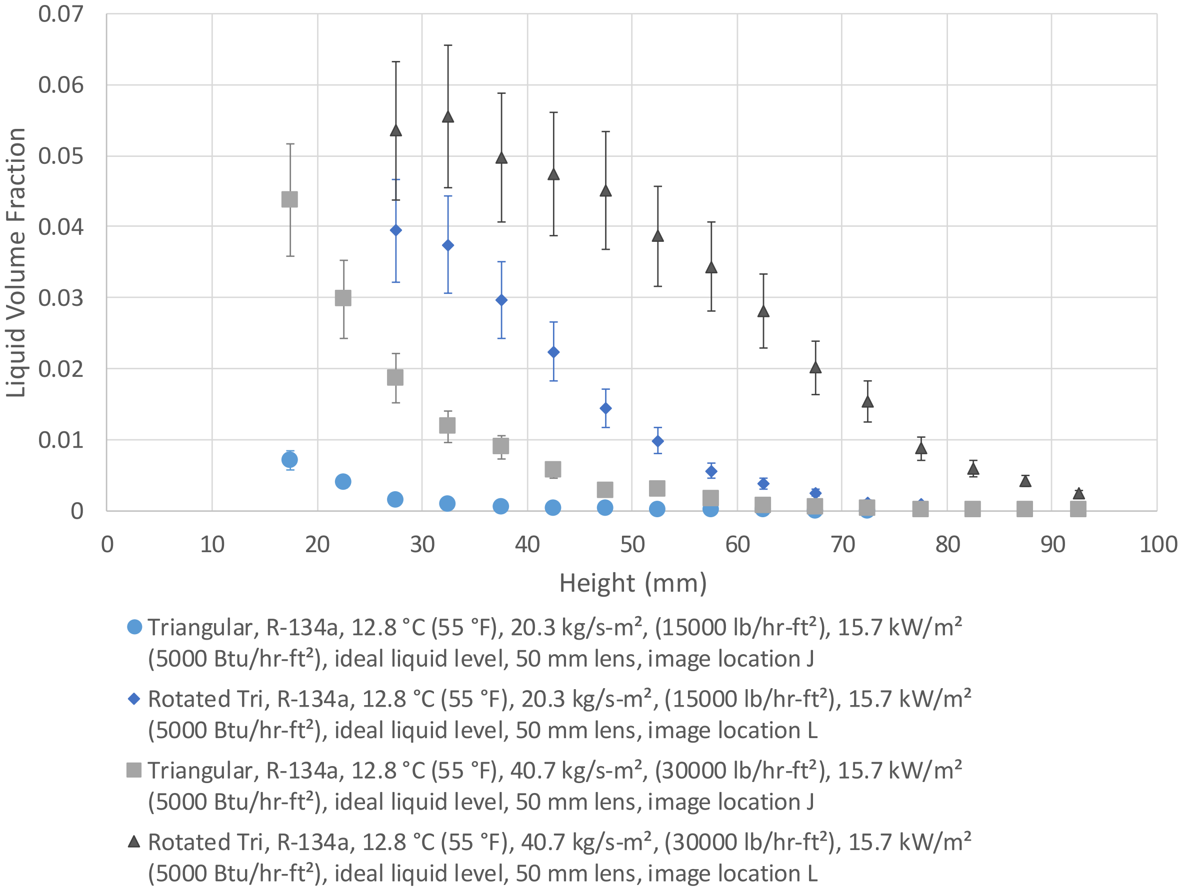

Figure 11.12 Bundle orientation variation, R-134a, liquid volume fraction vs height

A similar result with R-123 is seen in Figure 11.13. While the liquid fraction for the triangular bundle eventually drops off nearly to zero as the top of the headspace is approached, the rotated triangular bundle shows a nearly uniform liquid fraction throughout the headspace. Not only does the liquid fraction not appreciably decrease, but it is also 0.01 to 0.02 higher than the maximum value of 0.03 seen with the triangular bundle. Again, rotated triangular arrangement results in a fountain effect, both throwing more liquid to the sight glass that can affect results as well as a higher droplet density in the center of the bundle.

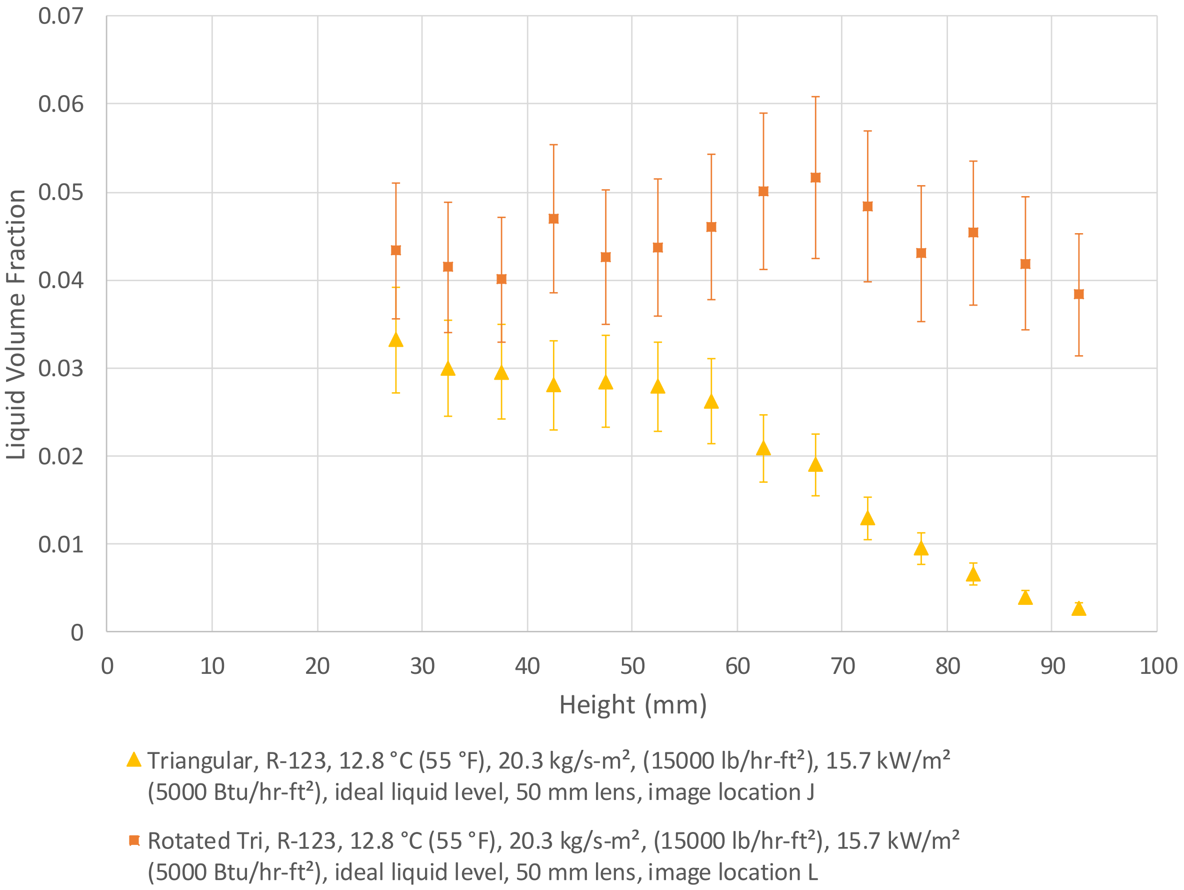

Figure 11.13 Bundle orientation variation, R-123, liquid volume fraction vs height

11.6 Liquid Level

In Figure 11.14 four liquid levels are shown for R-134a at our base condition, ranging from near-dryout to a flooded liquid level approximately 25 mm (1 inch) above the tubes. Little difference is seen between the two flooded conditions, while the ideal liquid level shows a far lower liquid volume fraction. Whereas the flooded results have no liquid by 80 mm above the tubes, the ideal case has done so by 40 mm. The near-dryout level has a liquid fraction even lower than the ideal, but both curves lie atop each other by about 30 mm.

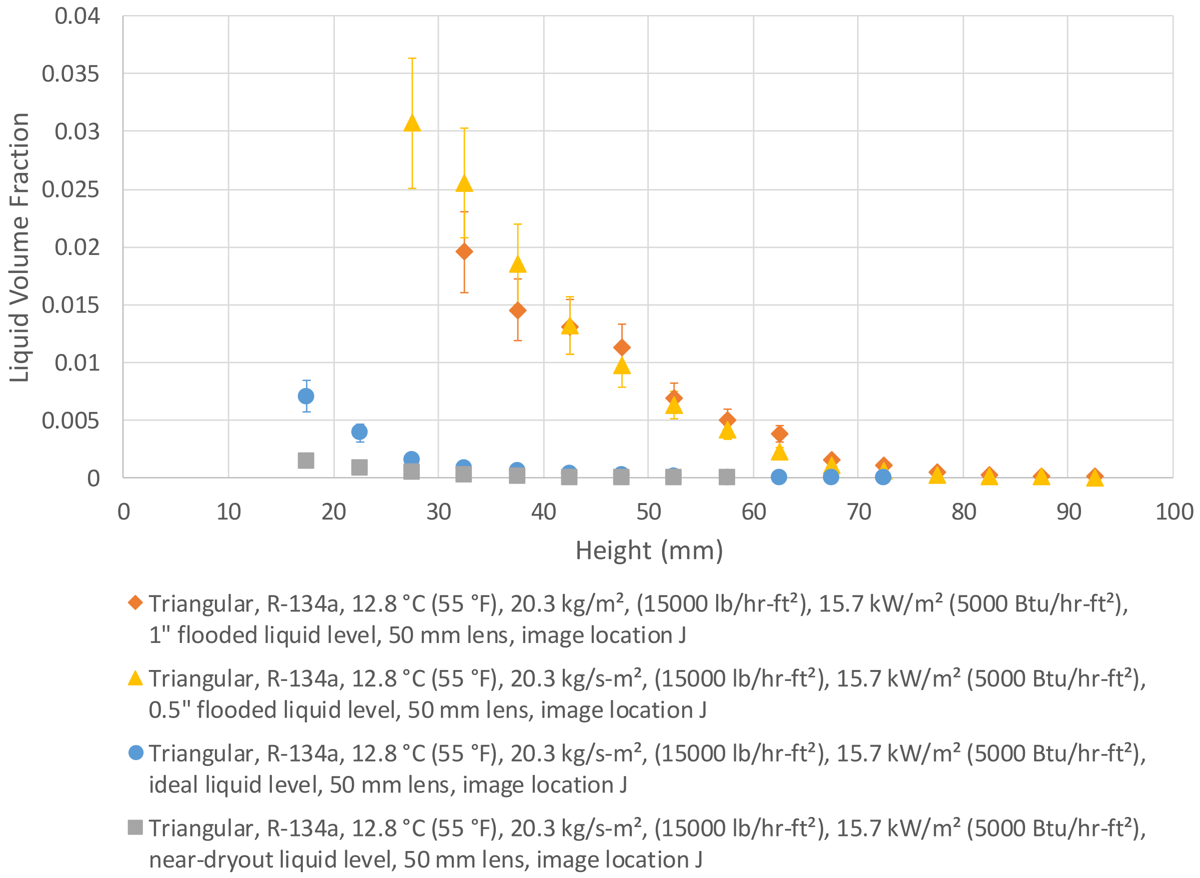

Figure 11.14 Liquid level variation, liquid volume fraction vs height, triangular bundle with R-134a

The effect of liquid level with R-123 for the triangular bundle is shown in Figure 11.15. Recall that with R-123 no real liquid level was seen. Rather, when an apparent droplet density near the tubes was impossible to image through, that was considered the liquid level. The flooded and ideal curves collapse upon each other at approximately 70 mm, indicating that larger droplets have fallen and that primarily droplets are the terminal size or smaller. The dryout level lies even below the ideal level, though even it does not fully drop to zero until approximately 90 mm above the tubes.

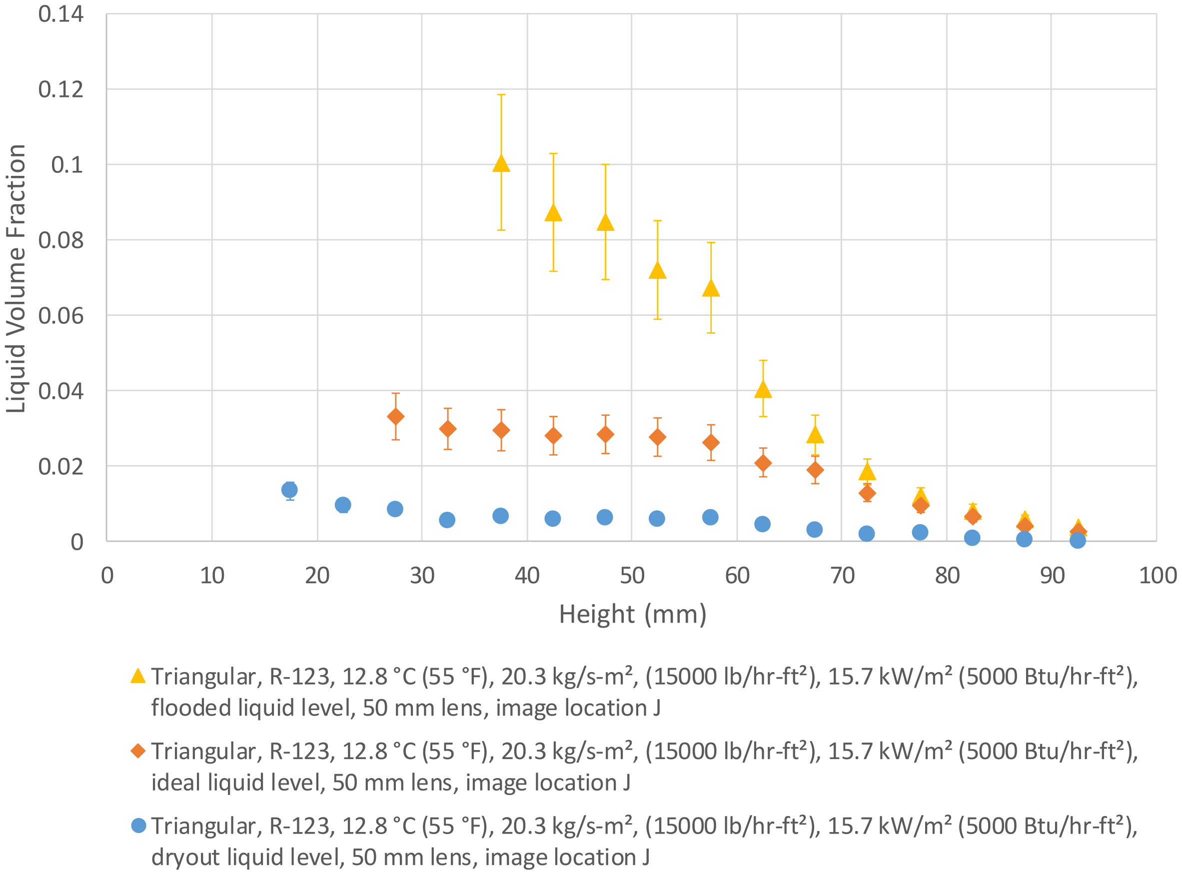

Figure 11.15 Liquid level variation, liquid volume fraction vs height, triangular bundle with R-123

Figure 11.16 compares liquid levels for R-134a with the rotated triangular bundle at a mass flux of 20.3 kg/m^2-s (15000 lb/hr-ft^2). Interestingly, for a liquid volume fraction, the ideal and flooded curves are separated nearly uniformly by a height difference of approximately 13 mm (0.5 inch), half the depth of the pooled liquid defined by the flooded level. Meanwhile, the dryout level barely even registers an appreciable liquid fraction.

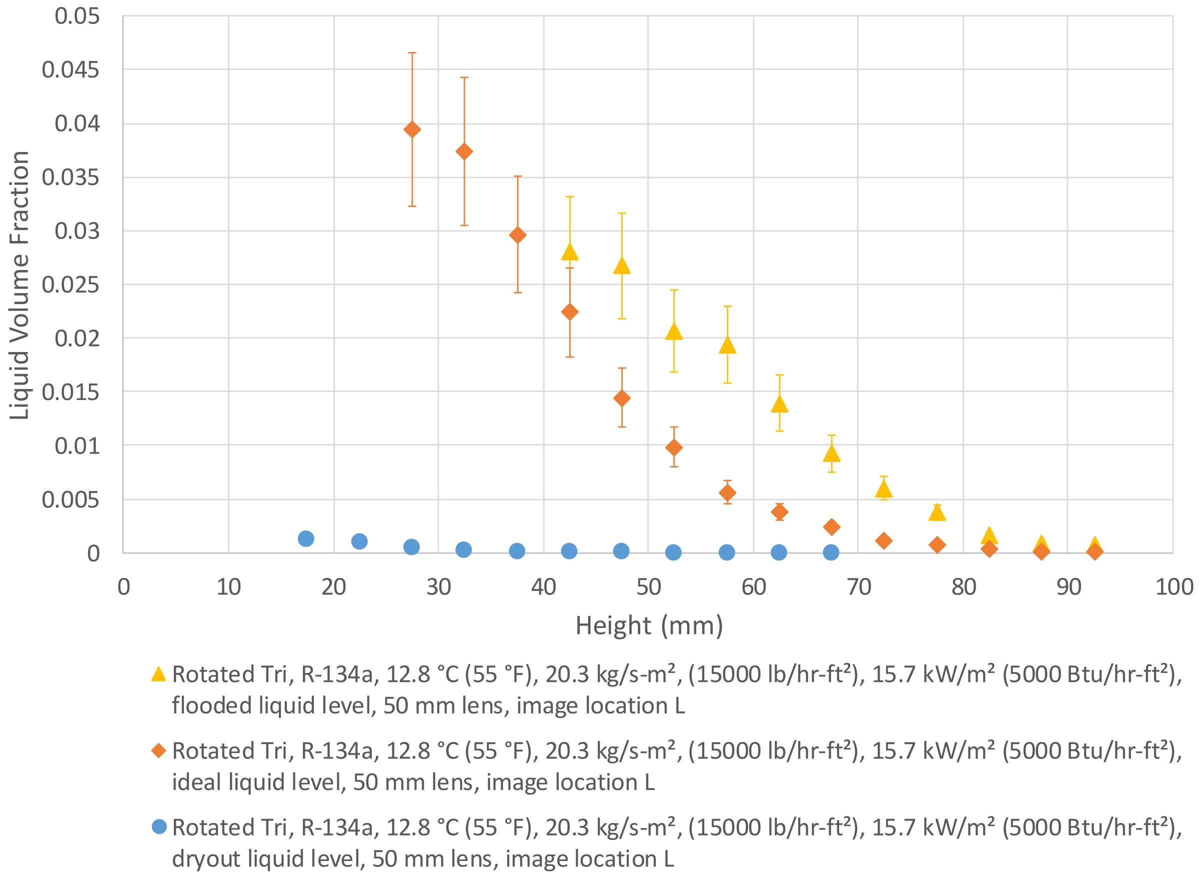

Figure 11.16 Liquid level variation, liquid volume fraction vs height, triangular bundle with R-134a

The effect of liquid level with R-123 and the rotated triangular bundle is shown in Figure 11.17. Recall that the flooded level was discontinued with R-123 as the droplet density was too high to capture images. The liquid fraction throughout the headspace is 4 to 5 times higher for the ideal liquid level than the dryout level. Both show a slight decrease with increasing height and even the dryout level shows liquid persisting to the top of the test section. As both are at the same mass flux, similar headspace velocities and thus terminal droplet diameters would be expected. As the liquid fraction for the dryout condition is much lower, this indicates that the dryout level is creating smaller droplets that are below the headspace terminal droplet size.

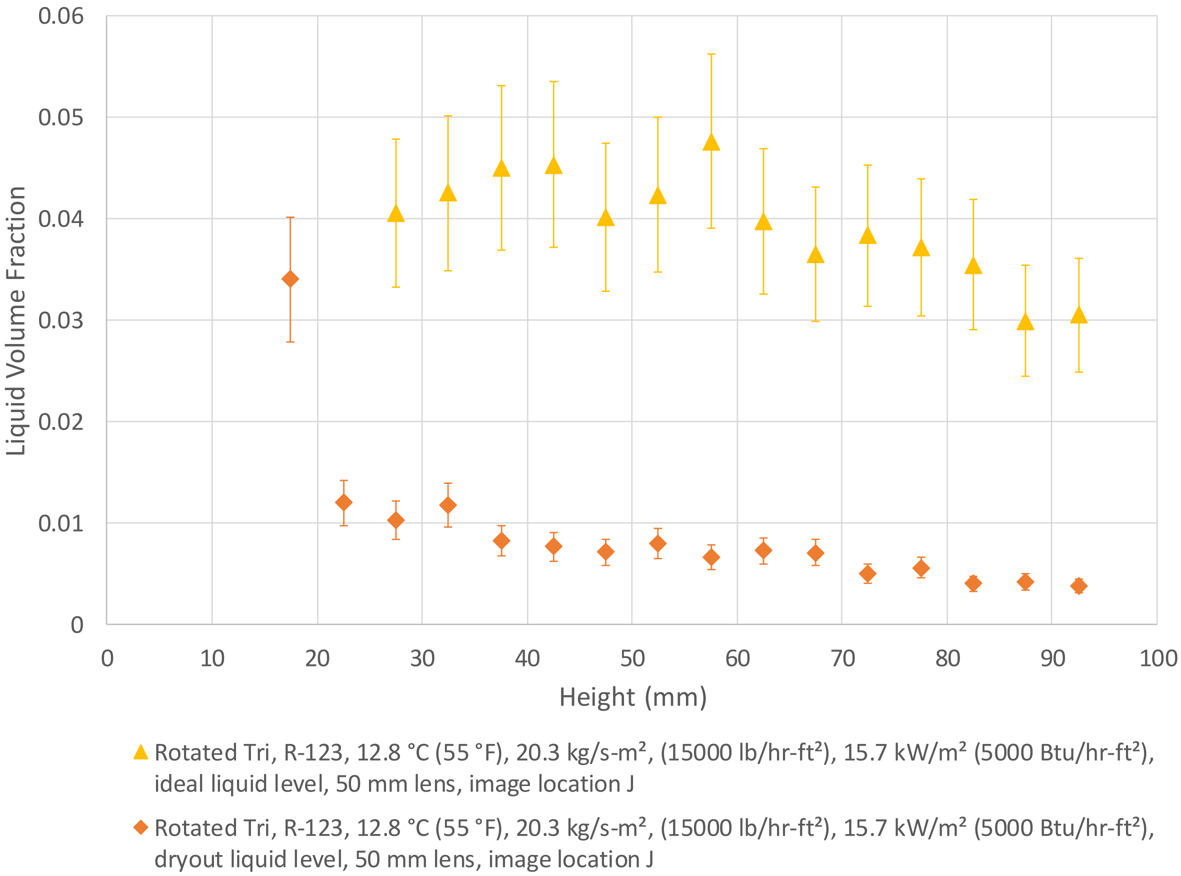

Figure 11.17 Liquid level variation, liquid volume fraction vs height, rotated triangular bundle with R-123

11.7 Refrigerant

The difference between the liquid distributions of R-134a and R-123 are displayed quite evidently in the preceding figures. The differences in liquid and vapor densities between the two refrigerants result in much higher velocities, and thus many more droplets, with R-123 over R-134a. However, it is interesting to compare cases where expected velocities are held constant between the refrigerants.

Figure 11.18 compares R-134a and R-123 at two nearly-matched velocities. For R-134a, the mass flux of 20.3 kg/m^2-s (15000 lb/hr-ft^2) corresponds to an expected between-tube vapor velocity of up to 0.92 m/s, corresponding to R-123 at 3.46 kg/m^2 (2550 lb/hr-ft^2). Likewise, R-

134a at 40.7 kg/m^2-s (30000 lb/hr-ft^2) would have an expected between-tube velocity of 1.84 m/s, corresponding to R-123 at 7.05 kg/m^2 (5200 lb/hr-ft^2). Unfortunately, results for R-123 with the triangular bundle were taken at 10.2 kg/m^2 (7500 lb/hr-ft^2), resulting in an expected vapor velocity of 2.7 m/s.

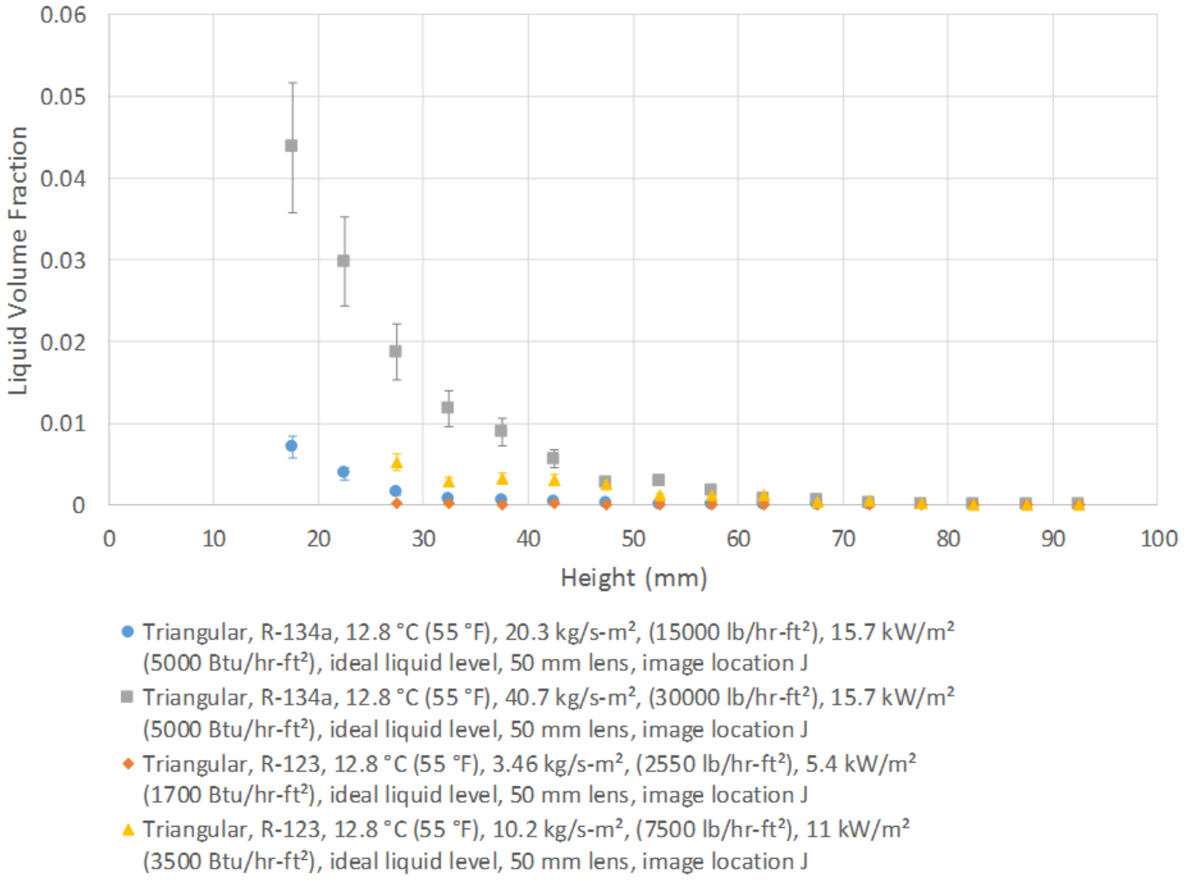

Figure 11.18 Refrigerant variation, matched velocities, liquid volume fraction vs height, triangular bundle

Even with the higher velocity, R-123 in the triangular bundle shows a much lower liquid volume fraction than R-134a a given height and velocity, at least until 50 mm above the tubes. All refrigerant and mass flux combinations result in no liquid by 70 mmm above the tubes, but significant difference is seen lower in the headspace. The difference between refrigerants is largely due to vapor density. For a droplet with a diameter of 100 μm and the same headspace velocity of 0.26 m/s, the drag force is over two times higher and buoyancy force nearly six times higher for R-134a than R-123, while the force of gravity is approximately the same for both refrigerants. The vapor density of R-134a at 12.8 ºC (55 ºF) is nearly six times higher than that of R-123. With the between tube velocity of 1.84 m/s, the drag force is over three times higher for R-134a than R-123. As such, given the same velocity, R-134a can loft larger droplets higher in the headspace.

Similar results are seen with the rotated triangular bundle in Figure 11.19. For this bundle, R-123 and R-134a velocities did match at 1.84 m/s for the higher mass fluxes. R-123 shows much less liquid at both velocities than R-134a. Referring back to Figure 11.4, we see that R-123 has a much lower droplet carrying capacity at the mass fluxes tested.

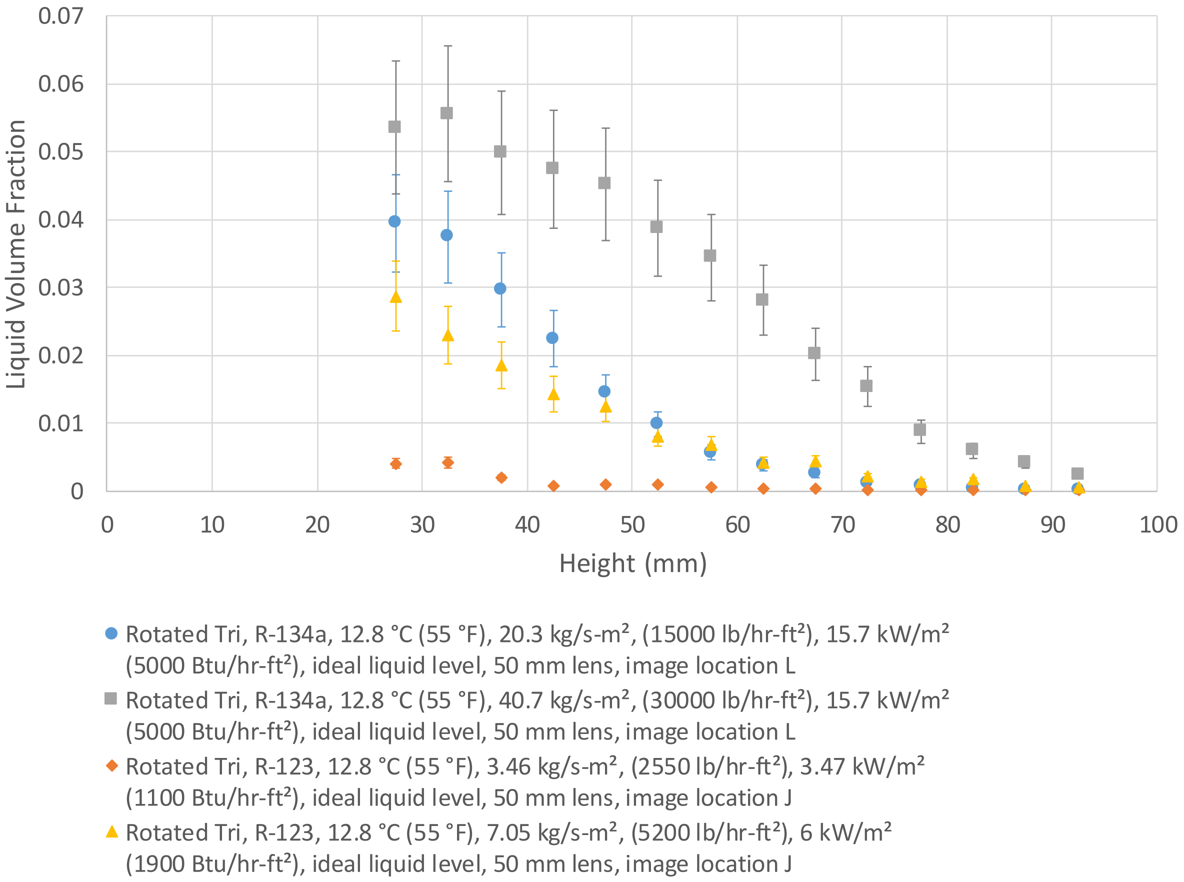

Figure 11.19 Refrigerant variation, matched velocities, liquid volume fraction vs height, rotated triangular bundle

11.8 Summary

All variations tested were shown to have an effect on droplet distribution throughout the headspace. Holding all of our specified variables constant, the choice of refrigerant has the largest impact on distribution, followed by mass flux and bundle orientation. The outlet saturation temperature has an effect similar but generally lesser than mass flux, explained by the effect on refrigerant liquid and vapor densities. Following temperature is heat flux, explained by changing the amount of liquid required at the top of the bundle. Finally, liquid level has a definite impact, but its effect is largely due to changing the eruption point of droplets into the headspace.

Chapter 12 - Numerical Simulation

To complement the experimental results, a section of the bundle was numerically simulated with the aim of finding a numerical method of replicating liquid distribution in the headspace. The flow field was first established by simulating pure vapor. Droplets were then injected as inert particles with Lagrangian particle physics, not influencing the vapor flow. The following sections first describe the models and equations driving the simulation. Next, the setup and results of the vapor simulation are presented. Finally, the setup and results of the droplet simulation are given.

12.1 Numerical Models

Numerous CFD software packages employ many models and methods to simulate flow. For this work, ANSYS Fluent [49] was used. The following sections describe the models and equations used with Fluent to simulate flow.

12.1.1 Single-Phase Vapor Flow

Conservation Equations

In order to simulate flow, the conservation equations are satisfied. According to the Fluent Theory Guide [48], the form of the continuity and conservation of momentum equations used by Fluent take the form

$$\frac{\partial \rho}{\partial t} + \nabla \cdot (\rho \vec{u}) = S_m \tag{12.1}$$

and

$$\frac{\partial}{\partial t}(\rho \vec{u}) + \nabla \cdot (\rho \vec{u} \vec{u}) = -\nabla p + \nabla \cdot (\bar{\bar{\tau}}) + \rho \vec{g} + \vec{F} \tag{12.2}$$

As conditions were modeled as adiabatic, conservation of energy is neglected from the discussion. For (12.1), the partial derivative of density (ρ) with respect to time (t) is related to the divergence ($\nabla \cdot$) of density multiplied by the velocity vector $\vec{u}$. The term on the right (S_m) is a source term for any mass added to the continuous phase, but is unused for this work as the vapor stays single phase. Also, as incompressible flow is assumed, the first term disappears as well. The additional terms of (12.2) include the static pressure (p), stress tensor ($\bar{\bar{\tau}}$), gravitational body force ($\rho\vec{g}$), and external body force ($\vec{F}$). The stress tensor is further given by

$$\bar{\bar{\tau}} = \mu\left[(\nabla\vec{u} + \nabla\vec{u}^T) - \frac{2}{3}\nabla \cdot \vec{u}I\right] \tag{12.3}$$

incorporating viscosity (μ) and the unit tensor (I).

Reynolds-Averaged Navier-Stokes Turbulence Model

The modeling of turbulence is achieved using a Reynolds-averaged Navier-Stokes turbulence model (RANS) combined with the Reynolds Stress model. Reynolds decomposition is used in the RANS model to separate the ensemble-averaged or time-averaged mean and fluctuating components. An example of Reynolds decomposition can be shown by

$$u_x = \bar{u}_x + u'_x \tag{12.4}$$

in which the x-component of velocity (u_x) has been separated into its mean ($\bar{u}_x$) and fluctuating (u'_x) components. The same decomposition can be performed on the other components of velocity as well as scalar properties such as pressure. Substitution of flow variables decomposed in this manner into the continuity equations of (12.1) and (12.2) yields the RANS equations of (12.5) and (12.6) [48].

$$\frac{\partial\rho}{\partial t} + \frac{\partial}{\partial x_i}(\rho\bar{u}_i) = 0 \tag{12.5}$$

$$\frac{\partial}{\partial t}(\rho\bar{u}_i) + \frac{\partial}{\partial x_j}(\rho\bar{u}_i\bar{u}_j) = -\frac{\partial\bar{p}}{\partial x_i} + \frac{\partial}{\partial x_j}\left[\mu\left(\frac{\partial\bar{u}_i}{\partial x_j} + \frac{\partial\bar{u}_j}{\partial x_i} - \frac{2}{3}\delta_{ij}\frac{\partial\bar{u}_i}{\partial x_i}\right)\right] + \frac{\partial}{\partial x_i}\left(-\rho\overline{u'_i u'_j}\right) \tag{12.6}$$

These equations (in Einstein notation form) show the Navier-Stokes equations based on the mean (time- or ensemble-averaged) variables of flow, with the addition of the Reynolds stresses ($\rho\overline{u_i'u_j'}$). A scheme such as the Reynolds Stress Model (RSM) must be used to find the unknown Reynolds stresses and close the Navier-Stokes equations.

Reynolds Stress Model

The Reynolds Stress Model is the most complicated type of RANS turbulence model available for use with Fluent [48], requiring the solving of seven additional transport equations when used in a three-dimensional simulation to find the Reynolds stresses of ($\rho\overline{u_i'u_j'}$). The transport equation for the transport of the Reynolds stresses is given by

$$\frac{\partial}{\partial t}\left(\rho\overline{u_i'u_j'}\right) + C_{ij} = D_{T,ij} + D_{I,ij} + P_{ij} + G_{ij} + \varphi_{ij} + \epsilon_{ij} + F_{ij} + S_{user} \tag{12.7}$$

where terms from left to right are the partial derivative of the Reynolds stresses with respect to time, followed by stresses from convection, turbulent diffusion, molecular diffusion, stress production, buoyancy production, pressure strain, production by system rotation, and stresses from a user-defined function. The description of these terms and the models that define them are described in detail in the Fluent Theory Guide [48]. Note that in implementing the Reynolds stress model, this work used the default ε-based Reynolds stress model using the linear pressure-strain model as well as Enhanced Wall Treatment.

12.1.2 Multi-phase Droplet Flow

Droplets were simulated in Fluent by use of the Euler-Lagrange approach. With this method, the continuous phase (in this work's case being vapor) is solved using the Navier-Stokes equations described in section 12.1.1 while the dispersed phase (in this case being droplets) are solved by tracking the droplets through the vapor flow field [48]. Exchanges of momentum, mass, energy between the phases are possible using this method. Care must be used when applying this method that volume fractions of the dispersed phase are low, typically between 10% to 12%, as Fluent's formulation assumes that particle-particle (droplet-droplet in this case) interactions are negligible. That is not a concern with the current application of the model with R-134a, as liquid volume fractions stay well below the limit. However, examination of R-123 results shows liquid volume fractions at times reaching and exceeding the limit.

Fluent predicts a particle's motion by integrating the force balance on the particle given by

$$\frac{d\vec{u}_p}{dt} = \frac{\vec{u} - \vec{u}_p}{\tau_r} + \frac{\vec{g}(\rho_p - \rho)}{\rho_p} + \vec{F} \qquad \textbf{(12.8)}$$

wherein a particle's inertia is equated to the forces acting upon the particle. Here, $\vec{u}_p$ is the particle velocity, $\vec{u}$ is the fluid velocity as found from Navier-Stokes, τ_r is the particle relaxation time, ρ_p is the density of the particle, $\vec{g}$ is gravitational acceleration, and $\vec{F}$ is an additional acceleration term of the form force/unit particle mass [48]. For this work, no simulation options chosen resulted in the inclusion of any terms to $\vec{F}$. The particle relaxation time is found from

$$\tau_r = \frac{\rho_p d_p^2}{18\mu} \frac{24}{C_{drag} Re} \qquad \textbf{(12.9)}$$

where d_p is the particle diameter, Re the relative Reynolds number, and C_d is the drag coefficient. The relative Reynolds number is defined by

$$Re = \frac{\rho d_p |\vec{u} - \vec{u}_p|}{\mu} \qquad \textbf{(12.10)}$$

and the correlation for the drag coefficient is dependent on the drag law assumed. For this work, particles were assumed to be spherical.

12.2 Vapor Simulation Setup

The vapor simulation was bounded by the test-section walls and restricted to an axial length of 76.9 mm. Features include three rows of tubes and half tubes as well as two pairs of distribution-plate holes (circled) as shown in Figure 5(a). The space above the distribution plate carried the same dimensions as the real test section, but flow was directed axially and narrowed to remove reverse flow at the outlets. The axial flow also simulates conditions that exist above the viewing windows in the physical test section as there, the outlet manifold carries refrigerant away from the test section on either side of the window.

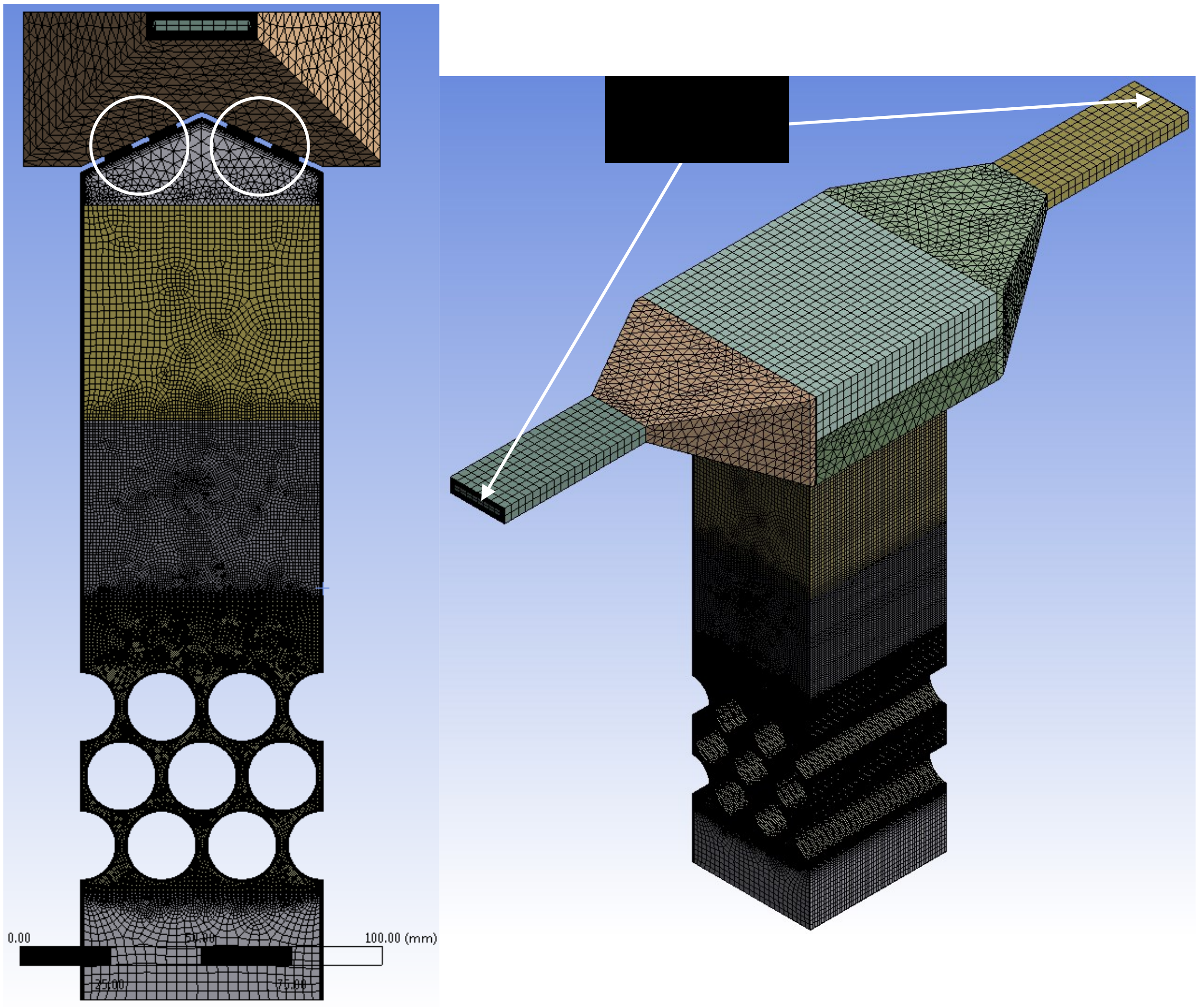

(a) (b)

Figure 12.1: Meshed simulation volume – (a) axial view, (b) isometric view

Views of the meshed volume are shown in Figure 12.1. An inlet region below the tubes with a height of 30 mm was created and set to have a coarse mesh size of 3 mm. The region containing the tubes had a nominal mesh size of 0.5 mm, extending to 20 mm above the top tubes. A size of 0.5 mm was chosen to achieve at least five elements between the opposing inflation layers between tubes once mesh inflation was applied. The region from 20 mm to 70 mm above the top tubes had a mesh size of 1 mm. The region from 70 mm to 130 mm above the top tubes had a mesh size of 2 mm. The preceding meshes were all swept hexahedral meshes, having 40 elements across the axial length of the simulation space. The region following extended to the distribution plate and contained a free mesh consisting of tetrahedral and hexahedral elements of 2-mm size, with a region of influence centered at each distribution- plate hole of a diameter of 5 mm and a mesh size of 0.5 mm. The region above the plates consisted of a mixture of swept and free meshes of sizes from 2 to 4 mm. An inflation of 15 layers and thickness of 0.8 mm was applied to all wall surfaces in the swept regions below the distribution plate while a smooth inflation of 15 layers was applied to all other walls. The resultant mesh contained 3.29e6 elements and 3.66e7 nodes. A grid independence study was performed by progressively doubling the size of elements as previously described, up to a maximum size of 4 mm. The resulting static pressure drops from inlet to outlet are shown in Table 12.1, converging on a pressure drop of 1388 Pa with the two finest meshes

Table 12.1: Pressure drop from inlet to outlet as function of mesh refinement

Number of elements ($x10^5$)	Pressure drop (Pa)
4.8	1263
7.3	1352
15.0	1388
32.9	1388

Mesh quality is further defined by the y+ values in Table 12.2 on the simulation boundaries.

Table 12.2: y+ values of simulation

Tsat	Mass Flux	Tubes			Headspace walls			Above distribution plate		
(°C)	(kg s^{-1} m^{-2})	Min	Max	Mean	Min	Max	Mean	Min	Max	Mean
12.8	20.3	0.01	0.9	0.3	0.01	1.6	0.3	0.1	8.3	1.9
12.8	40.7	0.03	1.6	0.5	0.02	2.8	0.5	0.2	12.8	3.2

A translational periodic boundary condition was applied to the axial surfaces below the distribution plate to simulate a long test section. For separate simulations, mass inflow boundary conditions of 0.0149 and 0.0298 kg s^{-1} were applied to the bottom inlet, corresponding to mass fluxes of 20.3 and 40.7 kg $s^{-1}m^{-2}$, with the properties of the fluid set to those of R-134a at a saturation temperature of 12.78 °C. The axial outlets were set as pressure outlets with a total gauge pressure of 0 kPa while the operating pressure was set to 454 kPa.

Initially run with 2000 iterations at steady-state, the simulation was then switched over to transient. The transient simulation was run using adaptive time-stepping to match the required residuals of 1e-4 for a simulation time of 2 minutes, though no changes beyond the development of the flow field were observed after the first 20 seconds. For the transient simulation the solution methods shown in Table 12.3 were used. In general, settings that promoted stability and accuracy were used instead of those that would have sped simulation.

Table 12.3: Solution Methods Settings

Method	Setting
Pressure-Velocity Coupling Scheme	Coupled
Gradient	Least Squares Cell Based
Pressure	Second Order
Momentum	Second Order Upwind
Turbulent Kinetic Energy	Second Order Upwind
Turbulent Dissipation Rate	Second Order Upwind
Reynolds Stress	Second Order Upwind

12.3 Vapor Simulation Results

The vapor flow patterns within the bundle were found to default to two modes, depending on the method of initialization of the steady-state simulation. The first was as in Figure 12.2

[both (a) and (b)], where one planar jet emerging from between the tubes immediately attaches to the headspace wall while the other two jets immediately merge. Near the top of the headspace, the merged jet combines with the jet attached to the wall. In the other mode observed, all three planar jets emerging from the tubes immediately merged and attached to a wall. Both modes were stable, albeit with small fluctuations, even after several minutes of simulated time. The same two flow patterns were observed at both mass fluxes, albeit with different velocities. The first mode was used for droplet simulation as it was closest to uniform headspace flow as could be achieved.

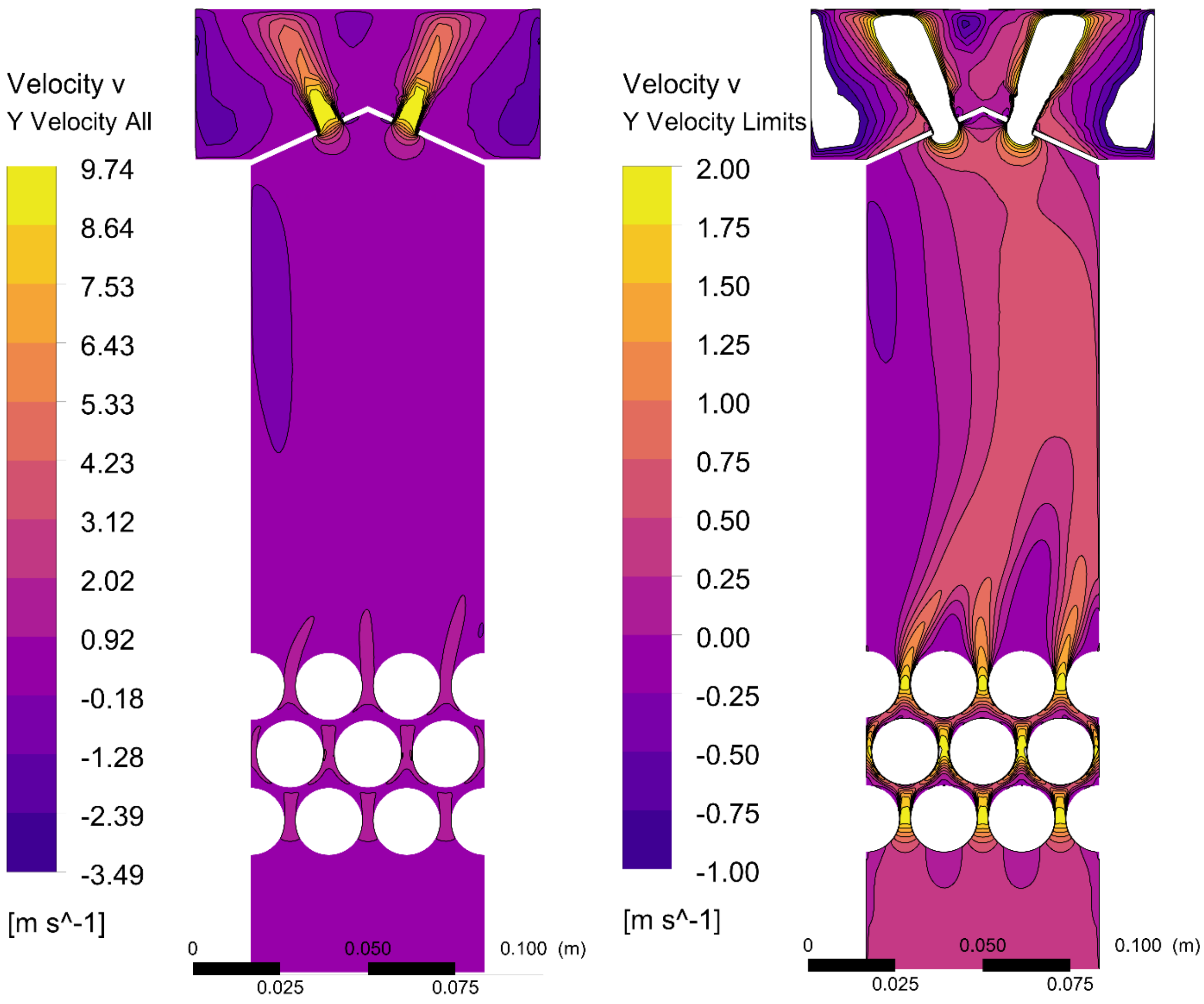

(a) (b)

Figure 12.2: Vertical velocity in x-y plane for 40.7 kg $s^{-1}m^{-2}$ (a) global range (b) constrained range for detail

The highest velocities observed in Figure 12.2 occurred at the holes in the distribution plate, reaching velocities of 9.74 m s^{-1} for the higher mass flux and 4.87 m s^{-1} for the lower mass flux. These velocities were approximately five times higher than the highest velocities observed between the tubes. Large recirculation regions were noted for both mass fluxes within the headspace, seen as the negative velocities (darker colors) on the upper left side of the headspace in Figure 12.2(b). The jets in the headspace exceed 0.5 m s^{-1} from 30 mm above the tubes all the way to the distribution plate, two times higher than the velocity of 0.26 m s^{-1} if flow were uniform. Small perturbations were observed in the axial direction but flow was largely steady. Following the establishment of the flow field, the discrete phase model was enabled to allow simulation of droplets.

12.4 Droplet Simulation Setup

Use of a discrete-phase method for simulating droplet injection requires discretizing a particle mass flow both in velocity and size. For this simulation, a 9 by 9 grid of 81 uniform points 10 mm above the top of the tubes was chosen as the injection site. From each of these points, droplet parcels representing a number (or fraction) of droplets was released, having a specified diameter, velocity, and mass-flow rate, with the number or fraction of droplets per parcel calculated from the mass-flow rate, diameter, and time step [71]. So, with the choice of 50 bins of diameters per 10 velocities, and 81 injection points, 40,500 parcels were injected into the simulation at each time step, with 500 discrete mass-flow rates. The number of diameter bins was chosen to roughly match the size of bins used in the experimental data acquisition. The velocity bin number was chosen to give a reasonable distribution based on measured velocities. In essence, the mass-flow rate of each velocity-diameter combination can be given by (12.11).

$$\dot{m}_{v,d} = \dot{m}_T\left(Y_{v,high} - Y_{v,low}\right)\left(Y_{d.low} - Y_{d,high}\right) \tag{12.11}$$

The variable $\dot{m}_T$ is the total mass flow of all liquid droplets into the simulation, Y_v is the cumulative mass fraction as a function of velocity, Y_d is the cumulative mass fraction as a function of diameter, and subscripts low and high denote the bounds of each bin by diameter or velocity.

The simulation software used allowed for automated discretization of the size distribution. However, discrete velocities had to be set by the user, meaning the parameters of the size distribution had to be set for each chosen velocity. For this simulation, 10 discrete velocities were used and placed at the mean velocity of each bin. The simulation software method for discretizing by size employed the Rosin-Rammler distribution equation, given in (12.12) [71].

$$Y_d = e^{-(d/\bar{d})^n} \qquad \textbf{(12.12)}$$

The variable Y_d is the mass fraction of droplets greater than d, e is Euler's number, d is diameter, $\bar{d}$ is the mean diameter, and n is the spread parameter. The parameters of $\dot{m}_v$, d_{min}, d_{max}, and k had to also be set in the software to make use of the automatic discretization. The parameters d_{min} and d_{max} represent the minimum and maximum diameters of a distribution. Together they definie the bounds of the size distribution as well as bin sizes. The mass-flow rate per velocity, $\dot{m}_v$, could also be described by (12.13):

$$\dot{m}_v = \dot{m}_T\left(Y_{v,high} - Y_{v,low}\right) \qquad \textbf{(12.13)}$$

meaning the mass flow per velocity is calculated based on the total mass flow of liquid and the mass fraction. Altogether, the preceding values define a discrete particle injection. The values used to simulate droplet flow for the 40.7 kg $s^{-1}m^{-2}$ mass flux at 12.8 °C are shown in Table 12.4.

Table 12.4: Injection settings for 40.7 kg $s^{-1}m^{-2}$, $\dot{m}_T$=0.13 kg s^{-1}, 12.8°C

Velocity per bin (m s^{-1})			Mass			Diameter Distribution (N=50)			
Min	Max	Mean (simulation setting)	Cumulative Fraction (Y_v)	Fraction $(Y_{v,high} - Y_{v,low})$	Flow rate ($\dot{m}_v$, kg s^{-1})	d_{min}	$\bar{d}$	d_{max}	n
0.000	0.198	0.099	7.26E-01	7.26E-01	9.43E-02	1.286E-04	2.00E-03	2.76E-03	3.568
0.198	0.395	0.296	9.19E-01	1.94E-01	2.52E-02	1.286E-04	1.54E-03	2.04E-03	3.568
0.395	0.593	0.494	9.75E-01	5.56E-02	7.22E-03	1.286E-04	1.31E-03	1.69E-03	3.568
0.593	0.790	0.691	9.83E-01	8.64E-03	1.12E-03	1.286E-04	1.16E-03	1.47E-03	3.568
0.790	0.987	0.889	9.89E-01	5.23E-03	6.80E-04	1.286E-04	1.05E-03	1.31E-03	3.568
0.987	1.185	1.086	9.92E-01	3.66E-03	4.76E-04	1.286E-04	9.63E-04	1.19E-03	3.568
1.185	1.382	1.284	9.95E-01	2.72E-03	3.54E-04	1.286E-04	8.94E-04	1.10E-03	3.568
1.382	1.580	1.481	9.97E-01	2.11E-03	2.74E-04	1.286E-04	8.37E-04	1.02E-03	3.568
1.580	1.777	1.679	9.99E-01	1.67E-03	2.17E-04	1.286E-04	7.88E-04	9.47E-04	3.568
1.777	1.975	1.876	1.000E+00	1.35E-03	1.76E-04	1.286E-04	7.46E-04	8.89E-04	3.568

With the exception of $\dot{m}_T$, total mass flow of liquid injected, settings of the discrete-phase simulation come from an analysis of the experimental results previously discussed. As discussed in Section 12.5, $\dot{m}_T$ currently must be found by trial and error.

Experimental results from R-134a with a triangular arrangement (Chapter 7) for dryout conditions for both mass fluxes, saturation temperatures, and the highest heat flux were analyzed to determine droplet size and velocity distributions. Dryout conditions were chosen as this is the liquid level at which a pure vapor leaving the tubes is closest to reality. Droplets with a height above the bundle from 5 to 15 mm were binned by velocity and a least-squares fit to the Rosin-Rammler distribution was found per velocity bin. As the simulation involves the injection of particles, only particles with a zero or positive vertical velocity were used for analysis. Results of the analysis are shown in Figure 12.3 are least-squares curve fits. The velocity axis denotes the maximum velocity of each bin.

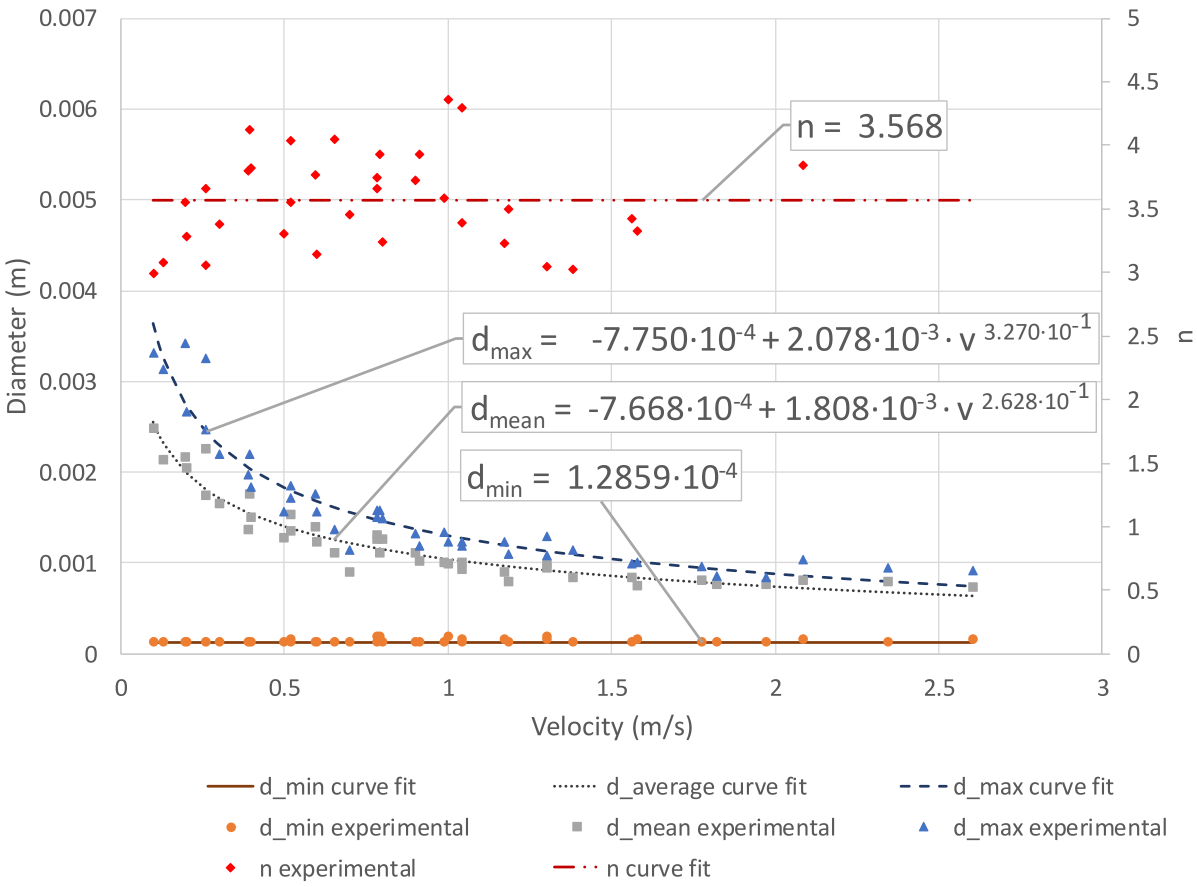

Figure 12.3: Experimental and curve-fit parameters of Rosin-Rammler distribution by velocity, R-134a with triangular arrangement at dryout conditions

Note that d_{min} is a constant (largely constrained by the minimum resolution of the camera and lens) and that n is chosen to be as well (note that n is displayed on the secondary axis on the right). The data for n are randomly distributed at about a value of 3.568. The experimental data for d_{max} and d_{mean} are fit well by a power fit with an offset.

A curve fit to correlate the cumulative mass fraction with velocity was also found using least squares, the equations for which are given in Figure 12.4.

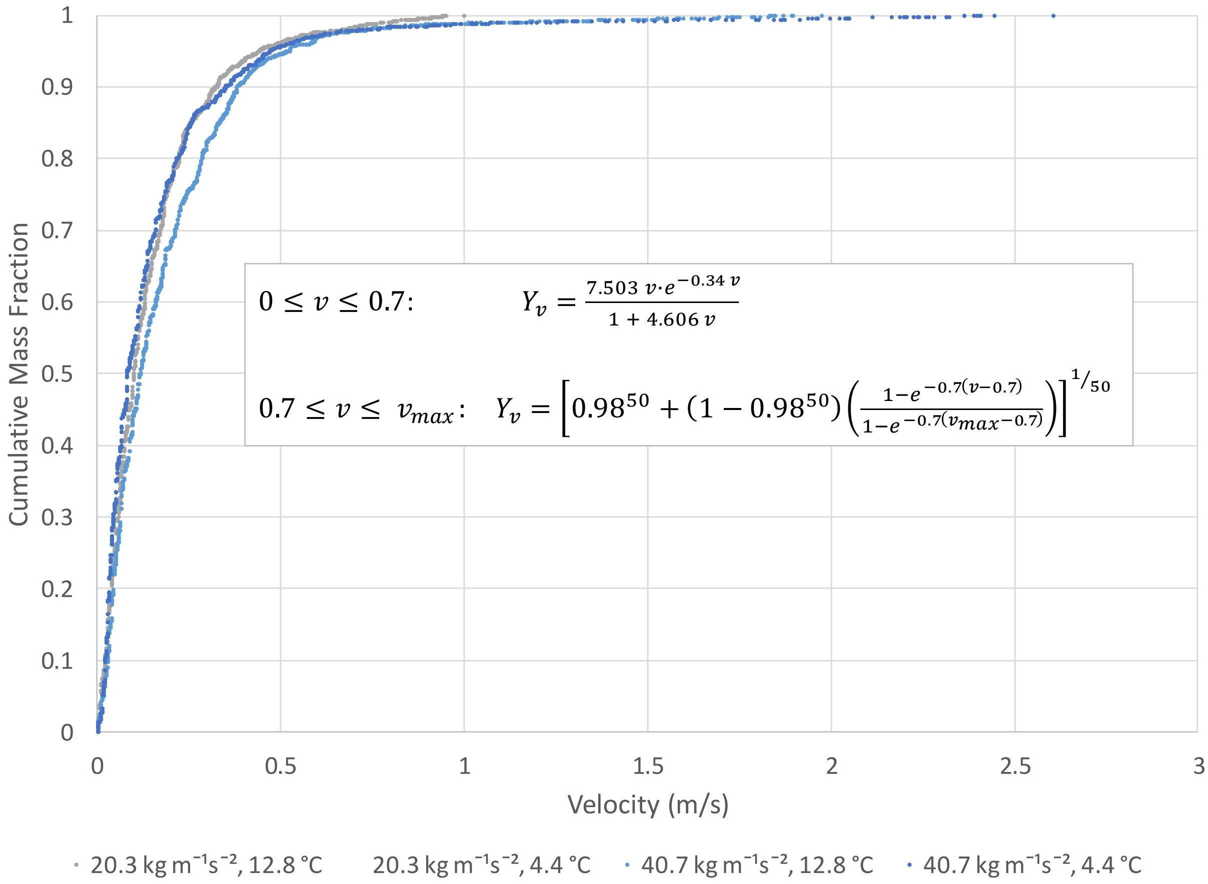

Figure 12.4: Cumulative mass fraction as a function of maximum bin velocity

One curve fit is used to represent the data up to a velocity of 0.7 m s^{-1}, where all experimental data converge on a cumulative mass fraction of 0.98. From a velocity of 0.7 m s^{-1} to v_{max}, a separate curve applies. The term v_{max} denotes the maximum vapor velocity expected for full vapor flow between the tubes and was found from the vapor simulations of Section 12.3. The values of v_{max} are given in Table 12.5.

Table 12.5: v_{max} as function of mass flux and T_{sat}

Mass Flux (kg s^{-1} m^{-2})	Saturation Temp (°C)	v_{max} (m s^{-1})
20.3	12.8	1.00
20.3	4.4	1.30
40.7	12.8	1.97
40.7	4.4	2.61

To complete the simulations, the droplets were given the density of saturated liquid R-134a corresponding to saturation temperature. The walls of the test section below the distribution plate, as well as the tubes, were set to have an “escape” boundary condition for the discrete phase, meaning any droplet that touched the walls was removed from the simulation. The walls above the distribution plate were set to a “reflect” boundary conditions, ensuring any droplets above the distribution plate left through the simulation’s outlets.

The simulation was run with 12 iterations per time step of 0.01 s, resulting in scaled residuals below 1e-03. The rates of mass escaping through the tubes, walls, and outlets were monitored to determine when the headspace had reached a steady-state saturation. The simulation was then run an additional three times the length of time required to reach this saturation.

12.5 Droplet Simulation Results

A 10 mm slice showing an instantaneous droplet parcel distribution is shown in Figure 12.5. The slice is centered on one set of the distribution plate holes. Larger droplets are restricted to the lower portion of the headspace while smaller droplets fill the entirety of the headspace and escape through the distribution plate. Medium sized droplets reach higher on the right side of the simulation than on the left side, corresponding with the recirculation and jetting seen in the vapor simulation in Figure 12.2(b).

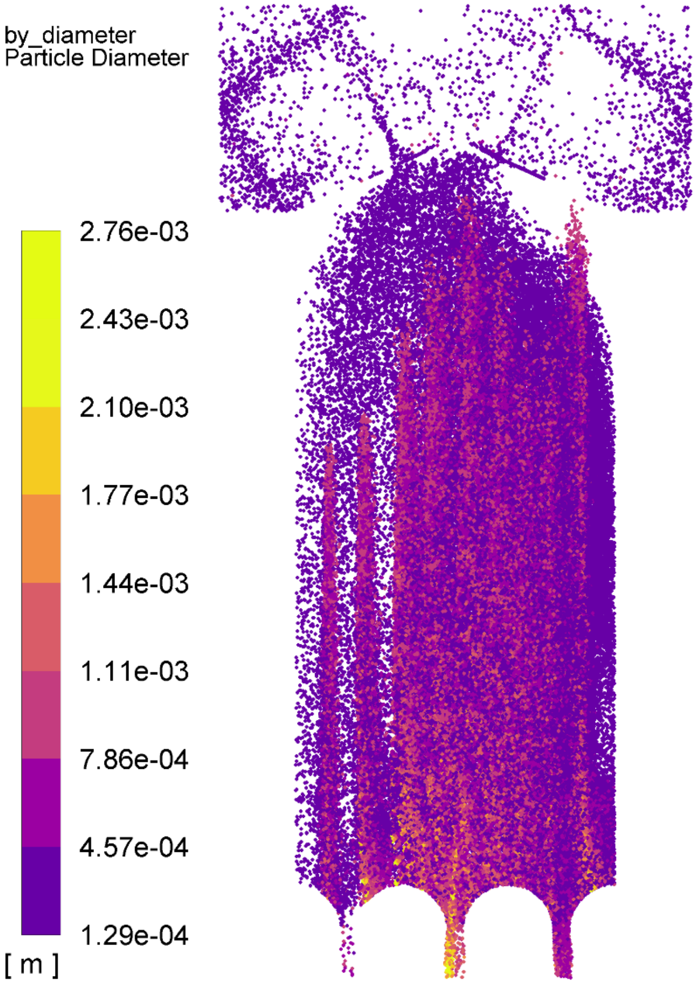

Figure 12.5: Droplet parcel distribution in 10 mm slice, 40.7 kg $s^{-1}m^{-2}$, 12.8°C

The distribution of liquid volume fractions was used to compare the experimental and simulation results. A trial-and-error method was used to determine the total mass-flow rate to be injected such that results matched the experimental results. Figure 12.6 and Figure 12.7 show the comparisons of liquid volume fractions for 12.8 °C at both 20.3 and 40.7 kg s^{-1} m^{-2} for several different simulated mass-flow rates of liquid.

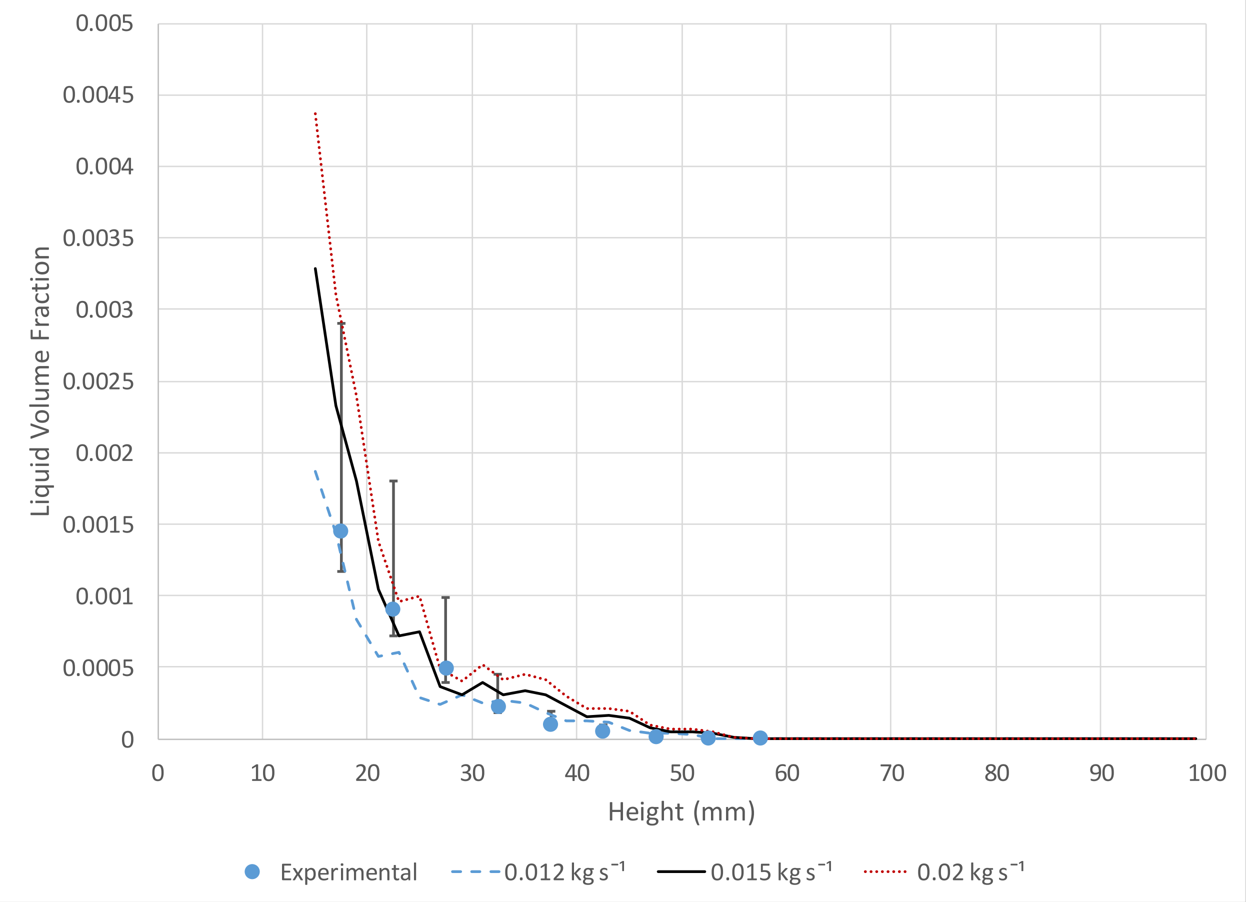

Figure 12.6: Experimental vs simulation liquid volume fraction, 12.8 °C, 20.3 kg s^{-1} m^{-2}

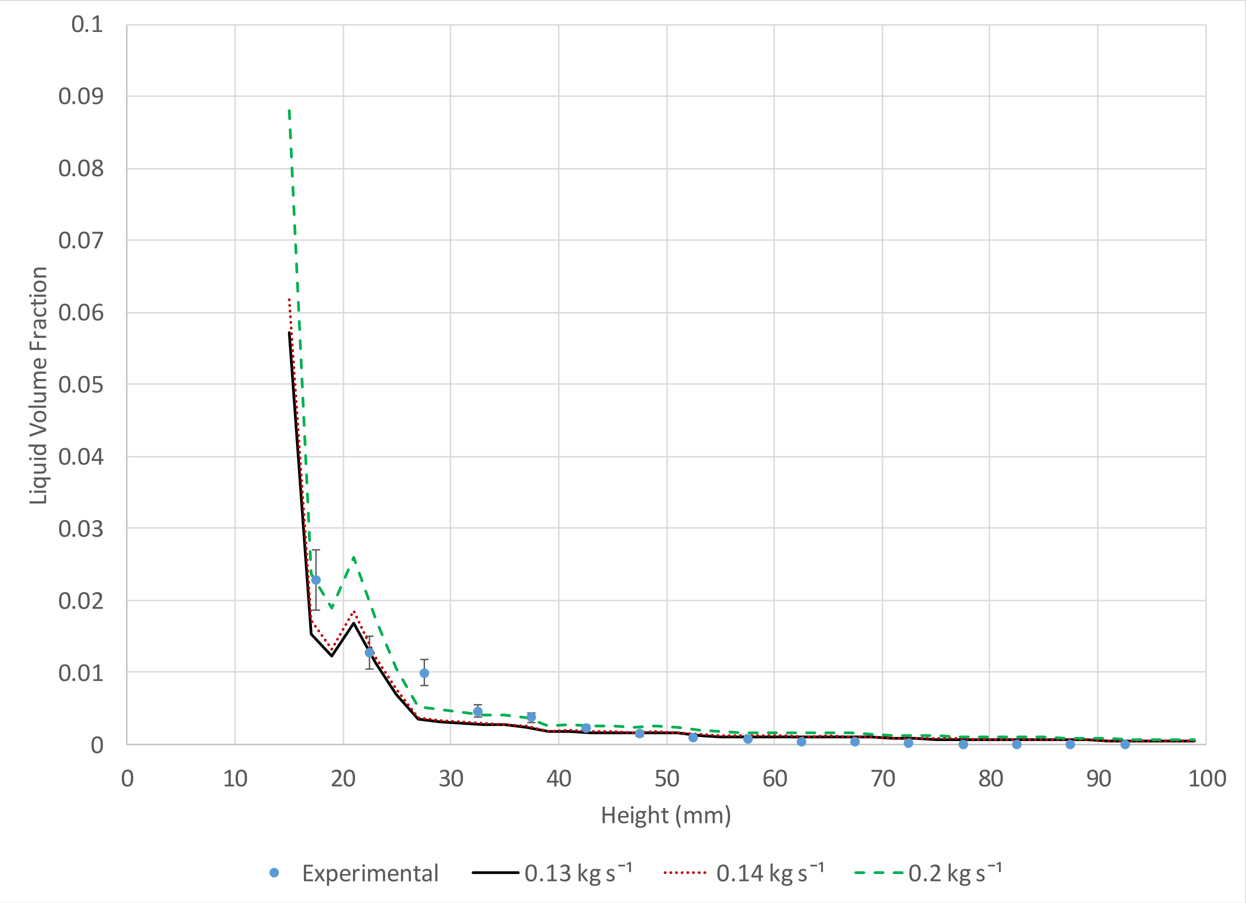

Figure 12.7: Experimental vs simulation liquid volume fraction, 12.8 °C, 40.7 kg s^{-1} m^{-2}

For conditions of 12.8 °C, total liquid-mass-flow injections of 0.015 and 0.2 kg s^{-1} provide a good match between experimental and simulated results. Interestingly, an initially non-intuitive result is that the mass-flow rate of the liquid injected can be much greater than the total vapor and liquid flow being simulated. This can be explained, however, by the differences between the simulation and physical system. In the physical system, droplets that would hit the walls largely collect into a film that flows down the wall back to the tubes, with the liquid being re-entrained. In the simulation, droplets that contact most walls disappear, negating the extra processing needed to handle collision, merging, and droplet breakup. As the intent is to explore both the liquid distribution and how much liquid escapes through the normal path of the distribution plate, the additional mass flow rate is acceptable.

Chapter 13 - Conclusions

The distribution, size, and velocity of liquid droplets emerging from an evaporator tube bundle were characterized for refrigerants R-123 and R-134a with triangular and rotated triangular tube arrangements of pitch 1.167 for a series of mass flux, saturation temperature, heat flux, and liquid level combinations. The tubes used in the study were internally and externally enhanced Wolverine Turbo-ESP with a nominal outer diameter of 19.05 mm (0.75 inch) and a pitch-diameter ratio of 1.167. The two orientations tested were triangular, comprised of 20 active tubes, and rotated triangular, consisting of 24 active tubes. Mass fluxes for R-123 varied from 3.46 kg/m^{2}s (2550 lb/hr-ft^2) to 40.7 kg/m^{2}s (30000 lb/hr-ft^2), while R-134a was tested with mass fluxes of 20.3 kg/m^{2}s (15000 lb/hr-ft^2) and 40.7 kg/m^{2}s (30000 lb/hr-ft^2). Outlet saturation temperatures were held at 4.4 °C (40 °F) and 12.8 °C (55 °F). Heat fluxes varied from 3.47 kw/m^2 (1100 Btu/hr-ft^2) to 31.5 kw/m^2 (10000 Btu/hr-ft^2) and liquid levels varied from dryout to flooded approximately 25 mm (1 inch) above the bundle, both dependent on refrigerant, mass flux, saturation temperature, and bundle orientation.

The volume above the bundle was imaged with a camera and a dual-pulse laser backlight as in conventional shadowgraphy, with commercial software used to recognize and match droplets. A set of 100 image pairs was captured with two different magnification lenses at each image location, with a minimum of three image locations imaged per test condition. The 50 mm focal length lens and 100 mm focal length lens used were capable of resolving with the processing software droplets as small as 114 μm and 51 μm in diameter, respectively. The capture software was set with a limit in diameter up to 4000 μm.

To capture both droplet number and size, a liquid volume fraction was calculated as a function of height. The volume fraction provides a measure of the effect of varying conditions that combines both droplet counts and size distributions.

The results of this work are as follows:

- All variables tested were found to effect droplet distribution in the headspace.
- For a given set of conditions, the choice of refrigerant had the strongest effect. The use of R-123 instead of R-134a results in liquid volume fractions at minimum 12x higher at the top of the headspace, with most tests with R-134a not resulting in any measured liquid volume fraction at the top of the headspace. The much lower liquid volume fractions with R-134a compared with R-123 is due to the very low vapor density of R-123 when compared with R-134a for a given set of conditions.
- Mass flux had the next greatest effect on the liquid volume fraction, though that would be expected as the highest mass flux of 40.7 kg/m^{2}s (30000 lb/hr-ft^2) was double that of the base case of 20.3 kg/m^{2}s (15000 lb/hr-ft^2). Velocity itself was not the only factor, however, as the matched-velocity conditions with R-123 resulted in less liquid in the headspace than with R-134a.
- Outlet saturation temperature followed mass flux in degree of influence on the liquid volume fraction. The 8.4 °C (15 °F) difference in saturation temperatures would be expected to cause a 30% difference in velocities for R-134a and 40% difference in velocities for R-123, similar in effect to a change in mass flux.
- The influence of varying heat flux on the liquid volume fraction was dependent on both refrigerant and bundle orientation. Heat flux’s effect can be explained by

the increased amount of liquid required for a higher heat flux at the top of the bundle. Both the rotated triangular orientation and use of R-123 result in locally higher velocities that can launch the additional liquid further at a higher heat flux.

- Liquid level did influence the volume fraction distribution as a function of height, but its magnitude can be explained by changing the eruption point of droplets into the headspace. Meaning, a shift in liquid level results in the same maximum liquid volume fraction, but simply shifts that point higher in the headspace.
- Determination of a liquid level is difficult through means other than a visual inspection. The only point possible to determine with certainty is the onset of dryout where an abrupt decrease in top row heat flux is seen.
- For all but the lower mass flux R-134a tests and the matched-velocity R-123 tests, a constant-area headspace with a height of 100 mm is not sufficient to separate droplets from the flow. Even the inclusion of the distribution plate 40 mm above the top of the viewing area was not sufficient to eliminate all liquid escaping the test section, apparent in the low thermodynamic exit qualities seen with R-123 at the higher mass flux.
- An area expansion above the tube bundle would lower vapor velocities further, decreasing the carrying capacity of vapor. There exists for any vapor velocity some droplet small enough to be carried out, provided the droplet is generated.
- Larger droplets can be carried out of the test section by momentum alone. Vanes, screens, and plates are possible measures to counter these droplets.
- An induced pressure drop may eliminate any remaining droplets in the flow by boiling off any remaining liquid.

Should replication of this study occur, a suggestion would be to improve viewing conditions. These may include but are not limited to flowing vapor across the inner surface of the sight glass, heating the sight glass, and determining a method to image from the end instead of the sides.

In addition to the experimental work, the numerical method presented shows promise for assisting in the design of an evaporator headspace. Though it has only been correlated for changes in velocity (through mass flux and saturation temperature), an expansion of correlations involving liquid level and bundle arrangement could advance this work. Components and parameters such as the distribution plate dimensions, tube-gap sizes, and liquid level settings could all be varied with the simulation to define an optimal headspace.

Further studies into the behavior of droplets in the headspace could include the effect of pitch-diameter ratio which would vary the ejection velocity of droplets from the bundle. Another study that would be beneficial would be to increase the size of the imaging headspace above the bundle. A headspace of 100 mm was not sufficient to see the separation of larger droplets from terminal droplets. As stated previously, there exists for any headspace vapor velocity some droplet small enough to be carried out, provided the droplet is generated. Imaging the headspace sufficiently far above the tube bundle with sufficient magnification would allow for determination of whether these droplets exist for certain. Comparisons of the project’s results with computational simulations of the bundle and headspace would allow for validation of models used in CFD. Further advancement in the CFD method presented could be undertaken. Finally, the exploration of the effects of separation strategies such as vanes, screens, or expansion of the headspace with height would help to understand the relative effectiveness of these strategies.

References

[1] Asher, W., and Eckels, S., 2018, "RP-1556 -- Characterization of Liquid Refrigerant Flow Emerging from a Flooded Evaporator Tube Bundle," ASHRAE, ed.Atlanta, GA.

[2] Elson, J., and Eckels, S., 2015, "An objective method for screening and selecting personal cooling systems based on cooling properties," Applied Ergonomics, **48**, pp. 33-41.

[3] Elson, J., and Eckels, S., 2018, "Contribution of wetted clothing to body energy exchange and heat stress," Journal of Thermal Biology.

[4] Elson, J. C., McCullough, E. A., and Eckels, S., 2013, "Evaluation of personal cooling systems for military use," International Conference on Environmental Ergonomics (ICEE), S. J. L. a. T. M. James D Cotter, ed.Queenstown, New Zealand, p. 280.

[5] McCullough, E. A., and Eckels, S., 2008, "Evaluation of Personal Cooling Systems for Soldiers Using a Human Subjects," *International Textile and Apparel Association (ITAA) Proceedings*.

[6] McCullough, E. A., Eckels, S., and Harms, C., 2009, "Determining temperature ratings for children's cold weather clothing," Applied Ergonomics, **40**(5), pp. 870-877.

[7] McCullough, E. A., Eckels, S., and Schlabach, M., 2008, "Evaluation of Personal Cooling Systems for Soldiers Using a Sweating Manikin," *International Textile and Apparel Association (ITAA) Proceedings*.

[8] Schlabach, M., McCullough, E. A., and Eckels, S. J., 2018, "Determining temperature ratings for children's sleeping bags," International Journal of Industrial Ergonomics, **65**, pp. 153-160.

[9] Asher, W., 2014, "Fluid Dynamics of Cavitating Sonic Two-Phase Flow in a Converging-Diverging Nozzle," Masters, Kansas State Unversity.

[10] Asher, W., and Eckels, S. J., 2018, "Characterization of liquid refrigerant R-123 flow emerging from a flooded evaporator tube bundle," Sc. Tech. Built Environ., pp. 1-13.

[11] Asher, W. E., and Eckels, S. J., 2015, "Analysis of Cavitating High Speed Liquid Flow Through a Converging-Diverging Nozzle," *ASME 2015 (IMECE2015-52060)*, ASME, pp. V07AT09A006-V007AT009A006.

[12] Gorgy, E., 2011, "Experimental evaluation of heat transfer impacts of tube pitch on highly enhanced surface tube bundle."

[13] Gorgy, E., and Eckels, S., 2013, "Convective boiling of R-134a and R-123 on an enhanced tube bundle with standard pitch, RP-1316," HVAC&R Research, **19**(2), pp. 193-206.

[14] Gorgy, E., and Eckels, S., 2016, "Convective boiling of R-134a on enhanced-tube bundles," International Journal of Refrigeration, **68**, pp. 145-160.

[15] Gorgy, E., and Eckels, S., 2019, "Convective Boiling of R-123 on Enhanced-Tube Bundles," International Journal of Heat and Mass Transfer.

[16] Gorgy, E., and Eckels, S., 2010, "Average heat transfer coefficient for pool boiling of R-134a and R-123 on smooth and enhanced tubes (RP-1316)," HVAC&R Research, **16**(5), pp. 657-676.

[17] Gorgy, E., and Eckels, S., 2012, "Local heat transfer coefficient for pool boiling of R-134a and R-123 on smooth and enhanced tubes," International Journal of Heat and Mass Transfer, **55**(11), pp. 3021-3028.

[18] Li, P., Eckels, S. J., Mann, G. W., and Zhang, N., 2018, "A Method of Measuring Turbulent Flow Structures With Particle Image Velocimetry and Incorporating Into Boundary Conditions of Large Eddy Simulations," Journal of Fluids Engineering, **140**(7), pp. 071401-071401-071411.

[19] Li, P. E., Steven; Mann, Garrett; Zhang, Ning, 2014, "Experimental Measurements in Near-Wall Regions by Particle Image Velocimetry (PIV)," FEDSM2014-21918. 4th Joint US-European Fluids EngineeringChicago IL.

[20] Mann, G., Madamadakala, G., and Eckels, S., 2016, "Heat transfer characteristics of R-134a in a converging-Diverging nozzle," International Journal of Heat and Fluid Flow, **62**, pp. 464-473.

[21] Mann, G. W., and Eckels, S., 2019, "Multi-objective heat transfer optimization of 2D helical micro-fins using NSGA-II," International Journal of Heat and Mass Transfer, **132**, pp. 1250-1261.

[22] Van Rooyen, E., and Thome, J. R., 2014, "Flow boiling data and prediction method for enhanced boiling tubes and tube bundles with R-134a and R-236fa including a comparison with falling film evaporation," International Journal of Refrigeration, **41**, pp. 60-71.

[23] Van Rooyen, E., and Thome, J. R., 2013, "Pressure drop data and prediction method for enhanced external boiling tube bundles with R-134a and R-236fa," International Journal of Refrigeration, **36**(6), pp. 1669-1680.

[24] Robinson, D. M., and Thome, J. R., 2004, "Local bundle boiling heat transfer coefficients on a turbo-BII HP tube bundle (RP-1089)," HVAC and R Research, **10**(4), pp. 441-457.

[25] Ribatski, G., Saiz Jabardo, J. M., and da Silva, E. F., 2008, "Modeling and experimental study of nucleate boiling on a vertical array of horizontal plain tubes," Exp. Therm. Fluid Sci., **32**(8), pp. 1530-1537.

[26] Kondo, M., 1984, "Experimental Investigation of Air-Water Two-Phase Upflow across Horizontal Tube Bundles : Part II, Pressure Drop," Bulletin of JSME, **27**(230), pp. 1616-1624.

[27] van Rooyen, E., Agostini, F., Borhani, N., and Thome, J. R., 2012, "Boiling on a tube bundle: Part I --Flow visualization and onset of dryout," Heat Transfer Engineering, **33**(11), pp. 913 - 929.

[28] Schlup, J., and Eckels, S., 2017, "Two phase flow visualization in evaporator tube bundles using experimental and numerical techniques," 2nd Thermal and Fluids Engineering Conference and 4th International Workshop on Heat Transfer, ASFTE, Las Vegas.

[29] Kanizawa, F. T., and Ribatski, G., 2016, "Two-phase flow patterns across triangular tube bundles for air-water upward flow," International Journal of Multiphase Flow, **80**, pp. 43-56.

[30] Cheng, L., Ribatski, G., and Thome, J. R., 2008, "Two-phase flow patterns and flow-pattern maps: Fundamentals and applications," Appl Mech Rev, **61**(1-6), pp. 0508021-05080228.

[31] Grant, I. D. R., and Chisholm, D., 1979, "TWO-PHASE FLOW ON THE SHELL-SIDE OF A SEGMENTALLY BAFFLED SHELL-AND-TUBE HEAT EXCHANGER," J Heat Transfer Trans ASME, **101**(1), pp. 38-42.

[32] Ulbrich, R., and Mewes, D., 1994, "Vertical, upward gas-liquid two-phase flow across a tube bundle," International Journal of Multiphase Flow, **20**(2), pp. 249-272.

[33] Kondo, M., and Nakajima, K.-i., 1980, "Experimental investigation of air-water two phase upflow across horizontal tube bundles - 1. flow pattern and void fraction," Bulletin of the JSME, **23**(177), pp. 385-393.

[34] Dai, Z., Chou, W. H., and Faeth, G. M., 1998, "Drop formation due to turbulent primary breakup at the free surface of plane liquid wall jets," Physics of Fluids, **10**(5), pp. 1147-1157.

[35] Hay, K. J., Liu, Z. C., and Hanratty, T. J., 1998, "A backlighted imaging technique for particle size measurements in two-phase flows," Experiments in Fluids, **25**(3), pp. 226-232.

[36] Patruno, L. E., Marchioro Ystad, P. A., Marchetti, J. M., Dorao, C. A., Svendsen, H. F., and Jakobsen, H. A., 2010, "Liquid entrainment from a wetted wire exposed to a high gas flow rate in cross flow," Chemical Engineering Science, **65**(24), pp. 6397-6406.

[37] Castrejón-García, R., Castrejón-Pita, J. R., Martin, G. D., and Hutchings, I. M., 2011, "The shadowgraph imaging technique and its modern application to fluid jets and drops," Revista Mexicana de Fisica, **57**(3), pp. 266-275.

[38] Blaisot, J. B., and Yon, J., 2005, "Droplet size and morphology characterization for dense sprays by image processing: application to the Diesel spray," Experiments in Fluids, **39**(6), pp. 977-994.

[39] Kashdan, J. T., Shrimpton, J. S., and Whybrew, A., 2003, "Two-phase flow characterization by automated digital image analysis. Part 1: Fundamental principles and calibration of the technique," Particle and Particle Systems Characterization, **20**(6), pp. 387-397.

[40] Kashdan, J. T., Shrimpton, J. S., and Whybrew, A., 2004, "Two-Phase Flow Characterization by Automated Digital Image Analysis. Part 2: Application of PDIA for Sizing Sprays," Particle & Particle Systems Characterization, **21**(1), pp. 15-23.

[41] Legrand, M., Nogueira, J., Lecuona, A., and Hernando, A., 2016, "Single camera volumetric shadowgraphy system for simultaneous droplet sizing and depth location, including empirical determination of the effective optical aperture," Exp. Therm. Fluid Sci., **76**, pp. 135-145.

[42] Ahmadpour, A., Noori Rahim Abadi, S. M. A., and Meyer, J. P., 2018, "Numerical investigation of pool boiling on a staggered tube bundle for different working fluids," International Journal of Multiphase Flow, **104**, pp. 89-102.

[43] Gupta, A., 2005, "Enhancement of boiling heat transfer in a 5×3 tube bundle," International Journal of Heat and Mass Transfer, **48**(18), pp. 3763-3772.

[44] Jung, D., Kim, Y., Ko, Y., and Song, K., 2003, "Nucleate boiling heat transfer coefficients of pure halogenated refrigerants," International Journal of Refrigeration, **26**(2), pp. 240-248.

[45] Kang, M.-G., 2016, "Pool boiling heat transfer from an inclined tube bundle," International Journal of Heat and Mass Transfer, **101**, pp. 445-451.

[46] Minocha, N., Joshi, J. B., Nayak, A. K., and Vijayan, P. K., 2016, "3D CFD simulation of passive decay heat removal system under boiling conditions: Role of bubble sliding motion on inclined heated tubes," Chemical Engineering Science, **145**, pp. 245-265.

[47] Asher, W., and Eckels, S. J., submitted 2019, "Characterization and numerical simulation of liquid refrigerant R-134a flow emerging from a flooded evaporator tube bundle," International Journal of Refrigeration.

[48] 2017, "ANSYS® Fluent Theory Guide, Release 18.2," ANSYS, Inc., Canonsburg, PA.

[49] 2017, "ANSYS® Fluent, Release 18.2," ANSYS, Inc., Canonsburg, PA.

[50] Bagul, R. K., Pilkhwal, D. S., Vijayan, P. K., and Joshi, J. B., 2018, "Air Water Loop for investigation of flow dynamics in a steam drum: Carryover experiments and CFD simulation," Nucl Eng Des, **333**, pp. 145-160.

[51] Beetham, S., and Capecelatro, J., 2019, "Biomass pyrolysis in fully-developed turbulent riser flow," Renewable energy, **140**, pp. 751-760.

[52] Behjat, Y., Shahhosseini, S., and Marvast, M. A., 2010, "Modeling gas oil spray coalescence and vaporization in gas solid riser reactor," International communications in heat and mass transfer, **37**(7), pp. 935-943.

[53] Ghaffarkhah, A., Dijvejin, Z. A., Shahrabi, M. A., Moraveji, M. K., and Mostofi, M., 2019, "Coupling of CFD and semiempirical methods for designing three-phase condensate separator: case study and experimental validation," Journal of petroleum exploration and production technology., **9**(1), pp. 353-382.

[54] Hua, J., 2015, "CFD simulations of the effects of small dispersed bubbles on the rising of a single large bubble in 2D vertical channels," Chemical Engineering Science, **123**, pp. 99-115.

[55] Jiang, X., Siamas, G. A., Jagus, K., and Karayiannis, T. G., 2010, "Physical modelling and advanced simulations of gas–liquid two-phase jet flows in atomization and sprays," Progress in Energy and Combustion Science, **36**(2), pp. 131-167.

[56] Laleh, A. P., Svrcek, W. Y., and Monnery, W., 2012, "Design and CFD studies of multiphase separators - a review," The Canadian journal of chemical engineering, **90**(6), pp. 1547-1561.

[57] Laleh, A. P., Svrcek, W. Y., and Monnery, W., 2013, "Computational Fluid Dynamics-Based Study of an Oilfield Separator--Part II: An Optimum Design," SPE-161036-PA, **2**(01), pp. 52-59.

[58] Mancini, M., Alberti, M., Dammann, M., Santo, U., Eckel, G., Kolb, T., and Weber, R., 2018, "Entrained flow gasification. Part 2: Mathematical modeling of the gasifier using RANS method," Fuel, **225**, pp. 596-611.

[59] Rafee, R., Rahimzadeh, H., and Ahmadi, G., 2010, "Numerical simulations of airflow and droplet transport in a wave-plate mist eliminator," Chemical Engineering Research and Design, **88**(10), pp. 1393-1404.

[60] Sardina, G., Jareteg, K., Ström, H., and Sasic, S., 2019, "Assessing the ability of the Eulerian-Eulerian and the Eulerian-Lagrangian frameworks to capture meso-scale dynamics in bubbly flows," Chemical engineering science, **201**, pp. 58-73.

[61] Ström, H., Lundström, A., and Andersson, B., 2009, "Choice of urea-spray models in CFD simulations of urea-SCR systems," Chemical engineering journal, **150**(1), pp. 69-82.

[62] Torfeh, S., and Kouhikamali, R., 2015, "Numerical investigation of mist flow regime in a vertical tube," International Journal of Thermal Sciences, **95**, pp. 1-8.

[63] Xu, Y., Liu, M., and Tang, C., 2013, "Three-dimensional CFD-VOF-DPM simulations of effects of low-holdup particles on single-nozzle bubbling behavior in gas-liquid-solid systems," Chemical engineering journal, **222**, pp. 292-306.

[64] Zhao, B., Yang, C., Yang, X., and Liu, S., 2008, "Particle dispersion and deposition in ventilated rooms: Testing and evaluation of different Eulerian and Lagrangian models," Building and Environment, **43**(4), pp. 388-397.

[65] Lemmon, E. W., Huber, M. L., and McLinden, M. O., 2013, "NIST Standard Reference Database 23: Reference Fluid Thermodynamic and Transport Properties-REFPROP, Version 9.1, National Institute of Standards and Technology,"Gaithersburg.

[66] Tillner-RothR., and Baehr, H. D., 1994, "An international standard formulation of the thermodynamic properties
of 1,1,1,2-tetrafluoroethane (HFC-134a) for temperatures from 170 K
to 455 K at pressures up to 70 MPa," J. Phys. Chem. Ref. Data, **23**, pp. 657-729.

[67] Wagner, W., and Pruss, A., 2002, "The IAPWS Formulation 1995 for the Thermodynamic Properties of Ordinary Water Substance for General and Scientific Use," J. Phys. Chem. Ref. Data, **31**, pp. 387-535.

[68] Younglove, B. A., and McLinden, M. O., 1994, "An International Standard Equation of State for the Thermodynamic Properties of Refrigerant 123 (2,2-Dichloro-1,1,1-trifluoroethane)," J. Phys. Chem. Ref. Data, **23**, pp. 731-779.

[69] Figliola, R. S., and Beasley, D. E., 1991, Theory and design for mechanical measurements, John Wiley & Sons, Inc, New York.

[70] White, F. M., 1991, Viscous fluid flow, New York : McGraw-Hill, New York.

[71] 2017, "ANSYS® Fluent User's Guide, Release 18.2," ANSYS, Inc., Canonsburg, PA.